UNIVERSITÀ
DEGLI STUDI
DI PADOVA

Head Office: Università degli Studi di Padova

Department of Industrial Engineering

Ph.D. COURSE IN: Science and Engineering of Materials and Nanostructures (SIMN)

SERIES XXXI

ELECTRICAL ENERGY STORAGE BY ELECTROCHEMICAL VANADIUM REDOX FLOW BATTERY METHODS

Thesis written with the financial contribution of HPS srl

Coordinator: Prof. Giovanni Mattei
Supervisor: Prof. Vito Di Noto

Ph.D. student : Chuanyu Sun

Abstract

Redox flow batteries (RFBs) are electrochemical cells that are able to reversibly convert the chemical energy stored into the redox couples into electrical power. Vanadium redox flow batteries (VRFBs) exploit redox couples both based on vanadium species. To make VRFB technology commercially viable, technical and economic barriers including high capital cost and rapid capacity decay need to be addressed. The primary objective of this thesis is to achieve high performance VRFB with long durability, mainly by reducing the vanadium permeability through the membrane. Nowadays perfluorosulfonic acid membranes are widely used in VRFB, such as Nafion. Nafion has high chemical and mechanical stability, and it exhibits good proton conductivity. Nevertheless, the VRFB cell with Nafion membrane has fast capacity decay due to the high vanadium crossover.

In an effort to overcome the limitations of Nafion, this thesis reports the synthesis and characterization of hybrid inorganic-organic proton-conducting membrane alternatives to classic perfluorinated ionomers. Two families of hybrid membranes were synthesized:
1) Nafion membrane doped with WO_3 nanofiller, in order to reduce its vanadium crossover while maintaining the high proton conductivity;
2) synthesis of sulfonated poly (ether ether ketone) (SPEEK) membrane with optimized degree of sulfonation as an alternative low-cost membrane. Then further dope the SPEEK membrane with WO_3 to reduce vanadium crossover.

For all the hybrid membranes prepared by a solvent-casting procedure, the introduction of WO_3 nanoparticles does not alter significantly the thermal degradation events of the polymer host and the hybrid membranes maintain the good thermal stability. MDSC reveals that in hybrid membranes the endothermic events are slightly shifted attributed to the formation of *"dynamic crosslinks"* between the WO_3 nanoparticles and the polymer host, that stabilize the hybrid membrane. The hydrophilic domains of the polymer host are reduced in size as the content of WO_3 is raised. The water uptake of hybrid membranes decreases with the increasing loading of WO_3 nanofillers; as a consequence, the pathways of charge migration become more tortuous. While the higher charge migration tortuosity would correspond to a dramatically lower permeability to vanadium species. The tortuosity for protons is likely much less than that for vanadium, as the vanadium ions are only passing through the bulk water, while the protons are also delocalized at the polymer-nanofiller interfaces in the presence of interface water. The vanadium permeability of hybrid membranes decreases significantly and the ion selectivity is much improved in comparison with Nafion. The hybrid membranes with highest ion selectivity are chosen for VRFB single cell test. They exhibits a higher coulombic efficiency in comparison with the Nafion 212 reference. The reduced permeation of vanadium species is also revealed by the lower discharge capacity decay and longer self-discharge times for the hybrid

membranes. Therefore, the new family of hybrid membranes may be promising candidates for application in VRFBs.

The final chapter describes the study by Raman spectroscopy of the species present in the positive feed of a VRFB as a function of the state of charge (SOC). Changes in complexation due to presence of stable oxygenated coordination complexes of vanadium, also interacting strongly with HSO_4^- and SO_4^{2-} ligands, are put in evidence. In particular, it is demonstrated that the positive feed includes additional species beyond VO^{2+} and VO_2^+, with a particular reference to dimers such as $HV_2O_5^-$ and $H_3V_2O_7^-$. Such species may be accounted to understand in detail the charge-discharge processes taking place at the electrodes of a VRFB. Indeed, on these bases, the processes are expected to involve a broad distribution of V(IV) and V(V) species, that may end up affecting significantly crucial macroscopic features of the overall VRFB.

Sommario (in Italian)

Le batterie Redox a Flusso (RFB) sono celle elettrochimiche capaci di convertire reversibilmente l'energia chimica immagazzinata in coppie redox in energia elettrica. Le batterie a flusso al vanadio (VRFB) sfruttano coppie redox entrambe basate su specie di vanadio. Per far sì che la tecnologia VRFB sia commercialmente valida, occorre superare barriere tecniche ed economiche che includono elevati costi di capitale ed un rapido decadimento della capacità. L'obiettivo principale di questa tesi è di ottenere VRFB ad alte prestazioni e di lunga durata, principalmente riducendo la permeabilità del vanadio attraverso la membrana. Al giorno d'oggi nelle VRFB vengono utilizzate membrane a base di acido perfluorosolfonico, come il Nafion. Il Nafion ha un'elevata stabilità chimica e meccanica, e presenta una buona conducibilità protonica. La VRFB con membrana al Nafion hanno un rapido decadimento della capacità a causa dell'alto crossover del vanadio.

Per superare i limiti del Nafion, questa tesi riporta la sintesi e la caratterizzazione di membrane ibride inorganico-organiche conduttrici di protoni alternative agli ionomeri perfluorurati. Due famiglie di membrane ibride sono state ottenute:

1) membrana di Nafion drogata con nanofiller WO_3, per ridurre il crossover del vanadio mantenendo un'elevata conducibilità protonica;

2) sintesi di una membrana a base di poli(etere-etere-chetone) solfonato (SPEEK), con grado di solfonazione ottimizzato. Anche la membrana a base di SPEEK viene poi drogata con WO_3 per ridurre il crossover del vanadio.

Nelle membrane ibride preparate mediante una procedura di solvent-casting, l'introduzione di nanoparticelle di WO_3 non altera in modo significativo gli eventi di degradazione termica della matrice polimerica, mantenendo così una buona stabilità termica. Misure MDSC rivelano che nelle membrane ibride gli eventi termici sono leggermente spostati a causa della formazione di "crosslink dinamici" tra le nanoparticelle di WO_3 e la matrice polimerica, che stabilizzano la membrana. La dimensione dei domini idrofili e l'assorbimento d'acqua della mambrana si riducono all'aumentare del contenuto di WO_3. Di conseguenza, i percorsi di migrazione di carica diventano più tortuosi. Questa maggiore tortuosità alla migrazione di carica corrisponde ad una permeabilità inferiore delle specie vanadio. Al contrario del vanadio, la tortuosità ha probabilmente un effetto inferiore per i protoni, poiché gli ioni di vanadio attraversano solo i domini massivi di acqua, mentre i protoni vengono scambiati anche alle interfacce polimero-nanofiller. Così, la permeabilità al vanadio delle membrane ibride diminuisce significativamente e la selettività degli ioni è molto migliorata rispetto al Nafion. Le migliori membrane ibride sono scelte per il test in cella VRFB. Esse esibiscono una maggiore efficienza coulombica rispetto al riferimento Nafion 212. La ridotta permeazione delle specie di vanadio è rivelata anche dal minore decadimento della capacità di scarica e dai tempi di autoscarica più lunghi per le membrane ibride. Pertanto, la nuova famiglia di membrane

ibride è un promettente candidato per l'applicazione in VRFB.
Il capitolo finale descrive lo studio, attraverso la spettroscopia Raman, delle specie presenti nella soluzione positiva (catolita) di una VRFB in funzione dello stato di carica (SOC). Gli equilibri dovuti alla presenza di complessi di coordinazione del vanadio, che interagiscono fortemente con i leganti HSO_4^- e SO_4^{2-}, vengono evidenziati. In particolare, viene dimostrato come il catolita includa specie addizionali oltre a VO^{2+} e VO_2^+, quali $HV_2O_5^-$ e $H_3V_2O_7^-$. La presenza di tali specie deve essere considerata per comprendere in dettaglio i processi di scarica e carica che avvengono agli elettrodi di una VRFB. Infatti, su queste basi, ci si aspetta il coinvolgimento di un'ampia distribuzione di specie V(IV) e V(V), che potrebbero influenzare le caratteristiche macroscopiche significativamente cruciali di una VRFB.

Acknowledgments

Firstly, I would like to thank my academic advisor Prof. Vito Di Noto, for giving me the opportunity to research in the interesting topic and for all of the support and guidance throughout my entire doctoral study. Your mentoring, patience and inspiration have largely helped me to grow and be a professional researcher in my fields. Thank you for being my endless source of knowledge.

I would like also to thank the HPS srl, especially Ing. Gabriele Caoduro and Ing. Paolo Tondello, for the financial support they provided for the realization of this PHD project.

The supporting from other members in Prof. Di Noto group, also helped me a lot in my research work at Padova. The atmosphere in the group is full of friendliness, creativity, and cooperation, making my study and research very enjoyable. I want to particularly give my gratitude to Prof. Enrico Negro, who taught me a lot of lab skills and helped me so much in scientific writing. It was wonderful to work with colleagues Dr. Keti Vezzù, Dr. Giuseppe Pace, Dr. Agnieszka Zlotorowicz, Dr. Gioele Pagot, Dr. Graeme Nawn, Dr. Antoine Bach Delpeuch, Dr. Federico Bertasi, Dr. Yannick Hervé Bang, Dr. Angeloclaudio Nale, Dr. Sara Tonello, Dr. Edoardo Donà and Dr. Marco Bandiera. I appreciate the help and collaboration from all the group members.

I appreciate the support from Department of Industrial Engineering and Chemical Science, and the University of Padova. My department and university offered me a valuable opportunity to study on a creative and friendly campus.

I also want to express my deep gratitude to all my Chinese friends meeting in Padova, for all your company, help and sharing: Bai Chengying, Tu Chengyi, Liu Lu, Yang Sheng, Xiao Hubing, Zheng Meng, Sun Xiaohuan, Wang Yawei, Lai Can, Hu Yan, Peng Wei, Jin Xin, Wang Wenjie, Wen Shutao, Zhong Bili, Zhu Bin, Song Sha, Tong Daming, Zhang Xiaoyu, Fei Wenwen, Chen Yang, Zhuang Qiuyu, Chen Yutao, Chang Lei, Zheng Jian, Li Qianqian, Yang Yang, Prof. Xu Li, Feng Lisi, Ding Ding, Liang Ning, Xiong Rongchuan, Ni Tao, Lyu Yanchao, Tang Panjuan, Yu Jiaying, Chen Rui and Guo Tianyi.

Finally, I really want to express my lofty gratitude to my family, my mother and father, who have been educating me to be an honest and kind person for years. And they always support me to pursue my dream and work hard for it. Their supporting is the best comfort for me in undertaking the doctoral study in the University of Padova and improving myself, far away from my homeland.

Sun Chuanyu

Table of Contents

Chapter I Introduction

The large-scale use of CO_2-emitting fossil fuel and the exhaustion of fossil energy reserves pose a great impact on the already severe environmental and energy issues facing our planet today. Therefore, the utilization of sustainable energy is believed to help release the stress of energy shortage in our times and in the future [4]. The mismatch between the intermittent energy production from sustainable sources, such as solar, wind and tide sources, and the fluctuating energy consumption requires energy storage and conversion systems with large capacity [5]. Electrochemical Energy Storage (EES) systems are promising solutions to tackle this challenge.

1.1 Electrochemical energy storage systems

Nowadays, using and developing renewable energy sources, notably solar and wind power, on a large scale is urgent for the sustainable development. However, because of their intermittent nature, the potential of these energy sources can be fully exploited only if efficient, safe, cost-effective, and reliable electrical energy storage systems are available [6, 7]. Energy storage systems (ESS) will be critical to improving the robustness and efficiency of the electrical distribution grid by peak shaving and load leveling. While the need for energy storage in renewable energy storage applications has been understood for several decades, energy storage in general was largely ignored until recently due to the additional cost that would be introduced into any power generation system [8]. Governments around the world are now stressing the need for integrating storage into the so-called “Smart Grids” of the future [6, 9]. In addition to renewable energy, ESS can also be used in existing thermal power grid systems by burning fossil fuel. By making better use of the power in the power grid, we can effectively reduce the consumption of fossil fuels as well. An example of energy storage and load/peak shifting of solar energy is shown in Figure 1.1. As can be seen from the figure, the intermittent solar energy can be used continuously, depending on the customers as the

demand arises. Specifically, the unconsumed energy generated when there is sunlight radiation is stored in the energy storage device, and the energy is released from the energy storage device when there is no solar energy generation (e.g. cloudy and rainy weather).

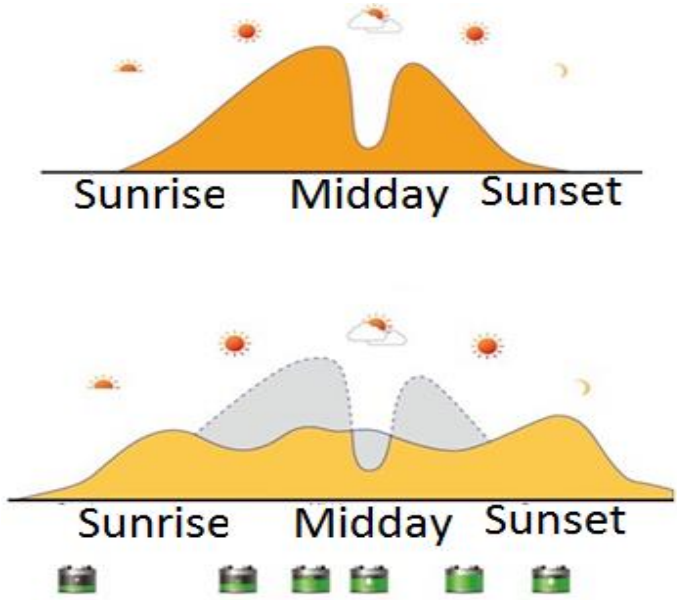

Figure 1.1 Example of energy storage and load/peak shifting for solar energy

EES systems are systems utilizing electrochemical phenomena to realize the energy conversion between the form of electrical and chemical ones, which is reversible [10]. Depending on the utilized electrochemical phenomena, EES systems can be divided into supercapacitors in which charge storage occurs in the electrode-electrolyte interface, into fuel cells and batteries where electrochemical reactions (charge transfer) occur [10]. The energy conversion in fuel cells and some batteries (primary battery) is irreversible, while in supercapacitors and some batteries (secondary batteries) it is reversible. Regenerative fuel cells are also capable to act as electrolyzers and are thus reversible. The principle of all fuel cells is basically the same: convert the chemical energy from a fuel into electricity through an electrochemical reaction of the fuel with oxygen. Fuel cells are different from batteries in requiring a continuous source of the fuel and oxygen (usually from air) to sustain the chemical reaction, whereas in a battery the chemical energy comes from chemicals already present in the battery. Fuel cells can produce electricity continuously for as long as fuel and oxygen are supplied. However, in the sense of electrochemical reversibility, primary batteries

are the same as non-regenerative fuel cells.

A number of different energy storage technologies has been developed and a comparison of these technologies for different applications is presented in Table 1.1. Each technology has some inherent limitations or disadvantages that make it practical or economical for only a limited range of applications. For instance, although pumped hydro and compressed gas are now cost-effective in certain situations, these technologies are significantly limited by geography. Supercapacitors have split-second response times, deep discharge capability, and can deliver high power, but only for short durations, making them more suitable for power quality management rather than grid energy storage. When combining performance requirements with cost, EES systems are seen to be superior to the other forms of energy storage since they can provide direct conversion between chemical energy and electrical energy and are therefore particularly suited to the storage of electrical energy from all sources [11-14]

The EES technologies, also offer additional advantages compared with other types of energy storage systems, including:

1) can be sited anywhere, which means they have no specific geographical or geological requirements;

2) can be easily scaled up and thus can be used in applications ranging from a few kWh to several MWh;

3) have relatively fast response times so that they can be used simultaneously for both power quality and energy management applications;

4) have low environmental footprints so can be sited near residential areas.

Table 1.1 Comparison of technicalities of different energy storage devices.

Technology option	Power (MW)	Durations (hours)	Efficiencies (%)	Cost (USD/kWh)	Limitations
Pumped hydro	10-1000	>8	70-85	80-200	Special geological and geographic requirements
Compressed air	10-1000	0.1-15	60-70	50-110	Special geological and geographic requirements
Super-capacitors	<0.1	0.02-1	>95	~2000	Low energy density
Lead-acid batteries	~10	0.1-4	70-80	~350	Short life time and environmental issue
Lithium ion batteries	~100	0.1-1	>90	850-5000	High cost and low safety
Lithium sulfur batteries	-	disputed	>98	200	Rapid discharge and low electrical conductivity of sulfur cathode
Molten-salt battery	-	disputed	>69	100	Insulator corrosion leads to insulator becomes conductive, and the self-discharge rate increases.
Sodium-ion battery	-	Testing	>85	48	Inferior cycling performance

Nevertheless, in both types of EES, the electrolyte/electrode is confined in the interior of the battery, therefore the capacity is limited by the size of the battery. To increase the capacity of some secondary batteries (e.g. lithium ion batteries) for the application in large-scale energy storage possesses potential security risks, therefore the concept of redox flow battery (RFB) is devised.

1.2 Redox flow battery

Among different battery technologies, RFB has been regarded as a leading technology for grid-scale energy storage due to its unique flow cell architecture, which offers several great advantages for the large-scale applications, including excellent system scalability, long cycle-life, high efficiency, and site-independence. An RFB differs from a conventional secondary battery in the way that the liquid electrolyte in a flow battery can be circulated between the stack and the tank as desired. Putting it simply, a redox flow battery consists of two reservoirs for storing catholyte and anolyte containing soluble active species for charge/discharge purposes as they are able to undergo the desired redox reactions, an energy converting device composed of positive and negative electrodes separated by a membrane, pumps for pumping the electrolytes through the energy converting device and external circuit connected to the power source or load, as shown in Figure 1.2 [15].

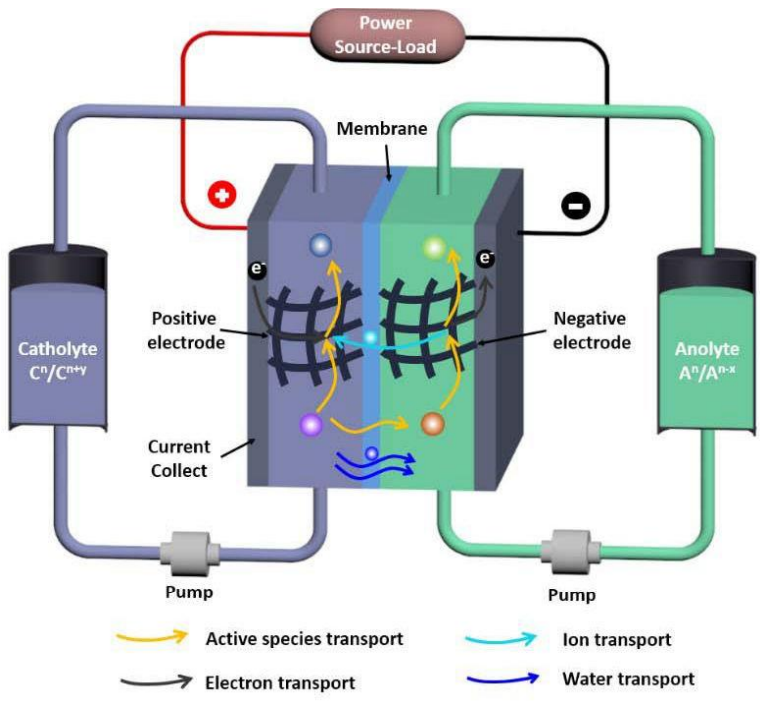

Figure 1.2 A schematic diagram of a redox flow battery with electron transport, ion transport, and active species transport in the electrode, active species transport, water transport and ion transport through the membrane.

As seen in Figure 1.2, an RFB cell typically consists of two porous carbon electrodes separated by an ion-exchange membrane (or a separator). Porous carbon electrodes are used due to their wide operating potential range, stability as both an anode and a cathode, availability in high surface activity and high surface area for electrochemical reactions to minimize the activation loss, and excellent electronic conductivity to minimize the ohmic loss [16]. During the battery operation, positive and negative electrolytes, including active species and supporting electrolyte(mainly acid form, which provides ionic conductivity, especially proton conductivity), are stored in the respective external tanks and circulated through the porous carbon electrodes, where the electrochemical reactions occur to store or release electricity. During the operation, oxidation or reduction reactions at the positive and negative electrodes can be expressed as [17]:

In the positive electrode:

$$C^{n} \underset{\text{Discharge}}{\overset{\text{Charge}}{\rightleftharpoons}} C^{n+y} + ye^{-}$$

In the negative electrode:

$$A^{n+x} + xe^{-} \underset{\text{Discharge}}{\overset{\text{Charge}}{\rightleftharpoons}} A^{n}$$

The key transport processes are illustrated in Figure 1.2. During operation, mass transport of the active species in both positive and negative electrodes can be described as follows:

i) reactants are transferred from the inlet to the pores of the porous electrode, which is subjective to the so-called representative element volume(REV) level transport;

ii) reactants are then transported from the pores to the surfaces of the electrode, which is the so-called pore-level transport;

iii) after electrochemical reactions, resulted products transport from the electrode surface back to the pores and then transfer to the outlet.

Hence, the mass transport processes should be subject to a tran-scale process (macro-scale REV level and micro-scale pore level), which is also coupled with the complex fluid flowing

porous media and electrochemical reactions. To maintain the electrical neutrality, the charged ions (non-active) are required to be transported from the macro-scale pores in one porous electrode to pores in another one through the ion exchange membranes where the transport channels are usually several nanometers in sizes. Electron transportation in the solid matrix of electrode are fairly straightforward. In practical operations, in addition to the non-active charged ions, the active species are transported through the membrane due to that the membrane is not ideal to be impermeable to the active species, identified as active species crossover, resulting in self-discharge and thereby capacity decay. Similarly, solvent (water) also can transport through the membrane from one half-cell to another, leading to preferential water transfer. Studies show that the transfer of water across the membranes during the charge and discharge cycling process involves a number of processes, such as water transported by ions moving under a concentration gradient, water carried by the charge balancing species and water transport due to the osmotic pressure difference between the two half-cell solutions [18]. In the case of the VRFB used cation membrane, the transfer of water is from negative half-cell to positive half-cell caused by the hydration shells of V^{2+} and V^{3+} ions carrying a large amount of water [19, 20]. This phenomenon leads to problems associated with the establishment of concentration difference in the electrolytic solutions feeding both electrodes. The detailed mechanism on the basis of water transfer across Nafion membrane is not comprehensively understood. However, it has been suggested that it is mainly caused by the transfer of hydrate vanadium ions between the two half-cells [18, 19, 21, 22].

During the RFB operation, energy is stored in the solutions and the capacity of the system is determined by the concentration of the active redox couple species and the solution volume. On the other hand, the power rating of the system is determined by the number of cells in the cell stack and the electrode area. In this regard, the energy and power of this type of energy storage system can be scaled independently, which enables flexibility in the design of flow batteries. By simply increasing the volume of electrolyte and the concentration of electro-active species, a large capacity can be attained for grid-scale energy storage [4, 7].

In addition, the electrode itself does not undergo chemical or morphological changes during the electrochemical reactions, enabling an ultra-long cycle life. Furthermore, since the electrochemical reactions involve no phase change and are highly reversible (especially VRFB), the round-trip efficiency of this technology can be very high. These desirable merits of redox flow batteries make the present technology highly promising for the large scale energy storage applications.

Historically, the first modern RFB is an aqueous iron-chromium system, which was developed at NASA in the 1970s [23]. After that, numerous aqueous RFBs have been proposed and investigated, including all-vanadium [24], bromine-polysulfide [25] and vanadium-polyhalide [26]. In addition, some aqueous hybrid batteries have been developed, where electrode reactions involve the deposition/dissolution process, e.g. zinc bromine system [27]. Recent years, several kinds of non-aqueous systems have been pursued [9, 28]. The main features of each type of RFB are introduced in Table 1.2

For the aqueous RFBs, some of them have been demonstrated successfully at large-scale, approaching commercialization. The current research effort is to further improve the performance in terms of power density, efficiency and cyclability. With regard to the non-aqueous RFBs, the main issue at the current stage is the lack of qualified candidates of redox couples, solvents as well as supporting electrolytes [5, 29, 30]. The basic chemistry and standard cell potentials (E^0) of these flow batteries are listed in Table 1.2. In this table, the direction of the electrochemical reactions depicts the one during the battery discharge.

One disadvantage of the use of two separate redox species in the half-cells, leading to the potential for cross-contamination of active electrolytes by transport through the membrane. For example, there has been little recent interest in the development of the iron/chromium redox flow cell due to this problem [31]. Among the RFBs listed in Table 1.1, all-Vanadium Redox Flow Battery (VRFB) has shown cycle life as long as 100,000 charge-discharge cycles (duration of 20 years) [5]. The presence of the same element in both catholyte and anolyte prevents the cross-contamination of electrolyte encountered in all other types of RFBs. These

features make VRFB the most promising one among other types of RFBs. This thesis mainly focuses on the development of materials for all vanadium redox flow battery (VRFB), which has been regarded as the most promising chemistries among different RFBs.

Table 1.2 Different redox flow batteries.

Type	Positive Terminal	Negative Terminal	E^0 / V	References
Polysulfide Bromide	$Br_3^- + 2e^- \rightarrow 3Br^-$	$2S_2^{2-} \rightarrow S_4^{2-} + 2e^-$	1.35	[7, 32]
All Vanadium	$VO_2^+ + 2H^+ + e^- \rightarrow VO^{2+} + H_2O$	$V^{2+} \rightarrow V^{3+} + e^-$	1.26	[7, 32]
Vanadium Bromine	$ClBr_2^- + 2e^- \rightarrow 2Br^- + Cl^-$	$2VBr_2 + 2Br^- \rightarrow 2VBr_3 + 2e^-$	1.30	[7, 32]
Iron Chromium	$Fe^{3+} + e^- \rightarrow Fe^{2+}$	$Cr^{2+} \rightarrow Cr^{3+} + e^-$	1.18	[7, 32]
Zinc Bromine	$Br_3^- + 2e^- \rightarrow 3Br^-$	$Zn \rightarrow Zn^{2+} + 2e^-$	1.85	[32]
Zinc Cerium	$Ce^{4+} + 2e^- \rightarrow 2Ce^{3+}$	$Zn \rightarrow Zn^{2+} + 2e^-$	2.40	[32]
Iron Vanadium	$Fe^{3+} + e^- \rightarrow Fe^{2+}$	$V^{2+} \rightarrow V^{3+} + e^-$	1.02	[33]

1.3 All-vanadium redox flow batteries

1.3.1 General description

Research on the all-vanadium redox flow battery first began in 1984 at the University of New South Wales (UNSW), Australia under funding from the National Energy Development and Demonstration Council. The VRFB was first proposed by Skyllas-Kazacos and co-workers to overcome the inherent problem of cross contamination by diffusion of different redox ions across the membrane. By employing the same element in both half-cells, any cross-contamination would be avoided, allowing the electrolyte life to be extended indefinitely [32, 34, 35].

A pioneering 1 kW VRFB stack was built by Kazacos group. 1.33 kW power and 72% energy efficiency were achieved on the battery stack at a current density 80 $mA \cdot cm^{-2}$, with 1.5 $mol \cdot L^{-1}$ vanadium in 4 $mol \cdot L^{-1}$ total sulfate electrolyte solutions at room temperature [36]. The stack showed steady voltage and coulombic efficiencies over 100 cycles without obvious capacity loss. Later, several other experimental kW-level VRFB stacks built by other researchers have been reported [37, 38]. Over 80% energy efficiency can be achieved in a current density range of 50 to 140 $mA \cdot cm^{-2}$ on various systems. The 20 kW cell stack developed by Sumitomo Electric Industries (SEI) was reported to have lasted over 12,000 cycles with over 80% energy efficiency at 50 $mA \cdot cm^{-2}$ current density [39]. The high cycle number achieved by the Sumitomo demonstration product proved the high durability and reliability of VRFB. Since the invention of VRFB, a number of practical VRFB systems, most of them at MW/MW·h power/capacity level, have been built and operated for different applications in many countries [40-42].

The charge-discharge reactions for both half-cells are shown as follows:

Positive electrode (catholyte):

$$VO^{2+} + H_2O \underset{\text{Discharge}}{\overset{\text{Charge}}{\rightleftharpoons}} VO_2^{+} + 2H^{+} + e^{-}$$

E^0= + 1.00 V vs. SHE

Negative electrode (anolyte):

$$V^{3+} + e^{-} \underset{\text{Discharge}}{\overset{\text{Charge}}{\rightleftharpoons}} V^{2+}$$

E^0= - 0.26 V vs. SHE

Overall reaction:

$$VO^{2+} + V^{3+} + H_2O \underset{\text{Discharge}}{\overset{\text{Charge}}{\rightleftharpoons}} VO_2^{+} + V^{3+} + 2H^{+}$$

E^0= + 1.26 V vs. SHE

At the standard reference temperature and pressure (T=25 °C and P=1.0 atm), the reversible cell voltage is 1.26 V vs. SHE. This system has been successfully operated over a temperature range of 10-40 °C [32, 34, 35]. The energy density for 2.0 M vanadium electrolytes is approximately 25 Wh/g [43].

The function of each component in VRFB cell determines the characteristic requirements of the system. The membrane separator in the cell separates electrolyte to prevent direct contact and reaction between vanadium ions of varying redox states and minimizes unwanted mass transport. To conduct ionic current, the separator should have high ion conductivity to minimize ohmic loss. A cation exchange membrane such as Nafion is commonly used as the electrolyte separator [36, 44, 45]. However, cation exchange membrane performance can be limited because of its conductivity decrease when in contact with the vanadium-acid electrolyte and its low ion selectivity [46, 47]. It is reported a strong decrease of membrane conductivity is observed upon vanadium existence in the membrane. Since the concentrations of vanadyl ions and protons in the membrane are balanced by the number of sulfonic acid groups, uptake of vanadyl can reduce the proton concentration. Because metallic cations have

much lower mobility than protons in fully hydrated Nafion, membranes containing cations generally have much lower conductivity than unexchanged proton-form membranes [46]. The electrode in a VRFB cell is generally a porous carbon material, which is electronically conductive and resistant to chemical and electrochemical corrosion in electrolyte [48, 49]. The porous electrode structure can also provide a relatively high surface area to support vanadium redox reactions to improve mass transport. The current collector (or bipolar plate in a cell stack) connects the electrode and external circuit to conduct electricity. In addition, the current collector should be impermeable to the electrolyte solution and air to prevent electrolyte leakage and air penetration. Good resistance to electrolyte corrosion is also required to improve battery durability and reliability.

A few experimental investigations into flow fields of VRFBs have been reported [48-50]. Zhu et al. [50] investigated the effects of two different flow fields, one with a flow-by pattern while the other with a flow-through pattern, on the performance of a VRFB. The experimental results suggested that the flow-through pattern tended to increase the electrode effective active area and to enhance the uniformity of liquid electrolyte, resulting in an improvement in the energy efficiency by up to 5%. In a flow-by battery cell architecture, flow channels are built into the current collector to distribute electrolyte solution into the electrodes [48, 49]. In this case, the mechanical durability of the current collector is also of great importance to withstand any friction from electrolyte flow. Recently, Zawodzinski et al. [48, 49, 51] introduced a zero-gap cell architecture with a serpentine flow field similar to fuel cells with carbon paper electrodes, enabling the peak power density to be 767 mW cm^{-2}, which is significantly higher than the conventional cell configuration. The zero-gap structure and thin carbon paper electrodes enable lower ohmic resistances in the cell due to better contact between all components, and lower charge transfer distances across the cell. In addition, the application of a serpentine flow channel greatly enhances the mass transfer in the porous electrode by the distribution of the electrolyte across the entire membrane surface area. In this thesis, we adopt the zero-gap cell architecture and the detailed components will be introduced in Chapter 2.

The electrolyte solution carries energy in the form of dissolved vanadium redox couples. Typically, the electrolyte solution is an aqueous solution of 1 to 2 mol·L^{-1} vanadium sulfate salt ($VOSO_4$) and excess sulfuric acid as supporting electrolyte [45, 48, 49]. The practical concentration of vanadium is limited by the stability of vanadium in electrolyte solution [52]. The sulfuric acid influences vanadium solubility and conductivity. As the sulfuric acid concentration increases, the solubility decreases for V(II), V(III), and V(IV) ions [53] due to the common ion effect; with increasing H_2SO_4 concentration, the total sulfate concentration increases, which shifts the equilibrium to lower dissociation of vanadium sulfate. Rahman [53] measured the V(IV) ion solubility with varying H_2SO_4 concentration and temperature. It is reported that the rate of the decrease of V(IV) solubility with H_2SO_4 concentration is higher for the low acid concentration regime than that for high acid concentration regime due to a higher dissociation of bisulfate ions (HSO_4^-) to sulfate ions (SO_4^{2-}). However, for V(V) ions, its stability increase with increasing H_2SO_4 concentration. To achieve higher energy density and better electrochemical performance, several methods have been used to improve vanadium solubility and electrolyte stability [54, 55]. More detailed discussion about electrolyte performance improvement will be presented in a later section.

The electrolyte storage and transport subsystem is a supporting part of the flow battery. Since V^{2+} is very sensitive to air oxidation, electrolytes, especially negative electrolyte, must be stored and sealed in oxygen-free containers and tubing/pipe with high tolerance to corrosive environment in the electrolyte. Several kinds of polymeric materials, such as polypropylene (PP) and polytetrafluoroethylene (PTFE), are stable enough to contact the electrolyte and may be used for the tubing/pipe materials. To prevent battery capacity loss due to V^{2+} oxidation, a nitrogen atmosphere is usually kept in the electrolyte reservoir in lab setups [56]. During operation, the electrolytes are continuously circulated by pumps between the reservoir and cells. The flow rate must be optimized by balancing battery performance and pump pressure loss [48].

1.3.2 Advantages

As mentioned before, the active species in both catholyte and anolyte are only vanadium ions at different oxidation states, the cross contamination issue would be avoided, allowing the electrolyte life to be extended indefinitely. In addition, its features also include: tolerance to deep discharge without any risk of damage, active thermal management, independence of energy and power ratings and high efficiency (the round-trip energy efficiency is higher than 80%).

1.3.3 Challenges

Although the VRFB offers a promise for high-efficient large-scale energy storage, its commercialization progress is still hindered by technical and economic issues, which are briefly summarized as follows:

One of the biggest issues encountered in the VRFB is the relatively low power density than the expected level, mainly due to the limited solubility of vanadium species. Improvement in the power density has at least three-fold benefits:
1) requiring a smaller total area of electrodes and membranes to attain the same power, thereby reducing the cost of a VRFB;
2) upgrading the energy-conversion efficiency at high power density;
3) enabling the VRFB to be operated at a wider current range without dramatically sacrificing the efficiency and thus making it more flexible to an unpredictable change of grid power.

In general, the power density is determined by the kinetic, ohmic and mass-transport polarization. The kinetic polarization and mass-transport polarization depend on electrode materials and structural properties such as pore dimension, pore size distribution and electrode thickness. For given electrodes and membranes, the ohmic and mass-transport polarization are directly related to the coupled transport of charge and mass species. Therefore, it is of great significance to develop new electrodes with sufficient highly-active

areas and gain a deep insight into the unique transport phenomena in a VRFB. However, realizing these goals is rather challenging because the VRFB is a complex trans-scale system with the length scale ranging from nanometer(electrode and membrane) to millimeter (flow field), and involves multi-component flow through porous electrodes with redox reactions. However, relatively few efforts have been made to investigate the transport characteristics and their corresponding effects on the power density of a VRFB.

Another well-recognized issue that hinders the commercialization of VRFBs is the precious Nafion membrane and the significant crossover of vanadium ions through membranes. The ion exchange membrane (IEM) is a key component of VRFBs, which not only separates the catholyte and anolyte but also transports protons to ensure the electro-neutrality of the system. Currently, the widely used membranes in VRFBs system are perfluorosulfonic cation membranes (such as Nafion). Nafion membranes show high ionic conductivity and good chemical stability when applied in VRFBs but suffer from significant active species crossover and high material cost. The crossover of vanadium ions through the membrane will cause self-discharge with the chemical energy loss [57]. The self-discharge of VRFB is mainly attributed to the diffusion of vanadium ions from one half-cell to the other half-cell driven by concentration difference between the two half-cells, as well as crossover driven by electrical potential gradient and hydraulic pressure gradient across the membrane [58]. Previous studies show that crossover of vanadium ions not only results in a reduction of columbic efficiency but also causes an imbalance of state of charge between the positive half-cell and negative half-cell, resulting in a capacity decay during cycling [19]. To address this issue, it is of great significance to develop new membranes with both high ion conductivity and low vanadium permeability and gain a deep insight into the unique transport phenomena inside the membrane. Although a lot of alternative membranes have been investigated and tested in VRFBs, there is still no suitable membrane that can replace Nafion membranes and provide ideal properties so far. In addition, the vanadium transport mechanism has not been fully understood and thus limited strategies have been proposed to suppress the vanadium crossover.

As shown in Figure 1.3, the basic function of a membrane in VRFB is isolating electro-active V^{n+} ions (V^{2+}, V^{3+}; VO^{2+}, VO_2^+) while allowing the passage of charge-carriers (mostly H^+) at a sufficiently high rate, which essentially means high H^+/V^{n+} transport selectivity and high H^+ conductivity [58]. The harsh application environment of a membrane in VRFB involves strong acids (2 - 4 M H_2SO_4) and the oxidative VO_2^+/reductive V^{2+} ions present in the electrolyte [59]. Therefore, membranes should ideally also be chemically durable for more than 10 years as suggested [60]. Currently, the research focus on non-fluorinated ionomers [61, 62] or porous separators [63, 64] is aimed at finding efficient and durable, yet low-cost alternatives to PFSA membranes [58, 59].

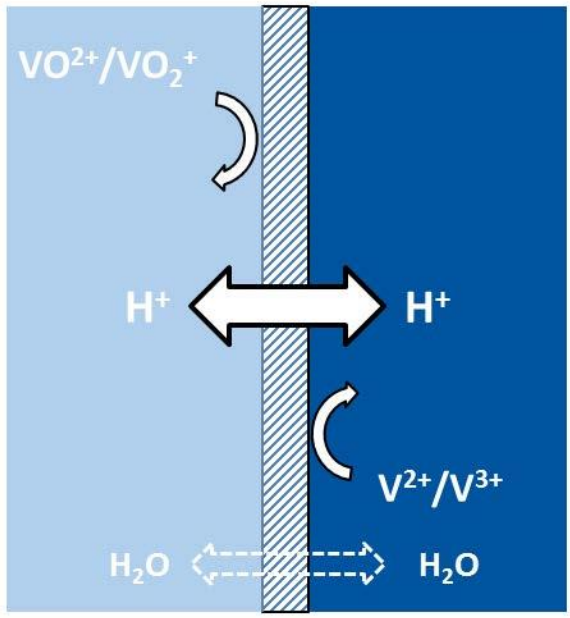

Figure 1.3 The various requirements of an ideal membrane separator in VRFB.

A detailed description of the effort devoted to developing membrane separators for VRFB in the past decade can be found in the literature [58, 59, 65]. A short summary of the key requirements can be enumerated in priority as follows:

1) low V^{n+} ion permeability, to reduce vanadium cross-over and capacity decline over cycles;

2) high ionic conductivity, to increase the energy efficiency;

3) sufficient chemical stability, especially stability against VO_2^+ ions, to increase the service lifetime;

4) low preparation cost, to decrease the price;

5) easy and scalable membrane preparation method, for large-scale fabrication;

6) low water cross-over, to avoid flooding and deterioration of battery performance.

The first two requirements mean a very high H^+/V^{n+} transport selectivity (typically more than 10^{-4} $S \cdot min \cdot cm^{-3}$) of the membranes. The new porous ion exchange membrane for VRFB presented in this thesis is characterized according to these criteria.

1.3.4 Carbon Electrode and Its Improvement

The function of the electrode in VRFB requires its material to be electrically conductive, resistant to chemical and electrochemical corrosion in the electrolyte, to be porous to support facile transport of electrolyte and to provide a large active surface area to support redox reactions. Porous carbon was selected as the electrode material for both positive and negative electrodes, due to its conductivity and chemical stability, relatively low cost and porous structure [49, 66-68]. Several carbon materials are available with highly variable pore structure, surface chemistry, internal surface area and other properties.

Graphite felt was first used as an electrode material in the early stage studies on vanadium redox flow battery cells [44]. The electrode material exhibited good stability over 2000 hours and performed well in the battery system in which 70% energy efficiency can be reached at current density of 40 $mA \cdot cm^{-2}$. Later, a comparative study was carried out to probe the

suitability of various carbon-based electrode materials [67, 69, 70]. It was found that the average separation between carbon layers in the material and the functional groups on electrode surface can have significant effects on battery efficiency and resistance [71]. The carbon electrode corrosion caused by higher overpotential in the acidic electrolyte was also reported for bulk graphite and fibrous carbon material [67]. Later, various porous carbon materials (graphite felt, carbon felt or graphite foil) were chosen as electrode materials in literatures which reported VRFB setups [37, 38]. Recently, hydrophilic SGL carbon papers which originally designed and manufactured for PEM fuel cell application, have been used as electrode materials in novel zero-gap battery cell [49, 51]. Compared to more traditional battery cell designs, high power output was achieved by the new cell configuration with these special electrode materials.

Various methods have been used to modify these porous carbon electrode materials to improve their performance. The effort to modify the surface of carbon electrode materials in VRFB mostly intends to increase its surface area, introduce more catalytic functional groups (e.g. oxygen and nitrogen functional groups) or decorate the catalyst to reduce activation loss in the battery. The primary strategies of electrode improvement include modification of existing electrode material, catalyst adoption and new electrode material development.

Chemical modification is a method to improve electrode material performance by introducing more active functional groups onto the electrode surface or increase the roughness of the electrode surface. The oxygen or nitrogen containing functional groups on the electrode surface is found to catalyze vanadium redox reaction. Sun et al. initially used boiling in concentrated sulfuric acid and 200 to 500°C heating in air to modify the surface of graphite felt for VRFB application [72, 73]. Surface characterization by X-ray photoelectron spectroscopy showed that the prevalence of C-O and C=O bonds on the electrode surface was substantially increased by applying these two treatments. The oxygen functional groups on the surface of the electrode substrates played a very important role in decreasing the reaction activation energy. They also improved the hydrophilicity of the electrode and behave as active sites which may catalyze the redox processes. In battery tests with the treated graphite felt,

enhanced battery energy efficiency and lowered internal resistance were observed. Similar strategies have also been utilized to modify carbon-based electrode materials to introduce oxygen-containing functional group onto the material surface by many other research groups [74-76]. With the zero-gap flow-by cell design, Pezeshki et al. reported 77% energy efficiency at 200mA·cm^{-2} current density in a battery cycling test in a zero-gap cell with Nafion 117 when employing SGL 10AA carbon paper heat-treated in 400°C air [56]. Electrode material modification by treatment in an NH_3 atmosphere at an elevated temperature (220°C) has also been reported to improve electrode performance and thereby improve battery performance [74, 77, 78]. A detailed study on the properties of nitrogen-doped graphene suggested that the quaternary nitrogen is most stable in the acidic electrolyte and active enough to catalyze VO^{2+}/VO_2^+ redox reactions, as shown in Figure 1.4 [78]. Some other methods for surface modification, such as plasma treatment, gamma-ray irradiation [79], and Fenton reagent oxidation [80], were also utilized to treat electrode materials. Another method to improve electrode performance is to increase the active surface area of the electrode. A nanoporous layer consisting of multilayers of carbon nanotubes was built on SGL 10AA carbon paper, and effectively increase the output of the battery [66]. Carbon felt decorated by reduced graphene oxide was also used in a VRFB to provide a finer degree of oxygen content control on the electrode surface [81].

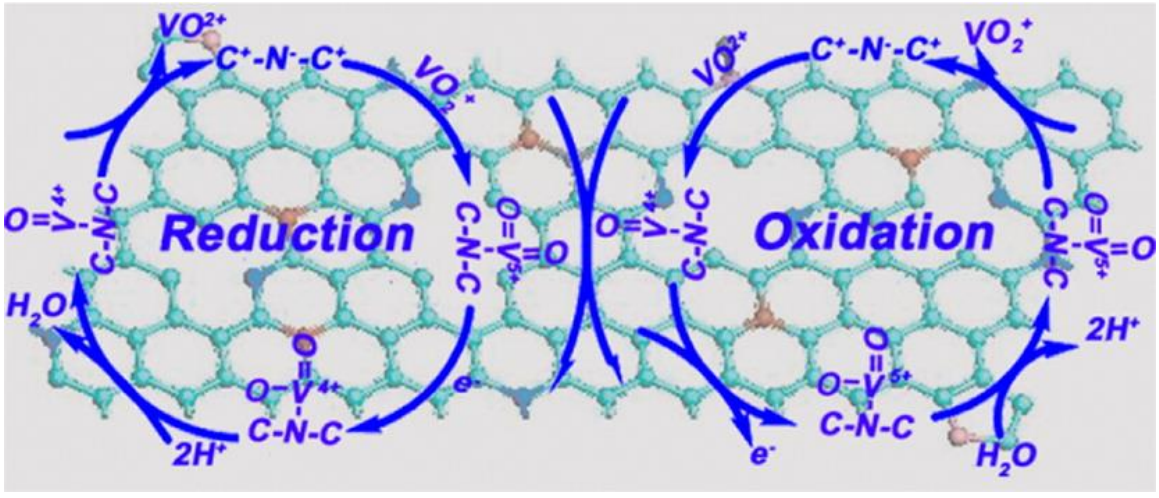

Figure 1.4 A possible pathway for quaternary nitrogen to catalyze VO^{2+}/VO_2^+ redox reactions on nitrogen doped graphene electrode surface[78].

To improve the reaction kinetics for vanadium redox reactions, a great amount of research attention has been paid to introducing a catalyst into a VRFB. Sun et al. did a wide range of screening work to evaluate the catalytic ability of several common catalysts impregnated in graphite fiber electrodes, including platinum, palladium, gold, manganese and iridium[82]. It was found that carbon fiber electrode with iridium had the best overall performance as a catalyst for various vanadium redox reactions, while precious metal can cause copious hydrogen evolution as a side-reaction, limiting its application in VRFB. Iridium-decorated carbon felt and iridium-decorated graphene electrodes were respectively developed based on this observation [16, 83]. With the Ir coated carbon felt electrode, it was reported that the reaction overpotential of VO^{2+}/VO_2^+ couple was substantially reduced and cell internal resistance was lowered [16]. Ti/IrO_2:Ta_2O_5 was synthesized and used as an electrode in the vanadium system, and showed a higher electrochemical activity than graphite electrode[84]. Other catalytic electrodes have also been developed based on tungsten and bismuth. A tungsten trioxide/super active carbon (WO_3/SAC) composite electrode and catalyst-coated membrane (CCM) were developed and adopted in a VRFB using a CCM configuration by Yao et al [85, 86]. The WO_3/SAC promotes very high charge transfer rates within VO^{2+}/VO_2^+ and V^{3+}/V^{2+} redox couples relative to pure SAC [85]. The cell with WO_3/SAC CCM performed at higher voltage and energy efficiencies (85.9% and 81.2%) than a regular cell (81.3% and 76.9%) at 120 $mA{\cdot}cm^{-2}$ current density [86]. A carbon felt electrode decorated with nanoparticles of bismuth (Bi) has been developed as both positive and negative electrodes for VRFB [87, 88]. It was found that the Bi nanoparticle doped graphite felt electrode had an 11% increase in battery energy efficiency at 150 $mA{\cdot}cm^{-2}$ compared to untreated graphite felt electrode. Mn_3O_4 has also been used as an electrocatalyst on carbon felt electrodes for VRFB [89]. Graphene-supported monometallic Platinum and bimetallic $CuPt_3$ cubic catalysts have been developed for positive electrodes in VRFB [74, 90].

1.3.5 Ion exchange membrane (IEM) and its development

As a key component in the cell, the IEM as electrolyte separator physically separates liquid electrolyte compartments and provides an ionic connection between the catholyte and anolyte to conduct ionic current. The function of the IEM requires it to possess high ionic conductivity to minimize ohmic loss while simultaneously exhibiting low vanadium and water transfer to inhibit vanadium crossover and electrolyte imbalance [91]. Since the VRFB system has a very long lifetime target, the separator needs to be very stable to withstand the highly acidic, oxidative and corrosive electrolyte solution. Finally, the membrane should be low cost to reduce the overall capital cost of the battery system to enhance its marketing competitiveness.

Currently, several types of separator have been used or tested in the VRFB system. A polymeric ion exchange membrane is commonly used as the electrolyte separator [58, 91]. In reported scaled VRFB systems, Selemion CMV cation exchange membrane [36], anion exchange membrane [39] and Nafion cation exchange membrane [37, 38] were used as electrolyte separators and exhibited good durability in long-term operation. The polymer ion exchange membrane, primarily the cation exchange membrane, such as Nafion, has several drawbacks as an electrolyte separator in electrolytes with high acid and vanadium cation concentration. Due to the relatively deep understanding of the property and performance of Nafion, which has been intensively studied as polymer electrolyte in PEM fuel cells, Nafion is widely used as a standard or reference membrane in VRFB research.

As a result of being exposed to electrolyte solutions, acid and vanadium ions are taken into the Nafion and they can drastically reduce the membrane conductivity in VRFB [46]. Although acid in the membrane can elevate its proton content to carry current, proton mobility in the membrane is reduced. In the work reported below [46], it is shown that the proton transport in sulfonated polymer ion exchange membranes is highly favored by high content and activity of water in the membrane [92, 93]. The presence of acid in membrane can cause a major proton mobility loss due to water content reduction, which mainly contributes to conductivity

loss in the membrane, compared to a water-saturated membrane. In addition, vanadium ions can occupy sulfonic acid group sites in the ionic channel, leading to a lower proton concentration and less efficient charge conduction. With VO^{2+} in the membrane, proton motion can be slowed down via an unknown mechanism, leading to further proton mobility loss. Compared to the 0.1~0.2 ohm·cm^{-2} area specific resistance (ASR) observed in a PEM fuel cell with similar membranes [94-96], the internal resistance of zero-gap battery cell with Nafion 117 is about 0.4~0.6 ohm·cm^{-2} [49, 51, 66]of which the major part is the resistance of separator [46].

High rates of permeation of vanadium and electrolyte across separator is another bottleneck limiting VRFB performance in long term operation [97, 98]. During VRFB operation, vanadium ions can penetrate the separator and immediately react with vanadium ions of separated valence state as indicated in the following formulas:

$$V^{2+} + VO^{2+} + 2H^{+} \rightarrow 2V^{3+} + H_2O$$

$$V^{2+} + VO_2^{+} + 2H^{+} \rightarrow V^{3+} + VO^{2+} + H_2O$$

$$V^{3+} + VO_2^{+} \rightarrow 2VO^{2+}$$

The vanadium crossover can reduce concentrations of reactive vanadium species, V^{2+} and VO_2^{+}, to bring down battery capacity. Self-discharge reactions can also bring down the battery energy efficiency by lowering both voltage and coulombic efficiencies. Water osmosis is another unfavorable mass transport process happening during battery operation [19, 99]. Along with the charged species migration, water molecules can be dragged across the membrane by electro-osmosis. Water also can diffuse across the membrane, driven by a water activity gradient between catholyte and anolyte. The transfer of water across the membranes during the charge and discharge cycling process involves a number of processes, such as water transported by ions moving under a concentration gradient, water carried by the charge balancing species and water transport due to the osmotic pressure difference between the two half-cell solutions. When a cation exchange membrane is used between the two vanadium redox half-cell electrolytes, a significant amount of water is transferred from the

negative half-cell electrolyte to the positive half-cell electrolyte by the hydration shells of V^{2+} and V^{3+} ions which carry a large amount of water and can easily permeate through cation exchange membranes [18]. In long-term battery cycle test, it has been shown that the net water transport can cause electrolyte imbalance due to such electrolyte transfer [19].

Stability of Nafion exposed to vanadium electrolyte solution is also a serious issue limiting its reliability in VRFB system [100-102]. Stability and lifetime tests have been carried out on several commercial ion exchange membrane and newly synthesized membrane by several groups. The strong oxidizing ability of VO_2^+ ion is one of the main means of attack of the polymer structure in the membrane [101, 103, 104]. Unfortunately, the long-term membrane stability in scaled battery setup has not been well studied. However, membrane stability is of great significance to improve VRFB's systematic reliability and overall maintenance cost.

Much effort has been devoted to developing alternative separators more suitable for VRFB application. Several pathways, including hydrocarbon membrane, composite membrane, anion exchange membrane and nanofiltration membrane, have been taken to develop new materials for the VRFB separator. One strategy is to design and synthesize new ion exchange membranes with hydrocarbon polymer which can provide low production costs, high enough proton conductivity, and higher selectivity between protons and vanadium ions as a result of the tighter polymeric structure [105, 106]. Another strategy to improve membrane performance is to manufacture the ionomer/functional component composite membrane [107, 108]. In this type of membrane, the ionomer can maintain its conductivity, and the functional component (filling or polymer layer) is expected to reduce the unwanted transport across the membrane. Anion exchange membranes have been used in running VRFB systems [39] and these are subjected to more fundamental research to develop its performance in VRFB [106, 109]. In an anion exchange membrane, the cationic group site in the membrane can establish a potential barrier to exclude vanadium cations. To somewhat extent, the vanadium crossover in the battery can be suppressed [106]. Examples of these strategies are provided in the following context.

1.3.5.1 Nafion/filler hybrid membranes

A Nafion/SiO_2 hybrid membrane was initially fabricated by an in-situ sol-gel method by Mauritz et al. to reduce methanol crossover in the direct methanol fuel cell (DMFC) [110]. This method introduces SiO_2 nanoparticles into nanopores in Nafion to impede methanol transport within the ionic cluster channel. During the preparation process of sol-gel derived Nafion/SiO_2 hybrid, the TEOS molecules will preferentially migrate to the polar clusters inside the Nafion membrane and the subsequent hydrolysis of sorbed TEOS are confined to these clusters to form SiO_2 nanoparticles filled Nafion/SiO_2 hybrid membrane. The slight decrease in water uptake for Nafion/SiO_2 hybrid membrane can be attributed to the filling of polar clusters by SiO_2 nanoparticles. The same strategy was borrowed by Xi et al. To manufacture Nafion/SiO_2 hybrid membrane for vanadium flow battery, as is presented in Figure 1.5 [111].

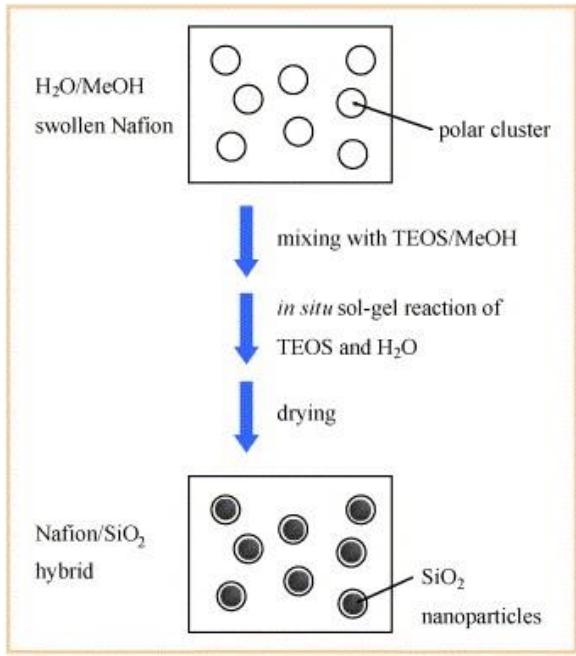

Figure 1.5 The synthesis of Nafion/SiO_2 composite membrane with sol-gel method [111].

The embedded nano-sized SiO_2 particles in micropores of Nafion were used to impede vanadium permeation. The Nafion/SiO_2 hybrid membrane was prepared by the In-Situ sol-gel method, as for the DMFC. The weight fraction of SiO_2 in the hybrid membrane was roughly 9.2%. The membrane's fundamental properties were measured and compared to Nafion 117.

The hybrid membrane thickness was 204 to 215μm, close to that of Nafion 117. The hybrid membrane and Nafion 117 had very similar ion exchange capacity and conductivity, although water uptake by the hybrid membrane was apparently lower than that of pristine Nafion. The authors attributed lower water content in the hybrid membrane to decreased volume available in the ionic cluster as a consequence of SiO_2 occupation of space. In charge-discharge cycle tests, the setup with Nafion/SiO_2 hybrid membrane had a higher discharge capacity than Nafion 117, implying that vanadium crossover is lower in the Nafion/SiO_2 membrane than in unmodified Nafion. The battery voltage, coulomb and energy efficiencies are consistently higher with the Nafion/SiO_2 membrane, and open circuit voltage decay at 75% SOC in the battery with the hybrid membrane was three times slower than that in the battery with Nafion 117. The hybrid membrane also showed considerable stability in the battery cycling test, consistently showing 90% coulomb efficiency and 72% energy efficiency at 60 $mA \cdot cm^{-2}$ after 100 cycles.

Besides SiO_2, some other materials have been embedded in Nafion polymeric matrix to form hybrid membranes for vanadium redox flow batteries. Nafion/TiO_2 [112], ZrO_2 [113], ZrP [114] hybrid membranes were fabricated and characterized by a similar method to the Nafion/SiO_2 hybrid membrane papers. In counter diffusion measurements and battery tests, Nafion/TiO_2 hybrid membrane exhibited low vanadium permeability when compared to Nafion membranes, similar to the Nafion/SiO_2 hybrid membrane. Since it was pointed out that TiO_2 was not stable enough in vanadium electrolyte solution, a Nafion/Si/Ti composite membrane was developed [107]. Authors used an in-situ gel-sol method with embedded dimethylsiloxane (DEDMS) and tetrabutyl titanate into Nafion framework to fabricate the Nafion/Si/Ti composite membrane. This membrane showed an eight times lower VO^{2+} permeability than Nafion with a slightly lower conductivity. Also, this composite membrane did not show any apparent degradation after 100 charging-discharging cycles. Nafion/organically modified silicate hybrid membranes were prepared via in-situ sol-gel reactions with mixtures of tetraethoxysilane (TEOS) and diethoxydimethylsilane (DEDMS), and compared with Nafion and Nafion/SiO_2 [115].

1.3.2 Nafion modification with ion exchange polymer

Some researchers have been trying to combine the advantages of Nafion and some other polymers to meet the requirements for VRFB separator [108, 116, 117]. The purpose of this method is to build an extra layer of polymer with the positive charge to establish a positive charge barrier for vanadium ion crossover. Multilayers of functional polymers are polymerized on Nafion surface to improve its ionic selectivity and water osmosis, e.g. the Nafion/PSS/PDDA composite membrane is shown in Figure 1.6 [116].

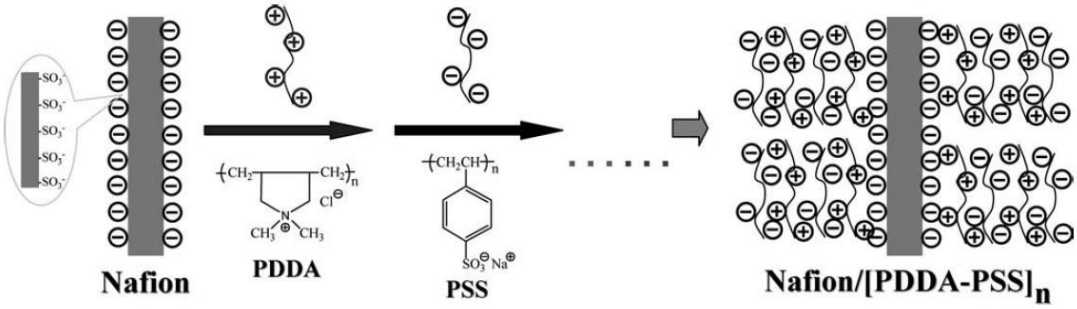

Figure 1.6 Schematic representation of Nafion modification with multilayers of poly(diallyldimethylammonium chloride) and anionic poly(sodium styrene sulfonate) by self-assembly with interfacial polymerization [116].

Electrolyte soaking, oxidation polymerization and electro-deposition were used to generate a vanadium diffusive barrier layer of polypyrrole on the surface of Nafion 117 [117]. Compared to Nafion 117, the membrane modified by electro-deposition showed an obvious reduction in ionic permeability and water crossover, but without adversely affecting the membrane conductivity. A surface modification-adsorption method was utilized to introduce a layer of polyethylenimine (PEI) onto the surface of Nafion 117 to form a cationic barrier to expel vanadium ions by the Donnan potential [108]. The cationic charged layer on the surface of Nafion membrane acts as an electrostatic repulsion barrier and vanadium permeability is reduced due to the Donnan exclusion effect. Although the membrane area specific resistance of Nafion with deposited PEI was slightly higher than Nafion 117, 1.24~1.34 ohm·cm^2 vs. 1.06 ohm·cm^2 in a battery test, the permeability of VO^{2+} was reduced from 36.55×10^{-7} cm^2·min^{-1} to

1.70~5.23×10^{-7} $cm^2 \cdot min^{-1}$, in comparison to untreated Nafion. However, it was pointed out that ionic selectivity improvement did not effectively enhance the battery system's energy efficiency, because increased membrane resistance brought down battery's voltage efficiency. Similarly, a multilayered modification was conducted on Nafion 117 to deposit multiple cationic poly(diallyldimethylammonium chloride) (PDDA) and anionic poly(sodium styrene sulfonate) (PSS) microlayers on Nafion 117 surface by direct-soaking [116]. This multilayered Nafion exhibited significantly lowered vanadium permeability and also helped to increase the battery energy efficiency. A thin layer of Nafion was also crosslinked with sulfonated poly(ether ether ketone) to produce a dual-layered Nafion/SPEEK composite membrane [118]. This method provided a possibility to develop a suitable VRFB separator by enhancing the proton conductivity of some low-cost materials with good stability and low vanadium permeability.

1.3.5.3 Non-ion exchange polymer modification

Introducing ion exchange material into a non-ion exchange polymer is another strategy to manufacture composite ion exchange membranes with good stability. Since polyvinylidene difluoride (PVDF) and polyethylene tetrafluoroethylene (PTFE) have considerable chemical stability in extreme chemical environments, they have been tried to develop new VRFB separators [119-121]. The essence of this strategy is to introduce ionomers into the pores of a framework polymer to form the ionic channel to transport proton. Several ionomers, such as polystyrene sulfonic acid (PSSA) or dimethylaminoethyl methacrylate (DMAEMA), were grafted onto infrastructure of PVDF or PTFE and then sulfonated to introduce ionic conducting ability. These membranes demonstrated 20 to 40 times lower vanadium crossover in diffusion measurements and comparable conductivity to Nafion 117. The Daramic membrane is a low-cost microporous separator which is widely used in lead-acid batteries. It contains a special mineral oil as a stabilizer against oxidation. However, without modification, it is unsuitable for the VRFB due to its high permeability which will lead to low coulombic efficiencies. Nafion was also incorporated into Daramic membrane pore to enhance its proton conducting ability, without consuming a large amount of Nafion [122].

1.3.5.4 Hydrocarbon polymer

In recent years, non-fluorinated aromatic polymers have been used in the VRFB application because of their lower cost, tunable properties and good chemical and thermal stability [58, 91, 123]. Aromatic hydrocarbon cation exchange membranes are the primary alternative cation exchange membrane for PFSA cation exchange membrane in VRFB application because its performance is comparable to Nafion in electrochemical devices [124]. Such membranes are generally developed from thermoplastics by sulfonation, which results in high chemical/ thermal stability, good mechanical properties and low cost [125, 126]. A series of sulfonated poly(ether ether ketone) (SPEEK) and modified SPEEK membranes have been manufactured and tested for VRFB applications [127-129]. These SPEEK membranes have different sulfonation degrees and various modifications, including SPEEK/heteropolyacid (PTA)/Polypropylene, or SPEEK/PTFE and SPEEK/polypropylene/Nafion composite membranes. Similarly, sulfonated poly(fluorenyl ether ketone) (SPFEK) membranes and SPFEK/SiO_2 hybrid membranes were fabricated by Chen et al. [130, 131].

Another series of membranes, sulfonated poly(arylene thioether ketone) (SPTK) and sulfonated poly(arylene thioether ketone ketone) (SPTKK) based on poly(arylene thioether) framework polymer, were synthesized and investigated [132]. Sulfonated poly(sulfone) (S-Radel) membrane has also been synthesized and subjected to VRFB testing by Kim et al. [102, 103]. The S-Radel membrane showed a comparable cycling performance to Nafion, and much lower vanadium permeability than for Nafion. However, S-Radel was chemically vulnerable in vanadium electrolyte, especially to highly oxidative VO_2^+. Recently, sulfonated Diels Alder poly(phenylene)s (SDAPP) membranes have been synthesized and tested for VRFB application by Fujimoto et al. [105]. SDAPP membranes degrade faster than Nafion in VO_2^+ containing electrolyte, and the degradation rate is proportional to the ion exchange capacity.

Good conductivity comparable to Nafion and low phenomenal vanadium ion permeability can both be achieved by most of the membranes mentioned above, but the chemical stability of

these polymers in electrolyte solution still needs to be improved. Also, more insightful research is also required to establish a solid understanding of the relation between polymer structure and its performance in electrolyte conditions, especially the polymer property influence on membrane transport behavior and durability in the battery.

1.3.5.5 Anion Exchange Membranes

Although anion exchange membranes have been used in commercial VRFB system for over 15 years [39], the research effort devoted to anion exchange membranes was significantly less than that for cation exchange membrane. Due to the presence of cationic functional groups in the polymer backbone, the anion exchange membrane was proposed to reduce vanadium permeation in VRFB by Donnan exclusion, as shown in Figure 1.7 [133].

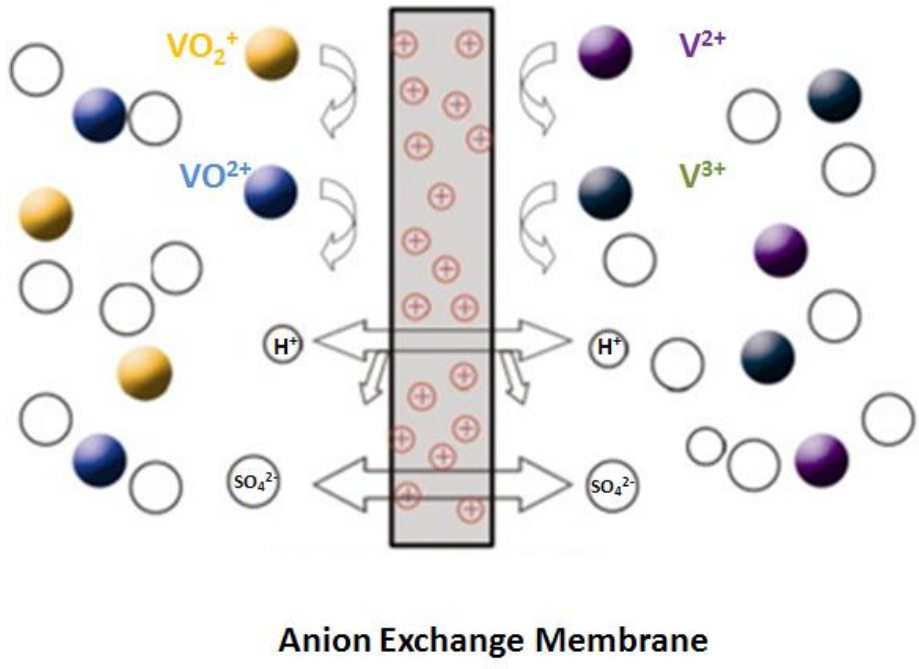

Figure 1.7. The Donnan potential generated by the positively charged ionic group in the membrane can prevent vanadium permeation by electrostatic repulsion mechanism between positively electric charges [133].

Crosslinked polysulfone anion exchange membranes were initially crosslinked by accelerated electron beam irradiation [134]. The battery system using this membrane reached 80% energy efficiency in 8 cycles at a current density of 60 $mA \cdot cm^{-2}$. Another polysulfone based AEM was manufactured by functionalization with quaternary benzyl trimethylammonium groups ($PSF\text{-}TMA^{+}$) by Jung et al. [135]. The $PSF\text{-}TMA^{+}$ membrane had good stability in 1.5 $mol \cdot L^{-1}$ VO_2^{+} solution for over 90 days. A series of quaternized poly(phthalazinone ether sulfone) (QPPES), quaternized poly(phthalazinone ether ketone) (QPPEK) and quaternized poly(phthalazinone ether ketone ketone) (QPPEKK) AEMs were synthesized and analyzed in a series of tests, including battery testing, by Jian et al. [109, 136, 137]. Ethylene–tetrafluoroethylene (ETFE) based AEMs were also manufactured by grafting poly(methacryloxyethyl dimethyl ammonium chloride) (PMAOEDMAC) [121]and dimethylaminoethyl methacrylate (DMAEMA) [138, 139]. Quaternary ammonium functionalized Radel (QA-Radel) and quaternary ammonium functionalized poly(fluorenyl ether) (QA-PFE) were respectively synthesized and tested by Chen et al. [69, 133]. In both of these AEMs, lower vanadium permeability was reflected by lower coulombic efficiency and slower capacity decay in the cycling tests.

1.3.6 Vanadium solutions and their improvement

As the energy in VRFB is carried by the vanadium redox couple dissolved in solution, the energy density of VRFB is favored by a high concentration of vanadium salts in the solution. However, the solubility of vanadium in solution was limited by several factors, leading to a stability problem in battery operation [52, 140]. It was pointed out that when the battery was operated with the unstablized solution, VO_2^{+} and V^{3+} can respectively precipitate in the forms of $V_2O_5 \cdot xH_2O$ and $V_2(SO_4)_3 \cdot xH_2O$ [140]. To understand the stability of vanadium ions, as well as ionic structure features, research has been conducted to illustrate the state of vanadium ions in solutions. A Raman spectroscopy investigation was conducted on the positive electrolyte solution with varying VO_2^{+} and sulfate concentration, state of charge and temperature by Kausar et al. [141]. Various VO_2^{+} ionic forms were suggested by the

spectroscopy work. It was concluded that the lack of H^+ and sulfate supporting solution was the main reason for VO_2^+ precipitation at elevated temperature. Nuclear magnetic resonance (NMR) and density functional theory (DFT) simulation studies have been conducted to probe the vanadium ions (III, IV, V) in vanadium-sulfuric acid solution [142, 143]. The detailed mechanism of VO_2^+ and V^{3+} precipitation was proposed on these works [143, 144]. The precipitation of VO_2^+ is caused by deprotonation and dehydration of its hydration structure [143, 144]. In detail, the V(V) species exist as hydrated penta coordinated vanadate ion, i.e. $[VO_2(H_2O)_3]^+$ in the electrolyte solution. This hydrated structure is found to be stable in the low temperatures (<330 K) but at elevated temperature it changes to the neutral H_3VO_4 molecule by deprotonation process. This neutral species undergoes a condensation reaction through its highly reactive hydroxyl groups and forms the V_2O_5 precipitate in the electrolyte solution. Hence, the precipitation can be avoided by preventing the deprotonation process which is followed by the structural transition to the neutral H_3VO_4 molecule. A simple way to prevent the deprotonation process is to increase the solvent acid concentration. The V^{3+} precipitation was caused by the nucleation in the V^{3+}-sulfate ion complex form by water-sulfate exchange in the hydration structure of V^{3+} [142, 145]. The formation of neutral molecules through deprotonated sulfate complexed molecules $[VSO_4(OH)5H_2O)]$ and ion-paired $[V(SO_4)_2(H_2O)_4][H_5O_2]^+$as the initial step in the precipitation process. At low temperatures, the ligand exchange process slows down and renders relatively stable and rigid neutral molecules. These neutral molecules can act as a seed for continuous nucleation which can lead to ordered solid structure and subsequent powder precipitation. The sulfate complexation with V(III) cation and excess proton concentrations are a crucial process in the observed precipitation process. Stability of electrolytes with practical vanadium concentration was also examined by researchers [52, 140]. The stability of VO_2^+ and V^{3+} was evaluated with respect to temperature, vanadium concentration and acid concentration. While high sulfuric acid concentration in the solution can favor stabilization of VO_2^+ in catholyte, it would cause more severe V^{3+}precipitation in anolyte.

To improve the performance of vanadium-sulfuric acid solution in VRFB, several methods were used to increase electrolyte stability. The effort was mainly focused on the improvement of electrolyte thermal stability [54, 55, 146, 147]. Several organic acid additives have been tested as the catholyte additives to stabilize $VO_2^+$to reduce its precipitation. These additives included polyacrylic acid and acetic acid mixture [54], coulter dispersant [148], inositol and phytic acid [146] glycerin/n-propyl alcohol [149], l-glutamic acid [55], methanesulfonic acid (MSA) and aminomethylsulfonic acid [147]. Besides solution stabilization, the electrolyte additive can also act as a catalyst to improve electrochemical reaction kinetics of vanadium redox couples on the electrode [55, 147, 149]. The organic additives can introduce oxygen and nitrogen containing functional groups adsorbed on the electrode surface to catalyze vanadium redox reactions. The catalytic activity attributed to the additives is similar to that of carbon electrode surface heating treated in oxygen and ammonia atmosphere. A vanadium sulfate and chloride mixed electrolyte are also proved to be stable with a vanadium content of up to 2.5 M over a temperature range of -5-50 °C because of the formation of stable $VO_2Cl(H_2O)_2$ at elevated temperatures and reduction in SO_4^{2-} concentrations [150]. The vanadium redox couples in mixed electrolytes demonstrated improved reaction kinetics while remaining as highly reversible as the sulfate system. The VRFBs with the mixed electrolytes were successfully demonstrated with the same high efficiencies as those of the sulfate systems, but over a much broader temperature window. The battery tests result along with thermodynamic calculations demonstrated that there was no concern of chlorine gas evolution during the battery operation.

1.4 Aim of the work

As reported in the previous sections, the VRFB cell with reference Nafion membrane has fast capacity decay due to the high vanadium crossover. It is reported that the capacity decay for a Nafion 212 membrane is 50% when operated at 35.7 mA cm^{-2} for 50 cycles (125 hours) [151]. The vanadium permeability of Nafion 212 is reported as high as 2×10^{-6} cm^2min^{-1} [152]. Water transfer from one half cell to the other through the IEM is also observed. In the case of VRFBs using cation-exchange membranes, the transfer of water is from the negative half-cell to the positive half-cell. The water transfer is caused by the hydration shells of V^{2+} and V^{3+} ions, that carry a larger amount of water in comparison with VO^{2+} and VO_2^{+} [19, 20]. Therefore, the concentration of vanadium species in the negative half-cell is raised; this phenomenon may lead to the precipitation of V^{3+}, which may block the tubes and reduce the flow rate. Extremely serious precipitation can cause the flow of anolyte to stop altogether, terminating the operation of the VRFB system. The drawbacks mentioned above limit the wide spread commercial use of VRFB. To make this technology commercially viable, to reducing the vanadium permeability through the membrane (*i.e.*, below $2 \times 10^{-6} cm^2 \cdot min^{-1}$) is a critical factor.

In an effort to overcome the limitations of conventional IEMs, this thesis reports the synthesis and characterization of hybrid inorganic-organic proton conducting membrane alternatives to classic pristine perfluorinated ionomers for application in VRFBs. According to our previous studies [153-155]. The distribution of nanofillers in the polymeric matrix and the compatibility between the two phases (polymer and inorganic filler phase) plays an essential role in defining the physicochemical properties of the nanocomposite membranes. It can be assumed that proton transport through the nanocomposite IEM will occur through a more direct and shorter pathway in comparison with vanadium ions. Indeed, the vanadium ions most likely migrate easily only through the 'bulk' water deep within the hydrophilic domains of the ionomer, while protons are able to pass through the 'interface' water as well, that is found at the boundary between hydrophilic and hydrophobic domains. The incorporation of WO_3 nanofiller leads to the formation of hydrogen bonds and dynamic crosslinks; these

interactions are expected to reduce the size of the hydrophilic domains and therefore to reduce the amount of bulk water which is located in the hydrophilic domains. The lower amount of bulk water may be the critical issue to reduce the vanadium permeability significantly. The amount of interface water may further increase. Therefore, the transport of vanadium ions is more hindered than protons. Hence, a nanofiller incorporated hybrid membrane can enhance ion selectivity by reducing the vanadium crossover. It is necessary to optimize the quantity of nanofiller which plays an important role into a proton conductivity and water uptake. High loading of nanoparticles will lead to an excessive reduction in the proton conductivity; an excessive enrichment of nanoparticles can even lead to membrane cracking. Instead, a low content of nanofiller (below 5% wt) may not be sufficient to reduce the vanadium permeability significantly.

The second advantage of incorporating inorganic nanoparticles into polymer matrix is attributed to the inorganic particles' ability to increase the mechanical stability of the membrane. This is due to the hydrogen bond formed between the $-SO_3H$ group from polymer and the -OH group from the inorganic particles. Even weak interactions between nanoparticle and polymer matrix may contribute to the mechanical stability. Therefore, the selection of nanofiller and the control of the interaction between the nanofiller and the polymer chains plays a decisive role in the performance of the resultant composite membranes.

In this work, tungsten oxide (WO_3)was chosen as a nanofiller due to the good stability in high concentrated sulfuric acid and low price compared to other metal oxides(e.g., Ta_2O_5, NbO_2, IrO_2 and MoO_2) which are used for application in VRFBs.

Two different kinds of hybrid membranes were synthesized:

1) Doped Nafion membrane with WO_3 nanofiller in order to reduce its vanadium crossover while maintaining the high proton conductivity. The high proton conductivity of [Nafion/(WO_3)]$_x$ membranes can be applied to both low and high current density range. This is because a VRFB operating at high current densities requires a high proton conductivity through the membrane in order to ensure electrical neutrality and complete the circuit.

   In Chapter 3, [Nafion/$(WO_3)_x$] hybrid membranes with varying loading levels of WO_3 nanofiller are prepared and investigated as candidates for application as solid electrolytes in VRFBs. The thermal properties of hybrid membranes are probed both by high-resolution thermogravimetric analysis (HR-TGA) and by modulated differential scanning calorimetry (MDSC) to study the thermal stability and thermal transitions of the hybrid membranes. Vibrational spectroscopy studies are carried out by Attenuated Total Reflectance - Fourier Transform Infrared spectroscopy (ATR-FTIR) and (ii) Raman spectroscopy, to elucidate the secondary structure of [Nafion/$(WO_3)_x$] and study the interactions taking place between the nanofiller and the Nafion matrix. The electrical response of [Nafion/$(WO_3)_x$] is determined by Broadband Electrical Spectroscopy (BES) in order to determine the ionic conductivity and the permeability towards VO^{2+} is measured by UV-VIS spectrometry. A structural model and a conductivity mechanism for the [Nafion/$(WO_3)_x$] hybrid membranes are proposed, in order to rationalize the experimental results and correlate the electrical response with the transport properties. The ion exchange capacity (IEC) and the water uptake (WU) of each hybrid membrane are determined, in order to investigate the influence of nanofiller on hydrophilic domains of the polymer matrix. At the final step, ex-situ chemical stability test is measured for over 80 days to gauge durability.

   In Chapter 4, the morphology of prepared new hybrid inorganic-organic membranes [Nafion/$(WO_3)_x$] is further investigated by scanning electron microscopy (SEM). The influence of morphology on the membrane properties is investigated. One side of each

hybrid membrane exhibits a high concentration of the WO_3 nanofiller; while in the remaining part of each membrane, the concentration of the filler is lower. The asymmetric membrane structure may generate different effect on the prevention of vanadium permeability. The performance of the hybrid membrane exhibiting the highest ion selectivity (i.e., [Nafion/$(WO_3)_{0.587}$])is tested in a VRFB single cell and compared to Nafion as reference membrane. The single cell performance including efficiencies at different current densities, discharge capacity decay and efficiencies at fixed current density as evaluation of cycle life stability and open circuit voltage (OCV) curve are demonstrated. The improved efficiencies are observed for hybrid membrane at all measured current densities. The normalized discharge capacity decay of VRFB with hybrid membrane is much lower compared to Nafion 212. The OCV curve demonstrates the capacity fade time of hybrid membrane is 1.5 times longer than Nafion 212 membrane.

2) synthesis of sulfonated poly (ether ether ketone) (SPEEK) membrane with optimized degree of sulfonation (DS) as an alternative low-cost membrane to perfluorinated polymers. The cost of pristine SPEEK membrane is 20 \$/m^2,which is much lower than that for Nafion membranes (500\$/m^2) [156]. Then further doping of the SPEEK membrane with WO_3 reduces vanadium crossover. The interfacial interactions between the WO_3 filler and the SPEEK matrix may inhibit the formation of the large hydrophilic channels, which play a crucial role to transport the vanadium ions. The limited permeability is also correlated to the increased tortuosity of ionic transport paths for vanadium. Medium proton conductivity of [SPEEK/$(WO_3)]_x$ membranes can be applied to medium and low current density range (20 to 100 mA cm^{-2}), due to its medium proton conductivity may not be suitable to achieve electrical balance at extremely high current densities (above 150-200 mA cm^{-2}).

In Chapter 5, the preparation, characterization and single VRFB cell test of new asymmetric [SPEEK/$(WO_3)_x$] membrane is reported. Similarly to Chapter 3, the thermal stability is investigated by HR-TGA and thermal transitions are studied by MDSC. The physicochemical properties including IEC, WU and vanadium permeability of each hybrid

membrane are determined to understand the influence of nanofiller incorporation on the hydrophilic domains. The proton conductivity of [SPEEK/$(WO_3)_x$] is determined by BES. Vibrational spectroscopy studies are carried out by ATR-FTIR to demonstrate the interaction between nanofiller and polymer matrix. The morphology of the hybrid membrane with highest ion selectivity [SPEEK/$(WO_3)_{0.20}$] is investigated with SEM. Moreover, [SPEEK /$(WO_3)_{0.20}$] is tested in single-cell configuration under operating conditions and battery performance results are reported. Finally, to highlight the [SPEEK/$(WO_3)_x$] membrane as cost-effective membrane for VRFB application, a simplified capital cost analyses is used to illustrate its economic value as an alternative membrane.

The membranes characterization presented in this work follows a general approach which involved the study of the materials' thermal, electrical and structural properties determined from different measurement techniques (TG, MDSC, BES, FT-IR, Raman etc.). By correlating these results, it is possible to highlight the interactions between the different components present within the membranes. And most importantly, we may propose the related conductivity mechanism and evaluate how to tailor membranes characterized by the desired properties. The vanadium ions transport properties are the most directly involved during the operation of a VRFB, and it can be evaluated based on the correlated thermal and structural properties of a membrane.

Although the fundamental knowledge of VRFB is well known, the negative and positive electrode reactions are still important to be further understood, especially the existence forms of various vanadium species and how they are generated during the varied SOC. Several papers discussed the dissolved states of V(IV) and V(V) in concentrated sulfuric acid (H_2SO_4) solutions based on spectroscopic and/or electrochemical measurements, whereas not always the conclusions overlapped from all papers. However, it might be accepted that both V(IV) and V(V) form some complex species with sulfate (SO_4^{2-}) or hydrogen sulfate (HSO_4^-) anion. InChapter 6, we report in details the decompositions of the spectra for a positive electrolyte during State of Charge (SOC) and Depth of Discharge (DOD) in highly concentrated solutions of vanadium (V) and (IV) and H_2SO_4 by using Raman spectroscopy for the first time. As it is

well known, both V(IV) and V(V) form some complex species with sulfate (SO_4^{2-}) or hydrogen sulfate (HSO_4^-) anion. By Raman spectroscopy analysis, we may understand better the changes of complexation involving VO^{2+}/VO_2^+ with HSO_4^- and SO_4^{2-} species. Based on our result, it is evident that the dissolved variety of different ionic species in catholyte establish a complex series of equilibria. The concentrations of these ionic species are changed upon the charge/discharge processes (related to SOC), which may have important effects on the overall performance and durability of the system.

A brief description of the instruments used for the materials characterization is reported in Chapter 2 while the general conclusions of the work and a comparison between the different membranes are reported in Chapter 7.

Chapter II Instruments and methods

2.1 Introduction

In the present work, the prepared hybrid membranes are characterized by a common protocol that allows the study of their:

a) thermal properties using thermogravimetric (TGA) and calorimetric (DSC) analysis;
b) chemical structural properties analyzed by infrared spectroscopy (FT-IR) and Raman spectroscopy;
c) electrical properties by broadband electric spectroscopy (BES) measurements;
d) battery charge-discharge cycling performance by single VRFB cell tests;
e) UV-Vis Spectroscopy.

The use of different measurement techniques, conducted over a wide temperature range, allows for the identification and assignment of the phase transitions and the molecular relaxations that occur within the investigated materials in a unique way. In addition, the use of a common set of measurements allows the comparison of the properties of the different materials.

This chapter outlines the main characteristics of the instruments used for the study of the proposed materials. In the case of standard measuring techniques (TGA, DSC, FT-IR, Raman, BES, SEM/EDX and UV-Vis Spectroscopy), commonly used in the characterization of materials, the specifications of the instruments will be simply reported. The experimental conditions (ramp and temperature range, treatment of samples, etc.) adopted for the study of the different materials are reported in the different chapters present in this thesis.

Finally, this chapter describes the equipment assembled in this laboratory to perform the vanadium redox flow battery single-cell tests.

2.2. Thermal analysis [157, 158]

2.2.1 Thermogravimetric analysis

Thermogravimetric analysis (TGA) measures the amount and rate of change in the weight of material as a function of temperature or time in a controlled atmosphere. Measurements are used primarily to determine the composition of materials and to predict their thermal stability at temperatures up to 1000°C. The technique can characterize materials that exhibit weight loss or gain due to decomposition, oxidation, or dehydration.

For all the investigated materials the thermogravimetric analyses were carried out with a high-resolution TGA 2950 (TA Instruments) thermobalance (Figure 2.1), with a resolution of 1 μg. During the study of organic-inorganic hybrid membranes, the residual weight percentage of the sample at high temperature (above 600°C) demonstrates the actual amount of inorganic nanofiller within the hybrid membranes. The decomposition events associated with particular functional groups and structures can be identified by TGA measurements, including -SO_3H groups and backbones of the polymer matrix. The thermal stability of the polymer matrix upon embedding of the WO_3 nanofiller can be studied.

Figure 2.1 TGA 2950 (TA Instruments) thermobalance.

The heating ramp is varied from 50 °C·min^{-1} to 0.001°C min^{-1} on the basis of the first derivative of the weight change. Approximately 5 mg of sample is loaded onto a platinum pan, with measurements carried out under an air flux of 100 cm^3·min^{-1} over a temperature range between 20 and 900 °C. The resolution is 1 μg. The samples are exposed to a dry air flow for 24 h before the measurements.

2.2.2 Differential scanning calorimetry

The differential scanning calorimetry (DSC) determines the temperature and heat flow associated with material transitions as a function of time and temperature. It also provides quantitative and qualitative data on endothermic (heat absorption) and exothermic (heat evolution) processes of materials during physical transitions that are caused by phase changes, melting, oxidation, and other heat-related changes. The endothermic transitions of the prepared membranes can be detected, including thermal degradation of the -SO_3H groups and hydrophobic backbone. The relations between the temperature of each event and the level of nanofiller can be further investigated in order to understand the interactions between sulfonate groups and the tungsten oxide nanoparticles. In this work, DSC analyses were

performed using a DSC Q20 (TA Instruments). The DSC Q20 has two major parts: the Q20 CE instrument, which contains the system electronics, and the sample cell, which contains its own thermocouples (temperature sensor) for monitoring differential heat flow and temperature. The instrument measures differential heat flow of the sample and a reference. The sample and the reference are placed in aluminum pans that sit on raised platforms on a constantan disk, and heat is transferred through the disk up into the sample and reference. The differential heat flow is monitored by thermocouple wires welded to the disk. The DSC Q20 can be operated below ambient temperatures using the Liquid Nitrogen Cooling Accessory (LNCA). The LNCA provides automatic and continuous programmed sample cooling within the range of –150°C to 725°Cwhen used with the DSC heat exchanger installed on the DSC Cell. Heaters vaporize the liquid nitrogen in the LNCA tank. The cool gas is forced up and mixed with liquid nitrogen. The gas/liquid mix is delivered to the heat exchanger to cool the cell. For all the materials, the measurements were made under a helium flux of 30 cm^3 min^{-1} by loading about 6mg of the sample inside a hermetically sealed aluminum pan.

The specifications of DSC Q20 are listed below in Table 2.1.

Table 2.1 DSC Q20 specifications.

Temperature range	Room temperature to 725 ℃ range (inertatmosphere above 600 ℃) as supplied; to 150 ℃ with the LNCA
Cooling rate	Dependent on accessory used andtemperature range
Sample size	0.5 to 100 mg (nominal)
Sample volume	10 mm^3in hermetic pans
Sample pans	Various open or hermetically sealed
Purge gases Recommended	air, argon, helium, nitrogen, or oxygen
Typical flow	25–50 mL/min rate
Cell volume	2 cm^3
Temperature repeatability	+0.1 ℃
Differential thermocouples	CHROMEL®*-constantan (Type E)
Sample thermocouple	CHROMEL-ALUMEL®* (Type K)
Calorimetric sensitivity	0.2 μW (rms)
Calorimetric precision	1% (based on metal samples)

Modulated DSC (MDSC) is a technique which also measures the difference in heat flow between a sample and an inert reference as a function of time and temperature. In addition, the same "heat flux" cell design is used. In MDSC a different heating profile (temperature regime) is applied to the sample and reference. Specifically, a sinusoidal modulation (oscillation) is overlaid on the conventional linear heating or cooling ramp to yield a profile in which the average sample temperature continuously changes with time but not in a linear fashion. The net effect of imposing this more complex heating profile on the sample is the same as if two experiments were run simultaneously on the material - one experiment at the traditional linear (average) heating rate and one at a sinusoidal (instantaneous) heating rate. The actual rates for these two simultaneous experiments are dependent on three operator-selectable variables:

•Underlying heating rate (range 0-100°C minute^{-1})

•Period of modulation (range 10-100 seconds)

• Temperature amplitude of modulation (range ±0.01-10°C)

Modulated DSC determines the total, as well as these two individual heat flow components, to provide an increased understanding of complex transitions in materials. MDSC is able to do this based on the two heating rates seen by the material - the average heating rate which provides total heat flow information and the sinusoidal heating rate which provides heat capacity information from the heat flow that responds to the rate of temperature change.

2.3 Infrared spectroscopy

Infrared spectra in the medium infrared region (4000 to 400 cm^{-1}) were collected using an FT-IR Nicolet Nexus spectrometer. The source is a Globar lamp, consisting of a silicon carbide candle heated to a temperature between 1300 K and 1500 K. The beam splitter for the mid-infrared is KBr. The detector is a triglycine sulfate (TGS) pyroelectric material. The absence of water in the measuring chamber is ensured by a circulating dry air system, consisting of filters in which dehydration occurs initially through a pre-condensation process in the compressed atmosphere and then on a column of silica gel. The CO_2 is removed by zeolitic materials.

In this work, the infrared spectra of the polymeric membranes were collected in the ATR (Attenuated Total Reflection) mode using a Perkin-Elmer Frustrated Multiple Internal Reflections accessory 186-0174. In the ATR technique, the sample is in contact with a crystal with high refractive index. The radiation passes through the crystal and reaches the sample. If the angle of incidence is greater than the critical angle θ, equal to the ratio between the refractive indices of the crystal and the sample, the radiation incident on the sample is reflected within the crystal (total reflection). However, the radiation penetrates the surface of the sample for a few microns (0.5 - 5 μm depending on the type of crystal and the angle of incidence). The evanescent wave (the infrared radiation penetrating the surface of the sample) is then attenuated or altered by the sample. The infrared beam exits on the opposite side of the crystal and is collected by the detector of the spectrometer. It is possible to obtain the infrared spectrum of the polymer film by the difference between the evanescent waves in the presence and absence (by placing a sheet of brass in contact with the crystal) of the sample.

In the thesis, the obtained polymeric membranes were squeezed between the surfaces of a prismatic germanium crystal of 18(height)×51(width)× t(thickness) mm^3. 50% ca. of the crystal surface was covered by the membrane. An incident light angle of 45°C with 25 total internal reflections was adopted. The vibrational modes including hydrophobic backbone, side chains, WO_3 inorganic component, hydrophilic groups(-SO_3H) and water bending can be detected. The structural features and inter-chain interactions of hybrid membranes are critical and it can also distinguish between different polymer conformations.

2.4 Raman spectroscopy

Raman scattering spectroscopy is a technique that is used to study the diffusion of light emitted by a material made up of gas, liquid or solid molecules (amorphous or crystalline). The vibrational and lattice modes of WO_3 can be detected in order to study the structure change of the WO_3 nanofiller inside the hybrid membranes. To observe diffusion, it is necessary to emit a beam of light on the sample to be investigated and to observe the light diffused in a different direction from that of propagation. Generally, a monochromatic laser radiation υ_0 is sent to the sample with a certain intensity and the intensity of the scattered radiation, which has a frequency υ_{vib}, is measured at a certain scattering angle with respect to the incidence direction.

The scattered light components shifted to frequencies $\upsilon_{vib}<\upsilon_0$ (red-shift) are known as Stokes components, whereas those with $\upsilon_{vib}> \upsilon_0$ (blue shift) are known as Anti-Stokes. In the Raman spectrum, the scattering peak is independent of υ_0 and it is the characteristic of the particular vibrational state responsible for the diffusion. In fact, the spectra of this type can bring a relative value in Raman shift, which is the difference of wave number. It is the characteristic of the molecular species and independent of the frequency of the laser.

Raman shift:$\Delta\tilde{\upsilon} = \widetilde{\upsilon_{vib}} - \widetilde{\upsilon_0} = \frac{1}{\lambda_0} - \frac{1}{\lambda_{vib}}[\mathrm{cm}^{-1}]$

For the Stokes the Raman shift is positive, while for the Anti-Stokes it is negative. Raman scattering is produced by molecular vibrations in molecules and optical phonons in solids. It usually covers a range of 10 to 4000 cm^{-1}, which is also the typical range of IR vibrational transitions. Scattering is an extremely weak phenomenon, even more so in the visible and near IR. Photons may be emitted for any value of υ_0. However, in order to have a high scattering intensity, it is necessary to be in the resonance condition, i.e. when the frequency of the incident radiation is close to the transition frequency between the vibrational states of the system.

The instrument used in the thesis is Thermo Scientific DXR Raman Microscope (Figure 2.2) with a solid-layer laser of 532 nm (green) wavelength, power from 0 to 10mW and a microscope with 10X magnification. The instrument allows obtaining a spectrum from 50 to

3550 cm^{-1}, with a spectral resolution of 5 cm^{-1} and a sensitivity (signal to noise ratio) of 1000: 1. The parameters can be optimized by varying the intensity of the laser, the exposure time, the number of scans and the width of the slit, from which the laser beam striking the sample comes out. The presence of a diffraction grating of 900 lines/mm allows the dispersion of the radiation in the different wavelengths. The light diffused by the sample is then collected by a Charge-Couple Device (CCD) detector with 1650 pixels, before which a filter is placed that is able to eliminate the component of light spread elastically in order to avoid the saturation of the CCD.

Figure 2.2 Thermo Scientific DXR Raman Microscope

2.5 Broadband electric spectroscopy (BES) [159-161]

Broadband Electrical Spectroscopy (BES) involves the interaction between matter and electromagnetic radiation in a wide frequency range between 10^{-7} and 10^{12} Hz. In the frequency range investigated in the electric measurements presented in this work, the interaction of electromagnetic radiation with matter involves phenomena associated with macroscopic polarization phenomena due to:

a) the orientation of dipoles presents within the material (molecular relaxations);

b) the motion of free charges (in the case of ionic conductors).

In general, to analyze electric spectra, an overview is made of the spectra in various representations simultaneously to determine the types of events present, and then the data are fit using an empirical equation to determine the values of conductivities, dielectric strengths and relaxation times associated with the electric relaxations.

In dielectric polymers, molecular relaxations arising from local or collective fluctuations of molecular dipole moments are typically revealed with BES. The events present at the lowest temperatures are those associated with the shortest relaxation times and the highest frequencies. The electric spectra of conductive polymers show the coexistence of molecular (dielectric) and mesoscopic phenomena, which are generally associated with very different values of permittivity. Mesoscopic behavior, which is related to collective charge motion, exhibits strong electric responses, while molecular relaxations are associated with lower permittivity values that are generally less than 100.

The BES measurements were collected in the 10 mHz - 10MHz frequency range using an Alpha-A analyzer coupled with a temperature control system, consisting of a cryostat operating with a N_2 gas jet heating and cooling system (Figure 2.3). The temperature range varies for the investigated materials and is reported within the different chapters present in this thesis.

Figure 2.3 BES measuring system including the analyzer, temperature control system, the cryostat and sample holder cell, vacuum pump (hidden) and electronic data management.

The operating conditions for the Alpha-A analyzer are listed below in Table 2.2.

Table 2.2. Alpha A analyzer specifications.

Frequency range	3 μHz - 40 MHz
Frequency resolution	10^{-4}
Maximum sampleresistance	10^{14} Ω
Capacity range	10^{-15} – 10^{0} F

The analyzer measures the complex impedance (Z*(ω)) or capacitance (C*(ω)) of the sample over a wide frequency range and then calculates the complex permittivity and conductivity ε*(ω) and σ*(ω). A software is used to control the electrical experimental parameters and for the collection, storage and display of the imaginary and real components of the Z*(ω), σ *(ω) and ε*(ω) profiles.

The temperature control system consists of a cryostat, a gas heating module, and a microprocessor controller. It is essential to:

a) the correct temperature control of the sample, in order to ensure that the sample temperature does not exceed the set point temperature (especially near phase transition temperatures) to avoid damage or undermine the analyzed sample;
b) reduce the measuring time, because the time of sample conditioning, for frequencies lower than 0.1 Hz, occupies most of the measurement time.

For all the electric measurements carried out in this work, the temperature fluctuations are less than 0.2°C.

The microprocessor controller has four independent loops that control the sample and gas temperature (gas heater), the temperature of liquid nitrogen and the pressure in the dewar. Inside the dewar, the evaporator heats the liquid nitrogen until the desired pressure and the cold gas flows under the effect of pressure up to the heating module. The connection line between the dewar and heating module is isolated by an external vacuum chamber. The gas inside the module is heated to the set point temperature and finally reaches the cryostat (thermally isolated by an external vacuum chamber), where the sample is mounted.

The temperature of the sample is stable with an error of 0.01°C. The lower temperature limit is equal to -160°C, provided there is adequate pressure applied on the nitrogen liquid. The pressure in the dewar is directly controlled by the microprocessor and varies from 30 to 100 mbar according to the setpoint temperature. The upper temperature limit is 450°C.

The electrical measurements were performed by placing the samples between two platinum circular electrodes with a diameter of 13 mm. The cell constant was determined from the area of the electrodes and their distance d. For polymer membranes, d is equal to the thickness of the samples (measured with a digital micrometer).

All of the samples were placed between the electrodes within a sealed cell consisting of two Teflon bodies which are bound together through two external brass rings. The cell is shown in Figure 2.4. Electric contact with the external platinum electrodes through the Teflon cell body is secured by two steel cylinders, coaxial and in contact with the platinum electrodes. The system allows the insulation of the sample from the external environment in order to prevent:

a) sample dehydration during the measurement (for samples measured in wet conditions);

b) the absorption of water from the external environment (for samples measured in dry conditions).

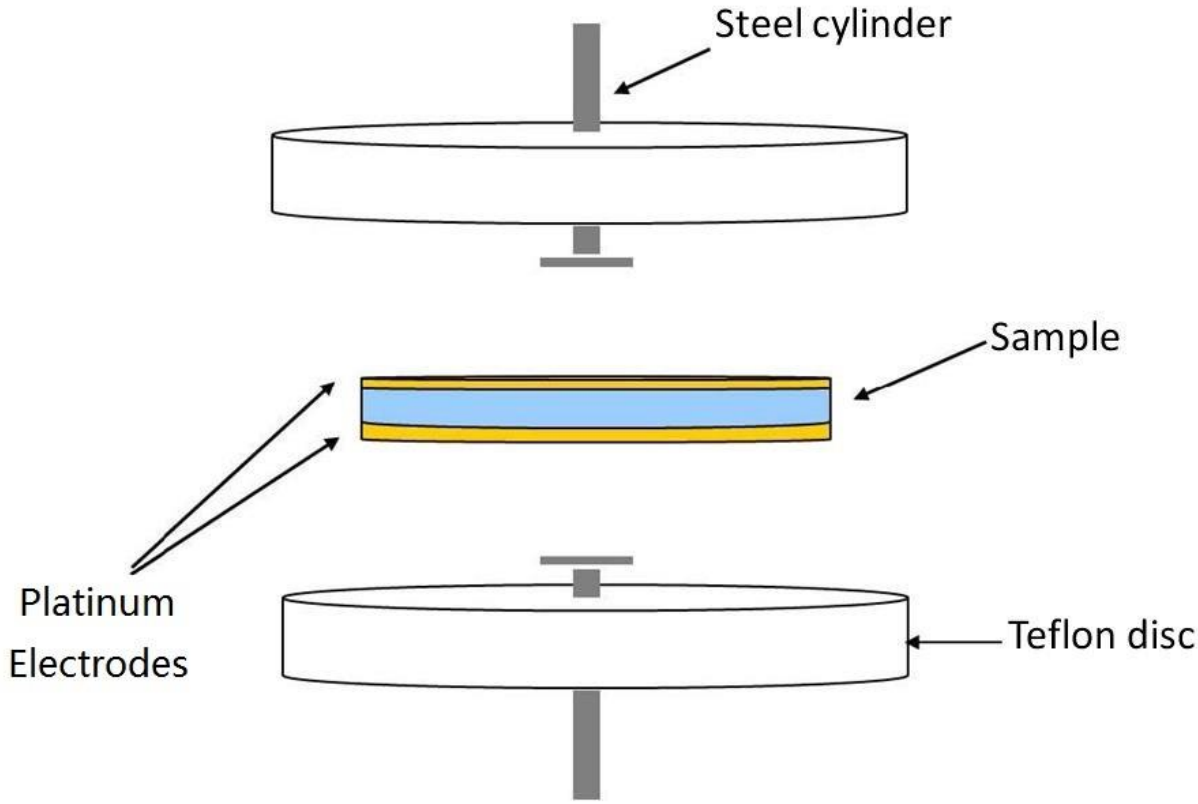

Figure 2.4 Cell for electric measurements

For wet samples, the free volume of the cell was partially filled with 100μL of bidistilled water in order to avoid sample drying during measurements at T>90°C. No corrections for thermal expansion of the cell were carried out. The absence of water loss during measurements was checked by weighing the closed cell before and after the measurements. The value of the high-frequency plateau ($f > 10^5$ Hz) of σ' is adopted as a good approximation of the ionic conductivity (σ_{DC}) of a fully hydrated Nafion-based membrane.

2.6 Facility for single VRFB cell tests

The facility used for testing the membrane in single VRFB cell is reported in Figure 2.5. The key components of the battery setup include a single battery cell, electrolyte solution reservoirs and pumps circulating the electrolytes. Catholyte and anolyte are respectively contained in two 100 mL glass reagent bottles and are circulated between the battery cell and reservoirs within 1/8″ or 1/4″ outside diameter polyethylene tubing by a two-channel ISMATEC 832C digital peristaltic pump with variable speed precision.

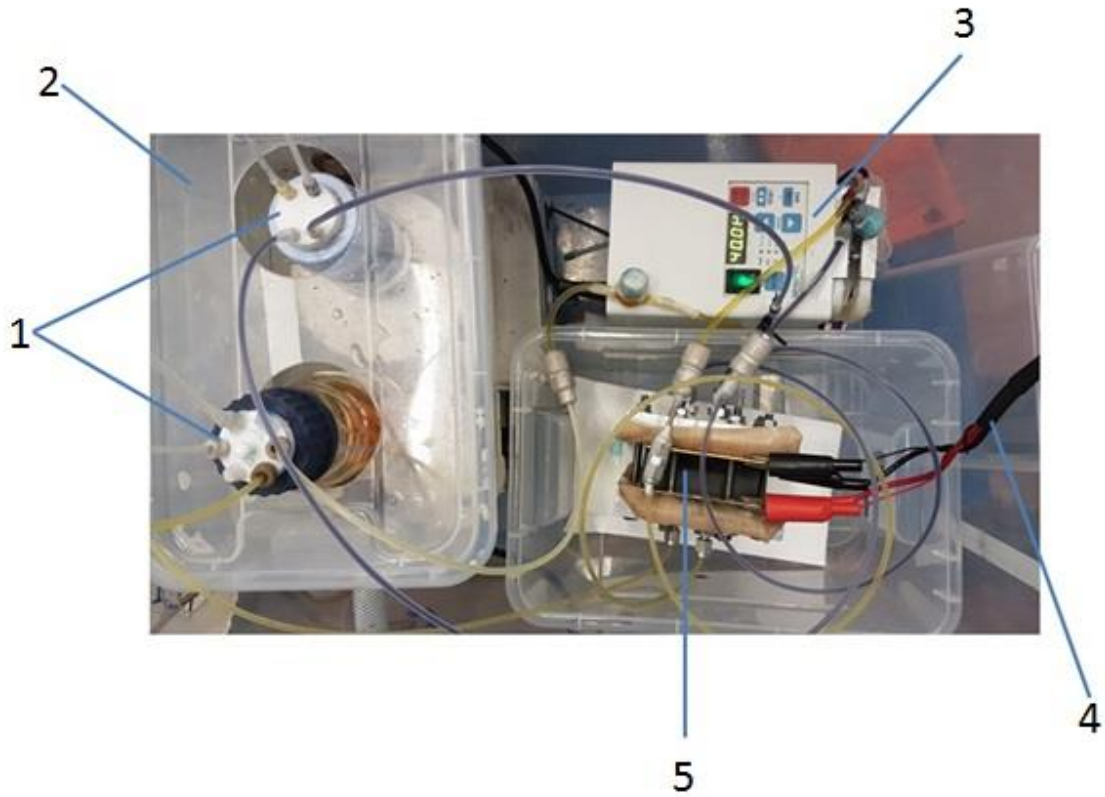

Figure 2.5 Facility for single VRFB cell tests.

The system shown in Figure 2.5 allows the investigation of the charge-discharge cycling characteristics of the membrane. The measurement conditions (temperature and reagents flows etc.) are controlled at optimized factors (temperature at 30 °C and flow rate 15mL min^{-1}). The various components in the test system are explained in detail as follows:

1-Bottles: as reservoirs for the storage of catholyte and anolyte. The center of the cap is made of Teflon material with four holes for the inflow and outflow of catholyte/anolyte and nitrogen gas.

2-Plastic box with controlled temperature water bath: it is connected to the Haake F3 K Circulating Water Bath Chiller through pipes. The settled temperature is 30 °C for the chiller and water at a constant temperature is circulating between the chiller and plastic box.

3-Peristaltic pump (Chapter 5.2.6) or Magnetic pump (Chapter 4.2.4): transport the catholyte/anolyte from the reservoir to the corresponding half-cell. After the redox reactions taking place in the cell, the reacted components are transferred back to the reservoir and fresh catholyte/anolyte enters the half-cell. The flow rate is controlled at 15mL/min.

4-Cables: as a connection between the current collectors of the single cell and Maccor Model 2300 Battery Test System is applied for single cell charge-discharge cycling test.

5-Single VRFB cell: which consists of the current collectors, graphite plates with the flow channels, membrane, gaskets and carbon electrodes.

A new zero-gap, flow-by battery cell architecture, shown in Figure 2.6, was applied to VRFB cell configuration in this thesis. The battery cell was modified from a 5 cm^2 direct methanol fuel cell (Fuel Cell Technology Inc.). In this cell, a flow-by flow pattern was introduced by graphite current collectors with serpentine flow channels (0.787 mm wide and 1.02 mm deep). The output capacity with the novel flow-by cell design is substantially higher than previously reported battery configurations [49] in which cells were mostly flow-through designs. The measuring single cell consists of two graphite bipolar plates that distribute the catholyte and anolyte within the cell and at the same time act as current collectors. The electrode material used in the single VRFB cell is Avcarb P75 (thickness: 245 microns), which is thermally pretreated in an oven at 400°C for 24h under air flow. The electrolyte separator used in all following measurements included Nafion 212 membrane as the reference, purchased from Ion Power Inc. The dry thickness of Nafion 212 was 50 μm. Before being installed in battery cell, the membrane was cut into a size fitting in the cells and pretreated with the protocol as described in each chapter.

The energy efficiency (EE) [equal to the ratio between the energy output of the VRFB during the discharge (I_dV_d) and the energy supplied (I_cV_c) during the charge], coulombic efficiency (CE) [the ratio between the charge withdrawn from the system during the discharge and the charge supplied during the charge] and voltage efficiency (VE) [defined for a charge/discharge cycle at a constant current] of the cell are evaluated with the following equations (2.6.1-2.6.3) [111]:

$$EE = \frac{\int_0^t V_d I_d dt}{\int_0^t V_c I_c dt} \times 100\% \qquad (2.6.1)$$

$$CE = \frac{\int_0^t I_d dt}{\int_0^t I_c dt} \times 100\% \qquad (2.6.2)$$

$$VE = \frac{EE}{CE} \times 100\% \qquad (2.6.3)$$

where I_c and I_d are the charge and discharge current respectively, while V_c and V_d are the charge voltage and the discharge voltage.

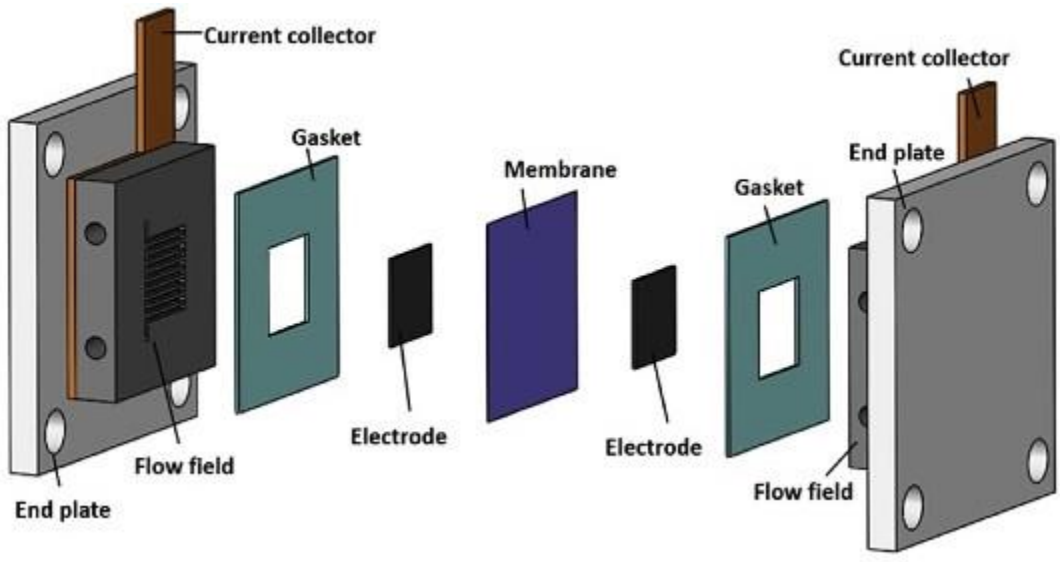

Figure 2.6 Sketch of the novel zero-gap VRFB cell configuration with a flow-by flow pattern [162].

The electrolyte solutions were originally made from $VOSO_4 \cdot xH_2O$ (Alfa Aesar, x=3.23, 99.9%), H_2SO_4 (Sigma Aldrich, 96~98%) and bidistilled water. All electrolyte solutions were charged from $VOSO_4/H_2SO_4$ solutions made from their agents. Electrolyte solution with 1M $VOSO_4$ concentration levels was prepared in 4M H_2SO_4. To prepare electrolyte solutions for the battery, electrolyte solutions were charged with a two-step charging protocol. The solutions were firstly charged by a 1.8V constant voltage across the battery to prevent overcharge (if the state of charge nearly reaches the maximum, side reactions including water splitting may take place). In the first charging step, the volume of $VOSO_4$ solution in catholyte is twice as the anolyte in order to accommodate a change of two oxidation states as expected (convert VO^{2+} to V^{2+} and VO_2^+). VO_2^+ and V^{2+} were obtained respectively in catholyte and anolyte of the battery. In order to maintain the same number of electron transfers between catholyte and anolyte during the charge-discharge cycling test, it is essential to make the catholyte and anolyte with the same volume. Therefore, before the charge-discharge cycling, a half volume of the catholyte was taken out. The detailed charge-discharge protocol is further described in related chapters. During battery operation, nitrogen was pumped into the negative electrolyte solution to protect V^{2+} and V^{3+} from the oxidation of air and oxygen.

2.7 UV-Vis Spectroscopy

UV-Vis spectroscopy is used to determine the absorption of the samples at different wavelengths. Absorbance is a measure of the light that does not pass through the sample and corresponds to the base ten logarithms of incident light, I_0, divided by light registered by the detector. This is known as Lambert-Beers law which is written as:

$$A = \log_{10}\left(\frac{I_0}{I}\right) = \varepsilon cl$$

Where A is the absorbance of the sample; the constant ϵ is called molar absorptivity or molar extinction coefficient and is a measure of the probability of the electronic transition; c is the concentration of the solution of the sample used in the experiment; l is the length of the light path; I_0 is the incident intensity and I is the transmitted intensity.

Figure 2.7 Perkin Elmer Lambda 40 UV-VIS Spectrophotometer

The permeability of the membranes is measured by UV-Vis spectrometry using a Lambda Technologies, Lambda 40 UV-Vis dual-beam spectrometer with quartz cuvettes.

The Lambda 40 is dual beam Ultraviolet-Visible spectrophotometer capable of scanning from 190 nm - 1100 nm. Rapid, reproducible results as well as an easy to use computer interface make these ideal instruments for spectral analysis in the ultraviolet and visible spectrums. The Lambda 40 are controlled by UV WinLab version 2.85, which allows for easy data extraction and analysis. Fixed wavelength, scans, and kinetic analysis are the most common uses for the Lambda 40. The standard 1 cm^2 cuvettes are used.

2.8 Water uptake, vanadium permeability and ion selectivity

The water uptake (WU%) of the membranes is gauged by comparing the weights of the dry and the wet membrane samples by means of Eq. (2.8.1). The dry membrane weight (W_{dry}) is obtained by drying the sample at 100°C for 12 h immediately before weighing it. The weight of the corresponding membrane in wet conditions (W_{wet}) is obtained by immersing the membrane sample in bidistilled water for 24 h, wiping off the surface moisture with filter paper and then quickly weighing it. The final water uptake is obtained from the average of three experiments.

$$\mathrm{WU\%} = \frac{W_{wet} - W_{dry}}{W_{dry}} \times 100\% \qquad (2.8.1)$$

The vanadium permeability is determined using a standard diffusion cell setup [20]. The effective area of the sample membrane is 3 cm^2. One reservoir is filled with 50 mL of the solution consisting of 1 M $VOSO_4$ in 4 M H_2SO_4; the other reservoir (blank) is filled with a 50 mL solution of 5 M H_2SO_4. The cell is left for 72 h with both halves kept under constant magnetic stirring. 1 mL aliquots are taken from both halves of the cell every few hours over a period of 3 days. The aliquots taken from the blank cell are then tested for vanadium content by means of UV-Vis spectroscopy without diluting the samples. The schematic diagram of the vanadium permeation test is demonstrated in Figure 2.8 and the vanadium permeability (P) of the samples is calculated by means of Eq. (2.8.2).

$$V_B \frac{dC_B(t)}{dt} = A\frac{P}{L}(C_V - C_B(t)) \qquad (2.8.2)$$

where P is the VO^{2+} permeability, C_V and $C_B(t)$ are the VO^{2+} ion concentrations in the vanadium and blank cells, L is the thickness of the membrane, A is the effective area of the membrane, and V_B is the solution volume of the blank reservoir.

The ion selectivity (S) of the membranes is defined as the ratio of proton conductivity vs. vanadium permeability, and as such is defined by equation (2.8.3).

$$S = \frac{\sigma}{P} \qquad (2.8.3)$$

where S is the ion selectivity, σ is the proton conductivity, and P is the VO^{2+} permeability.

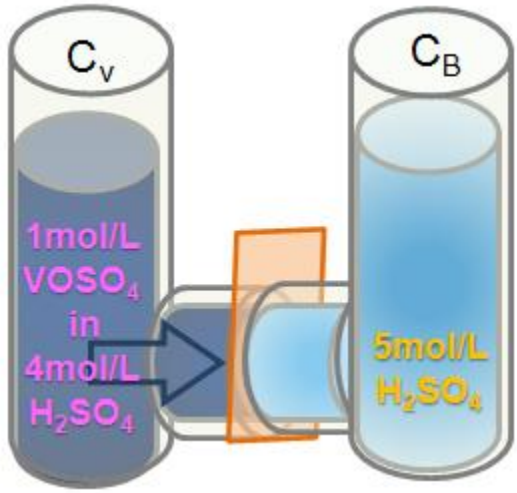

Figure 2.8 The schematic diagram of the vanadium permeation test

2.9 Chemical Stability test

The chemical stability of the membranes is investigated using an *"ex-situ"* method. The circular discs of each membrane are cut and immersed in 20 mL of electrolyte solution (1 M VO_2^+ in 4 M H_2SO_4) at room temperature. The electrolyte solution is obtained by oxidizing a solution including 1 M $VOSO_4$ in 4 M H_2SO_4 in a single VRFB [56]. The membrane oxidative stability was determined by weight, thickness and length change (%) which can be calculated by the following:

$$\text{Weight}^* \text{ Change } \% = \frac{W_0 - W_1}{W_0} \times 100\% \qquad (2.9.1)$$

*Weight, thickness or length

Where W_0 and W_1 are the weights* of the membranes before and after immersion in V (V) solution

Chapter III [Nafion/(WO_3)]$_x$ hybrid inorganic-organic proton conducting membranes for VRFB application: Synthesis, properties and vibrational studies

3.1 Introduction

The idea to prepare the hybrid inorganic-organic membranes based on perfluorinated ionomers such as Nafion was inspired by the research in direct methanol fuel cells (DMFCs) [163-166]. The methanol permeability of the IEM is decreased by the introduction of inorganic nanoparticles, as the latter block the hydrophilic regions through which the migration of methanol takes place.

As a nanofiller the WO_3 oxide was chosen because of its excellent properties, that can be exploited for applications in electrochemical devices [85, 167-171]. WO_3 is stable in high concentrated sulfuric acid and has a lower cost in comparison with other metal oxides typically used for this purpose, *e.g.* IrO_2 [172]. In addition, the presence of hydrated WO_3 in a [Nafion/(WO_3)$_x$] hybrid membrane may serve to keep the IEM hydrated, thus facilitating ion-conductivity under operating conditions that give rise to water loss [173].

According to our previous studies [153-155], the distribution of nanofillers in the polymeric Nafion matrix and the compatibility between the two phases (inorganic filler phase and polymer phase) play an essential role in defining the physicochemical properties of the nanocomposite membranes. Here we describe nanocomposite Nafion-based membranes containing a dispersion of tungsten oxide nanoparticles (NPs) in various weight percentages (*i.e.*, 0, 1, and 12 wt%). These values are selected to better elucidate the impact of the interactions between the WO_3 nanofiller and the Nafion polymer host. In detail, the membrane including 1 wt% of WO_3 reveals how even a very small amount of nanofiller affects

the Nafion matrix. On the other hand, the membrane including 12 wt% of WO_3 highlights the interplay between: (i) the distribution of nanofiller in the membrane, and (ii) the thermal stability, the conformation of the polymer chains and the permeability to vanadium species.

The thermal properties of [Nafion/$(WO_3)_x$] hybrid membranes are probed both by high-resolution thermogravimetric analysis (HR-TGA) and by modulated differential scanning calorimetry (MDSC). Vibrational spectroscopy studies are carried out by: (i) Attenuated Total Reflectance - Fourier Transform Infrared spectroscopy (ATR-FTIR); and (ii) Raman spectroscopy, to elucidate the secondary structure of [Nafion/$(WO_3)_x$] and study the interactions taking place between the nanofiller and the Nafion matrix. The electrical response of [Nafion/$(WO_3)_x$] is determined by Broadband Electrical Spectroscopy (BES) and the permeability towards VO^{2+} species is measured by UV-VIS spectrometry. It is demonstrated that the [Nafion/$(WO_3)_x$] hybrid membranes exhibit a high ion selectivity (up to $10.6 \cdot 10^3$ S·min·cm^{-3} for [Nafion/$(WO_3)_{0.329}$]) that is much improved in comparison with that characterizing recast Nafion ($6.5 \cdot 10^3$ S·min·cm^{-3}). A structural model and a conductivity mechanism for the [Nafion/$(WO_3)_x$] hybrid membranes are proposed, in order to rationalize the experimental results and correlate the electrical response with the transport properties.

3.2 Experimental

3.2.1 Reagents

A 5 wt% solution (water/propanol) of Nafion ionomer (perfluorosulfonic acid PTFE copolymer solution) with an ion-exchange capacity (IEC) of 0.92 $mEq \cdot g^{-1}$ (Alfa Aesar, ACS) is used. The WO_3 nanopowder is used as a homogenous suspension obtained by sonicating WO_3 nanopowders with a particle size of ca. 100 nm (Aldrich, ACS grade) in N, N-dimethylformamide (DMF) for 2hours. All the used solvents are provided by Aldrich and used as received; doubly distilled water is used throughout the experiments.

3.2.2 Membrane Preparation

[Nafion/$(WO_3)_x$] hybrid membranes are prepared with a solvent casting procedure as reported in our previous publication [27]. Briefly, the solvent is removed from the 5 wt% Nafion solution by heating at 80 °C until a thin film is obtained. The film is then dissolved in DMF and mixed with different amounts of WO_3. The resulting suspension is treated in an ultrasonic bath for 2 h, yielding a homogenous dispersion that is cast in a Petri dish (diameter: 90 mm) and placed in an oven at 80 °C for 12 h. The obtained membrane is then dislodged by immersing the Petri dish in bidistilled water at room temperature (25 °C). The thickness of all the membranes in this study falls between 50 and 65 μm (as measured under ambient air conditions).

3.2.3 Membrane Activation

The [Nafion/$(WO_3)_x$] hybrid membranes are activated in a four-step process. The membranes are heated at 80 °C in bidistilled water for 1 h. They are then removed from the water and immersed in a 3 wt% H_2O_2 solution for an additional hour at 80°C. The membranes are then soaked for 1 h in 1 M H_2SO_4 at 80°C, before finally being washed thoroughly with bidistilled water. The treated membranes are stored at room temperature inside plastic bags filled with bidistilled water. Three different membranes are obtained, with x = 0, 0.024 and 0.329

(corresponding to 0, 1 and 12 wt%, respectively). The membrane with x = 0 does not include WO_3, it is used as the reference throughout this work and is labeled "recast Nafion". The detailed composition of the membranes is shown in Table 3.1 and the detailed membrane preparation procedure is illustrated in Figure 3.1.

Table 3.1 Composition and molar ratios of [Nafion/$(WO_3)_x$] membranes.

Membrane	Wt% of WO_3[a]	x[b]	Ion exchange capacity [c] $_{calculated}(\varphi)$ / mEq·g^{-1}
Recast Nafion	0	0	0.9200
[Nafion/$(WO_3)_{0.024}$]	1	0.024	0.9108
[Nafion/$(WO_3)_{0.329}$]	12	0.329	0.8096

[a] Values determined on the activated membranes as the high-temperature residue measured on HR-TGA under an air atmosphere; [b]x = molWO_3/mol -SO_3H; [c]φ = meq$_{Nafion}$ /m$_{composite}$.

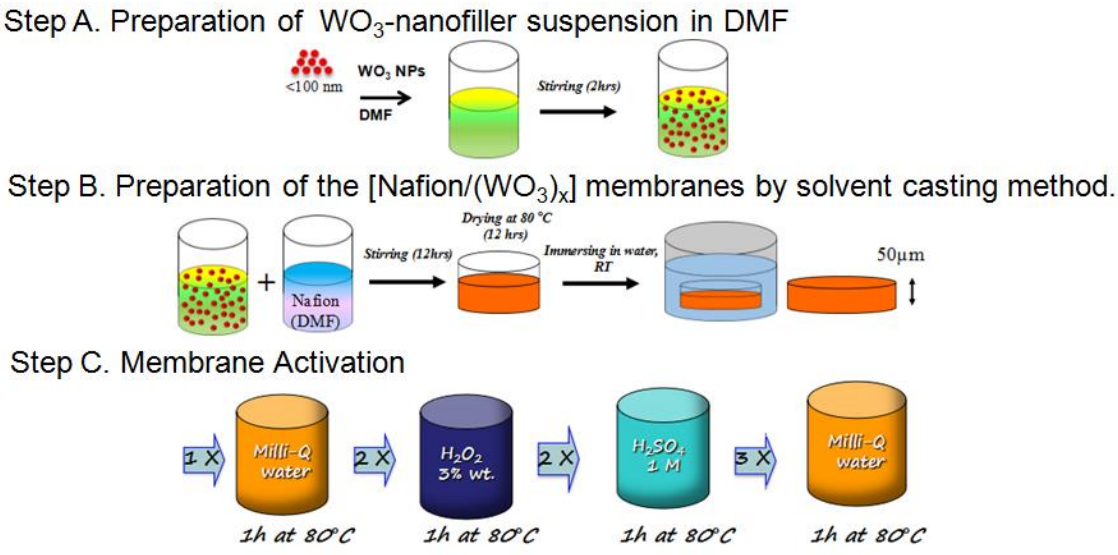

Figure 3.1 Hybrid membrane preparation procedure

3.2.4 Instruments and Methods

The thermogravimetric profiles were collected in the 20<T<900°C temperature range. The samples are exposed to a dry air flow for 24 hours before the measurements (this yields $\lambda \approx 2$, where is defined as the ratio between the number of water molecules and the number of $-SO_3H$ groups present in the system [174]). Modulated differential scanning calorimetry analyses were performed in the -150 to 200 °C temperature range with a ±1.000 °C modulation every 60 seconds.

FT-IR-ATR spectra of the membranes were collected in ATR mode on both sides of the membranes. The spectra are obtained averaging 1000 scans. Samples for ATR-FTIR are prepared in two different conditions: (i) storing samples at room temperature for 24 hours under a dry air stream; this yields $\lambda \approx 2$; and (ii) drying the samples at 100°C under vacuum for 3 days; this yields $\lambda = 0$. Condition (i) and (ii) are labeled "air flow condition" and "dry condition", respectively. The samples for Raman studies are prepared exclusively in "air flow condition".

Electrical properties of the new membranes were checked by a BES. A frequency range at 30 mHz ÷ 10 MHz, temperature range at-100 ÷ 200°C and a 10°C temperature interval is used for all the samples. BES studies are carried out on completely hydrated samples.

The permeability of the membranes is measured by UV-Vis spectrometry.

More information of each method and instrument is presented in Chapter II.

3.2.5 Water uptake, vanadium permeability and ion selectivity

The water uptake, vanadium permeability and ion selectivity were performed using the method and system described in Chapter 2.8.

3.2.6 Chemical Stability test

The chemical stability test was performed using the procedure described in Chapter 2.9 in this thesis. The variation in the diameter, thickness and weight of the membranes is measured over the course of 80 days.

3.3 Results and Discussion

3.3.1 Thermal analysis

The thermal stability of all membranes is gauged by HR-TGA (Figure 3.3(a)). All membranes exhibit four thermal decompositions (I-IV). The first mass loss (I), observed at 30 < T < 100°C and of a magnitude of less than *ca.* 1 wt%, is associated with the loss of residual water from the membranes. The second thermal event (II), observed in the region of between *ca.* 130 and 250°C and of a magnitude of approximately 1 wt% for all membranes, is associated with the loss of the -SO_3H groups [175, 176]. The third thermal decomposition (III), which is observed in the range between 300 and 400 °C, is attributed to the decomposition of the perfluoroethereal side chains of the Nafion host. The final mass loss (IV), observed at 400 ÷ 550 °C, corresponds to the decomposition of the polytetrafluoroethylene (PTFE) backbone. There are no detrimental effects observed to the thermal stability of the Nafion matrix upon embedding of the WO_3 nanofiller, with the only significant difference between the HR-TGA profiles being the differing residual weights owing to the presence of different nanofiller content.

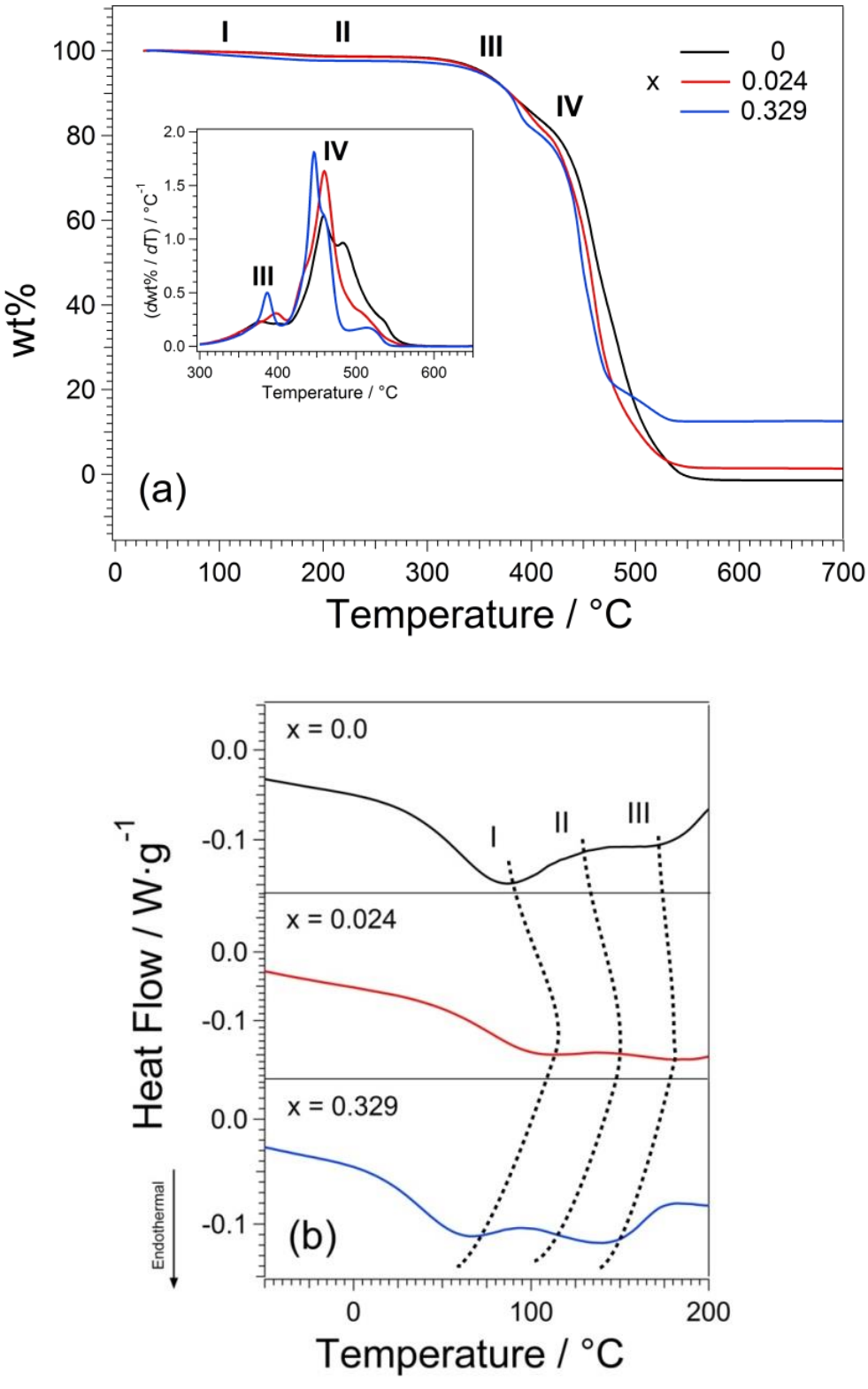

Figure 3.3 (a) HR-TGA profiles of [Nafion/$(WO_3)_x$] membranes; the first derivative of the wt% in the 300-700°C range is reported in the inset; (b) MDSC profiles of [Nafion/$(WO_3)_x$] membranes. The endothermic transitions are labeled I-III.

The MDSC profiles of the hybrid membranes, as well as that of pristine Nafion, are shown in Figure 3.3(b). Three endothermic transitions (I–III) can be observed for all the samples, with the temperature of these events being dependent on the level of nanofiller (x). Peak I is assigned to the melting of small and imperfect fluorocarbon nanocrystalline domains of Nafion [177]. For pristine Nafion, I occurs at 86°C. The addition of nanofiller (x = 0.024) into the Nafion matrix increases the size of the nanocrystalline domains. This is evidenced by an increase in the temperature of I to 99°C. Indeed, we have previously observed a similar effect in the Nafion matrix doped by other nanofillers [178]. At the higher nanofiller level (x = 0.329) this effect on the nanocrystalline domains is lost and their thermal behavior is reminiscent to that of pristine Nafion. This may be because the elevated nanofiller loading level results in a phase segregation resulting in nanofiller-rich and Nafion-rich domains [178]. Peak II is attributed to the thermal degradation of the $-SO_3H$ groups in accordance with the HR-TGA data. At the lower loading level (x = 0.024) the crosslinking interactions between sulfonate groups and the tungsten oxide nanoparticles lead to a slight increase to their thermal stability. At the higher nanofiller loading level (x = 0.329) this stabilizing effect is lost, again likely as a result of phase segregation. The third endotherm event (III) is associated with the melting of the hydrophobic fluorocarbon microcrystalline regions. For pristine Nafion, this melting occurs at 156°C. The stabilizing effect of the lower level of nanofiller is again observed by the increase in temperature of III to 180°C for x = 0.024. The phase segregation effect at x = 0.329 once again removes the enhancement to thermal stability.

3.3.2 Vibrational spectroscopy studies

Figure 3.4 reports the ATR-FTIR spectra of the two hybrid membranes (*i.e.*, [Nafion/$(WO_3)_{0.329}$] and [Nafion/$(WO_3)_{0.024}$]) and of recast Nafion. The ATR-FTIR spectra of both sides of each membrane are collected: the top *"Nafion-rich"* and the bottom *"WO_3-rich"* side are labelled *"Side A"* and *"Side B"*, respectively. The ATR-FTIR profiles are normalized on the peak at 981 cm^{-1}, which is assigned to the (COC) mode of the ether link of the perfluoroethereal side chain closest to the PTFE backbone of the Nafion host [174]. The peak is chosen for the normalisation as the intensity of side chain is not strongly affected by the incorporation of WO_3 nanofiller. The profiles in the third column of Figure 3.4 are obtained by subtracting the profiles of Side A from those of Side B. Figure 3.4 also shows the spectrum of neat WO_3 nanoparticles. The experiments are carried out in two different environmental conditions: (i) under a flow of dry air, corresponding to $\lambda \sim 2$ [see Figure 3.4(a)]; and (ii) in completely dry conditions [see Figure 3.4(b)]. The correlative assignment of the bands revealed in the ATR-FTIR and Raman profiles displayed in Figure 3.4 and Figure 3.5 is reported in Table 3.2.

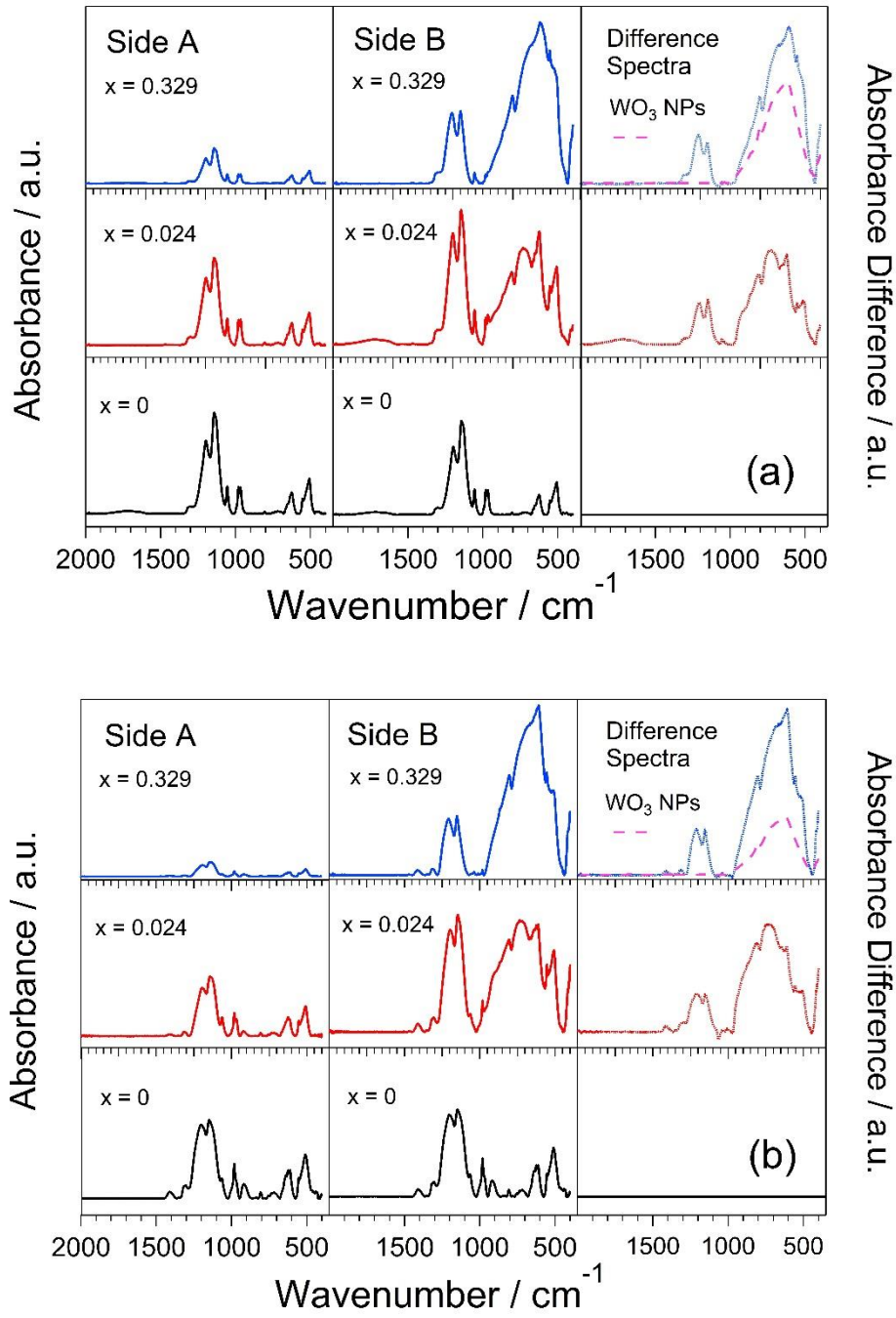

Figure 3.4 ATR-FTIR profiles and difference spectra of [Nafion/$(WO_3)_x$] membranes. Side A: top "Nafion-rich" side; Side B: bottom "WO_3-rich" side; Difference Spectra: they are obtained by subtracting the profiles of Side A from the corresponding profiles of Side B. The profiles are collected: (a) at $\lambda \sim 2$; and (b) in completely dry condition. The spectrum of neat WO_3 nanoparticles is also reported.

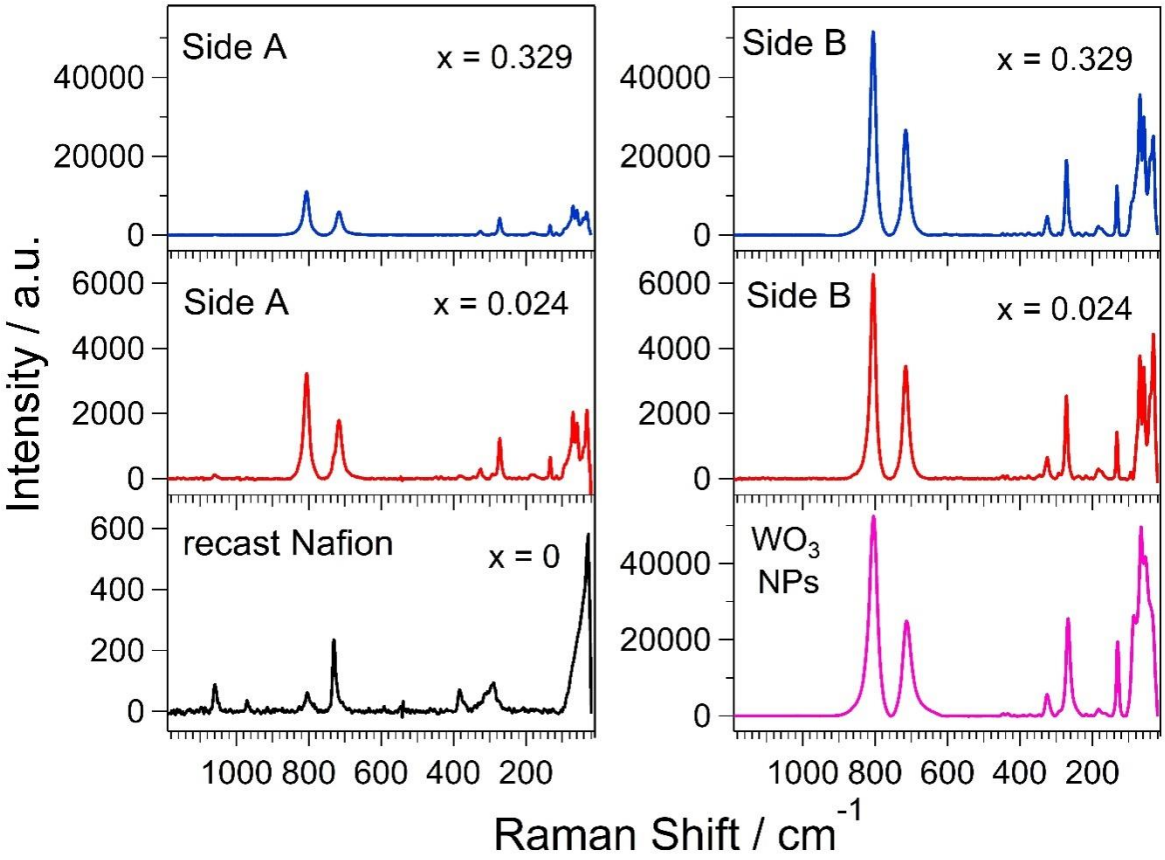

Figure 3.5 Raman profiles of [Nafion/$(WO_3)_x$] membranes collected at $\lambda \sim 2$. The explanation of the labels "Side A" and "Side B" is reported in the caption of Figure 3.4. The spectrum of neat WO_3 nanoparticles is also reported.

Table 3.2 ATR-FTIR and Raman band assignments of recast Nafion, [Nafion/$(WO_3)_{0.024}$] and [Nafion/$(WO_3)_{0.329}$] membranes.

Observed Modes[a] / cm^{-1}																		
Recast Nafion			[Nafion/$(WO_3)_{0.024}$]						[Nafion/$(WO_3)_{0.329}$]						WO_3 NPs		Band assignments[b]	Ref.
			Side A			Side B			Side A			Side B						
ATR		Raman	ATR		Raman	ATR		Raman	ATR		Raman	ATR		Raman	ATR	Raman		
$\lambda^c = 0$	$\lambda^c \sim 2$	$\lambda^c \sim 2$	$\lambda^c = 0$	$\lambda^c \sim 2$	$\lambda^c \sim 2$	$\lambda^c = 0$	$\lambda^c \sim 2$	$\lambda^c \sim 2$	$\lambda^c = 0$	$\lambda^c \sim 2$	$\lambda^c \sim 2$	$\lambda^c = 0$	$\lambda^c \sim 2$	$\lambda^c \sim 2$				
	1717 (vw)						1717 (vw)						1717 (vw)				$\delta[H_3O^+\cdots(H_2O)n]$	[179-181]
1413 (vw)			**1415 (vw)**			**1412 (vw)**			**1412 (vw)**			**1412 (vw)**					$\nu_s(SO_3H)$	[174, 179, 182]
1316 (vw)	1316 (vw)		**1316 (vw)**	1316 (vw)		**1316 (vw)**	1317 (vw)		**1319 (vw)**	1317 (vw)		**1319 (vw)**	1316 (vw)				10_3: ν[CC]	[179, 180]
1307 (vw)	1307 (vw)		**1307 (vw)**	1307 (vw)		**1307 (vw)**	1306 (vw)		**1306 (vw)**	1306 (vw)		**1309 (vw)**	1307 (vw)				10_3: ν[CC]	[174, 179]
1205 (vw)	1197 (vw)		**1196 (vw)**	1197 (vw)		**1198 (vw)**	1200 (vw)		**1196 (vw)**	1197 (vw)		**1208 (w)**	1207 (w)				15_7: $\nu_{as}[CF_2]$	[174, 179]
1149 (vw)	1144 (vw)		**1141 (vw)**	1143 (vw)		**1145 (vw)**	1146 (vw)		**1141 (vw)**	1143 (vw)		**1152 (w)**	1150 (w)				15_7: $\nu[CF_2]$	[174, 179]
1132 (vw)	1131 (vw)		**1132 (vw)**	1130 (vw)		**1134 (vw)**	1134 (vw)		**1134 (vw)**	1131 (vw)		**1135 (w)**	1132 (vw)				10_3: $\nu_{as}[CF_2]$	[174, 179]
1064 (vw)	1065 (vw)	1056 (vw)	**1063 (vw)**	1056 (vw)	1056 (vw)	**1063 (vw)**	1056 (vw)		**1063 (vw)**	1056 (vw)	1056 (vw)	**1063 (vw)**					$\nu_s(SO_3^-)$	[174, 179, 180, 182]
981 (vw)	982 (vw)		**981 (vw)**	982 (vw)		**981 (vw)**	982 (vw)		**981 (vw)**	982 (vw)		**982 (vw)**	982 (vw)				15_7: ν_s[C-O-C]	[179, 183]
967 (vw)	967 (vw)	969 (vw)		967 (vw)			967 (vw)			968 (vw)			967 (vw)				15_7: ν_s[C-O-C]	[179, 183]
						864 (vw)	864 (m)					**864 (m)**	864 (vw)		864 (vw)		W-O-W-O-W	[184]
808 (vw)	808 (vw)	804 (vs)	**808 (vw)**	808 (vw)	805 (vs)	**808 (w)**	808 (m)	805 (vs)	**808 (vw)**	808 (vw)	805.6 (vs)	**804 (s)**	802 (m)	805 (vs)	801 (vw)	803 (vs)	15_7+10_3: $\gamma[CF_2]$; δ[CCF]; ν[CO];δ[COC];ν[WO]	[179, 185, 186]
		731 (vw)			716 (vw)	**720 (vw)**	720 (vw)	716 (vw)			716 (vw)	**720 (vw)**	720 (vw)	716 (vw)	719 (vw)	716 (vw)	δ[WO]; 15_7; ν (CF_2)	[179, 185, 186]
611 (vw)	624 (w)		**611 (vw)**	624 (w)		**612 (vw)**	623 (vw)		**611 (vw)**	624 (w)		**608 (vs)**	619 (m)		613 (vw)		ν(O-W-O); 10_3 : ν[CF]; δ [CCF]; ν[CC]	[179, 185, 186]
554 (vw)	554 (vw)		**554 (vw)**	554 (vw)		**554 (vw)**	554 (vw)		**554 (vw)**	554 (vw)		**554 (s)**	554 (m)					
505 (vw)	505 (vw)		**505 (vw)**	505 (vw)		**507 (vw)**	507 (vw)		**505 (vw)**	505 (vw)		**509 (m)**	509 (w)				15_7+10_3: ρ(CF_2);ρ(CF_3); δ(OSO)	[179, 185]
						413 (vw)	413 (vw)					**414 (w)**	414 (vw)		414 (vw)		W–O	[183]
		381 (vw)			384 (vw)			376 (vw)			376 (m)			376 (vw)		370 (vw)	δ(O-W-O)	[186, 187]
		289 (vw)			274 (w)			272 (m)			273 (vw)			272 (m)		267 (m)	δ(O-W-O)	[186, 187]
					185 (vw)			184(vw)			184 (vw)			185 (vw)		182 (vw)	Lattice modes	[187, 188]
					133 (m)			132			133 (w)			131 (w)		130 (m)	Lattice modes	[186, 188]
					70 (m)			69 (m)			70 (m)			68 (s)		86 (m)	Lattice modes	[186, 188]
					59 (m)			58 (m)			60 (m)			58 (m)		66 (vs)	Lattice modes	[186, 188]
		28 (vs)			32 (m)			31 (s)			32 (m)			32 (m)		54 (m)	Lattice modes	[186, 188]

[a] vs = very strong, s = strong, m = medium, w = weak, vw = very weak; [b] ν = stretching, δ = bending, as = antisymmetrical, s = symmetrical; [c] λ = mol H_2O/mol -SO_3H.

The spectra reveal the vibrational modes associated to:

(a) the hydrophobic fluorocarbon chains of Nafion (1300-1000 cm^{-1})

(b) the perfluoroetheral side chains of Nafion (1000-940 cm^{-1})

(c) the WO_3 inorganic component (850-400 cm^{-1}).

The spectra of the samples at $\lambda \sim 2$ exhibits a broad, weak band at *ca.* 1700 cm^{-1}, that is ascribed to the bending modes of water (see Figure 3.4(a)). This band is not detected in the spectra of the dry samples (see Figure 3.4(b)); instead, the latter reveals two peaks at 920 and 1410 cm^{-1}, that are attributed to the undissociated $-SO_3H$ groups of Nafion [174]. The analysis of the ATR-FTIR profiles demonstrates that in [Nafion/$(WO_3)_x$] hybrid membranes the structural features and inter-chain interactions of Nafion are significantly influenced by x. The effect of the WO_3 nanofiller is as follows: (a) the intensity of the strong band at 615 cm^{-1}, that is also highlighted in the spectrum of neat WO_3 nanoparticles and is attributed to the ν(O-W-O) mode, increases as x is raised; (b) at $\lambda \sim 2$, water plasticization promotes the $15_7 \rightarrow 10_3$ conformational transition; however, the latter is inhibited at x = 0.329 (see Figure 3.4(b)); and (c) in the completely dry state, the lack of water plasticization inhibits the $15_7 \rightarrow 10_3$ transition, and the Nafion PTFE hydrophobic domains are mostly in the 15_7 conformation for all x values.

The Raman profiles of all the hybrid membranes, both on Side A and Side B, are dominated by the vibrational modes of the WO_3 nanoparticles of the filler. The most intense peaks are revealed at 805, 715 and 271 cm^{-1}; they are assigned to the ν(WO), δ(WO) and δ(O-W-O) modes of WO_3, respectively [186, 187]. Other peaks ascribed to WO_3 are present between 20 and 200 cm^{-1}. They are assigned to the lattice modes of WO_3 [186, 188]. The intensity of the features attributed to WO_3 in the Raman profiles of the hybrid membranes increases by a factor of *ca.* 2-5 from Side A to Side B, and by a factor of *ca.* 5-10 as x is raised from 0.024 to 0.329. This result is consistent with the higher concentration of WO_3 located on the B side of the hybrid membranes, and also in general as x is raised. The Raman profile of recast Nafion is similar to that typically reported in the literature [175]. The peak at 1056 cm^{-1} is ascribed to

the symmetric stretching of the sulfonate anion, $\nu_s(SO_3^-)$; its presence demonstrates that the $-SO_3H$ groups of Nafion are completely dissociated even at very low hydration degrees ($\lambda \sim 2$) [174]. This peak is also revealed in the profiles of Side A of the [Nafion/$(WO_3)_{0.329}$] and [Nafion/$(WO_3)_{0.024}$] hybrid membranes; it is not detected on Side B, as it is completely overwhelmed by the peaks of the WO_3 filler. Other peaks present in the Raman spectrum of pristine Nafion are found at 811 and 731 cm^{-1}. The former is assigned to a mode involving $\nu[CF_2]$, δ[CCF] and ν[CO] components; the latter is attributed to the stretching modes of CF_2 moieties [174].

3.3.3 Determination of water uptake and Broadband Electrical Spectroscopy studies

The water uptake (WU%) of [Nafion/$(WO_3)_x$] hybrid membranes, determined in accordance with Eq. (1), decreases as x is raised (see Table 3.3). This evidence is attributed to the establishment of *"dynamic crosslinks"* between the particles of the WO_3 nanofiller and the Nafion acid side groups [189]. Such dynamic crosslinks influence the macromolecular dynamics of the Nafion polymer host, improve the mechanical properties of Nafion-based hybrid membranes [175, 189], stabilize the system and inhibit the swelling of the hydrophilic domains of the Nafion host, reducing WU% [175, 185].

Table 3.3 WU% of [Nafion/$(WO_3)_x$] membranes

Membrane	WU%
Recast Nafion	18.0
[Nafion/$(WO_3)_{0.024}$]	14.0
[Nafion/$(WO_3)_{0.329}$]	12.5

The electrical response of the hybrid membranes and of recast Nafion is investigated by Broadband Electrical Spectroscopy (BES) in the frequency range between 30 mHz and 10 MHz, and from -100 to 200°C.

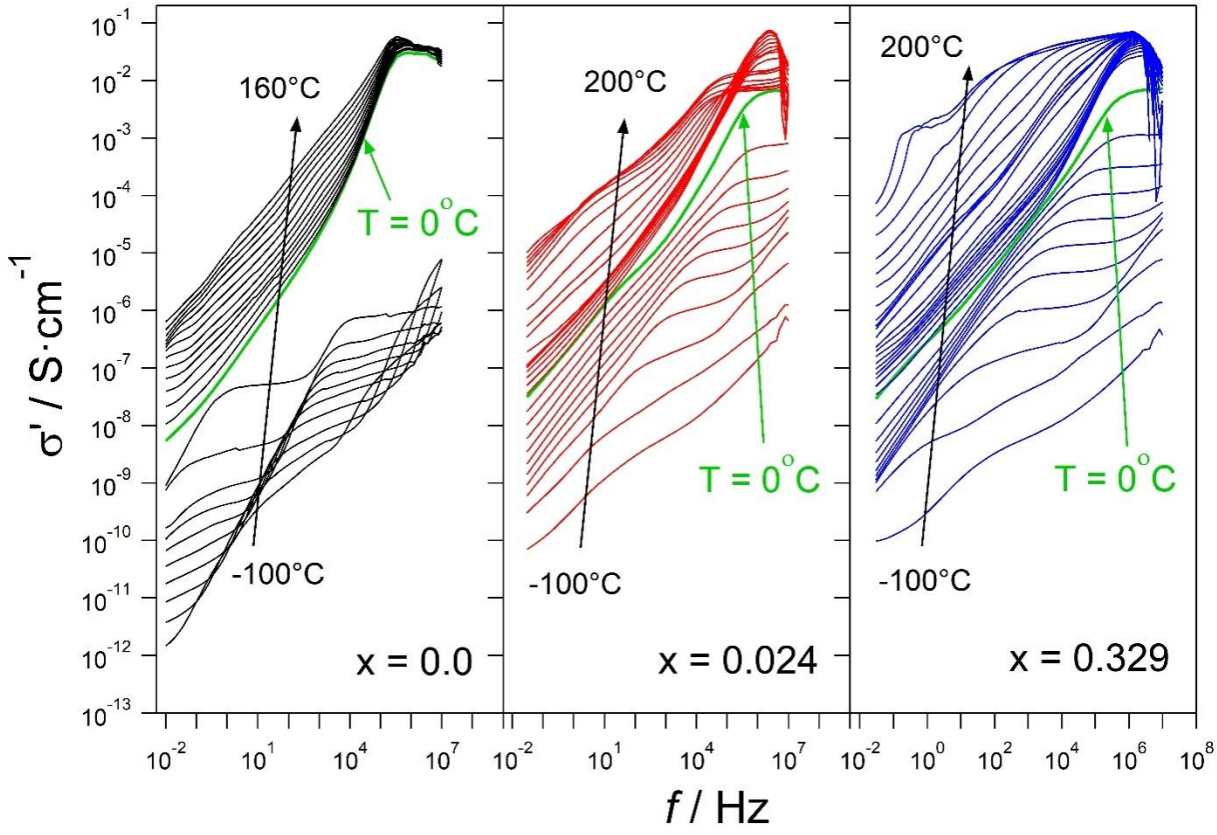

Figure 3.6 Real component (σ') of the complex conductivity *vs.* frequency for recast Nafion and [Nafion/$(WO_3)_x$] hybrid membranes. The curves collected at 0°C are plotted in green for the sake of clarity.

Figure 3.6 reports the profiles of the real part of the conductivity (σ') as a function of the frequency for the proposed samples in their fully hydrated states. In recast Nafion, a step rise is detected between 0 and 20°C; this feature is attributed to a phase transition involving the water embedded in the hydrophilic domains [190]. At the same temperature, the spectra of the hybrid membranes reveal a much weaker step, whose magnitude decreases as x is raised. This effect is associated with the introduction of the WO_3 nanoparticles, that change the morphology of the hydrophilic domains of the Nafion host in the hybrid membranes. With respect to recast Nafion, in the hybrid membranes the crosslinks R-SO_3^-···WO_3···SO_3^--R reduce the free volume in hydrophilic domains allowing a lower amount of 'bulk-like' water to be included that undergoes a phase transition at ca. 0°C. This interpretation is consistent with the behaviour of other similar nanocomposite membranes [175], and is further supported

considering that the overall water content of the hybrid membranes decreases significantly as x is raised (see the WU% results in Table 3.3). The value of the high-frequency plateau ($f > 10^5$ Hz) of σ' is adopted as a good approximation of the ionic conductivity (σ_{DC}) of a fully hydrated Nafion-based membrane [185]. These values are plotted *vs.* the inverse of the temperature to study the conductivity behaviour of the proposed membranes (see Figure 3.7).

Two conductivity regions are revealed in Figure 3.7, I and II, that are separated by the melting temperature of water, $T_{m,H2O} = 0°C$. In Region I the conductivity of recast Nafion is very low, on the order of 10^{-6} - 10^{-9} $S \cdot cm^{-1}$. Under the same conditions, the conductivity of the hybrid membranes: (i) is up to two-three orders of magnitude larger than that exhibited by recast Nafion; and (ii) is largely unaffected by x. The conductivity of the proposed membranes increases significantly upon passing from Region I to Region II. The increase in conductivity is equal to: (i) ca. 4 orders of magnitude in the case of recast Nafion; (ii) less than one order of magnitude for both hybrid membranes. In region II, the conductivity of the membranes rises in the order: [Nafion/$(WO_3)_{0.024}$] < [Nafion/$(WO_3)_{0.329}$] < recast Nafion; the difference between the conductivity values of all the membranes is relatively low, less than one order of magnitude.

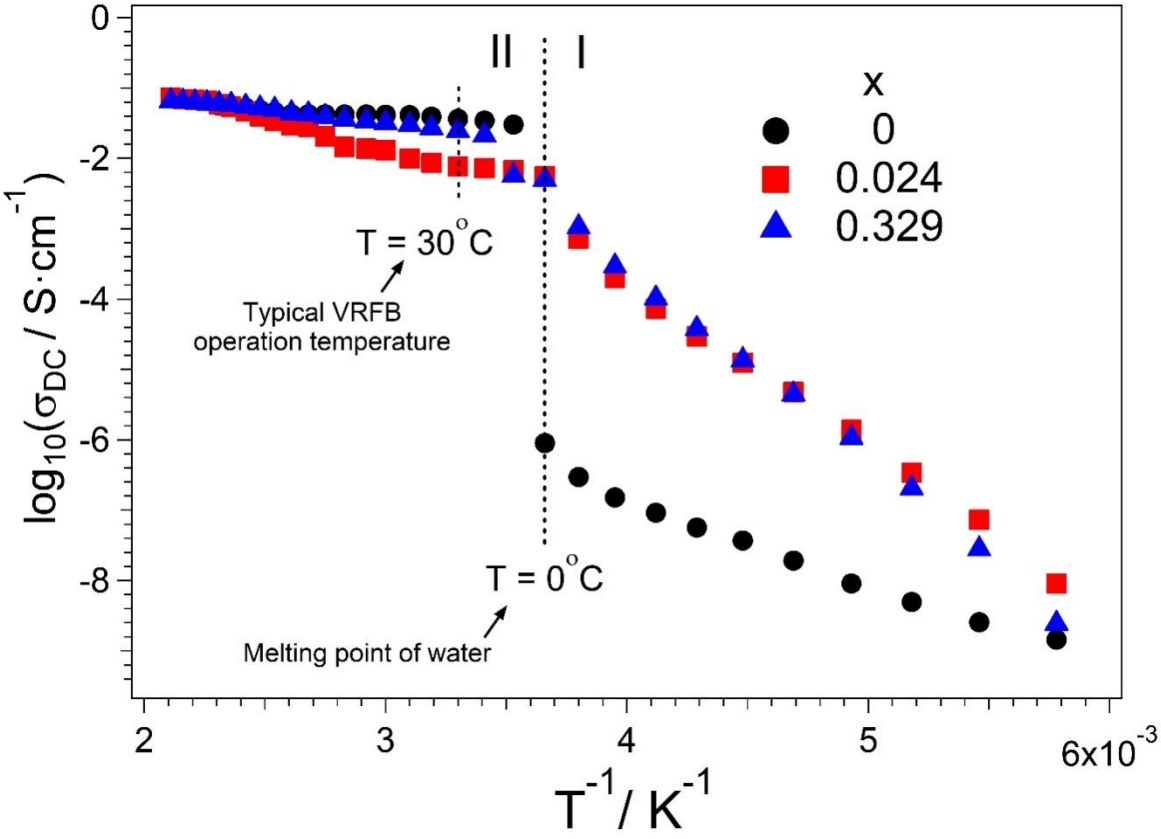

Figure 3.7 Dependence of σ_{DC} on the inverse of the temperature for the proposed membranes.

Furthermore, this difference decreases as T is raised; indeed, the three membranes exhibit essentially the same conductivity at T > 90-100°C. These results are interpreted assuming that the conductivity mechanism of the proposed hybrid membranes is similar to that of other nanocomposite Nafion-based membranes described in the literature [178]. In detail, in Region I the ion migration takes place through proton hopping processes between coordination sites present at the interface between the hydrophilic and the hydrophobic domains of the system. This process is mediated by [178]: (i) the relaxations of the perfluoroetheral side groups of Nafion; and (ii) the segmental motion of the PTFE backbones. The ion migration in Region I is promoted by the introduction of the WO_3 nanofiller, as it would give rise to the formation of much more extensive interfaces between the hydrophilic and hydrophobic domains. This is expected to promote the establishment of charge percolation pathways, allowing a more facile long-range charge transport. In Region II, the ion

conduction is taking place through a different mechanism, involving “delocalization bodies” (DBs). A DB corresponds to a portion of the material where the charge carriers (in this case, protons) are able to move so fast as to be considered delocalized; the long-range charge transfer occurs as different DBs come into contact with one another [178]. This process is bottlenecked by the charge transfer between different DBs, that is mediated by the relaxations of the hydrophobic domains. In fully-hydrated Nafion-based systems, the DBs typically correspond to the water-swollen hydrophilic domains [178]. In this interpretation framework, a high conductivity is achieved in the presence of large hydrophilic domains swollen with liquid water that can easily come into contact with one another, such as in the case of recast Nafion. On the other hand, with respect to the recast Nafion, in the hybrid membranes the total volume of the hydrophilic domains is likely smaller, as suggested by the lower WU% (see Table 3.3). This feature would somewhat hinder the long-range charge transport, owing to: (i) the more tortuous pathway that should be followed by the charges, and (ii) the larger number of charge transfer events between the smaller DBs. In the case of [Nafion/$(WO_3)_x$] hybrid membranes, the rate of increase in conductivity as T is raised is more marked than for recast Nafion. This evidence is ascribed to the *“dynamic crosslinks”*, that in hybrid membranes are more efficient in coupling the dielectric relaxations of PTFE domains with the charge transfer events occurring between different DBs. Cross-links occur when the sulfonic acid groups of the Nafion host polymer interact with the surface functionalities of the nanofiller particles. Hydrophobic nanodomains are stabilized owing to the density of dipolar nanofiller-Nafion cross-links present in hydrophilic regions. The crosslinks induced by dipole-dipole interactions between the side groups of the Nafion host polymer and nanoparticles significantly reduce the delocalization of the protons, which decreases the overall conductivity of materials. Taken all together, the data reported in Figure 3.7 indicate that at the temperature of operation of a typical VRFB (T ~ 30°C [191]) the hybrid membranes [Nafion/$(WO_3)_{0.024}$] and [Nafion/$(WO_3)_{0.329}$] exhibit a conductivity of $7.62 \cdot 10^{-3}$ and $2.45 \cdot 10^{-2}$ $S \cdot cm^{-1}$, respectively. As a comparison, at the same temperature the conductivity of recast Nafion is $3.64 \cdot 10^{-2}$ $S \cdot cm^{-1}$. It is thus revealed that the proposed [Nafion/$(WO_3)_{0.329}$] hybrid membrane exhibits a conductivity that is very close to that of a reference recast

Nafion. In conclusion, the proposed hybrid membranes, and in particular [Nafion/$(WO_3)_{0.329}$], exhibit a conductivity which is only slightly lower than Nafion that allows implementation in an operating VRFB.

3.3.4 Determination of membrane permeability and ion selectivity

The permeability to VO^{2+} (indicated as P) is a crucial figure of merit in order to evaluate the suitability of an ion-exchange membrane for application in VRFBs. Indeed, P illustrates the ability of the membrane to hinder the crossover between the feed stocks. P is evaluated by Eq. (2.8.3), and decreases as x is raised (see Table 3.4), likely on the basis of a tortuous pathway affecting the mobility of the VO^{2+} ions [192]. The vanadium ions may likely migrate easily only through the 'bulk' water, while protons are mainly passing through the 'interface' water.

Table 3.4 Permeability and ion selectivity of [Nafion/$(WO_3)_x$] membranes

Membrane	P / $cm^2 \cdot min^{-1}$	Ion selectivity / $S \cdot min \cdot cm^{-3}$
Recast Nafion	$55.8 \cdot 10^{-7}$	$6.5 \cdot 10^3$
[Nafion/$(WO_3)_{0.024}$]	$46.4 \cdot 10^{-7}$	$1.6 \cdot 10^3$
[Nafion/$(WO_3)_{0.329}$]	$23.1 \cdot 10^{-7}$	$10.6 \cdot 10^3$

The ion selectivity, which is calculated by Eq. (2.8.3), allows to gauge to what extent an ion-exchange membrane is able to effectively block the crossover of vanadium species, whilst at the same time providing good conductivity for the H_3O^+ ions involved in the charge/discharge processes taking place during VRFB operation [193]. The [Nafion/$(WO_3)_{0.329}$] membrane reveals the highest ion selectivity ($10.6 \cdot 10^3$ $S \cdot min \cdot cm^{-3}$, see Table 3.4), ca. 1.63 times greater than that of recast Nafion. On this basis, it is concluded that [Nafion/$(WO_3)_{0.329}$] shows a good potential for application in a VRFB.

3.3.5 Evaluation of the chemical stability

The ion-exchange membranes intended for application in VRFBs must be able to operate for long periods of time, on the order of several tens of thousands of hours [116]. In this span of time, they must tolerate both the strongly acidic reactant feeds and the oxidizing effect arising from VO_2^+ species dissolved in the catholyte. A first estimate of the chemical durability of the proposed membranes is obtained by exposing them to an environment closely mimicking that which is found in an operating VRFB, consisting of a highly acidic solution (4 M of H_2SO_4) to dissolve the 1 M of highly oxidizing VO_2^+ species. The results of the tests are reported in Figure 3.8.

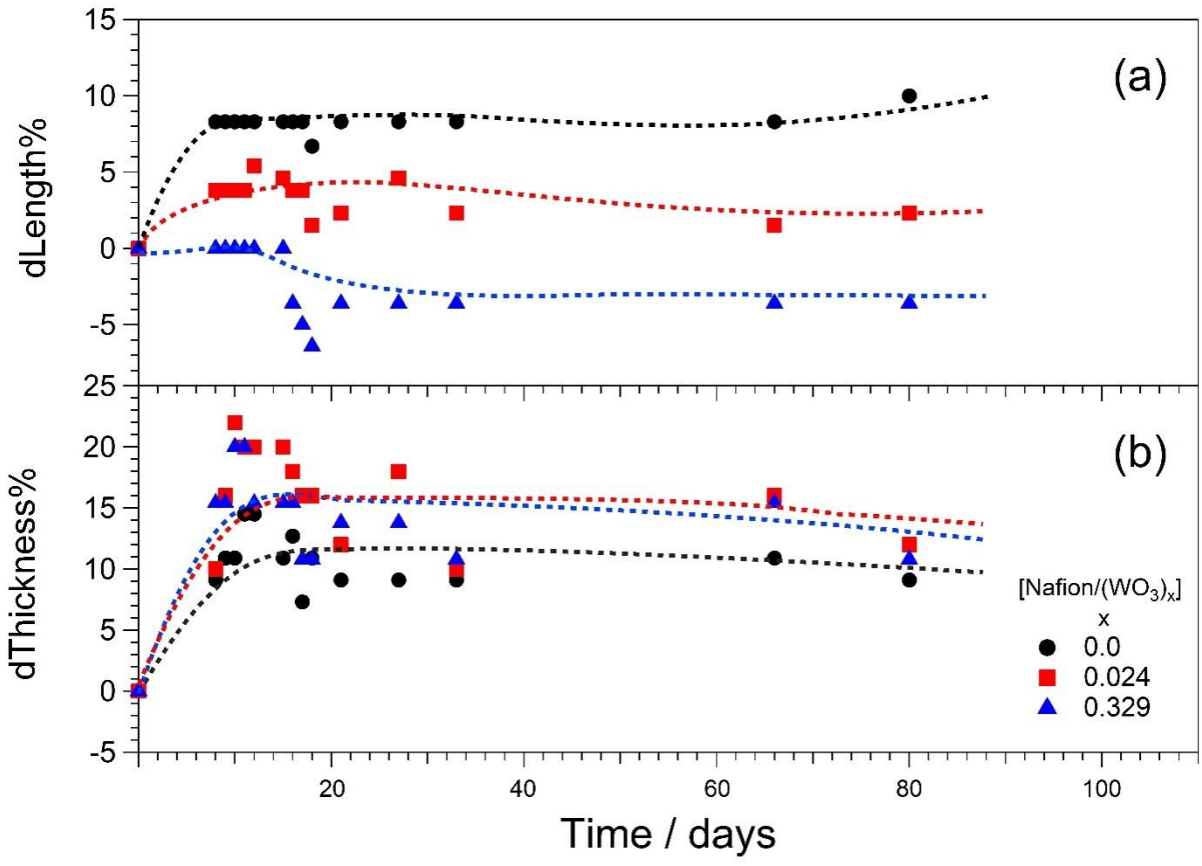

Figure 3.8 Relative variations in: (a) length; and (b) thickness of: (●) recast Nafion; (■) [Nafion/$(WO_3)_{0.024}$]; and (▲) [Nafion/$(WO_3)_{0.329}$] membranes as a function of immersion time in a solution including 1 M VO_2^+ in 4 M H_2SO_4. The lines are meant as a guide to the eye.

The relative percentage variation of the length and the thickness of the membranes (indicated in Figure 3.8 as dLength% and dThickness%, respectively) take ca. 20 days to reach stability, and do not change significantly in the subsequent 60 days. It is evidenced that the length of recast Nafion increases by ca. 10%. The nanofiller is shown to diminish in-plane elongation; in the case of [Nafion/$(WO_3)_{0.329}$] the length does not increase appreciably after 80 days. The thickness of all the membranes increases by ca. 10%, irrespective of the level of doping. These results indicate that, in first approximation, the hybrid membranes exhibit the same level of chemical stability as recast Nafion. It is further revealed that the introduction of WO_3 filler improves significantly the dimensional stability of the hybrid membranes. This result is attributed to a chemical-mechanical stabilization of the hybrid membranes triggered by the establishment of dynamic crosslinks between the nanoparticles of the WO_3 filler and the Nafion host [175, 189]. Finally, the relative variation in the weight of the membranes upon immersion in the solution described above is also measured; the results are reported in Figure 3.9. The weight of recast Nafion does not change appreciably upon testing, witnessing the outstanding chemical stability of perfluorinated membranes[194]. The weight of [Nafion/$(WO_3)_{0.024}$] and [Nafion/$(WO_3)_{0.329}$] increases respectively by ca. 8 and 12% in the first 20 days of the test; afterwards, no further changes in the weight of the membranes are revealed. This result is interpreted assuming that some VO_2^+ species are permanently adsorbed at the interface between the WO_3 filler and the Nafion host. However, this absorption phenomenon is not expected to affect the VRFB operability, and is consistent with the slightly lower conductivity of membranes in an operating VRFB system.

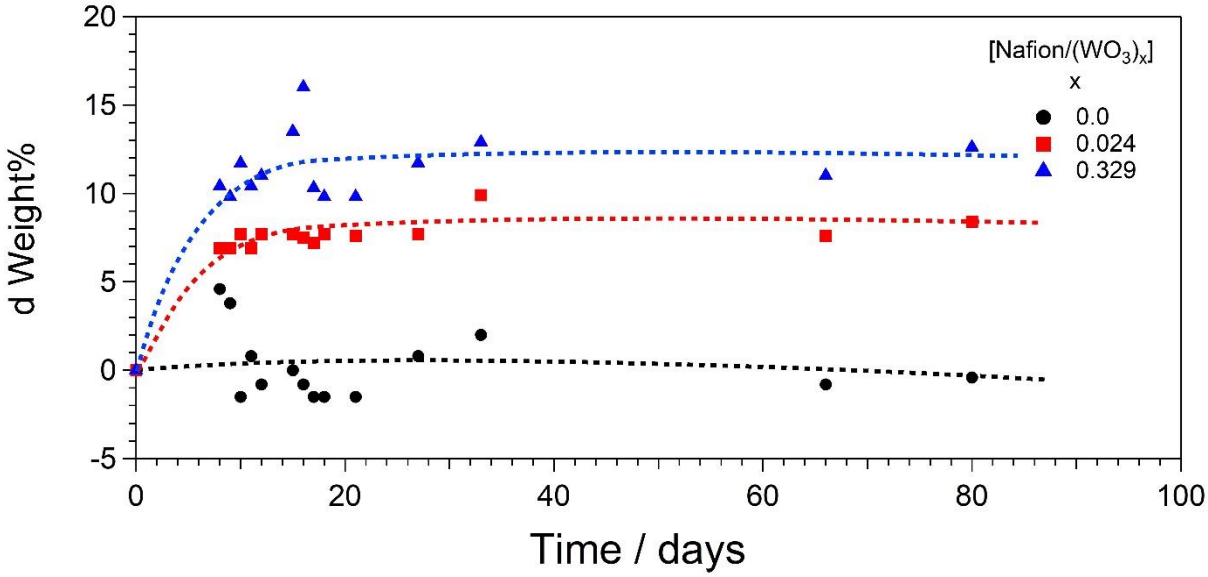

Figure 3.9 Relative variation in weight% of: (●) recast Nafion; (■) [Nafion/$(WO_3)_{0.024}$]; and (▲) [Nafion/$(WO_3)_{0.329}$] membranes as a function of immersion time in a solution including 1 M VO_2^+ in 4 M H_2SO_4.

3.4 Conclusion

This chapter reports the preparation, the physicochemical and the electrochemical characterization of two hybrid membranes consisting of WO_3 nanoparticles dispersed in a Nafion matrix. The hybrid membranes are indicated as [Nafion/$(WO_3)_{0.024}$] and [Nafion/$(WO_3)_{0.329}$], and are obtained by a solvent-casting procedure. In the hybrid membranes, the introduction of WO_3 nanoparticles does not alter significantly the thermal degradation events of the Nafion host. On the other hand, MDSC reveals that in [Nafion/$(WO_3)_{0.024}$] the endothermic events associated to the Nafion PTFE domains are shifted to higher temperatures by *ca.* 10-20°C. This evidence is attributed to the formation of *"dynamic crosslinks"* between the WO_3 nanoparticles and the Nafion host, that stabilize the hybrid membrane. No such stabilization is detected for the [Nafion/$(WO_3)_{0.329}$] membrane, indicating that, in this case, phase segregation occurs between the Nafion host and the WO_3 nanofiller. The nanofiller also affects the conformation of the PTFE backbone chains of the Nafion host, inhibiting the $15_7 \rightarrow 10_3$ conformational transition as revealed by ATR-FTIR spectroscopy. Raman spectra reveal that the structure of the WO_3 nanofiller is not affected by its introduction in the hybrid membranes. The interactions between WO_3 and the Nafion host have a strong impact on the structure of the hybrid membranes at the mesoscale. In detail, the hydrophilic domains of the Nafion host are reduced in size as the content of WO_3 is raised. Indeed, the water uptake of [Nafion/$(WO_3)_{0.329}$] and recast Nafion are equal to 12.5 and 18.0 wt%, respectively; as a consequence, the pathways of charge migration become more tortuous, slightly reducing the conductivity at 30°C from $3.64 \cdot 10^{-2}$ S·cm^{-1} for recast Nafion to $2.45 \cdot 10^{-2}$ S·cm^{-1} for [Nafion/$(WO_3)_{0.329}$]. Charged vanadium species are able to permeate Nafion-based membranes through very similar pathways than those followed by the H_3O^+ species involved in the charge-discharge processes of the VRFB [195]. The vanadium ions are likely only passing through the bulk water. The incorporation of WO_3 nanofiller leads to the formation of hydrogen bonds and dynamic crosslinks may break the hydrophilic domains and therefore reduce the amount of bulk water which locates inside the hydrophilic domains. The less amount of bulk water may be the critical issue to reduce the vanadium permeability significantly. The amount of interface water may further increase. Therefore, vanadium ions

are more hindered than protons. For the future work, we may use other instruments to focus more on the content change of bulk water and interface water to further explain the related mechanism of vanadium permeability reduction in hybrid membranes. Accordingly, the higher charge migration tortuosity expected for the proposed hybrid membranes would correspond to a dramatically lower permeability to vanadium species. Indeed, it is shown that the permeability of recast Nafion to VO^{2+} is $55.8 \cdot 10^{-7} cm^2 \cdot min^{-1}$, more than twice larger than the permeability of [Nafion/$(WO_3)_{0.329}$] (measured at $23.1 \cdot 10^{-7}$ $cm^2 \cdot min^{-1}$). As a result, the ion selectivity of hybrid membranes (up to $10.6 \cdot 10^3$ $S \cdot min \cdot cm^{-3}$ for [Nafion/$(WO_3)_{0.329}$]) is much improved in comparison with recast Nafion ($6.5 \cdot 10^3$ $S \cdot min \cdot cm^{-3}$). Finally, the WO_3 nanofiller improves the long-term dimensional stability of the hybrid membranes under conditions mimicking those found in VRFBs during operation. Taken all together the proposed hybrid membranes, owing to their good conductivity, remarkable ion selectivity and long-term stability are promising candidates for application as solid electrolytes in VRFBs.

Chapter IV [Nafion/(WO_3)]$_x$ hybrid inorganic-organic proton conducting membranes for VRFB application: single cell performance

4.1 Introduction

In a previous Chapter (Chapter III) we have demonstrated that the introduction of the WO_3 nanofiller in a Nafion matrix yields positive effects, as revealed by an in-depth structural characterization and thermal stability studies [196]. In this chapter, we are focusing more on the battery performance of the optimized [Nafion/(WO_3)$_x$] hybrid membranes. Therefore, an additional hybrid membrane with the loading of WO_3 nanoparticles as high as possible, [Nafion/(WO_3)$_{0.587}$], was prepared as it might further reduce vanadium permeability while maintaining similar proton conductivity compared to pristine Nafion. Beyond this WO_3 loading level, the resulting hybrid membrane is very susceptible to cracking and is difficult to apply for the VRFB testing. The morphology of all the membranes are characterized by scanning electron microscopy and two phases of the hybrid membranes are proved. One side of each membrane exhibits a high concentration of the WO_3 nanofiller; in the remaining part of each membrane, the concentration of the nanofiller is lower and constant. The battery testing under operating conditions, here we demonstrate how the morphology of the [Nafion/(WO_3)$_x$] membranes can hinder vanadium migration through the IEM, leading to an improved VRFB performance with respect to pristine Nafion. In this chapter, the performance of the hybrid membranes has been tested in a vanadium redox flow battery (VRFB). In comparison with the Nafion reference, at the same current density of 70 mA cm^{-2}, [Nafion/(WO_3)$_{0.587}$] demonstrates a higher coulombic efficiency (93%), a higher energy efficiency (73%) and a lower self-discharge rate. [Nafion/(WO_3)$_{0.587}$] also exhibits a stable performance over 100 charge/discharge cycles.

4.2 Experimental

4.2.1 Materials

All materials were used and described in a previous chapter of the reagents (Chapter 3.2.1)

4.2.2 Membrane preparation

All [Nafion/$(WO_3)_X$] membranes are prepared in accordance with our previous work with a slight modification made to the final activation steps [196, 197] and Chapter 3.2.2). The membranes are soaked for 1 h in 1 M H_2SO_4 at room temperature (25 °C) to avoid leaching of the WO_3 nanofiller. Four different [Nafion/$(WO_3)_X$] membranes are obtained, with x = 0;0.024;0.329 and 0.587 (see Table 4.1).

Table 4.1 Composition and molar ratios of [Nafion/$(WO_3)_x$] membranes.

Membrane	wt% of WO_3[a]	x[b]	$IEC^{calculated\ c}(\varphi)$ / meq·g^{-1}
Recast Nafion	0	0	0.9200
[Nafion/$(WO_3)_{0.024}$]	1	0.024	0.9108
[Nafion/$(WO_3)_{0.329}$]	12	0.329	0.8096
[Nafion/$(WO_3)_{0.587}$]	20	0.587	0.7360

[a] Values determined based on the residues that remained following HR-TGA carried out under an air atmosphere; [b]x = mol WO_3/mol -SO_3H; [c]$\varphi = meq_{Nafion}/m_{composite}$.

4.2.3 Permeability to VO^{2+}

The procedures and the calculations used for vanadium crossover measurement are reported elsewhere [152, 196] and Chapter 2.8 in this thesis. .On the vanadium-rich side of the cell, the 50 mL solution contains 1 mol·dm^{-3} VOSO4 dissolved in 4 M H_2SO_4. On the receiving side, 50 mL of 5 M H_2SO_4 is used. The two compartments are separated by an IEM. The VO^{2+} cross-over through the membrane is analyzed by taking aliquots of the receiving side at regular time intervals and testing the concentration of VO^{2+} via UV-Vis spectroscopy. During

the measurement, the solutions are continuously stirred to minimize the influence of vanadium distribution on the membrane surface. The diffusion cell is left standing for several days, with aliquots of solutions taken at regular time intervals from both the vanadium-rich side and the receiving side, in order to minimize osmotic effects.

4.2.4 VRFB single cell tests

VRFB testing protocol is described in Chapter 2.6 in this thesis. Charge-discharge experiments are performed at different current densities of 20, 30, 40, 50, 60 and 70 mA cm^{-2} with two cut-off voltages set at 1.65 and 1.00 V to avoid the degradation of the carbon electrode and side reactions. The self-discharging arises as a result of vanadium ion crossover and a comparison between commercial Nafion 212 and [Nafion/$(WO_3)_{0.587}$] is conducted, with termination of the test occurring once the open circuit voltage (OCV) falls below 1.10 V. The cycle life of the cell is carried out at the constant current density of 50 mA cm^{-2} for 30 charge/discharge cycles.

4.2.5 Instruments and Methods

4.2.5.1. Diffusion cell

A homemade diffusion cell is prepared and used in accordance with our previous work [196] and described in details in Chapter 2.8 (Figure 2.8).

4.2.5.2 SEM/EDX analysis

A Field Emission-Scanning Electron Microscopy (FE-SEM) and Energy-Dispersive X-ray analysis (EDX) are carried out on a Zeiss SUPRA 40VP instrument. A working distance of 15 mm with an acceleration voltage of 10-20 kV is applied. The instrument is operated in a high-vacuum mode. Samples for imaging of cross sections of membranes in SEM are prepared

by breaking frozen samples in liquid nitrogen.

4.2.5.3 Raman spectra

Raman spectra of the cross-section are obtained using a DXR-Micro Raman (Thermo Scientific) spectrometer, which uses an excitation laser having a wavelength of 532 nm. Samples for the measurement of the cross sections of the membranes are prepared by sandwiching them between two steel parts and cut by longitudinal chamfering.

4.3 Results and discussion

The SEM images of the cross sections of pristine Nafion, [Nafion/$(WO_3)_{0.024}$], [Nafion/$(WO_3)_{0.329}$] and [Nafion/$(WO_3)_{0.587}$] are displayed in Figure 4.1. Figure 4.1(a) shows an SEM image collected in the standard detection mode using secondary electrons. The thickness of recast Nafion and of [Nafion/$(WO_3)_{0.024}$] is similar, and is equal to *ca.* 52±2μm. Figure 4.1(b), 4.1(c) and 4.1(d) show SEM images in backscattered electrons of the membrane cross sections. The selected electron micrographs clearly indicate that the compositions of membranes are not homogeneous. The backscattered electrons are exploited to reveal the WO_3 layer on one side of the hybrid inorganic-organic membranes as a narrow light band on the bottom, and light spots inside the membrane due to the high atomic weight of W. The Nafion matrix is visible as the dark region. The thickness of the [Nafion/$(WO_3)_{0.329}$] and [Nafion/$(WO_3)_{0.587}$] is 54 μm and 59 μm respectively. Figure 4.1(b), 4.1(c) and 4.1(d) reveal that the two sides of the membranes are different.

The top side of each membrane is a wide layer, which is ascribed to the WO_3 nanoparticles that are homogeneously distributed in the Nafion matrix. The bottom side is a layer that is rich in WO_3 nanoparticles. Indeed, the two different compositional sides were revealed after the solvent casting procedure. The enrichment of WO_3 nanoparticles at one side and the phenomenon of phase separation may be due to the precipitation of WO_3 caused by its relatively higher density, thus Nafion polymer is distributed asymmetrically along the depth profile of the membrane. The images show that the thickness of the WO_3-rich layer increases as the loading of WO_3 in the hybrid inorganic-organic membrane is raised. The thickness of the WO_3-rich layer is equal to 2 μm, 6 μm and 9 μm respectively for [Nafion/$(WO_3)_{0.024}$] (1 wt% of WO_3), [Nafion/$(WO_3)_{0.329}$] (12 wt% of WO_3) and [Nafion/$(WO_3)_{0.587}$] (20 wt% of WO_3). No cracks between different layers are found, which indicates that the interactions between the Nafion matrix and the WO_3 filler are strong and probably mediated by hydrogen bonds [196]. Figure 4.2 shows a 3D image of the cross-section of the [Nafion/$(WO_3)_{0.587}$] in Raman spectra. The Raman profiles of all the hybrid inorganic-organic membranes are similar (only [Nafion/$(WO_3)_{0.587}$] is shown here).

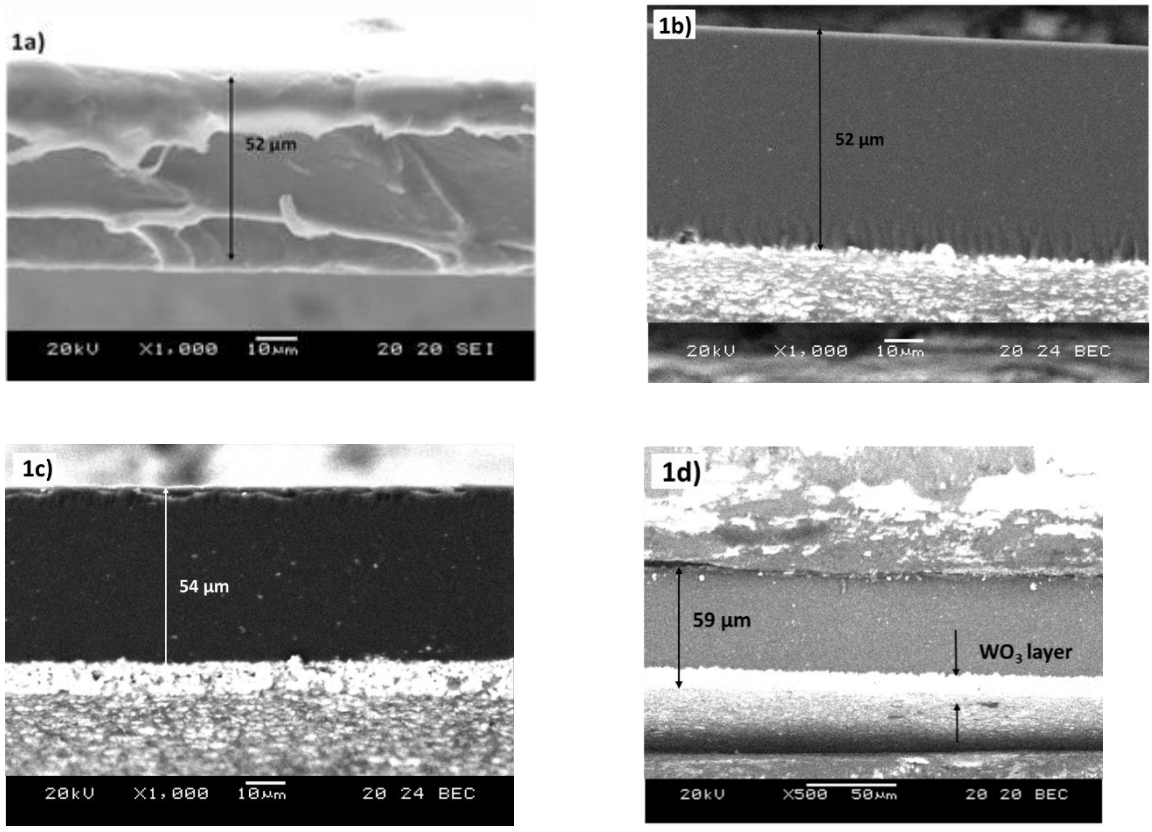

Figure 4.1 SEM images of the hybrid inorganic-organic [Nafion/$(WO_3)_x$] membranes with x = 0 (a), 0.024 (b), 0.329 (c) and 0.587 (d). (a) is collected with secondary electrons, while (b), (c) and (d) are collected with backscattered electrons. The top side is the upside surface of each membrane after the solvent casting process.

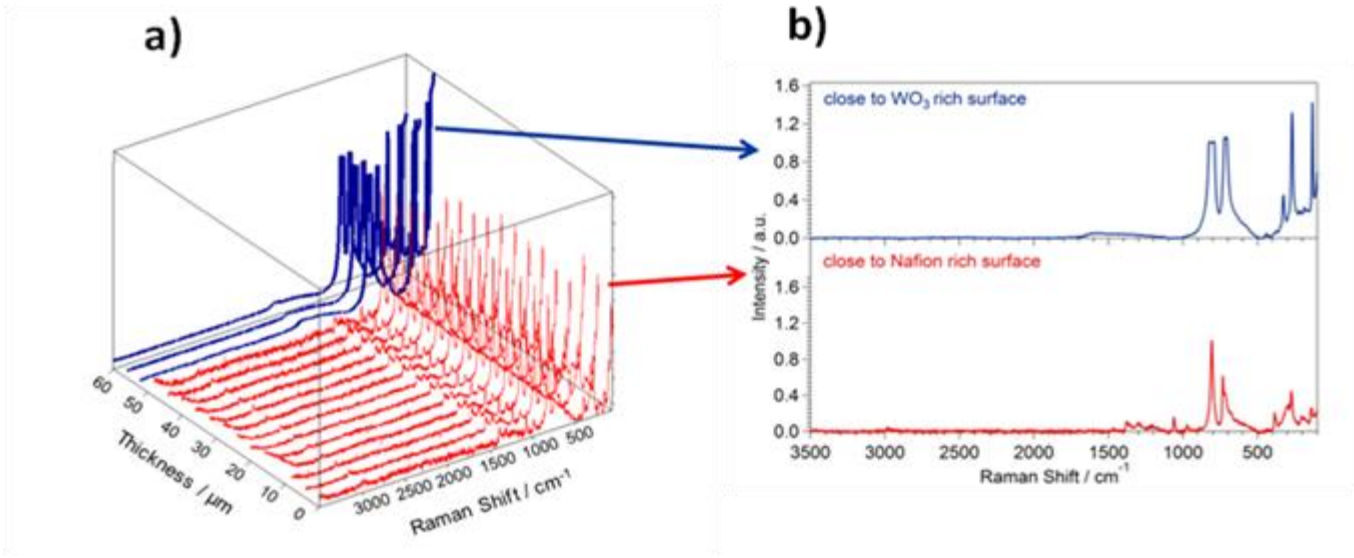

Figure 4.2 (a) 3D image based on the Raman spectra of the cross-section of [Nafion/$(WO_3)_{0.587}$] hybrid inorganic-organic membrane. The x-axis reports the Raman shift (expressed in cm^{-1}), the z-axis depicts the Raman intensity (expressed in arbitrary units), and y is the depth along the cross-section (expressed in micrometers; 0 is the topmost, "Nafion-rich" face of the membrane); (b) 2D image based on the Raman spectra of the cross-section close to WO_3 rich surface and Nafion rich surface.

The bottom face of the membrane in SEM image is dominated by the WO_3 filler, as revealed by the high intensity of the characteristic peaks at 805, 715 and 271 cm^{-1} in the cross-section Raman spectra. They are assigned to the ν(WO), δ(WO) and δ(O-W-O) modes of WO_3, respectively [196]. Other peaks ascribed to WO_3 are present between 20 and 200 cm^{-1}, and They are assigned to the lattice modes of WO_3 [196]. In the 2D cross-section spectra which is close to the WO_3 rich surface, the intensity of WO_3 peaks reaches the saturation which demonstrates extremely high WO_3 content. While these peaks are also detected throughout the cross-section of the membranes, revealing that WO_3 is also homogeneously distributed throughout the Nafion matrix, although at a lower concentration with respect to the bottom face (the intensity of peaks do not reach saturation but significant). As the intensities of Raman peaks are usually directly proportional to the concentration of the active species, it

can be estimated that the concentration of WO_3 in WO_3 rich surface is approximately 4 times higher than that in the Nafion rich surface.

The cross-section Raman profile close to Nafion rich surface is similar to that typically reported in the literature [198]. The peak at 1056 cm^{-1} is ascribed to the symmetric stretching of the sulfonate anion, $\nu_s(SO_3^-)$. It is not detected close to the WO_3 rich surface. Other peaks present in the Raman spectrum related to Nafion are found at 811 and 731 cm^{-1}. The former is assigned to a mode involving $\nu[CF_2]$, $\delta[CCF]$ and $\nu[CO]$ components; the latter is attributed to the stretching modes of CF_2 moieties [174].

Figure 4.3(a) and Figure 4.3(b) show the SEM images of the topside surface of the [Nafion/$(WO_3)_{0.587}$] membrane before and after charge-discharge tests in single VRFB, respectively.

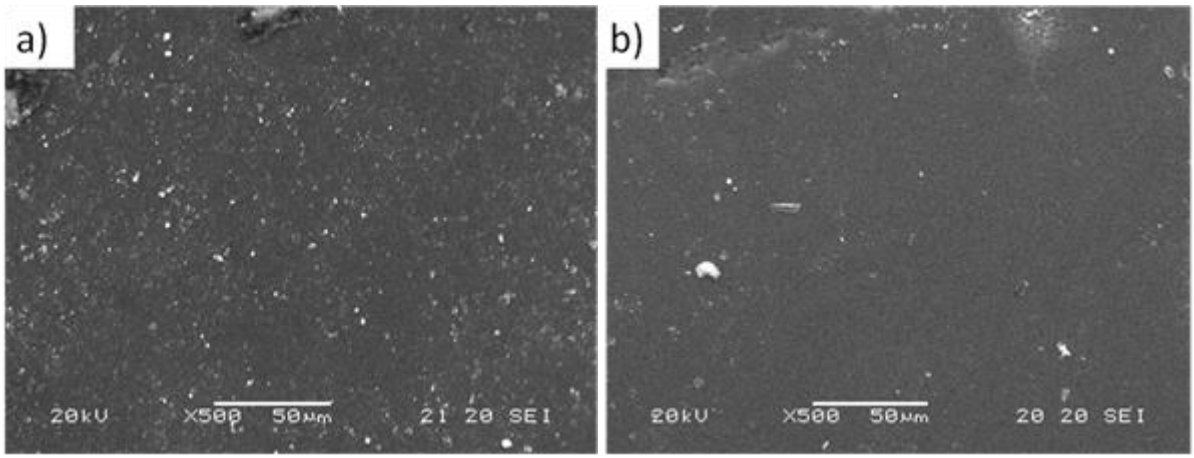

Figure 4.3 SEM image of the Nafion-rich topside of the [Nafion/$(WO_3)_{0.587}$] membrane. Pristine membrane (a); after 100 charge-discharge cycles in a VRFB (b).

In both images, the dark color corresponds to the Nafion matrix, whereas the white spots are ascribed to the WO_3 nanofiller. Although, in Figure 4.3 (b) there are less visible white spots, due to the loss of nanofiller during the disassembly the MEA (membrane electrode assembly). However, the surface of the hybrid inorganic-organic membrane is smooth and dense both before and after cycling. Thus, it can be concluded that the surface of the membrane does not undergo degradation upon cycling tests. Figure 4.4(a) and Figure 4.4(b) show the SEM images of the bottom side of the [Nafion/$(WO_3)_{0.587}$] membrane before and after charge-discharge tests in single VRFB, respectively.

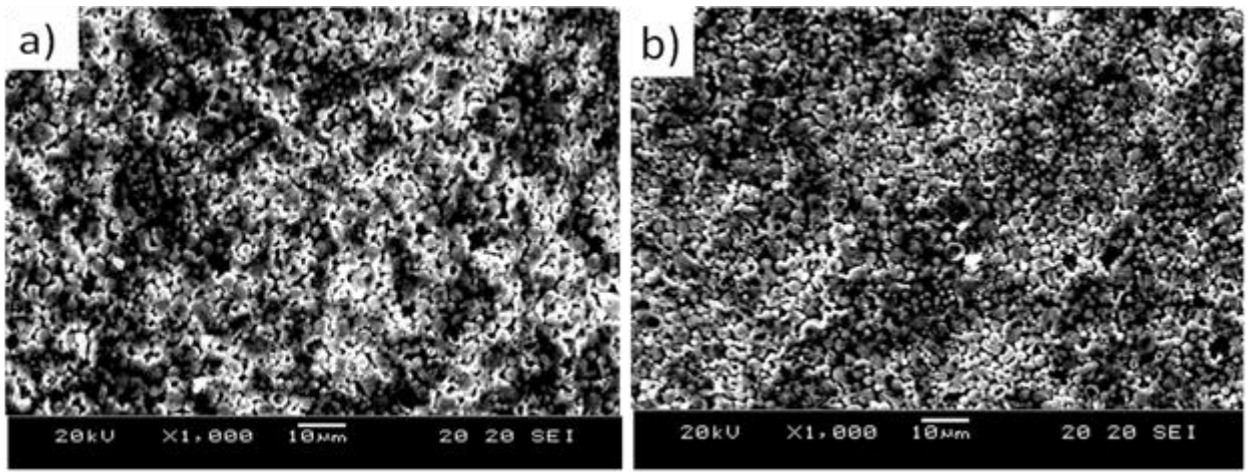

.

Figure 4.4 SEM micrographs of the WO_3-rich side (bottom side) of the [Nafion/$(WO_3)_{0.587}$] hybrid inorganic-organic membrane. Pristine membrane (a); after 100 charge-discharge cycles in a VRFB (b).

The images of the bottom side of the [Nafion/$(WO_3)_{0.587}$] hybrid inorganic-organic membrane display a clear granular texture. The size of the WO_3 nanoparticles and their distribution are found to be homogenous; no clear agglomeration is visible even at the high loading of WO_3. The surface morphology of the membrane is dense, without any obvious pinholes, which indicates that the WO_3 nanoparticles are homogeneously dispersed both before and after VRFB tests. No cracks or scratches are visible in Figure 4.4(b); this indicates that the membrane does not undergo degradation upon cycling in single VRFB. After such cycling, the

cross-section of the membrane is inspected by SEM to gauge the degradation of the membrane, and reveal the spatial distribution of vanadium (see Figure 4.5).

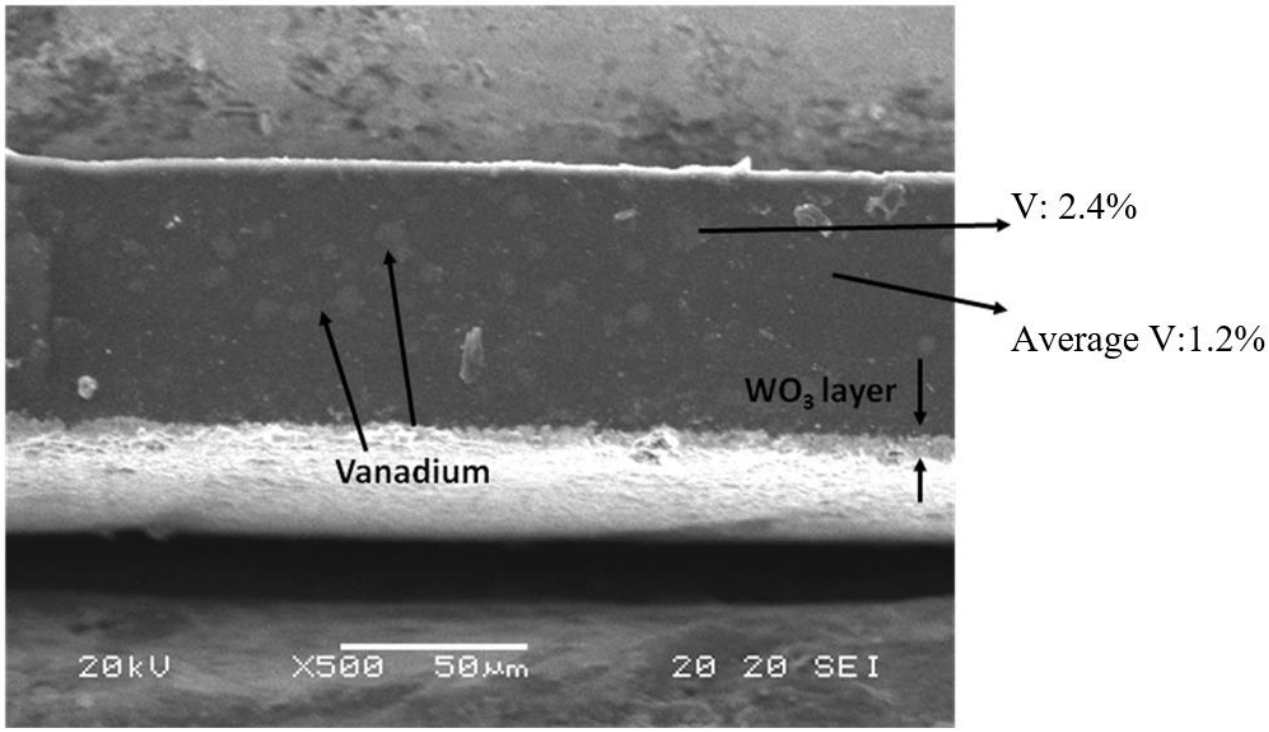

Figure 4.5 SEM image of the cross-section of the [Nafion/$(WO_3)_{0.587}$] hybrid inorganic-organic membrane after 100 charge/discharge cycles.

Figure 4.5 shows that the top side corresponds to the Nafion-rich layer, where WO_3 nanoparticles are homogeneously distributed. The visible big, irregular light grey spots are associated with vanadium, that is absorbed in the hydrophilic domains of the Nafion matrix. The very light layer at the bottom side of the membrane is associated with WO_3. No changes in thickness, or obvious holes/cracks are found when compared to the pre-test membrane, confirming the excellent stability of this family of [Nafion/$(WO_3)_x$] hybrid inorganic-organic membranes as we reported in a previous paper [196]. The presence of vanadium in the membrane after the charge/discharge cycling is confirmed by EDX analysis. The average vanadium content of the cross-section of the membrane is 1.2%, while as the SEM electron beam is aimed at the grey *"vanadium"* spots the vanadium content increased significantly to 2.4%.

Proton exchange membranes for application in VRFBs must exhibit a facile proton migration; at the same time, they must avoid the permeation of the redox active vanadium-based species, that leads to a low cycling efficiency and a fast capacity decay owing to self-discharge. The time-dependent concentration changes of VO^{2+} in H_2SO_4 solutions across the hybrid inorganic-organic membranes [Nafion/$(WO_3)_{0.024}$], [Nafion/$(WO_3)_{0.329}$], and [Nafion/$(WO_3)_{0.587}$] are compared with that of reference Nafion 212 (Figure4.6). A linear relationship between the VO^{2+} concentrations in an H_2SO_4 cell *vs*. time is observed and the slope of each curve is associated with the permeability of the membrane. It is clearly revealed that the VO^{2+} concentrations of the hybrid membranes are always lower than that of Nafion 212 after the same diffusion time; the lowest concentrations are revealed for the [Nafion/$(WO_3)_{0.587}$] membrane. The VO^{2+} permeability across the hybrid inorganic-organic membranes decreases as the WO_3 content is raised. It is obvious that Nafion 212 has the highest slope, which indicates it is the more prone to VO^{2+} crossover. The WO_3-rich layer of the hybrid inorganic-organic membranes can serve as an effective barrier to prevent the migration of vanadium species through the membrane. This phenomenon is ascribed to the well packed and homogeneously distributed WO_3 nanofiller. The interfacial interactions between the WO_3 filler and the Nafion matrix inhibit the formation of the large hydrophilic channels [196] that play a crucial role to transport the vanadium ions. Accordingly, in the hybrid inorganic-organic membranes the vanadium permeability is reduced. The limited permeability is also connected to the increased tortuosity of vanadium ionic transport paths and the impede-block exclusive effect on vanadium ions of the two different layers that are clearly evident in all the hybrid inorganic-organic membranes (see Figure 4.1). While the migration of protons is not significantly hindered (see the previous chapter).

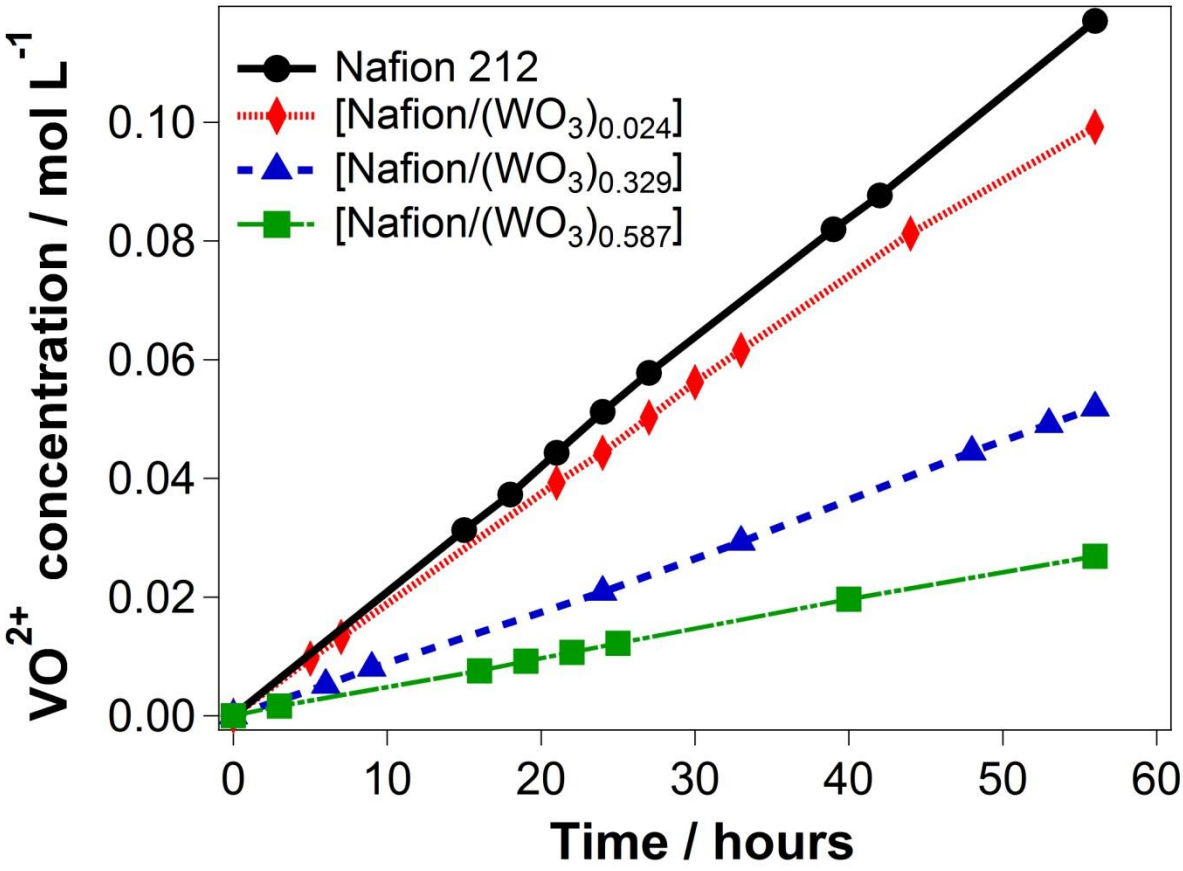

Figure 4.6 Concentration of VO^{2+} ions *vs.* diffusion time for the hybrid inorganic-organic membranes comprising different WO_3 loadings.

Figure 4.7 indicates that the hybrid inorganic-organic membranes exhibit the same reduced crossover of vanadium species in both directions. Indeed, permeability does not change depending on which side of the membrane is applied to the vanadium-rich reservoir. It does not matter if the vanadium ions meet the WO_3-rich blocking layer first, and then migrate through the tortuous migration path of Nafion dispersed with distributed WO_3 nanoparticles, or the other way around.

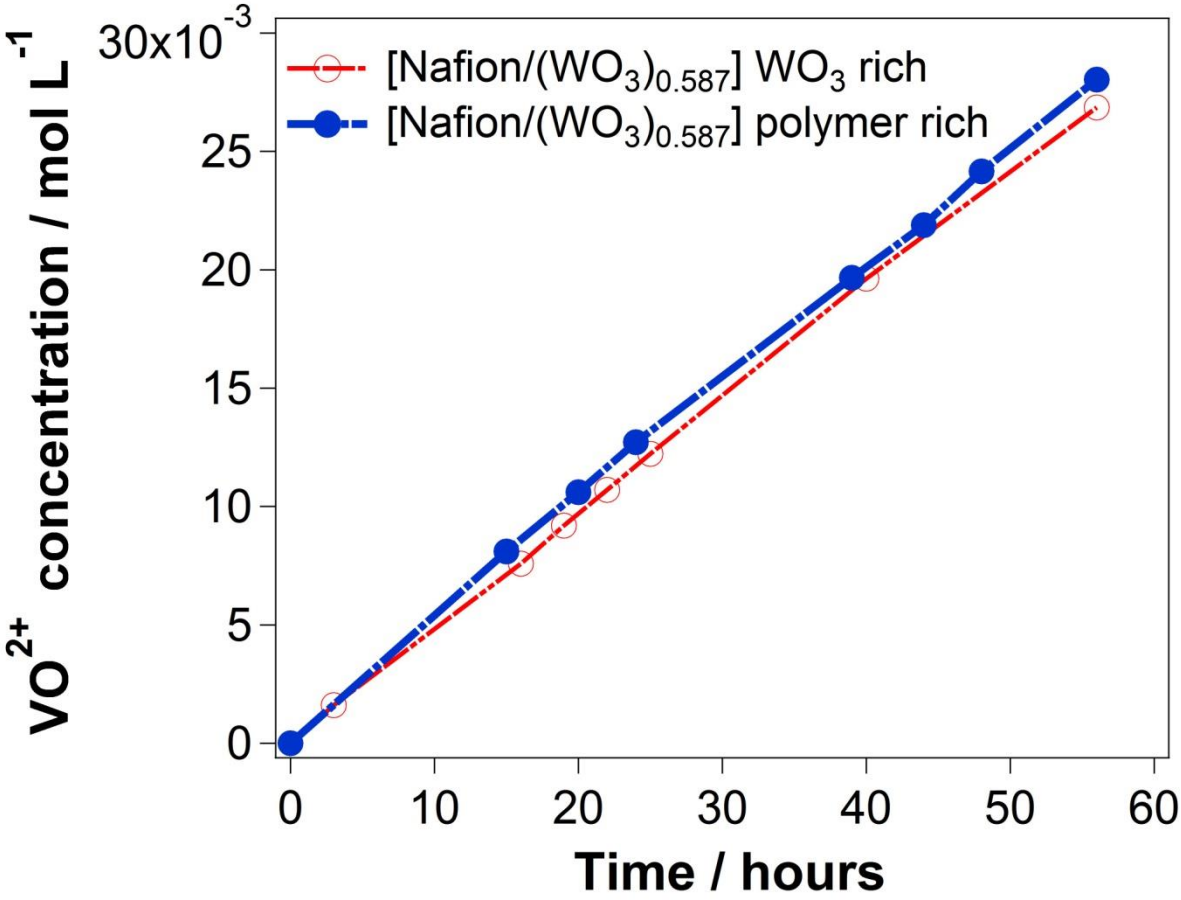

Figure 4.7 Concentration of vanadium ions *vs.* diffusion time on [Nafion/$(WO_3)_{0.587}$] membrane for two different sides in the diffusion cell.

The [Nafion/$(WO_3)_{0.587}$] membrane is chosen for the VRFB single cell test based on its low permeability ($13.2*10^{-7}$ $cm^2 \cdot min^{-1}$) and high proton conductivity ($2.9*10^{-2}$ S cm^{-1}, as measured by BES). The single charge-discharge curves of VRFBs mounting Nafion 212 and the [Nafion/$(WO_3)_{0.587}$] hybrid inorganic-organic membrane are presented in Figure 4.8. The charge-discharge tests are firstly carried out at a current density of 20 $mA \cdot cm^{-2}$, as it demonstrates a relatively low overpotential. The low permeability and high proton conductivity of the [Nafion/$(WO_3)_{0.587}$] hybrid inorganic-organic membrane are expected to improve the charge and discharge capacities. In comparison with the Nafion 212 reference, for the [Nafion/$(WO_3)_{0.587}$] hybrid inorganic-organic membrane the VRFB discharge voltage plateau is shifted to higher values and the charge voltage plateau becomes lower (see Figure 4.8).

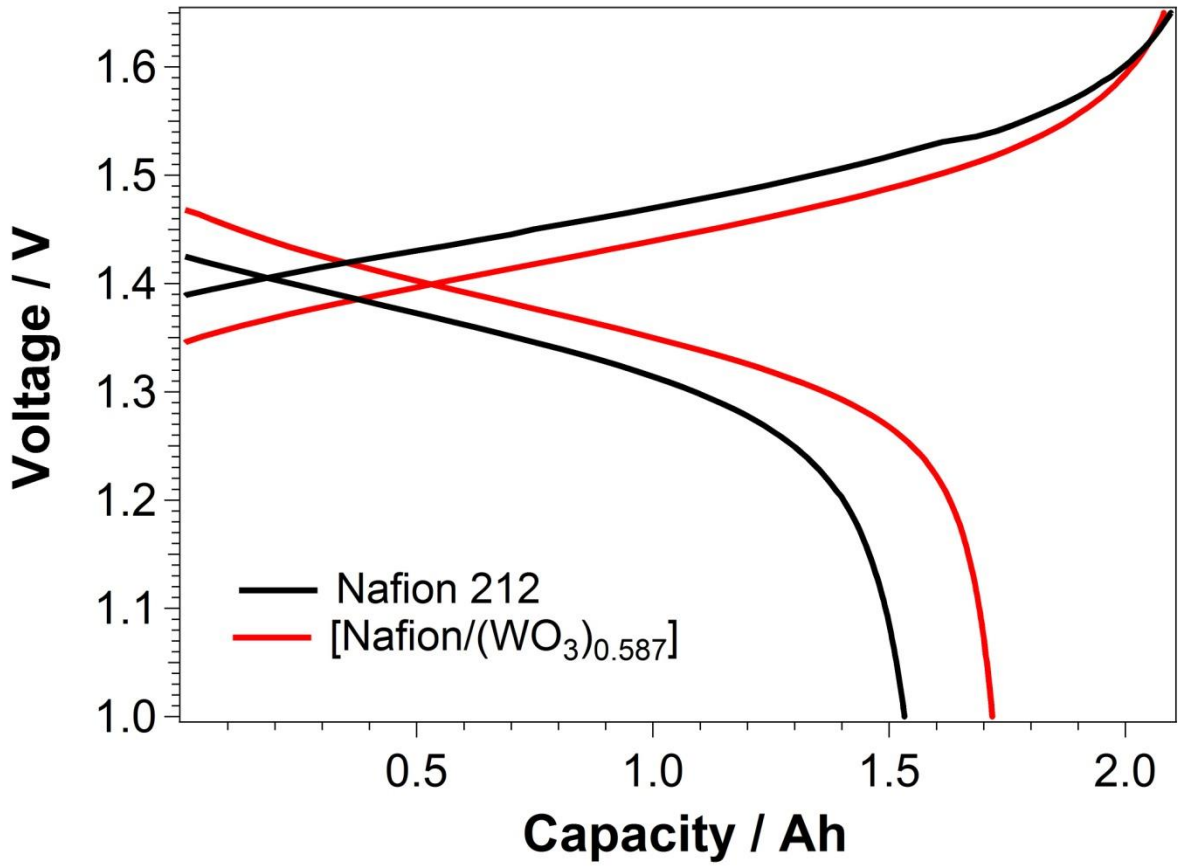

Figure 4.8 Charge-discharge curves of the single VRFB based on Nafion 212 and [Nafion/$(WO_3)_{0.587}$] membrane at charge/discharge current density of 20 mA cm^{-2}.

Figure 4.9 shows that the [Nafion/$(WO_3)_{0.587}$] hybrid inorganic-organic membrane exhibits a higher discharge capacity in comparison to the Nafion 212 membrane. This result is associated with the reduction of vanadium permeation as proven by the vanadium ion permeability test (see Figure 4.6). This is a clear proof indicating that the introduction of the WO_3 filler in Nafion is able to curtail the permeation of vanadium ions.

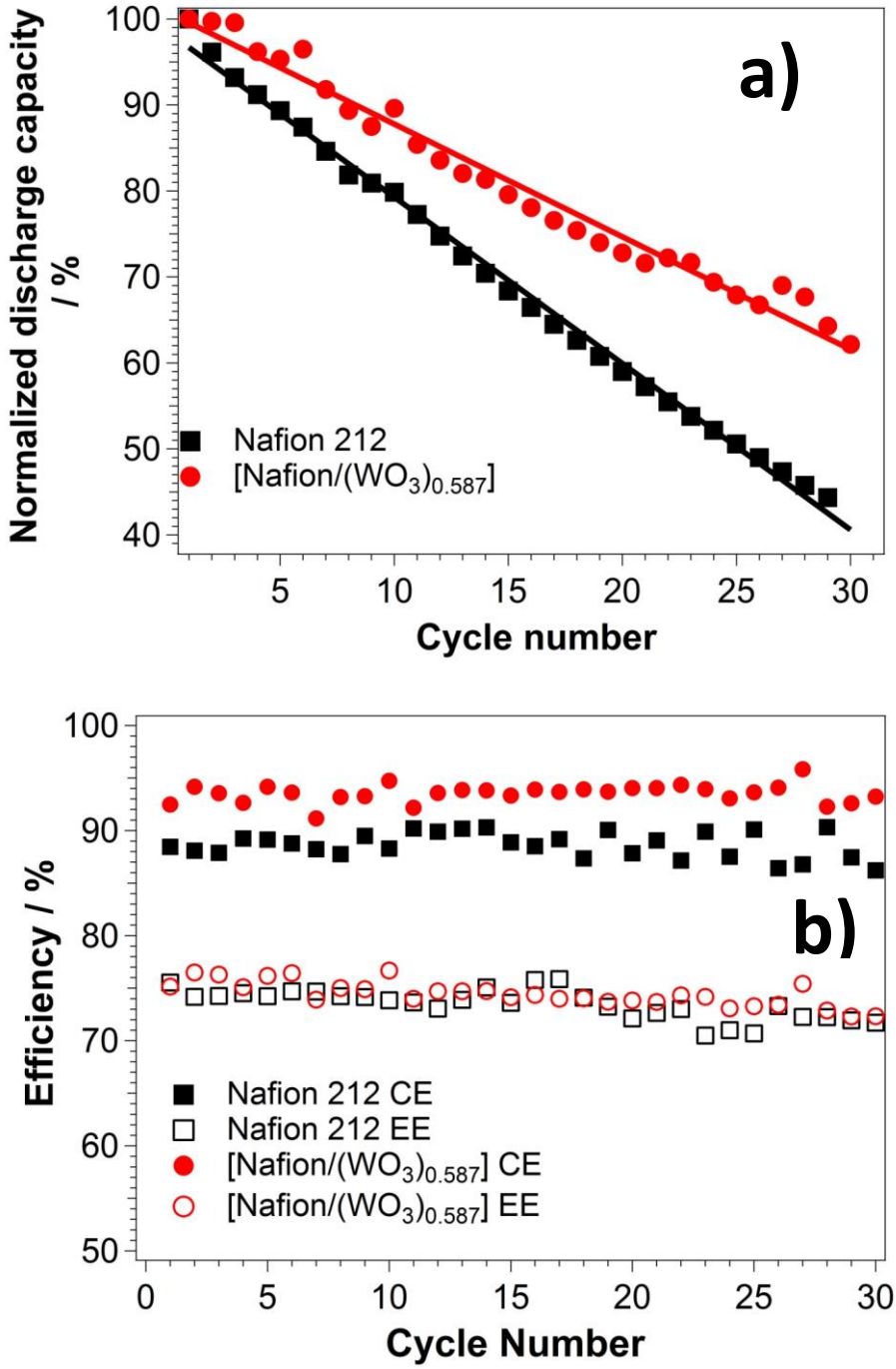

Figure 4.9 Discharge capacity decay (a) and efficiency of single VRFB (b) tested at 50mA·cm^{-2}.

The results presented above reveal that the [Nafion/$(WO_3)_{0.587}$] hybrid inorganic-organic membrane features good physicochemical properties, an excellent ion selectivity ($2.1 \cdot 10^4$ S·min·cm^{-3}), and a higher coulombic efficiency in comparison with Nafion 212. Considering the harsh conditions, the long-term cycling stability of the IEM is of importance for its practical application. In order to evaluate the long-term stability of the [Nafion/$(WO_3)_{0.587}$] hybrid membrane, VRFB single cells mounting either the [Nafion/$(WO_3)_{0.587}$] hybrid membrane or the Nafion 212 underwent charge/discharge testing at a current density of 50 mA·cm^{-2}over 30 cycles. Results are presented in Figure 4.9(a) (decay in discharge capacity) and Figure 4.9(b) (CE and EE changes *vs.* cycle numbers). It can be seen that the [Nafion/$(WO_3)_{0.587}$] membrane shows an improved performance. CE, defined as the ratio between the discharge capacity and the charge capacity, indicates the vanadium crossover degree through the membrane in a VRFB. As a result, the battery based on the optimized [Nafion/$(WO_3)_{0.587}$] hybrid membrane exhibits: (i) a coulombic efficiency of 93%, 5 % higher with respect to the reference Nafion 212; and (ii) an energy efficiency of 75%. There is no CE and EE decay after 30 charge-discharge cycles, suggesting that the performance of the [Nafion/$(WO_3)_{0.587}$] hybrid membrane is stable even under strongly acidic conditions in the presence of vanadium ions; thus, it is suitable for applications in VRFBs.

Capacity decay over cycling is a concern for VRFBs, therefore a superior ability to maintain a stable capacity over cycling is of paramount importance. The discharge capacity decline is typically caused by the migration of vanadium ions across the IEM. It can be seen that the discharge capacity of the [Nafion/$(WO_3)_{0.587}$] hybrid membrane is higher than that of Nafion 212 membrane throughout the cycle life test; this phenomenon is ascribed to the lower permeability of the hybrid membrane. Furthermore, the discharge capacity decay rate of VRFB mounting the [Nafion/$(WO_3)_{0.587}$] hybrid membrane is lower than that Nafion 212. After 30 charge/discharge cycles, the discharge capacity of the VRFB mounting the [Nafion/$(WO_3)_{0.587}$] hybrid membrane is 70% of the discharge capacity in the first cycle, which is clearly higher than that of Nafion 212 membrane, that is equal to 46% only.

The CE, VE, and EE of the VRFBs at current densities from 20 to 70 mA cm^{-2} are presented in Figure 4.10. As a whole, the CE of the VRFB both increase with the current densities due to the shorter charge-discharge time and shorter crossover time for vanadium species at higher current densities. Due to the lower vanadium ion permeability, the CE of the hybrid membrane is higher than that of Nafion 212. The VE of a VRFB is determined by the electrode activity and ohmic resistance. Due the identical electrodes used in both VRFBs, the internal resistance becomes a major factor in determining VE. VE of the VRFBs both decrease with the current densities due to the higher ohmic resistance and ohmic polarization at higher current densities. The VE of the [Nafion/$(WO_3)_{0.587}$] hybrid membrane is slightly higher than Nafion 212 as well. Energy efficiency (EE), determined by CE and VE, is an important parameter to evaluating the energy loss in a charge-discharge process of a VRFB. As can be seen, the EE of the [Nafion/$(WO_3)_{0.587}$] hybrid membrane is always higher than that of Nafion 212 at current densities between 20 and 70 mA·cm^{-2}.

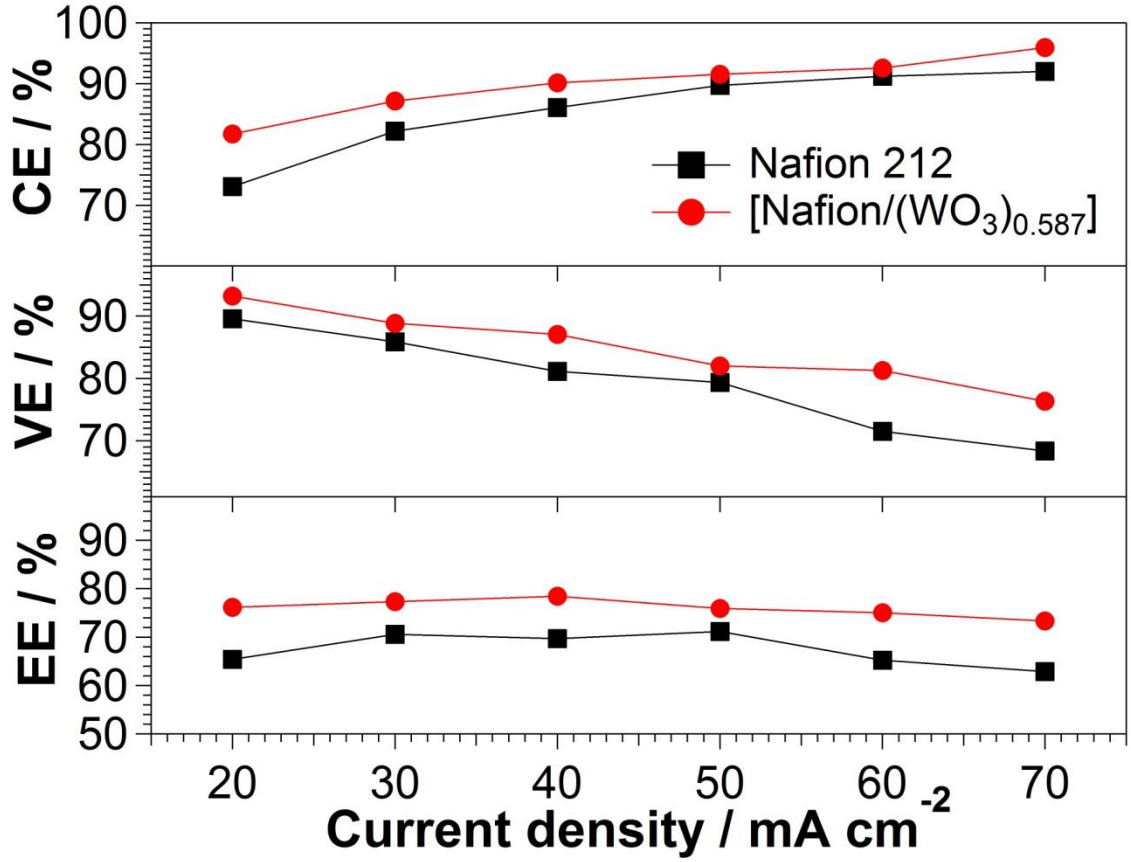

Figure 4.10 Coulombic efficiency (CE), voltage efficiency (VE) and energy efficiency (EE) of VRFBs assembled with Nafion 212 and [Nafion/$(WO_3)_{0.587}$]hybrid membrane at a current density ranging from 20 to 70 mA cm^{-2}.

Figure 4.11 shows the open circuit voltage (OCV) curve of the VRFB based on the [Nafion/$(WO_3)_{0.587}$] hybrid membrane in comparison with that of the reference Nafion 212 membrane. The OCV curve is typically used to demonstrate the retention capability of the charge capacity, by comparing the time difference of OCV decreasing due to the vanadium permeability and self-discharge phenomenon. The OCV for both VRFBs gradually decreases with time; as the OCV reaches 1.4 V, the rate of decrease becomes faster and the cutoff value of 1.1 V is reached soon after. The time to reach 1.1 V is 42 h and 64 h for Nafion 212 and the [Nafion/$(WO_3)_{0.587}$] hybrid membrane, respectively. Hence, the self-discharge time for the [Nafion/$(WO_3)_{0.587}$] hybrid membrane as evaluated from the OCV curve is about as 1.5 times higher than that of the Nafion 212 membrane, measured under the same conditions. From

this result, it is proven that the permeation of vanadium ions can be reduced significantly by the adoption of the [Nafion/$(WO_3)_{0.587}$] hybrid membrane; this outcome is also in accordance with the vanadium permeability experiments (see Figure 4.6 and Figure 4.7). It is clear that the [Nafion/$(WO_3)_{0.587}$] hybrid membrane has a longer charge retention capability than Nafion 212, resulting in a lower self-discharge influence in the single-cell VRFBs.

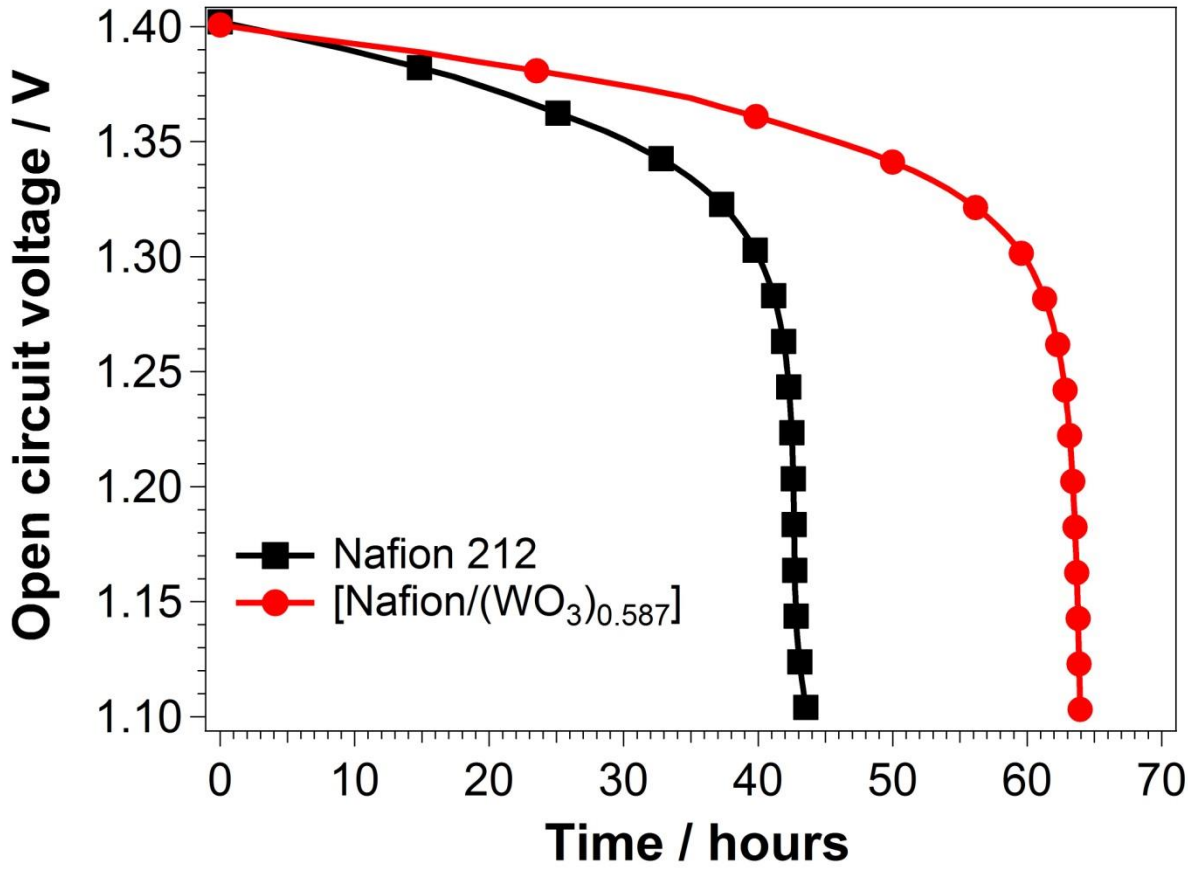

Figure 4.11 Open-circuit voltage (OCV) curve of the VRFB mounting the [Nafion/$(WO_3)_{0.587}$] hybrid membrane. The results obtained on the VRFB mounting the Nafion 212 membrane are included for sake of comparison.

4.4 Conclusions

Tungsten oxide (WO_3) is dispersed into a Nafion matrix to obtain a new family of hybrid inorganic-organic membranes. The [Nafion/$(WO_3)_x$] hybrid inorganic-organic membranes reveal a unique morphology, where: (i) most of the membrane consists of a Nafion matrix with homogeneously dispersed WO_3 filler; and (ii) on one side of the membrane a WO_3-rich layer is formed. This morphology plays a crucial role to limit the crossover of vanadium species, that is significantly reduced in comparison with pristine Nafion. The lowest vanadium crossover is detected for the [Nafion/$(WO_3)_{0.587}$] membrane, that comprises 20 wt% of WO_3. As a result, the VRFB mounting the optimized [Nafion/$(WO_3)_{0.587}$] hybrid membrane exhibits a coulombic efficiency of 93%, 5 % higher in comparison with the Nafion 212 reference. The reduced permeation of vanadium species is also revealed by the lower discharge capacity decay and longer self-discharge times that, for the optimized [Nafion/$(WO_3)_{0.587}$] hybrid membrane, are respectively 1.5 times lower and 1.5 times longer than those revealed from the pristine Nafion 212 reference. In conclusion, the introduction of WO_3 nanoparticles into a Nafion matrix allows to obtain [Nafion/$(WO_3)_x$] hybrid inorganic-organic membranes that: (i) are able to address several issues affecting the pristine Nafion IEM; (ii) yield improved results in single-cell VRFB tests; and, accordingly, (iii) are highly promising for practical applications.

Chapter V Preparation and characterization of SPEEK based proton exchange membranes by doping of WO_3 for vanadium redox flow battery

5.1 Introduction

It is well known that a perfluorinated sulfonic acid membrane such as Nafion (DuPont) is used as proton-exchange membranes due to its excellent proton conductivity and chemical stability under extreme conditions (aggressive and oxidative environment including VO_2^+ in acidic solution) [199]. Nevertheless, drawbacks such as low proton/vanadium ion selectivity and high cost limit their further application determine many researchers to focus on the development of more suitable materials for this application [200]. Sulfonated aromatic polymeric membranes have been suggested as a proton-exchange membrane in the early 2000s for RFBs [201]. Due to the aromatic backbone, sulfonated poly(ether ether ketone) (SPEEK) membranes have low production costs, high enough proton conductivity (between $4.2 \cdot 10^{-3}$ and $1.3 \cdot 10^{-2}$ S cm^{-1} with DS from 57% to 87%), and higher selectivity between vanadium and protons as a result of the tighter polymeric structure [202-206]. A higher degree of sulfonation (DS) gives a higher proton conductivity but directly affects the mechanical stability of the membranes. However, sulfonated groups increase the swelling of the membranes due to the higher content of the hydrophilic groups which affects the dimensional stability or even the solubilization in water [21, 207]. The mechanical properties of SPEEK with a high degree of sulfonation (DS) tend to deteriorate (SPEEK with DS=57% possesses breaking strength of 49.9 MPa, while SPEEK with DS=87% only 24.1MPa [205]), which lower the long-time stability for VRFB application. Furthermore, increasing the DS over 74% leads to excessive vanadium crossover, and thus affects the battery performances [205].

The synergistic effect including hydrogen bonds and dynamic crosslinks of hybrid inorganic-organic material gives a new opportunity to synthesis a novel membrane with good characteristics. Inorganic nanoparticles such as SiO_2, TiO_2, ZrO_2, WO_3 etc. have a substantial effect on proton conductivity, mechanical stability and reduces the effect of vanadium crossover due to the interaction between inorganic nanofiller and the sulfonic acid group of polymer matrix reduces the hydrophilic region in the hybrid membrane [114, 196, 208-217]. According to our previous studies [196, 211-213, 218-220], the distribution of nanofillers in the polymeric matrix and the compatibility between the polymer and inorganic filler phase play an essential role in defining the physicochemical properties of the nanocomposite membranes. As described in the previous chapter, the vanadium ions are likely only passing through the bulk water. The incorporation of nanofiller may lead to the formation of hydrogen bonds and dynamic crosslinks that break the hydrophilic domains and therefore reduce the amount of bulk water. The lower amount of bulk water reduces the vanadium permeability significantly. Therefore, vanadium ions are more hindered than protons, that are also able to migrate through the interfacial water. The composite membrane can enhance ion selectivity by reducing the vanadium crossover. It is necessary to optimize the quantity of nanofiller which plays an important role in a proton conductivity and water uptake [196]. The second advantage of incorporating inorganic nanoparticles into the polymer is attributed to the inorganic particles' ability to increase the mechanical stability of the membrane due to the hydrogen bond formed between the $-SO_3H$ group from SPEEK and the -OH group from the inorganic particles [221]. The stabilization also occurs due to the other weak interactions between the polymer backbone and the inorganic particles. Therefore, the selection of nanofiller and the control of the interaction between the nanofiller and the polymer chains plays a decisive role in the performance of the resultant composite membranes.

Tungsten oxide (WO_3) is a transition metal oxide with wide-ranging applications: solar water splitting [222], oxygen redaction [209, 223], supercapacitors [224]and vanadium redox flow battery [85, 170, 225, 226]. WO_3 is stable in highly concentrated sulfuric acid (nearly insoluble), which is critical during VRFB application (indeed, operates using feeds based on

highly concentrated sulfuric acid). WO_3 has a low cost compared to other metal oxides like Ta_2O_5 and IrO_2 which are also employed in VRFB membranes [84].

In this study, for the first time we describe SPEEK-based membranes containing a dispersion of tungsten oxide nanoparticles (NPs) in various molecular content (0, 0.09, 0.20, 0.29, 0.44), which correspond to the weight % (i.e., 0, 5.9, 12.2, 17.1 and 23.6) based on the TGA analysis. These values are selected to better elucidate the impact of different nanofiller loading levels on the interactions between the SPEEK polymer host and the WO_3 nanofiller. The effect of WO_3 nanofiller incorporation on the physicochemical properties, vanadium permeability, thermal stability and the chemical structure interaction of the composite membranes was studied. Results obtained for composite membranes were compared with those of pristine SPEEK and Nafion membrane as a reference.

5.2 Experimental

5.2.1 Reagents

Poly(ether ether ketone) (PEEK) (Victrex, Vicote® 704) was pretreated before using. The PEEK powder was dried at 100°C for 24 h under vacuum. The WO_3 nanopowder was used as a homogenous suspension obtained by sonicating WO_3 nanopowders (Aldrich, ACS grade) in N, N-dimethylformamide (DMF) for 2 h. The particles size of the nanofiller was 100 nm. All the used solvents are provided by Aldrich and used as received; bidistilled water is used throughout the experiments.

5.2.2 PEEK sulfonation

3 g of PEEK was dissolved in 30 mL of concentrated H_2SO_4 (97%, Sigma-Aldrich) and the solutions were stirred at 55 °C for 7 h. After the sulfonation reaction was completed, the mixture of the acidic solution was slowly transferred and poured into 300 mL of bidistilled water. Then, the solution was cooled in an ice water bath with continuous stirring to terminate sulfonation reaction, resulting in precipitation of the SPEEK polymer. After 12 h, the ensuing suspensions including precipitated SPEEK was washed and filtered with bidistilled water until the pH reached 6–7 and then dried in a vacuum oven at 80 °C for 24 h. The degree of the sulfonation (DS) demonstrates how many sulfonic acid groups in the sulfonated polymer. DS is defined as follows:

$$DS = \frac{n_{SPEEK}}{n_{SPEEK} + n_{PEEK}} \times 100\%$$

In this work, the DS of SPEEK was determined by the elemental analysis method [227, 228] and the DS reached 58 %.

5.2.3 Membrane Preparation

[SPEEK/$(WO_3)_x$] hybrid membranes are prepared with a conventional solvent casting procedure as reported in our previous publication [196, 229]. A various quantity of WO_3 nano-oxides (Sigma-Aldrich) were dispersed in DMF (Sigma-Aldrich) at room temperature (25 °C) for 4 h and sonicated several times, and then the solution of SPEEK in DMF was slowly added into the previous dispersion. The resulting suspension was treated in an ultrasonic bath for 2 h, yielding a homogenous dispersion that is cast in a Petri dish (diameter: 90 mm) and placed in an oven at 80°C for 12 h. Afterward, the obtained membrane was dislodged by immersing the Petri dish in bidistilled water at room temperature. The membrane was soaked firstly in 1 M H_2SO_4 solution for 24 h and then in bidistilled water for 24 h to remove the excess acid. The acidified membranes were stored in bidistilled water at ambient temperature before using. The SPEEK/WO_3 composite membranes were denoted as [SPEEK/$(WO_3)_x$], where x was the molar ratio of WO_3 to SPEEK. The thickness of all the membranes in this study falls between 50 and 70 μm (as measured under ambient air conditions). For comparison, a pristine casted SPEEK membrane was prepared and treated using the same procedure without the addition of WO_3 nano-oxide. Five different membranes are obtained, with x = 0, 0.09, 0.20, 0.29 and 0.44 (corresponding to 0, 5.9, 12.2, 17.1 and 23.6 wt%, respectively). The membrane with x = 0 does not include WO_3, it is used as the reference throughout this work and is labeled 'Pristine SPEEK'. The composition and molar ratios of [SPEEK/$(WO_3)_x$] membranes are listed in Table 5.1.

Table 5.1 Composition and molar ratios of [SPEEK/$(WO_3)_x$] membranes.

Membrane	wt% of WO_3[a]	x[b]	Ion exchange capacity $^{calculated}(\varphi)$ [c] / mEq·g^{-1}
Pristine SPEEK	0.00	0.00	1.73
[SPEEK/$(WO_3)_{0.09}$]	5.90	0.09	1.63
[SPEEK/$(WO_3)_{0.20}$]	12.20	0.20	1.52
[SPEEK/$(WO_3)_{0.29}$]	17.10	0.29	1.44
[SPEEK/$(WO_3)_{0.44}$]	23.60	0.44	1.32

[a] Values determined on the activated membranes as the high-temperature residue measured on HR-TGA under an air atmosphere; [b] $x = mol_{WO3}/mol_{-SO3H}$; [c] $\varphi = meq_{SPEEK}/m_{composite}$.

5.2.4 Instruments and Methods

The thermogravimetric analysis (TGA) and modulated differential scanning calorimetry analysis (MDSC) were performed using the instruments and methods described in Chapter II. MDSC analyses were performed in the -10 to 300 °C temperature range. Broadband Electrical Spectroscopy (BES) was used to establish an electrical property of the new hybrid membranes. A frequency range of 30 mHz ÷ 10 MHz and room temperature condition is used for all the samples. BES studies are carried out on completely hydrated samples.

A Field Emission-Scanning Electron Microscopy (FE-SEM) and Energy-Dispersive X-ray analysis (EDX) are carried out on a Zeiss SUPRA 40VP instrument. A working distance of 15 mm with an acceleration voltage of 10-20 kV is applied. The instrument is operated in a high-vacuum mode. FT-IRATR spectra of the membranes were collected in ATR mode on both phases of each membrane; the spectra are obtained averaging 1000 scans.

5.2.5 Water uptake, vanadium permeability, ion selectivity and ex-situ chemical stability testing

The water uptake, vanadium permeability and ion selectivity were performed using the procedure described in Chapter 2.8 in this thesis. The weight and length of each sample were recorded before and after being soaked in the mentioned solution to observed the changes. The variation in the length and weight of the membranes was measured over a one month.

5.2.6 VRFB single cell tests

VRFB testing is conducted using a zero-gap cell configuration as described in Chapter 2.6 in this thesis. Charge-discharge cycling experiments are performed at different current densities of 20, 30, 40, 50, 60, 70 and 80 mA cm^{-2} with two cut-off voltages set at 1.65 and 1.00 V. The cut-off is voltage is specially chosen in order to avoid the degradation of the carbon electrode and side reactions. The self-discharging arises as a result of vanadium ion crossover and a comparison between commercial Nafion 212 and [SPEEK/$(WO_3)_{0.20}$] is conducted, with termination of the test occurring once the open circuit voltage (OCV) falls below 0.8 V. The cycle life of the cell is carried out at the constant current density of 50 mA cm^{-2} for 30 charge-discharge cycles.

The energy efficiency (EE), coulombic efficiency (CE) and voltage efficiency (VE) of the cell are evaluated as described in the previous chapters.

5.3 Results and Discussion

5.3.1 Thermal analysis

The thermal stability of all membranes is gauged by HR-TGA (Figure 5.1(a)). All the membranes show similar degradation curves and exhibit three thermal decompositions (I-III). It can be seen that the residual weight ratio of sample membranes increases with the increasing of WO_3 mass ratio, which can be attributed to the high thermal stability of WO_3 and is not removed even at high temperature. The first mass loss (I), observed at T < 150 °C and characterized by a magnitude lower than ca. 0.5 wt%, is associated with the loss of residual adsorbed water from the membranes. Another two distinct weight loss steps of SPEEK and hybrid membranes can be observed, which is reflected by the two peaks in separate temperature ranges. The second thermal event (II), observed in the region around 300°C is due to the decomposing and splitting-off the $–SO_3H$ groups in the SPEEK polymer [206, 230]. The third thermal decomposition (III), which begins at 500 °C, is attributed to the oxidative degradation and decomposition of the SPEEK polymer main chain and backbone.

The introduction of the WO_3 nanofiller does not exert a negative influence on the thermal stability of the SPEEK matrix. The only significant difference between the HR-TGA profiles of the [SPEEK/$(WO_3)_x$] membranes is the different value of the high-temperature residue, that increases as the amount of WO_3 therein is raised. This evidence is interpreted admitting that the residue consists of WO_3, that is thermally stable and is not removed even at a high temperature under an oxidizing atmosphere during the measurements. In general, all the [SPEEK/$(WO_3)_x$] membranes show a similar thermal stability in comparison with pristine SPEEK. The thermal stability of all the membranes is adequate for operation in a VRFB, that runs at T < 50°C [158], as witnessed by the negligible mass loss revealed at T < 150°C (event I).

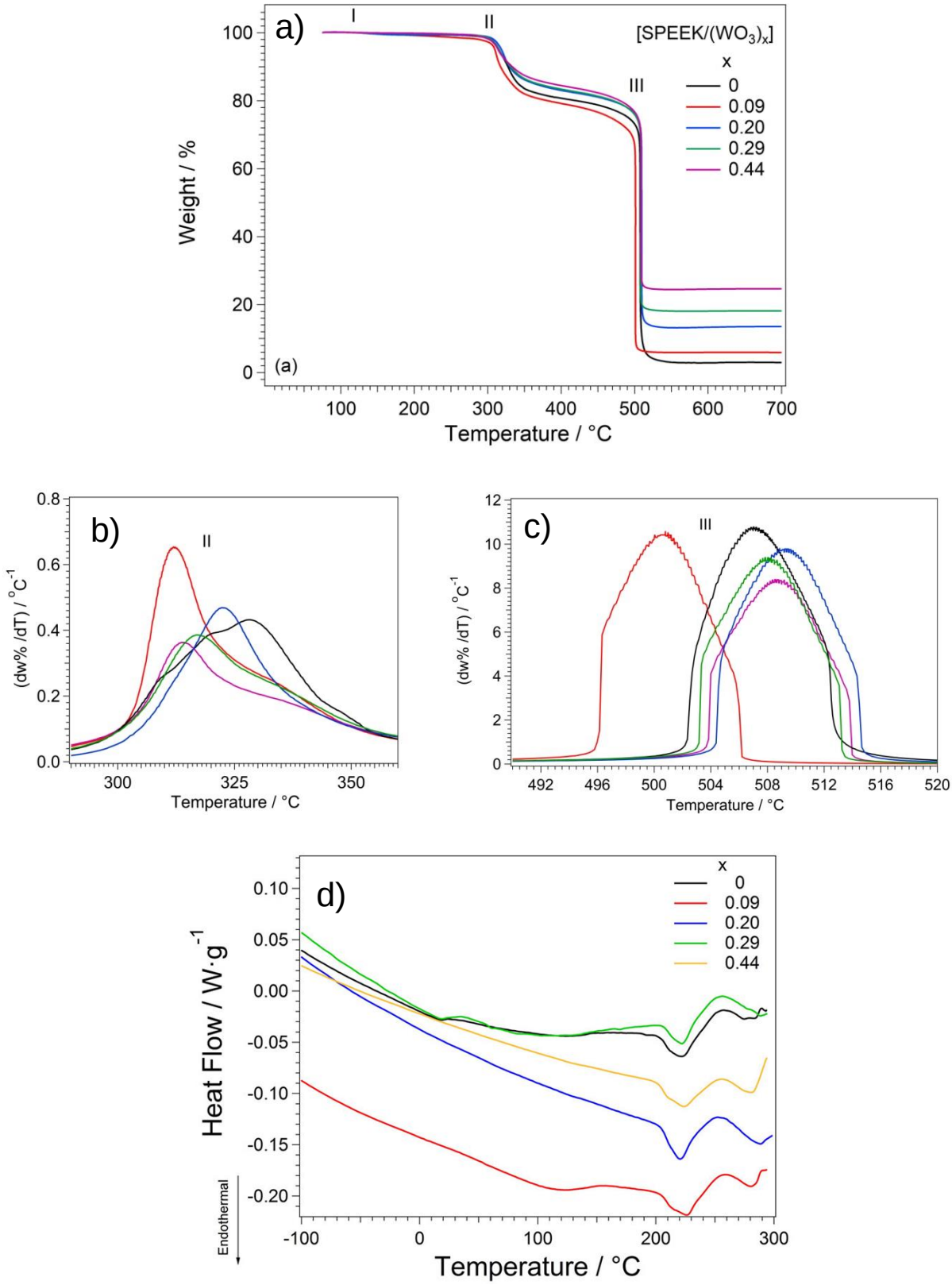

Figure 5.1 (a) HR-TGA profiles of [SPEEK/$(WO_3)_x$] membranes; the first derivative of the wt% is reported in (b) and (c); (d) MDSC profiles of [SPEEK/$(WO_3)_x$] membranes.

Figure 5.1(d) shows the representative MDSC thermograms of SPEEK and hybrid membranes [SPEEK/$(WO_3)_x$], where x= 0.09, 0.20, 0.29, 0.44. The existence of a single well-defined T_g over the entire composition examined, indicating that miscibility existed for these blend systems. Pure SPEEK membrane showed the T_g at around 220 °C, which was slightly higher than that of the value reported [231]. The T_g of pristine SPEEK and hybrid membranes is shown in Table 5.2.

Table 5.2 Glass transition temperature (T_g) of [SPEEK/$(WO_3)_x$] membranes.

Membrane	Wt% of WO_3[a]	x[b]	T_g/ °C
Pristine SPEEK	0.00	0.00	220
[SPEEK/$(WO_3)_{0.09}$]	5.90	0.09	224
[SPEEK/$(WO_3)_{0.20}$]	12.20	0.20	220
[SPEEK/$(WO_3)_{0.29}$]	17.10	0.29	221
[SPEEK/$(WO_3)_{0.44}$]	23.60	0.44	223

[a] Values determined on the activated membranes as the high-temperature residue measured on HR-TGA under an air atmosphere; [b] $x = mol_{WO3}/mol_{-SO3H}$.

As shown, a low percentage of SPEEK in the blends led to a small shift in the T_g to higher temperatures. The [SPEEK/$(WO_3)_{0.09}$] membrane displayed the T_g at 224 °C, [SPEEK/$(WO_3)_{0.20}$] T_g at 220 °C, [SPEEK/$(WO_3)_{0.29}$] at 221 °C and [SPEEK/$(WO_3)_{0.44}$] at 223 °C. The slight increase in T_g indicated higher thermal energy is required to overcome the rotation interactions between the polymer chains owing to increased chain mobility. The increase of T_g values in all hybrid membranes [SPEEK/$(WO_3)_x$] was mainly due to the stiffening of the segmental motion of polymer chain. The stronger intermolecular orientation between the polymer chains may be caused by the dynamic cross-linking arising from specific attractive interactions betweenWO_3 and SPEEK polymer matrix [232].

5.3.2 Determination of water uptake and Broadband Electrical Spectroscopy studies

The water uptake (WU%) of [SPEEK/$(WO_3)_x$] hybrid membranes, determined in accordance with Eq. (2.8.1), (Chapter 2.8) decreases as x is raised (see Table 5.3). This evidence is attributed to the establishment of "dynamic crosslinks" between the SPEEK polymer matrix and the particles of the WO_3 nanofiller [198]. Such dynamic crosslinks stabilize the [SPEEK/$(WO_3)_x$] membrane and inhibit the swelling of the hydrophilic domains of the SPEEK host, thus reducing WU% [213, 233]. With the increasing of WO_3 nanofiller mass ratio, the volumetric density of dynamic crosslinks would be higher and the hydrophilic domain formed by -SO_3H groups would be smaller, which would further restrain the water absorption of the hybrid membrane and makes the membrane more difficult to swell. Normally, lower WU% would lead to lower vanadium ion permeability due to the decrease of bulk water and therefore lead to higher VRFB performance.

Both recast SPEEK membrane and [SPEEK/$(WO_3)_x$] hybrid membranes have a higher WU% than Nafion. These differences can be related to polymer properties like polymer structure, molecular weight and branching degree. Higher WU% in hybrid membrane plays a remarkable role in order to achieve good proton conductivities [125]. Higher WU% generally improves the proton conductivity with the facilitating of -SO_3H groups dissociation and proton migration [234]. However, excessively high levels of WU% can result in membrane fragility and dimensional change leading to failures in mechanical properties, and in extreme cases, solubility in water at elevated temperatures [235]. Other researchers, such as Chang [236] have already prepared stable membranes from SPEEK with a similar sulfonation degree DS= 57% to 67% for the application of VRFB. Therefore, in our work, the pristine SPEEK membrane with DS=58% is suitable for VRFB application.

The proton conductivity and electrical response of recast SPEEK, [SPEEK/$(WO_3)_x$] hybrid membranes and of recast Nafion are investigated by Broadband Electrical Spectroscopy (BES) in the frequency range between 30 mHz and 10 MHz at room temperature (30 °C).

Figure 5.2 reports the profiles of the real part of the conductivity (σ') as a function of the frequency for the proposed samples in their fully hydrated states. Typically, the value of the high-frequency plateau (f > 10^5 Hz) of σ' is adopted as a good approximation of the ionic conductivity (σ'_{DC}) of a fully hydrated Nafion and SPEEK-based membrane [213, 220]. In general, for ionomeric membranes, the proton conductivity depends on the number of available acid groups and their dissociation capability in water, which is accompanied by the generation of protons. Water molecules dissociate acid functionality and facilitate proton transport, so the WU is an important parameter in studying IEMs [126]. Therefore, the proton conductivity of the membrane is highly dependent upon its WU% and IEC. As shown in Table 5.1 and 5.2, both WU and IEC of the SPEEK-based membranes are higher than that of Nafion membrane. However, the proton conductivity of SPEEK based membrane is lower than that of Nafion membrane. Nafion membrane gives the maximum proton conductivity among these membranes. This is possibly attributed to the different proton transfer paths containing ionic clusters and unique hydrophilic-hydrophobic micro-phase separation structure. It is reported the water channels in the hydrated SPEEK membrane are narrower than in the case of Nafion. Although the polymer matrix of SPEEK tends to confine water than in Nafion, the average cross-sectional area of the hydrophilic channels in hydrated SPEEK is comparable to that known for Nafion at the same water content [126, 206]. One major consideration influencing the conductivity of sulfonic acid polymers that is often overlooked is the acidity of the sulfonic acid group itself [237]. Normally, sulfonic acids are referred to as "strong acids". The sulfonic acid groups in SPEEK are all located on rings ortho to an electron-donating ether substituent. The presence of a second electron-donating ether substituent in the SPEEK molecule lowers the acidity even further [237]. However, Nafion has much higher acidity than SPEEK. Although the water content and microstructure of the membrane are also important, a major contributor to the higher conductivity of Nafion is due to its greater acidity and its effect on

effective ion density. The lower conductivity of SPEEK can be attributed to chain rigidity, lack of ion channels, and lower acidity [237].

Table 5.3. WU% of Nafion and [SPEEK/$(WO_3)_x$] membranes

Membrane	WU%
Recast Nafion	18.0
Recast SPEEK	35.1
[SPEEK/$(WO_3)_{0.09}$]	32.6
[SPEEK/$(WO_3)_{0.20}$]	30.2
[SPEEK/$(WO_3)_{0.29}$]	29.1
[SPEEK/$(WO_3)_{0.44}$]	25.5

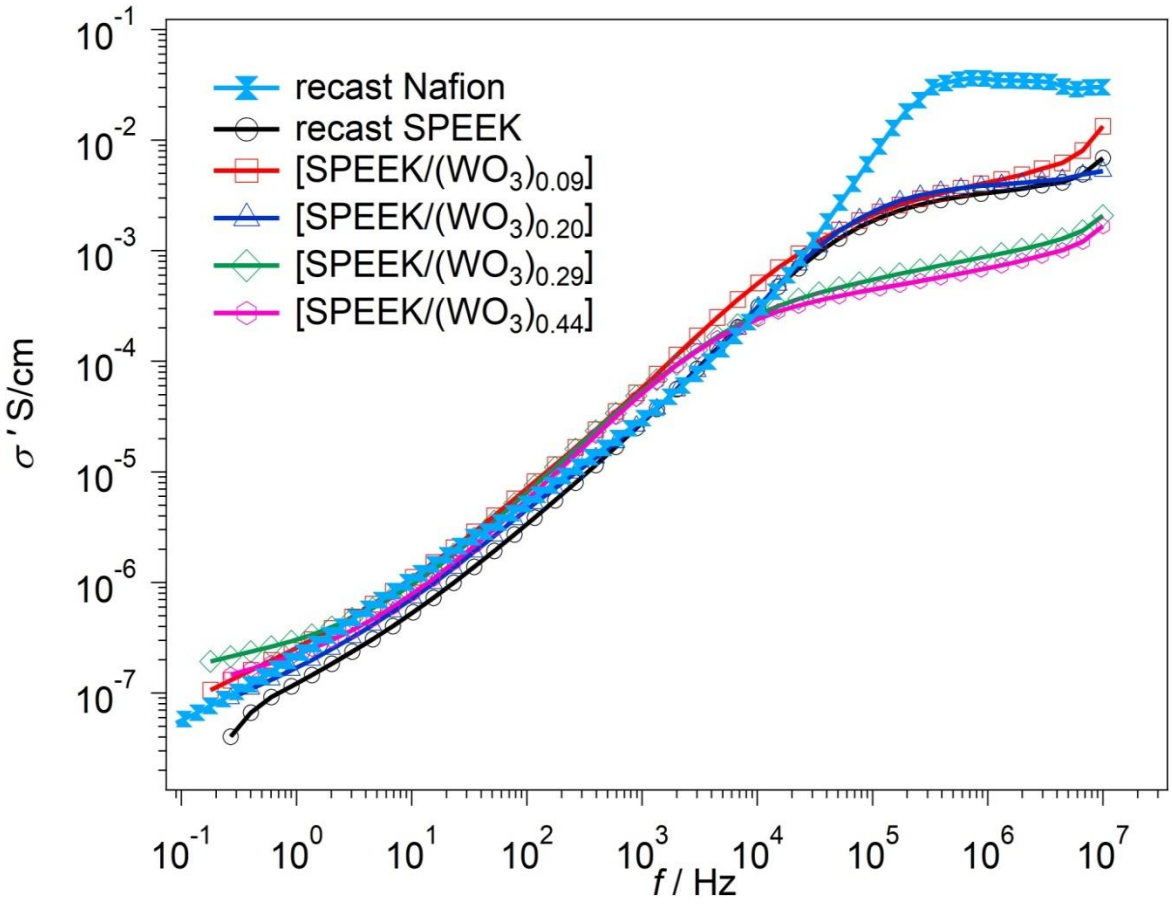

Figure 5.2 Real component (σ') of the complex conductivity vs. frequency for recast Nafion, recast SPEEK and [SPEEK/$(WO_3)_x$] hybrid membranes at room temperature (30 °C).

For [SPEEK/$(WO_3)_x$] hybrid membranes, an interesting variation tendency is found with the content of the incorporated $(WO_3)_x$ nanofillers. At a low and medium content of WO_3 loading in [SPEEK/$(WO_3)_x$] hybrid membranes (x=0.09 and 0.20), the proton conductivity of hybrid membrane is slightly higher than that of pristine SPEEK membrane. At x= 0.09, [SPEEK/$(WO_3)_{0.09}$] exhibits the highest proton conductivity (4.9×10^{-3} S cm^{-1}) among these hybrid membranes due to its high WU and IEC. When the WO_3 content is higher (x=0.29 and 0.44), the proton transports channel is dominated by "blocking effect", and the proton transfer behavior decreases dramatically [238]. With the introduction of the WO_3 nanoparticles, it is assumed that the morphology of the hydrophilic domains of the SPEEK host in the hybrid membranes changes. In detail, with respect to recast SPEEK, in the hybrid membranes the crosslinks R-SO_3-···WO_3···SO_3-R reduce the free volume in hydrophilic domains allowing a lower amount of 'bulk-like' water. This interpretation is consistent with the behavior of other similar nanocomposite membranes [198], and is further supported considering that the overall water content of the hybrid membranes decreases significantly as x is raised (see the WU% results in Table 5.3).

Taken all together, the data reported in Figure 5.2 indicate that at the temperature of operation of a typical VRFB (25 °C) [8], the [SPEEK/$(WO_3)_x$] hybrid membranes exhibit a conductivity ca. $1\sim5 \times 10^{-3}$ S cm^{-1}, respectively. As a comparison, at the same temperature the conductivity of recast Nafion is $3.64 \cdot 10^{-2}$ S·cm^{-1}. It is thus revealed that the proposed [SPEEK/$(WO_3)_{0.09}$] hybrid membrane exhibits the highest conductivity among [SPEEK/$(WO_3)_x$] hybrid membranes. The proposed hybrid membranes, in particular [SPEEK/$(WO_3)_{0.09}$] and [SPEEK/$(WO_3)_{0.20}$], exhibit a conductivity that allows implementation in an operating VRFB. While for [SPEEK/$(WO_3)_{0.44}$] owns the lowest proton conductivity, which is not suitable for the application of VRFB.

5.3.3 Determination of membrane permeability, ion selectivity and evaluation of the chemical stability

The permeation of the active vanadium species leads to low cycling efficiency and fast capacity decay owing to vanadium crossover and self-discharge. The time-dependent concentration changes of VO^{2+} in H_2SO_4 solutions across the hybrid inorganic-organic membranes [SPEEK/$(WO_3)_{0.09}$], [SPEEK/$(WO_3)_{0.20}$] and [SPEEK/$(WO_3)_{0.29}$] are compared with that of reference Nafion 212 (Figure 5.3). A linear relationship between the VO^{2+} concentrations in H_2SO_4 cell vs. time is observed and the slope of each curve is associated with the permeability of the membrane. The pristine SPEEK demonstrates lower linear slope than Nafion 212, which indicates lower vanadium permeability. As expected, it is clearly revealed that the VO^{2+} concentrations of the [SPEEK/$(WO_3)_x$] are further decreased compared to that of pristine SPEEK and Nafion 212 after the same diffusion time; the lowest vanadium crossover concentrations are revealed for the [SPEEK/$(WO_3)_{0.29}$] membrane, which owns the highest loading of WO_3 nanofiller. The VO^{2+} permeability across the [SPEEK/$(WO_3)_x$] membranes decreases as the WO_3 content is raised. It is obvious that Nafion 212 has the highest slope, which indicates it is more prone to VO^{2+} crossover. The WO_3-rich layer of the hybrid [SPEEK/$(WO_3)_x$] membranes may serve as an effective barrier to prevent the migration of vanadium species through the membrane. The interfacial interactions between the WO_3 filler and the SPEEK matrix inhibit the formation of the large hydrophilic channels and reduce the bulk water in hydrophilic domains, which play a crucial role to transport the vanadium ions. The limited permeability is also correlated to the increased tortuosity of vanadium ionic transport paths.

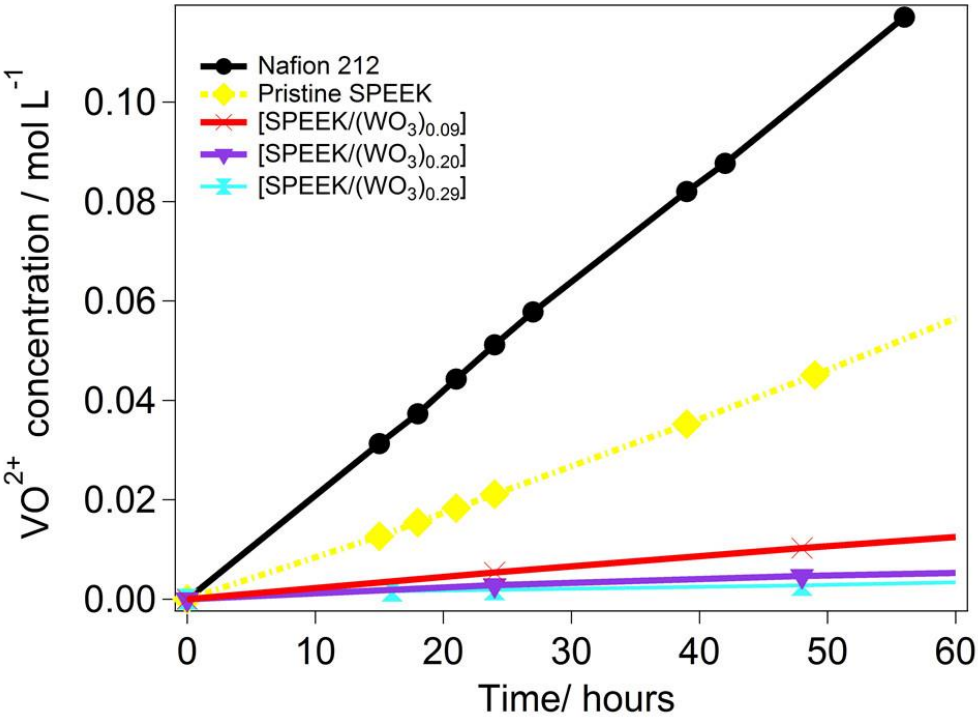

Figure 5.3 The concentration of VO^{2+} ions vs. diffusion time for the [SPEEK/$(WO_3)_x$] membranes comprising different WO_3 loadings.

Permeability (P) illustrates the ability of the membrane to hinder the crossover between the feedstocks. P is evaluated by Eq. (2.8.3) in Chapter 2.8 and decreases as x is raised (see Table 5.4), likely on the basis of a tortuous pathway affecting the mobility of the VO^{2+} ions [239]. All SPEEK-based hybrid membranes give much lower P values (1.3-4.9×10^{-7} cm^2 min^{-1}) than that of Nafion membrane (55.8×10^{-7} cm^2 min^{-1}).

Table 5.4 Permeability and ion selectivity of [SPEEK/$(WO_3)_x$] membranes

Membrane	P / $cm^2 \cdot min^{-1}$	Ion selectivity / $S \cdot min \cdot cm^{-3}$
Nafion 212	$55.8 \cdot 10^{-7}$	$6.5 \cdot 10^3$
Pristine SPEEK	$25.5 \cdot 10^{-7}$	$1.4 \cdot 10^3$
[SPEEK/$(WO_3)_{0.09}$]	$4.9 \cdot 10^{-7}$	$9.0 \cdot 10^3$
[SPEEK/$(WO_3)_{0.20}$]	$1.9 \cdot 10^{-7}$	$2.1 \cdot 10^4$
[SPEEK/$(WO_3)_{0.29}$]	$1.3 \cdot 10^{-7}$	$7.2 \cdot 10^3$

The ion selectivity, which is calculated by Eq. (2.8.3), allows to gauge to what extent an ion-exchange membrane is able to effectively block the crossover of vanadium species, whilst at the same time providing good conductivity for the H_3O^+ ions involved in the charge-discharge processes taking place during VRFB operation [240, 241]. [SPEEK/$(WO_3)_x$] hybrid membranes exhibit the higher selectivity than pristine Nafion and SPEEK membrane. The [SPEEK/$(WO_3)_{0.20}$] membrane reveals the highest ion selectivity ($2.1 \cdot 10^4$ $S \cdot min \cdot cm^{-3}$, see Table 5.4), ca. 3.2 times greater than that of Nafion 212 and is taken as an optimum content of WO_3. The addition of WO_3 to SPEEK can decrease vanadium ion permeability. For VRFB application, a high ion selectivity is beneficial to contribute the good membrane performance. On this basis, it is concluded that [SPEEK/$(WO_3)_{0.20}$] shows a good potential for application in a VRFB.

The mechanism of action can be illustrated as follows. One reason may be that the WO_3 nanofillers act as an effective barrier for vanadium ion's transportation. Vanadium ion can transport quickly without hindrance in the neat SPEEK membrane, while randomly dispersed WO_3 nanofillers in the hybrid membrane can effectively suppress the permeation of VO^{2+} by twisting its percolation pathway. As is reported [242], the SPEEK membrane has smaller hydrophobic/hydrophilic separation (the backbone is less hydrophobic and the sulfonic acid group is less acidic) compared to Nafion membrane, causing narrower and more branched water-filled channels. Moreover, the addition of WO_3 could make the separation between the hydrophobic and hydrophilic domains in the composite membrane and fragment the hydrophilic domains to be smaller due to the higher density of dynamic crosslinks, which leads to lower vanadium ion permeability and higher selectivity.

5.3.4 Scanning electron microscopy

The SEM images of the surface (top and bottom side) of hybrid membranes [SPEEK/$(WO_3)_{0.20}$] are displayed in Figure 5.4 (a) and (b) respectively. Figure 5.4 (a) shows an SEM image collected in the standard detection mode using secondary electrons. The dark color corresponds to the SPEEK polymer, whereas the white irregularly spots are ascribed to the WO_3 nanofiller.

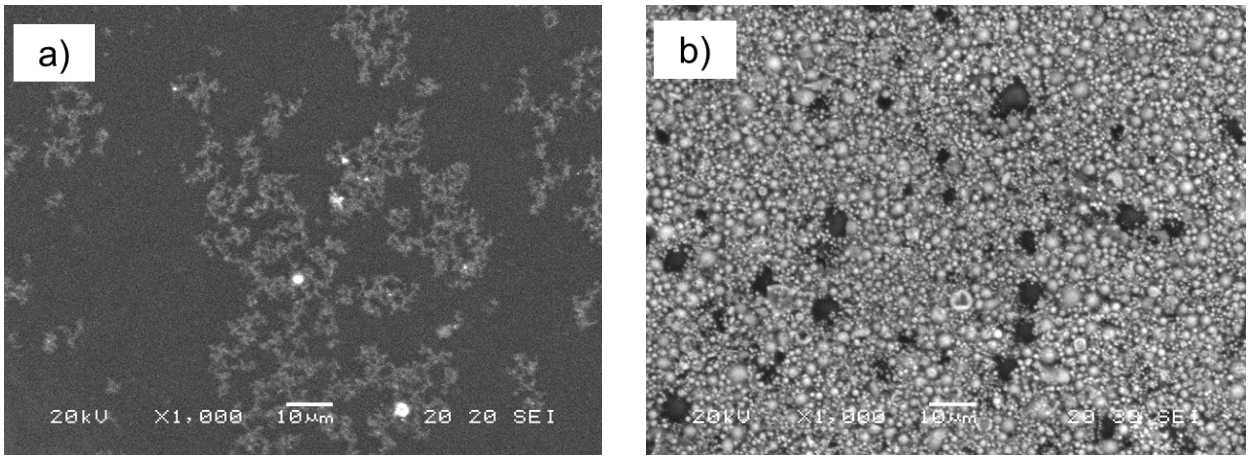

Figure 5.4 SEM image of (a) the SPEEK-rich topside and (b) the WO_3- rich bottom side of the [SPEEK/$(WO_3)_{0.20}$] membrane.

The surface of the hybrid inorganic-organic membrane is rather smooth. Whereas Figure 5.4 (b) shows a SEM image of the bottom side (WO_3 rich) [SPEEK/$(WO_3)_{0.20}$] membrane prepared by solution casting method: WO_3 nanoparticles are distributed homogeneously on the surface, appear as a thick layer.

5.3.5 Vibrational spectroscopy studies

Figure 5.5 reports the ATR-FTIR spectra of the four hybrid membranes and of recast SPEEK. The ATR-FTIR spectra of both sides of each membrane are collected: the top "SPEEK-rich" and the bottom "WO_3-rich" side are labeled "Side A" and "Side B", respectively. The ATR-FTIR

profiles are normalized on the peak at 1595 cm^{-1}, which is assigned to the (COC) mode of the SPEEK host and it is not influenced by the increasing WO_3 content. Figure 5.5 also shows the spectrum of neat WO_3 nanoparticles. The experiments are carried out in two different environmental conditions: (i) under a flow of dry air (see Figure 5.5(a)); and (ii) in completely dry conditions (drying the samples at 90°C under vacuum for 3 days, see Figure 5.5(b)). The correlative assignment of the bands revealed in the ATR-FTIR profiles displayed in Figure 5.5 is reported in Table 5.5.

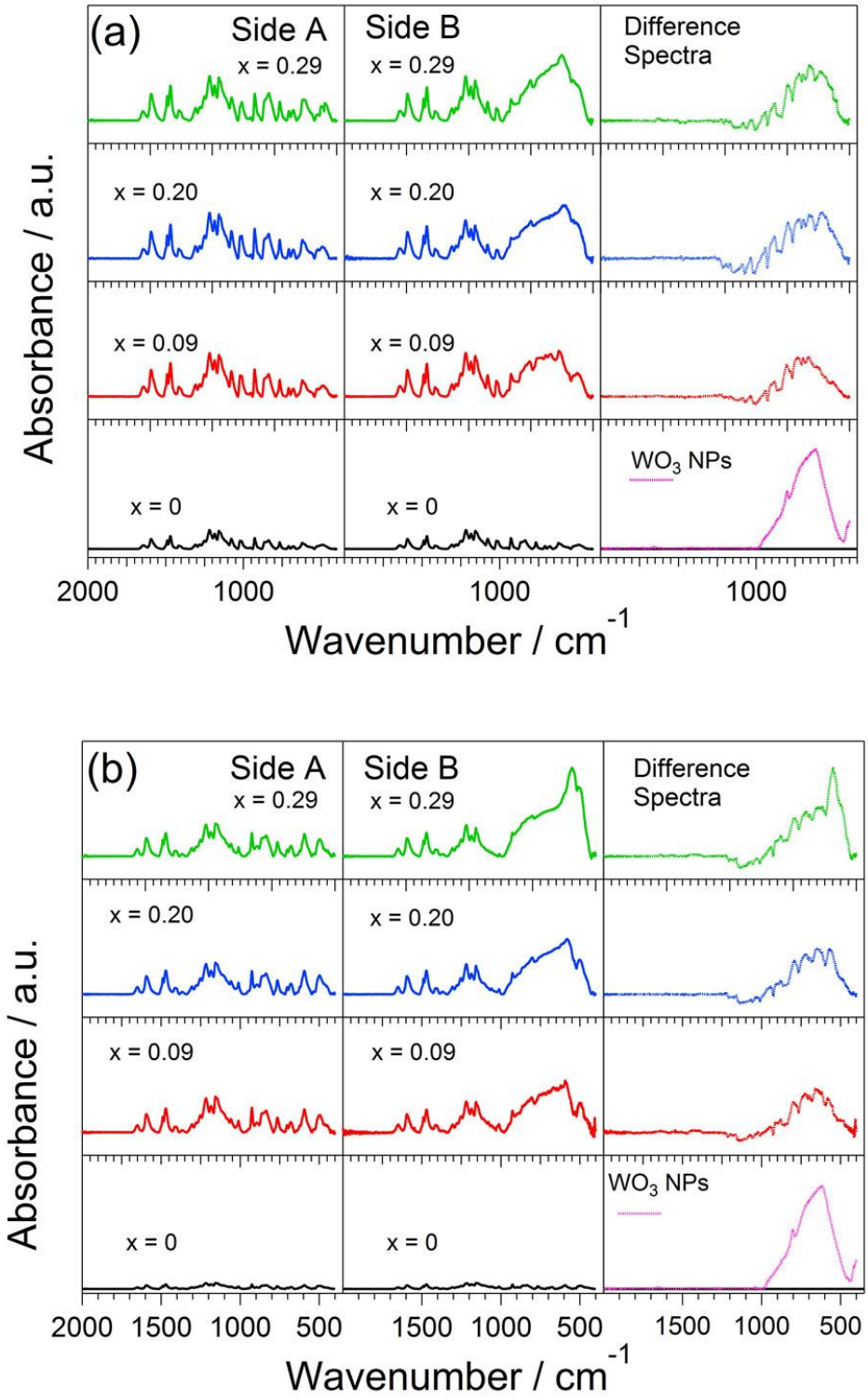

Figure 5.5 ATR-FTIR profiles and difference spectra of [SPEEK/$(WO_3)_x$] membranes. Side A: top "SPEEK-rich" side; Side B: bottom "WO_3-rich" side; The profiles are collected: (a) under a flow of dry air; and (b) in completely dry condition. The spectrum of neat WO_3 nanoparticles is also reported.

Table 5.5 ATR-FTIR band assignments of recast SPEEK, [SPEEK/(WO_3)$_x$] membranes, where x=0, 0.09, 0.20 and 0.29

Observed Modes [a] / cm^{-1}																Band assignments [b]	Ref.
Recast SPEEK		[SPEEK/(WO_3)$_{0.09}$]				[SPEEK/(WO_3)$_{0.20}$]				[SPEEK/(WO_3)$_{0.29}$]				WO_3 NPs			
		Side A		Side B		Side A		Side B		Side A		Side B					
dry	airflow	dry	Airflow	dry	airflow	dry	airflow	dry	airflow	dry	airflow	dry	airflow	airflow			
1650 (w)	1645 (vw)	1650 (vw)	1645 (vw)	1654 (vw)	1642 (vw)	1650 (vw)	1645 (vw)	1658 (vw)	1646 (vw)	1650 (vw)	1645 (vw)	1652 (vw)	1645 (vw)	1645 (vw)		ν [C=C] ν_s[C=O]	[181] [181]
1595 (m)	1594 (m)	1595 (m)	1594 (m)	1595 (vw)	1594 (w)	1595 (m)	1594 (m)	1592 (vw)	1594 (w)	1595 (m)	1594 (m)	1592 (vw)	1594 (w)			arom. ring ν_s [C=C]	[243]
1490 (m)	1488 (m)	1490 (m)	1488 (m)	1491 (vw)	1490 (w)	1490 (vw)	1488 (m)	1489 (vw)	1491 (w)	1490 (vw)	1488 (m)	1489 (vw)	1490 (w)			arom. ring ν_s [C=C]	[243]
1471 (s)	1469 (s)	1471 (s)	1469 (s)	1469 (vw)	1468 (w)	1471 (vw)	1469 (s)	1471 (vw)	1468 (w)	1471 (vw)	1469 (s)	1470 (vw)	1467 (w)			arom. ring ν_s [C=C]	[243]
1411 (vw)	1413 (vw)	1411 (vw)	1413 (vw)	1414 (vw)	1414 (vw)	1411 (vw)	1413 (vw)	1411 (vw)	1415 (vw)	1411 (vw)	1413 (vw)	1415 (vw)	1414 (vw)			ν_s[O=S=O]	[181, 244]
1368 (vw)	1369 (w)	1368 (vw)	1369 (w)			1368 (vw)	1369 (w)	1370 (vw)		1368 (vw)	1369 (w)	1367 (vw)				ν_s[-SO_3H]	[181]
1308 (w)	1311 (w)	1308 (w)	1311 (w)	1305 (vw)	1307 (vw)	1308 (w)	1311 (w)	1309 (w)	1308 (vw)	1308 (w)	1311 (w)	1304 (w)	1309 (vw)			[O=S=O]	[181, 244]
1281 (w)	1281 (w)	1280 (w)	1281 (w)	1281 (vw)	1281 (vw)	1280 (w)	1280 (w)	1281 (vw)	1279 (vw)	1280 (w)	1280 (w)	1281 (vw)	1285 (vw)			ν_s[-SO_3H]	[243]
1252 (m)	1251 (m)	1252 (m)	1251 (m)	1250 (vw)	1251 (w)	1252 (m)	1251 (m)	1251 (vw)	1251 (w)	1252 (m)	1251 (m)	1252 (vw)	1250 (w)			ν_s[OS=O]	[181]
1216 (vs)	1220 (vs)	1216 (vs)	1220 (vs)	1217 (vw)	1220 (m)	1216 (s)	1220 (vs)	1217 (vw)	12217 (m)	1216 (s)	1220 (vs)	1220 (vw)	1220 (m)			arom. ring [C-O-C]	[243]
1185 (s)	1184 (s)	1185 (s)	1184 (s)	1188 (vw)	1186 (w)	1185 (s)	1184 (s)	1185 (vw)	1186 (w)	1185 (s)	1184 (s)	1185 (vw)	1185 (w)				
1154 (vs)	1159 (vs)	1154 (vs)	1159 (vs)	1156 (vw)	1159 (m)	1154 (vs)	1159 (vs)	1159 (vw)	1158 (m)	1154 (vs)	1159 (vs)	1158 (vw)	1158 (w)			δ[C-H]	[181]
1079 (w)	1077 (m)	1079 (m)	1077 (m)	1080 (vw)	1079 (w)	1079 (m)	1077 (m)	1079 (vw)	1077 (w)	1079 (m)	1077 (m)	1078 (vw)	1078 (vw)			ν_{as}[O=S=O] ν_s[-SO_3H]	[244]
1020 (w)	1021 (m)	1021 (w)	1021 (m)	1020 (w)	1020 (m)	1020 (w)	1021 (m)	1021 (w)	1020 (m)	1021 (w)	1020 (m)	1021 (w)	1020 (m)			ν_s[O=S=O]	[243]
1009 (w)	1011 (m)	1009 (w)	1011 (m)	1013 (vw)	1020 (vw)	1009 (w)	1011 (m)	1012 (vw)	1021 (vw)	1009 (w)	1011 (m)	1010 (vw)	1019 (vw)	1035 (vw)		ν[C-O-C]	[181, 244]
	956 (vw)		956 (vw)		953 (w)		956 (vw)		950 (w)		956 (vw)		956 (w)			δ[C-H]	[244]
926 (s)	924 (m)	926 (s)	924 (m)	924 (vw)	928 (w)	926 (s)	924 (m)	926 (w)	929 (w)	926 (s)	924 (m)	927 (w)	927 (w)			δ[C-H]	[244]
895 (w)	898 (vw)	895 (w)	898 (vw)			895 (w)	898 (vw)			895 (w)	898 (vw)						
861 (m)	867 (w)	861 (m)	867 (w)			861 (m)	867 (w)			861 (m)	867 (w)			858 (w)			
836 (m)	840 (m)	836 (m)	840 (m)	506 (w)	810 (w)	836 (m)	840 (m)	802 (w)	801 (m)	836 (m)	840 (m)	803 (w)	802 (m)	799 (m)		δ[C-H]	[181]
764 (w)	765 (w)	764 (w)	765 (w)		768 (m)	764 (w)	765 (w)			764 (w)	765 (w)					ν_s[O=S=O]	[243]
704 (vw)	707 vw)	704 (vw)	707 vw)			704 (vw)	707 vw)			704 (vw)	707 vw)			717 (vs)		ν_s[-SO_3H] ν_s[S-O]	[181, 244]
678 (w)	683 (vw)	678 (w)	683 (vw)		676 (m)	678 (w)	683 (vw)			678 (w)	683 (vw)					ν_s[S-O]	[181, 244]
595 (m)	613 (w)	595 (s)	613 (w)	590 (w)	617 (m)	595 (s)	613 (w)	577 (w)	589 (m)	595 (s)	613 (w)		603 (s)	620 (vs)			
533 (vw)	530 (vw)	533 (vw)	530 (vw)			533 (vw)	530 (vw)			533 (vw)	530 (vw)	549 (m)					
499 (m)	496 (vw)	499 (m)	496 (vw)	501 (w)	499 (w)	499 (m)	496 (vw)	502 (vw)	491 (m)	499 (m)	496 (vw)	506 (w)	493 (m)				
447 (vw)	473 (w)	447 (w)	473 (w)			447 (w)	473 (w)			447 (w)	473 (w)						

[a] vs = very strong, s = strong, m = medium, w = weak, vw = very weak; [b] ν = stretching, δ = bending, as = antisymmetrical, s = symmetrical; [c] λ = mol H_2O/mol -SO_3H.

The spectra reveal the vibrational modes associated with:

(a) the four absorption peaks of -SO_3H group in SPEEK, including asymmetric and symmetric stretching of O=S=O (1250 and 1077 cm^{-1}), S=O stretching (1024 cm^{-1}), and S-O stretching (708 cm^{-1})

(b) the hydrophobic backbone of SPEEK, including carbonyl symmetrical stretching (1644 cm^{-1}), the skeletal in-plane vibration of phenyl rings(1491 and 1470 cm^{-1}),asymmetric stretching of biphenyl ether groups(1216 cm^{-1}) and C-O-C stretching (1010 cm^{-1}); and

(c) the WO_3 inorganic component (850-400 cm^{-1}).

The peak at 956 cm^{-1} is only detected in the spectra of the airflow samples (see Figure 5.5(a)). This peak is ascribed to the bending modes of the C-H groups of the aromatic rings as the H atoms establish weak interactions with the $–SO_3^-$ groups. Indeed, in these conditions, the small traces of residual water present in the system are sufficient to trigger the dissociation of the highly acidic – SO_3H groups, yielding $–SO_3^-$ species. Instead, in the completely dry samples no peak is detected at this wavenumber (see Figure 5.5(b)). In these conditions the $–SO_3H$ groups are not dissociated, thus they do not establish weak interactions with the H atoms bound to the aromatic rings. The bands ascribed to the hydrophobic backbone are almost unaffected by hydration level. The bending mode of H_2O appears as a shoulder of the C=O vibration (1650 cm^{-1}).

The little shift of O=S=O characteristic peaks is found for the composite membranes compared with pristine SPEEK membrane, verifying the presence of the intermolecular hydrogen bonds between the -HSO_3 groups of SPEEK and the WO_3 nanoparticles. The analysis of the ATR-FTIR profiles demonstrates that in [SPEEK/$(WO_3)_x$] hybrid membranes the structural features and inter-chain interactions of SPEEK are significantly influenced by x. In pristine SPEEK there are no relevant differences between the ATR-FTIR profiles of Side A and Side B. Instead, in the case of [SPEEK/$(WO_3)_x$] membranes with x = 0.09, 0.20 and 0.29: (i) the spectra of Side A are very similar to the spectra of both Side A and Side B of pristine SPEEK; and (ii) the spectra of Side A and Side B are very different between one another. In particular,

in Side B of [SPEEK/$(WO_3)_x$] membranes with x = 0.09, 0.20 and 0.29 it is possible to detect a strong band in the wavenumber range between 500 and 1000 cm^{-1}, peaking at 550-600 cm^{-1}. The intensity of this band increases as x is raised; no such band is revealed on Side A. This band, that is particularly evident in the difference is attributed to various vibrational modes of the WO_3 filler embedded in the membranes, mainly ν(WO), δ(WO) and ν(O-W-O). The same modes are also revealed in the ATR-FTIR profile of the pristine WO_3 nanoparticles. These results are interpreted admitting that in the proposed [SPEEK/$(WO_3)_x$] membranes with x = 0.09, 0.20 and 0.29 most of the WO_3 filler is deposited on the B side. Instead, the A side hardly comprises any filler. This interpretation is perfectly consistent other studies [245] and with the morphology of the membranes.

5.3.6 VRFB single cell test

The [SPEEK/$(WO_3)_{0.20}$] membrane is chosen for the VRFB single cell test based on its excellent ion selectivity ($2.1 \cdot 10^4$ S·min·cm^{-3}). The single charge-discharge curves of VRFBs mounting Nafion 212 and the [SPEEK/$(WO_3)_{0.20}$] hybrid inorganic-organic membrane are presented in Figure 5.6. The charge-discharge tests are carried out at a current density of 20 mA·cm^{-2}. The low permeability and acceptable proton conductivity of the [SPEEK/$(WO_3)_{0.20}$] hybrid inorganic-organic membrane are expected to improve the charge and discharge capacities. In comparison with the Nafion 212 reference, for the [SPEEK/$(WO_3)_{0.20}$] membrane the VRFB discharge voltage plateau is shifted to lower values and the charge voltage plateau becomes higher (see Figure 5.6). This may due to the slightly higher ohmic resistance of [SPEEK/$(WO_3)_{0.20}$] membrane. Despite the increase of overpotential for [SPEEK/$(WO_3)_{0.20}$], it is observed that VRFB with [SPEEK/$(WO_3)_{0.20}$] owns comparable discharge capacity as Nafion 212. While it is obvious that during the charging process, VRFB with Nafion 212 takes longer time (0.48h vs. SPEEK 0.42h) and possesses higher charge capacity (0.48Ah vs. SPEEK 0.42Ah). The CE of VRFB with [SPEEK/$(WO_3)_{0.20}$] and Nafion 212 is 95.5 and 84.9% at 20 mA·cm^{-2}, which makes significant performance difference as the [SPEEK/$(WO_3)_{0.20}$] has lower vanadium crossover, hence higher CE.

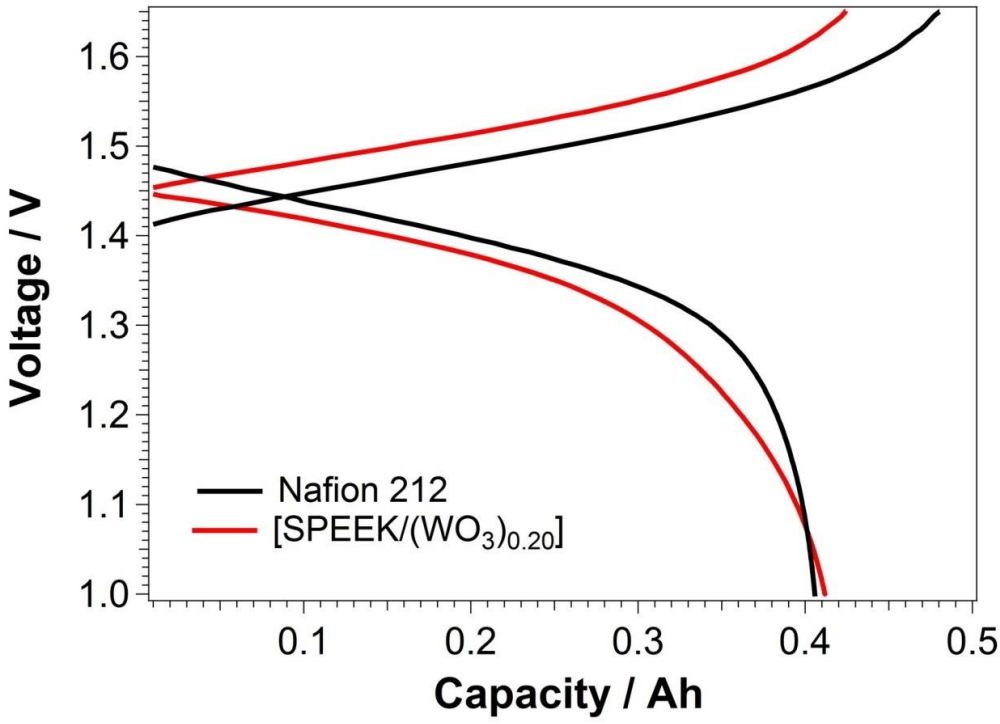

Figure 5.6 Charge-discharge curves of the single VRFB based on Nafion 212 and [SPEEK/$(WO_3)_{0.20}$] membrane at charge-discharge current density of 20 mA cm^{-2}.

To further demonstrate the vanadium crossover during the charge-discharge cycling, the in-situ open circuit voltage (OCV) curve during the cycling is measured. In detail, the in-situ OCV curve is measured during the discharge process after reaching a depth of discharge (DOD) equal to 10% for 2h, 3h, 4h and 5h. The charge-discharge curve with OCV result at 20 mA·cm^{-2} is reported in Figure 5.7. The observed self-discharging arises as a result of vanadium ions crossover. In comparison with the Nafion 212 as "reference" membrane, the self-discharging of the [SPEEK/$(WO_3)_{0.20}$] membrane is significantly lower. Indeed, in the case of Nafion 212 "reference" membrane, the OCV decreases by 17 mV over 5 hours, while in the same timespan the OCV of the [SPEEK/$(WO_3)_{0.20}$] decreases by less than 2 mV. This phenomenon indicates a much lower crossover of vanadium ions, which is in accordance to the vanadium permeability result as well (see Figure 5.3). This is a clear proof indicating that the introduction of the WO_3 filler in SPEEK is able to curtail the permeation of vanadium ions.

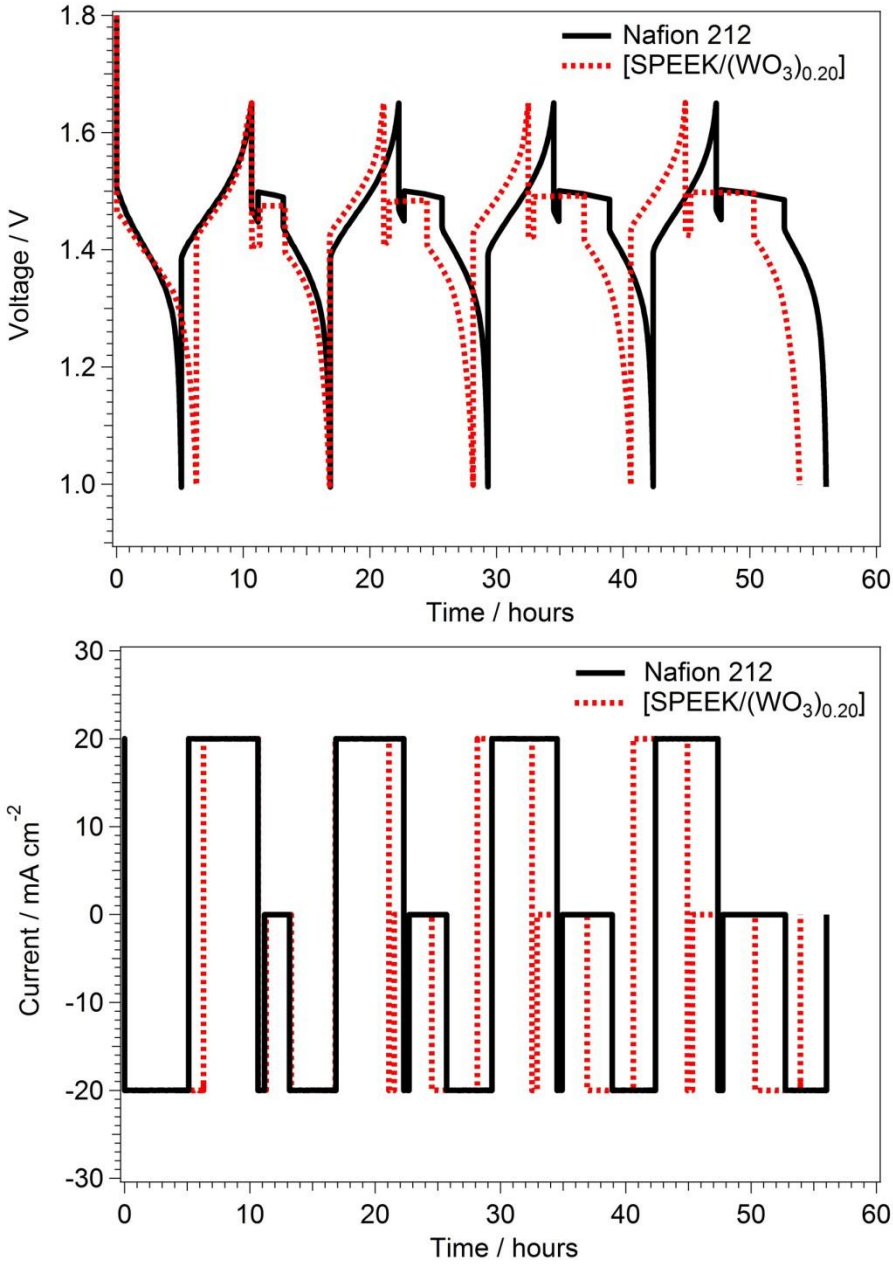

Figure5.7 Charge-discharge curves and measurement of OCV of VRFBs including the membrane [SPEEK/$(WO_3)_{0.20}$] and the Nafion 212 "reference" membrane at a current density of 20 mA cm^{-2}.

The results presented above reveal that the [SPEEK/$(WO_3)_{0.20}$] membrane features excellent ion selectivity and a higher CE in comparison with Nafion 212. However, the long-term cycling stability of the IEM is of importance for its practical application, especially for the sulfonated hydrocarbon membranes. In order to evaluate the long-term stability of the [SPEEK/$(WO_3)_{0.20}$]

membrane, VRFB single cells mounting either the [SPEEK/$(WO_3)_{0.20}$] membrane or the Nafion 212 underwent charge/discharge testing at a current density of 50 mA·cm^{-2} over 30 cycles. Results are presented in Figure 5.8(a) (decay in discharge capacity) and Figure 5.8(b) (CE and EE changes vs. cycle numbers). It can be seen that the [SPEEK/$(WO_3)_{0.20}$] membrane shows an improved performance. CE indicates the vanadium crossover degree through the membrane in a VRFB. As a result, the battery test at 50 mA·cm^{-2} based on the optimized [SPEEK/$(WO_3)_{0.20}$] hybrid membrane exhibits: (i) a coulombic efficiency of 96.8%, 3 % higher with respect to the reference Nafion 212; and (ii) an energy efficiency of 77.9%. There is no significant CE and EE decay after 30 charge-discharge cycles, suggesting that the performance of the [SPEEK/$(WO_3)_{0.20}$] hybrid membrane is stable even under strongly acidic conditions in the presence of vanadium ions; thus, it is suitable for applications in VRFBs.

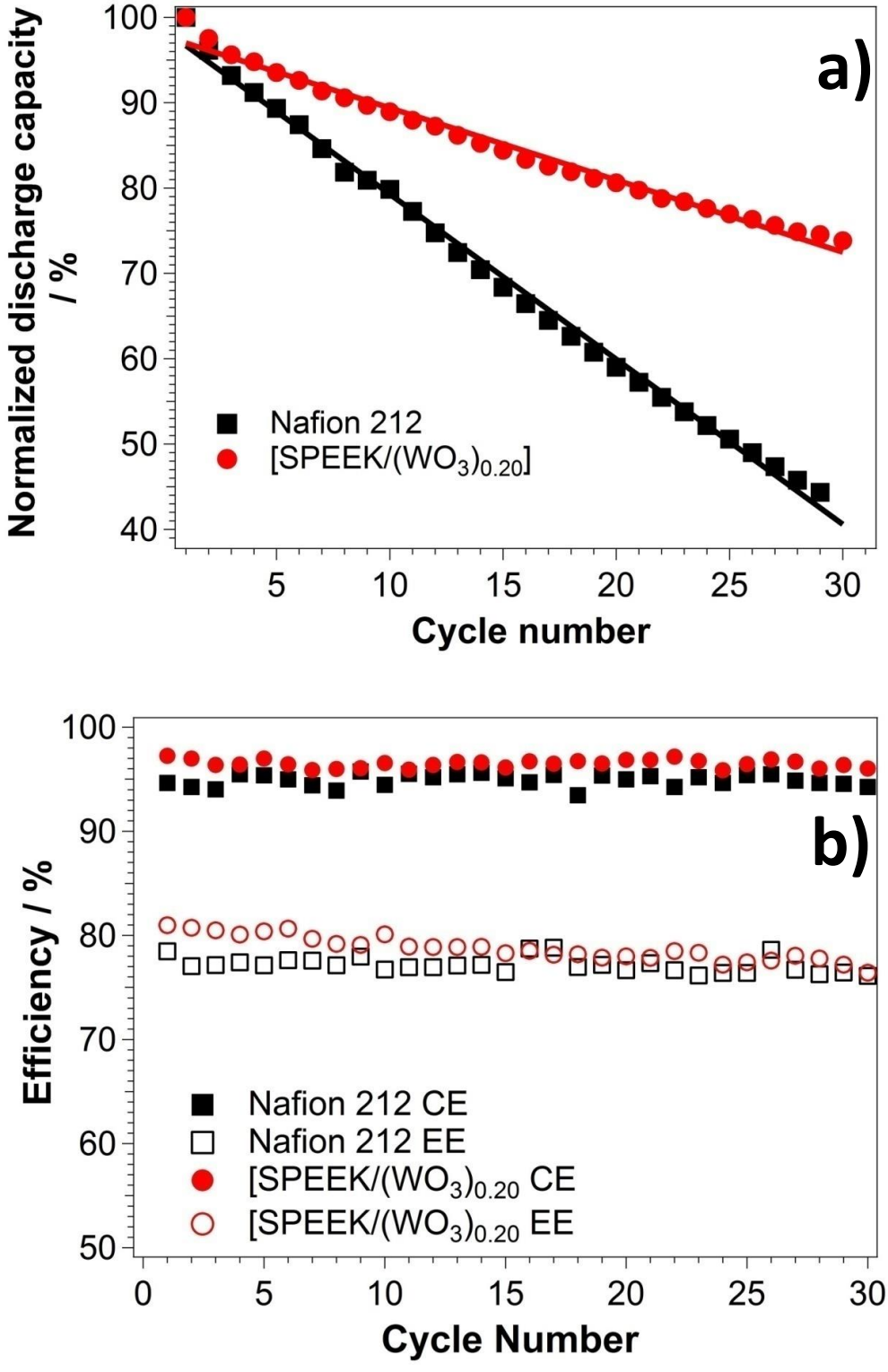

Figure 5.8 (a) Normalized discharge capacity decay, (b) coulombic and energy efficiency of single VRFB tested at 50 mA·cm^{-2}.

The discharge capacity decline is typically caused by the migration of vanadium ions across the IEM. It can be seen that the normalized discharge capacity of the [SPEEK/$(WO_3)_{0.20}$] hybrid membrane is higher than that of Nafion 212 membrane throughout the cycle life test; this phenomenon is ascribed to the lower permeability of the hybrid membrane. Furthermore, the discharge capacity decay rate of VRFB mounting the [SPEEK/$(WO_3)_{0.20}$] is lower than that Nafion 212. After 30 charge/discharge cycles, the discharge capacity of the VRFB mounting the [SPEEK/$(WO_3)_{0.20}$] hybrid membrane is 74% of the discharge capacity in the first cycle, which is clearly higher than that of Nafion 212 membrane, that is equal to 44% only.

The CE, VE, and EE of the VRFBs at current densities from 20 to 80 mA cm^{-2} are presented in Figure 5.9. The CE of the VRFB both increase with the current densities due to the shorter charge-discharge time and shorter crossover time for vanadium species at higher current densities. It is considered that during the VRFB operation the electro-osmotic drag has a minor effect. Due to the lower vanadium ion permeability, the CE of the [SPEEK/$(WO_3)_{0.20}$] is higher than that of Nafion 212 at the entire measured current densities, especially at lower current densities. The VE of a VRFB is determined by the electrode activity and ohmic resistance. Due to the identical electrodes used in both VRFBs, the internal resistance becomes a major factor in determining VE. VE of the VRFBs both decrease with the current densities due to the higher ohmic resistance and ohmic polarization at higher current densities. The VE of the [SPEEK/$(WO_3)_{0.20}$] hybrid membrane is comparable to Nafion 212 as well. Energy efficiency (EE), determined by CE and VE, is an important parameter for evaluating the energy loss in a charge-discharge process of a VRFB. As can be seen, the EE of the [SPEEK/$(WO_3)_{0.20}$] hybrid membrane is slightly higher than that of Nafion 212 at current densities between 20 and 80 mA·cm^{-2}, which indicates that the higher CE of [SPEEK/$(WO_3)_{0.20}$] due to lower vanadium crossover plays an important role that finally determines the higher EE.

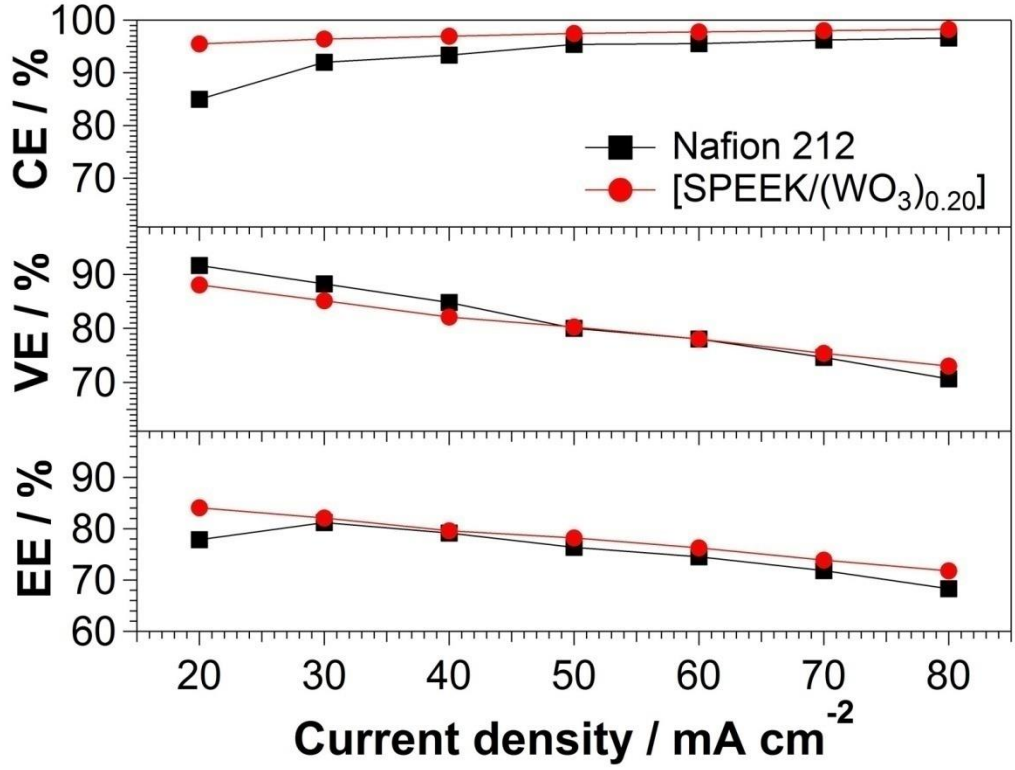

Figure 5.9 Coulombic efficiency (CE), voltage efficiency (VE) and energy efficiency (EE) of VRFBs assembled with Nafion 212 and [SPEEK/$(WO_3)_{0.20}$] hybrid membrane at a current density ranging from 20 to 80 mA cm^{-2}.

Figure 5.10 shows the OCV curve of the VRFB based on the [SPEEK/$(WO_3)_{0.20}$] hybrid membrane in comparison with that of the reference Nafion 212 membrane. The OCV for both VRFBs gradually decreases with time; as the OCV reaches 1.3 V, the rate of decrease becomes faster and the cutoff value of 0.8 V is reached soon after.

The time to reach 0.8 V is 21 h and 60 h for Nafion 212 and the [SPEEK/$(WO_3)_{0.20}$] hybrid membrane, respectively. Hence, the self-discharge time for the [SPEEK/$(WO_3)_{0.20}$] hybrid membrane as evaluated from the OCV curve is about as 2.8 times higher than that of the Nafion 212 membrane, measured under the same conditions. From this result, it is proven that the permeation of vanadium ions can be reduced significantly by the adoption of the [SPEEK/$(WO_3)_{0.20}$] hybrid membrane; this outcome is also in accordance with the vanadium permeability experiments (see Figure 5.3). It is clear that the [SPEEK/$(WO_3)_{0.20}$] hybrid

membrane has a longer charge retention capability than Nafion 212, resulting in a lower self-discharge influence in the single-cell VRFBs.

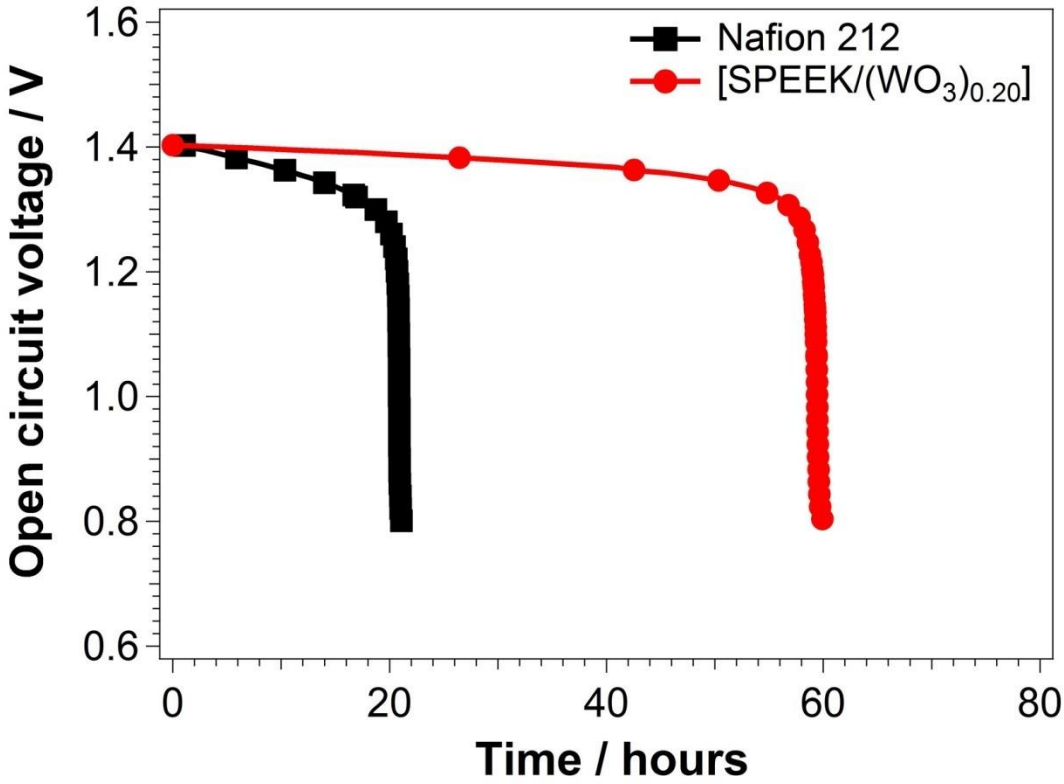

Figure 5.10 OCV curve of the VRFB mounting the [SPEEK/$(WO_3)_{0.20}$] hybrid membrane. The results obtained on the VRFB mounting the Nafion 212 membrane are included for sake of comparison.

5.3.7 Evaluation of the chemical stability

In the span of time for membranes in VRFB operation, they must tolerate both the strongly acidic reactant feeds and the oxidizing effect arising from VO_2^+ species dissolved in the catholyte. Further experiments were conducted to determine the rate at which the membranes are degrading in the vanadium solutions. A first estimate of the chemical durability of the proposed membranes is obtained by exposing them to an environment closely mimicking that which is found in an operating VRFB, as described in the previous chapter. The results of the tests are reported in Figure 5.11.

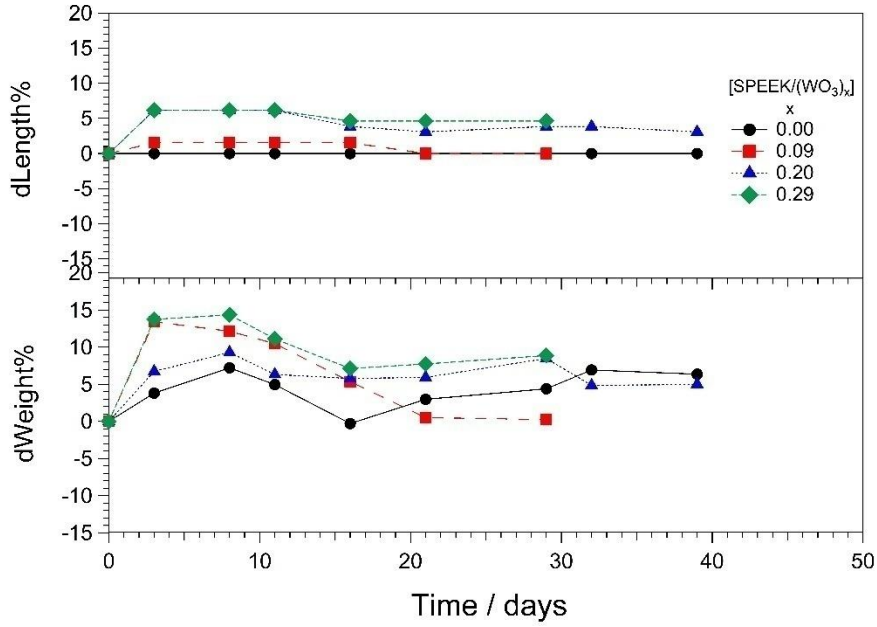

Figure 5.11 Relative variation in: (a) length and (b) weight of: (●) pristine SPEEK; (■) [SPEEK/$(WO_3)_{0.09}$]; (▲) [SPEEK/$(WO_3)_{0.20}$] and (♦) [SPEEK/$(WO_3)_{0.29}$] membranes as a function of immersion time in a solution including 1 M VO_2^+ in 4 M H_2SO_4.

The relative percentage variation of the length the membranes (indicated in Figure 5.11 as dLength%) takes ca. 3 days to reach stability, and does not change significantly in the subsequent 40 days. It is further revealed that the introduction of WO_3 filler improves slightly the dimensional stability of the hybrid membranes. Then the relative variation in the weight of the membranes upon immersion in the solution described above is also measured. The weight of all membranes does not change appreciably upon testing, witnessing the good chemical stability of [SPEEK/$(WO_3)_x$] membranes for VRFB application, which is comparable to Nafion membrane as shown in Figure 3.8 and 3.9 (Chapter 3). This result is interpreted assuming that some VO_2^+ species are permanently adsorbed at the interface between the WO_3 filler and the SPEEK host.

5.3.8 Capital cost analyses

For the design of a VRFB system, the energy and power demand directly define the amount of electrolyte and the size of the cell stacks, respectively. The cost of RFBs is typically determined by the energy and power part. The component cost data listed in Table 5.6 are referenced from the open literature [246-248]. The cost of VRFB electrolytes is calculated based on V_2O_5 and mixed acid as is commonly used for industrial application, due to its significantly lower cost compared to $VOSO_4$ [246]. The advanced VRFB based on mixed acids delivers better stability and wider operating temperature window [38, 150]. A vanadium sulfate and chloride mixed electrolyte proved to be stable with a vanadium content of up to 2.5 M over a temperature range of −5 ~ 50 °C because of the formation of stable $VO_2Cl(H_2O)_2$ at elevated temperatures and reduction in SO_4^{2-} concentrations [150]. Hence, the heat exchanger is unnecessary and not considered for electrolyte temperature control in the VRFB system. Such heat management can cause as much as 20% additional energy loss and significantly increases the overall operating costs [150].

Table 5.6 Component cost of redox flow batteries [17].

Component	Cost	Reference
Nafion Membrane, $/m²	500	[246]
Bipolar plate, $/m²	55	[246]
Graphite felt, $/m²	70	[246]
PVC frame, $/m²	16.56	[246]
V_2O_5, $/kg	24	[246]
Gaskets, bolts, end plates, $/m²	14	[246]
Mixed acid based on H_2SO_4 and HCl, $/ton	85	[246]
Stack manufactory	10% of stack material	[248]
Heat exchanger, $/kW	84	[246]
Power control system (PCS), $/kW	210	[246]
Thermal insulation material, $/m²	15	[247]
Tank, $/gallon	0.29	[246]
Pump, $/GPM	18	[246]
Rebalance cell, $/kW	8.27	one rebalance cell for a 100-cell stack
Pristine SPEEK membrane, $/m²	20	[156]
WO_3 nanopowder, $/kg	564	Sigma Aldrich
SPEEK based Membrane, $/m²	<25	

The capital cost of the VRFB system with Nafion membrane is reported as \$229 kWh^{-1} [17]. The VRFB electrolyte costs \$122 kWh^{-1}, accounting for 53% of the system capital cost due to the high cost of vanadium materials. However, it is worth noting that the membrane cost based on Nafion accounts for 19% of the overall VRFB cost. In order to achieve a more competitive and cost-effective energy storage system, cost-effective hydrocarbon membrane as an alternative membrane will further reduce the capital cost of VRFBs. The price of commercial Sigma Aldrich WO_3 nanopowder is 564 \$/kg. The calculated price of [SPEEK/$(WO_3)_{0.20}$] based on Pristine SPEEK membrane and commercial WO_3 nanopowder is 25 \$/m^2. The price may be further reduced if a cost-effective method is applied to prepare WO_3 nanopowder, such as high energy ball milling. In our study, the estimated overall cost of the VRFB system based on [SPEEK/$(WO_3)_x$] membrane is shown in Figure 5.12 compared with VRFB system based on Nafion membrane.

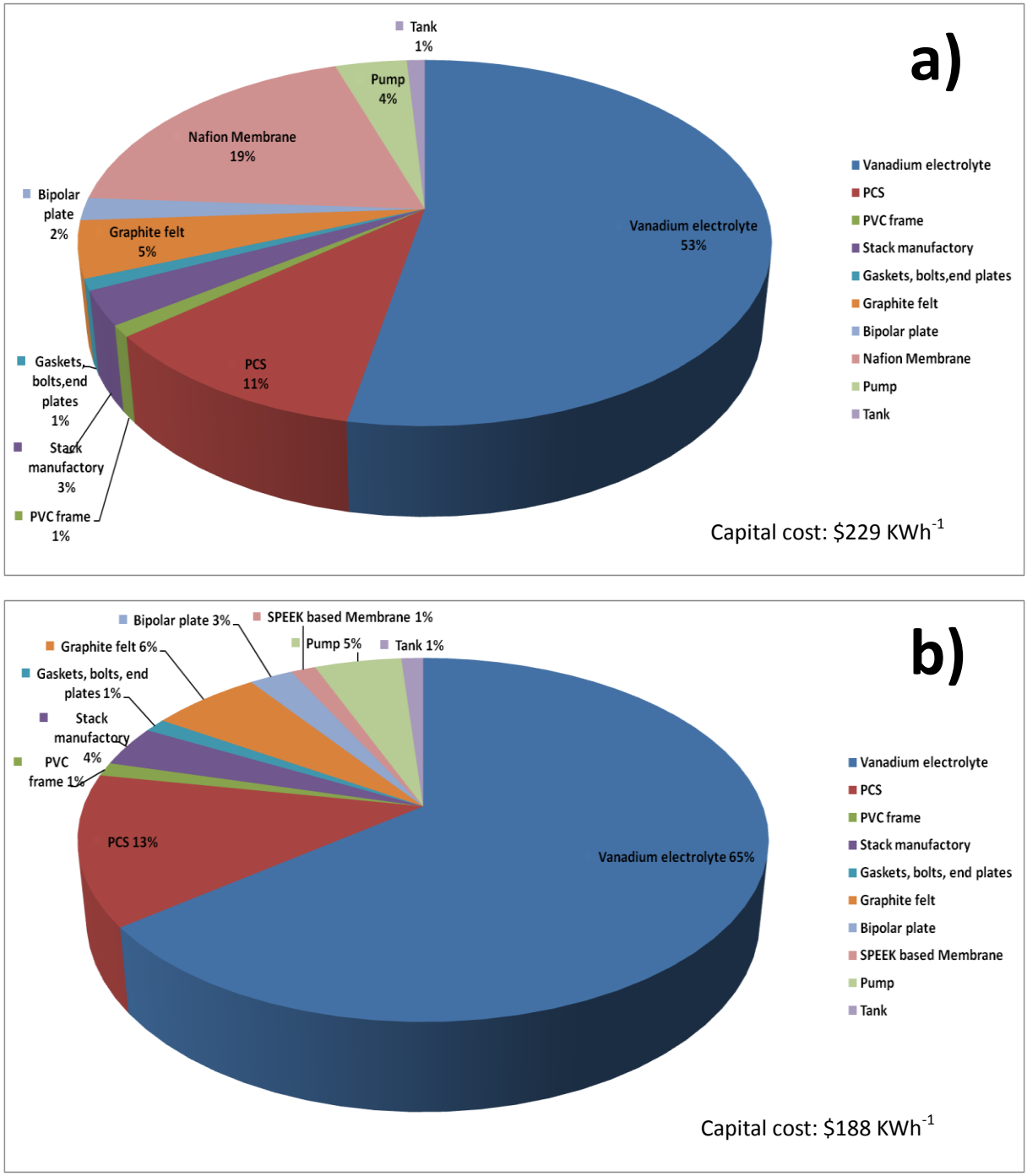

Figure 5.12 Capital cost breakdown of the base case for VRFB system with (a) Nafion and (b) [SPEEK/$(WO_3)_x$] membrane.

As can be seen from the Figure 5.12, the estimated cost of [SPEEK/$(WO_3)_x$] based VRFB system was ca. 188 \$ KWh^{-1}, which is reduced by 18% of the estimated cost of Nafion based VRFB system (229 \$ KWh^{-1}). Moreover, the cost of membranes as a percentage of overall system cost decreased from 19% to 1%, and the cost performance of the ion exchange membrane based on [SPEEK/$(WO_3)_x$] is significantly improved.

5.4 Conclusions

This chapter reports the preparation, the physicochemical and the VRFB single cell cycling performance of hybrid membranes consisting of WO_3 nanoparticles dispersed in a SPEEK matrix. The hybrid membranes are indicated as [SPEEK/$(WO_3)_x$] are obtained by a solvent-casting procedure. In the hybrid membranes, the introduction of WO_3 nanoparticles does not alter significantly the thermal degradation events of the SPEEK host. The MDSC demonstrates the slight increase of T_g values in all [SPEEK/$(WO_3)_x$] hybrid membranes. The stronger intermolecular orientation between the polymer chains may be caused by the dynamic cross-linking arising from hydrogen bonds formed between WO_3 and SPEEK polymer matrix. The interactions between WO_3 and the SPEEK host have a strong impact on the structure of the hybrid membranes at the mesoscale. In detail, the hydrophilic domains of the SPEEK host are likely reduced in size as the content of WO_3 is raised, due to the dynamic crosslink. The density of R-SO_3H•••[WO_3] crosslinks is responsible of the modulation of the water uptake of hybrid materials as well. Some water molecules typically stay close to the interfaces between hydrophilic and hydrophobic domains, which is called interface water, can transport protons but not vanadium species. The vanadium species are only able to migrate through bulk water, deep into the hydrophilic domains. Addition WO_3 nanoparticles cause the breaking of the hydrophilic domains and reducing the amount of bulk water. Accordingly, the higher charge migration tortuosity expected for the proposed hybrid membranes would correspond to a dramatically lower permeability to vanadium species. Indeed, it is shown that the permeability of Nafion212 to VO^{2+} is $55.8 \cdot 10^{-7} cm^2 \cdot min^{-1}$, more than 20 times larger than the permeability of [SPEEK/$(WO_3)_{0.20}$] (measured at $1.9 \cdot 10^{-7}$ $cm^2 \cdot min^{-1}$).The tortuosity effect is lower for protons transport due to the smaller size of protons compared to vanadium ions. As a result, the ion selectivity of hybrid membranes (up to $2.1 \cdot 10^4$ $S \cdot min \cdot cm^{-3}$ for [SPEEK/$(WO_3)_{0.20}$]) is much improved in comparison with recast Nafion ($6.5 \cdot 10^3$ $S \cdot min \cdot cm^{-3}$). The WO_3 nanofiller improves the long-term stability of the hybrid membranes under conditions mimicking those found in VRFBs during operation. The VRFB single cell assembled with the composite membrane of [SPEEK/$(WO_3)_{0.20}$] exhibits higher coulombic efficiency (CE, 98.2%) and energy efficiency (EE, 71.8%) than that assembled with Nafion212 as reference

membrane (CE 96.6% and EE 68.4%) at the current density of 80 mA cm^{-2}. Furthermore, the[SPEEK/$(WO_3)_{0.20}$] membrane maintains a stable performance during 30 cycles at the current density of 50 mA cm^{-2} and the performance is compared with Nafion as the benchmark. Therefore, taken all together the proposed [SPEEK/$(WO_3)_x$] hybrid membranes could be used as promising low-cost and high-performance membrane for VRFB application, owing to their good conductivity, remarkable ion selectivity and long-term stability.

Chapter VI Interplay between vanadium species and charge-discharge process in vanadium flow battery by Raman spectroscopy

6.1 Introduction

As described in the previous chapters, the effect of the capacity loss can be reduced by modification of the proton exchange membranes and by the regulation of the concentration the solutions in the half cells. However, the sides reactions will not be resorted totally [97]. The conditions are also crucial e.g. the system has to be closed and well sealing especially in the oxidation of vanadium (II) and (III) in the anode will reduce the ratio of V (II): V(V) in the system which also increases the capacity loss. Consider the effect of the side reactions and the surrounding conditions [249], it is necessary to make a study in order to understand how the state of charge (SOC) influences the various vanadium species included in the feeds. By investigating the various vanadium species and their stability, it may help us to avoid the formation of unstable species and side reactions by controlling suitable SOC for improving the long-term performance of VRFB system.

The simplest technique to estimate SOC of VRFB is the open circuit voltage (OCV) method described in detail by Skyllas-Kazacos [249] and co-workers. The method does not demand a complicate measurement and equipment. It has been proposed the use of individual half-cell SOC monitoring to detect excessive differences between the two half-cell SOCs as a result of any half-cell imbalance caused by diffusion and side reactions. These methods include half-cell electrolyte potential monitoring, electrolyte conductivity and UV-visible light absorption approaches that can monitor individual half-cell electrolyte condition [47, 250, 251]. Traditionally, open circuit cells are used to monitor the SOC of a cell by using the Nernst Equation to relate the reversible (or open-circuit potential) to the logarithm of the redox reaction ion ratio (corresponding to SOC). As referred in the previous chapters, vanadium

species V(II) and V(III) are very sensitive and can be oxidized easily by oxygen in the air. Therefore, the measurement of SOC must be carried out in the absence of other redox-active species, notably the existence of oxygen.

Most recently, researchers have been successful in demonstrating that spectrophotometric analysis can be used to determine the chemical composition of an electrolyte sample [252, 253]. However, for this method to be accurate requires compiling a large database containing the absorption or transmission spectrum of every possible combination of vanadium and sulfate concentrations. Only then can the spectrum of an electrolyte sample be matched with one from the database to determine its composition accurately.

Although the fundamental knowledge of VRFB is well known, the negative and positive electrode reactions are still important to be further understood, especially the existence forms of various vanadium species and how they are generated during the varied SOC. Several papers [52, 70, 141, 250, 254, 255] discussed the dissolved states of V(IV) and V(V) in concentrated sulfuric acid (H_2SO_4) solutions based on spectroscopic and/or electrochemical measurements, whereas not always the conclusions overlapped from all papers. However, it might be accepted that both V(IV) and V(V) form some complex species with sulfate (SO_4^{2-}) or hydrogen sulfate (HSO_4^-) anion.

In this study, we report in details the decompositions of the spectra for a positive electrolyte during SOC and depth of discharge (DOD) in highly concentrated solutions of vanadium V(V) , V(IV) and H_2SO_4 by using Raman spectroscopy.

6.2 Experimental session

6.2.1 Materials

Vanadium electrolyte solutions were prepared by dissolution of 1 M $VOSO_4 \cdot xH_2O$ in a 5 M sulfate according to the literature [256]. Commercial membrane Nafion 117 (DuPont) was used as IEM. Nafion 117 was activated according to the literature [257]. Carbon paper (AvCarb P75) was used as electrodes as described in the previous chapter. All solutions were prepared by using bidistilled water.

6.2.2 VRFB cycling protocol and Raman sampling measurements

A zero-gap single cell hardware with a 5 cm^2 geometric surface area was used as described in the previous chapter. The VRFB single cell was assembled by sandwiching a Nafion 117 membrane between two carbon paper electrodes. The positive electrolyte volume was initially 60 mL, corresponding to the twice volume of the negative electrolyte. The peristaltic pump was used to circulate the electrolyte solutions at the constant flow rate of 15 mL/min. The first-charging process is as described in the single cell cycling test section of Chapter 4 and 5. Finally, the electrolytes of 30 mL of 1 M VO_2^+ and 30 mL of 1 M V^{2+} in 5 M total sulfate solution were obtained.

During the cycling test, the charge-discharge protocol is slightly different from previous chapters. The discharge process took place at a fixed current density of 40 mA cm^{-2}, and the cut-off voltage was set as 1.0 V. While for the charging process, firstly the battery was charged at a fixed current density of 40 mA cm^{-2} until the potential reached 1.6 V. Then, the battery was further charged under constant voltage at 1.6 V until the current dropped to 0.1 A. The samples of catholyte were collected at certain state of charge (SOC) in the process of VRFB cycling. The volume of exact 0.5 mL of each anolyte and catholyte was taken by a syringe and collected them in a 2 mL volume of a glass vial under the inert gas environment. Spectra of all

obtained vanadium solutions were obtained by use of a DXR-Micro Raman (Thermo Scientific) spectrometer for the 200 to 1800 cm^{-1} region. Finally, spectra were acquired at regular intervals (as shown in Table 6.1) as the battery was charged from 0% and discharged from 100% SOC.

In our experiment, the SOC and DOD were calculated based on the following formula for simplification:

$$\mathrm{SOC} = \frac{C_{\mathrm{charge}}(t)}{C_{total\,\mathrm{charge}}} \times 100\% \qquad (6.1)$$

$$DOD = \frac{C_{discharge}(t)}{C_{total\,\mathrm{discharge}}} \times 100\% = 1 - SOC \qquad (6.2)$$

where $C_{charge}(t)$ and $C_{discharge}(t)$ is the charged or discharged capacity at certain time t, and $C_{total\ charge}$ and $C_{total\ discharge}$ is the overall capacity during the current charging or discharging cycle.

Table 6.1 (a) Capacity corresponding to SOC during charge. The total charge capacity is 0.47749 Ah; (b) Capacity corresponding to DOD during discharge. The total discharge capacity is 0.44569 Ah.

a)			**b)**		
Number of collected samples during charge	Capacity [Ah]	SOC [%]	Number of collected samples during discharge	Capacity [Ah]	DOD [%]
1	0.03	5.3	**1**	0.05	11.5
2	0.06	13.5	**2**	0.06	12.4
3	0.10	20.1	**3**	0.07	14.6
4	0.13	26.8	**4**	0.08	18.1
5	0.16	33.5	**5**	0.1	22.0
6	0.19	40.2	**6**	0.11	25.2
7	0.25	52.6	**7**	0.16	36.8
8	0.32	66.7	**8**	0.19	42.0
9	0.38	79.8	**9**	0.22	49.8
10	0.44	91.6	**10**	0.28	62.6
11	0.46	97.2	**11**	0.33	74.9
12	0.48	100	**12**	0.39	87.2
			13	0.44	95.5

*State of charge (SOC) is the equivalent of a fuel gauge for the battery. The units of SOC are percentage points (0%=empty; 100%=full). An alternate form of the same measure is the depth of discharge (DOD), the inverse of SOC (100%=empty; 0%=full). They are normally used when discussing the current state of a battery in use [104].

As SOC cannot be measured directly but it can be estimated from direct measurement variables. The current integration method, also known as “coulomb counting” can be an effective method to measure SOC. The energy contained in an electric charge is measured in Coulombs and is equal to the integral over time of the current which delivered the charge. The remaining capacity in a cell can be calculated by measuring the current entering (charging) or leaving (discharging) the cells and integrating this over time. The calibration reference point is a fully charged cell, and the SOC is obtained by subtracting the net charge flow from the charge in a fully charged cell. This method provides higher accuracy than most of other SOC measurements since it measures the charge flow directly.

In a VRFB with identical quantities of electrochemically available vanadium ions, the SOC of the battery can be expressed:

$$\mathrm{SOC} = \frac{[V^{2+}]}{[V^{2+}]+[V^{3+}]} = \frac{[VO_2^{+}]}{[VO^{2+}]+[VO_2^{+}]} \qquad (6.3)$$

The all-vanadium system is susceptible to several mechanisms of capacity loss that are asymmetric, i.e. that affect one of the electrolyte solutions disproportionately. For example, the negative electrolyte is susceptible to V^{2+} oxidation by atmospheric oxygen, while V^{3+} can be reduced if hydrogen is evolved at the electrode. Precipitation of V^{5+} as V_2O_5 is an example of capacity loss that is confined to the positive electrolyte. If one of these mechanisms is dominant, vanadium electrolyte systems may lose capacity by becoming unbalanced, such that the reduced capacity of one of the electrolyte reservoirs dominates battery performance. In the case of an electrolyte imbalance, the equality in Equation 6.1 no longer holds true.

6.3 Results and Discussion

In this study, the total concentration of vanadium was fixed at 1 M and the temperature was kept constant at 30 °C, while the SOC and DOD were varied. The sampling was collected during the 5th charge and discharge at the constant current density at 40 mA cm^{-2}. The collected data were taken during 70-90 hours of the VRFB process in order to keep the balance of the vanadium concentrations in the two half cells. Figure 6.1 shows the experimental circuit curves of charge and discharge, and Figure 6.2 shows the one of the charge-discharge curves during Raman sampling. The numbers in Figure 6.2 indicate the related SOC and DOD of samples from the catholyte for Raman measurements. Each of the samples with a different SOC or DOD: 12 taken during the charge and 13 taken during the discharge vs. the voltage (V) and current density (j).

The Raman spectra of the solutions taken from the catholyte during VRFB charge-discharge process are reported in Figure 3. The intensities of several peaks change depending on the SOC and DOD. At the start of charging indicates 0 % SOC, while fully charged status is described as 100 % SOC. Then for the relations between DOD and SOC can be calculated, e.g. 10 % DOD = (100-10%) SOC. At 100 % SOC the solution consists only of VO_2^+, while at 0% SOC the solution consists VO^{2+}. During charge of VRFB the intensity of the vanadium (IV) decreases, while the vanadium (V) increases. The measurements are performed by using the absorbance ratio (Figure 6.3) and the difference spectrometry (Figure 6.4) during charge and discharge process respectively.

The vanadium (V) solution was prepared by the electrolytic oxidation of V(IV) sulfates in sulfuric acid. Therefore, the solution is expected to consists of VO_2^+, H^+, HSO_4^- and SO_4^{2-} ions, the amount of each depends upon the pH and concentration of the solution [141, 258]. The Raman spectra of the obtained vanadium solution in the range of 350 to 1800 cm^{-1} is shown in Figure 6.3 with varied SOC and DOD respectively. All spectra are normalized to the peak at 594 cm^{-1}, which corresponds to ν_s [HSO_4^-]. This peak is specially chosen due to the peak

intensity is not significantly affected by the SOC and not involved with the change of vanadium species.

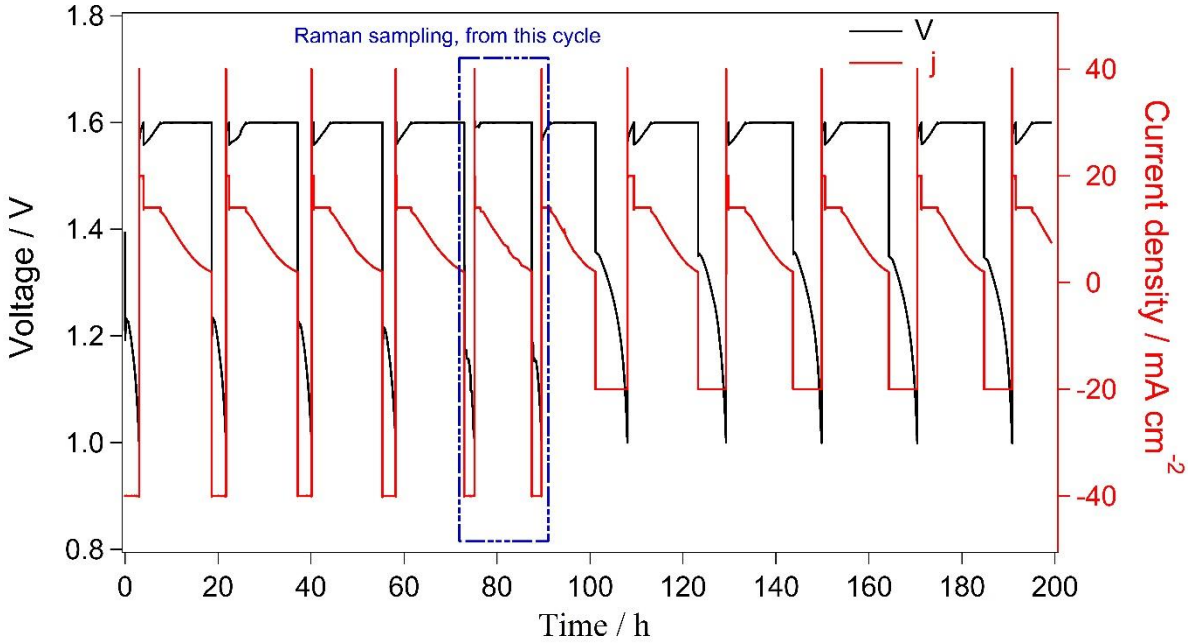

Figure 6.1 Charge-discharge curves of VRFB at 30 °C using a vanadium ion concentration of 1 M in 5 M H_2SO_4. The current density was kept constant at 40 mA cm^{-2} during charge and discharge.

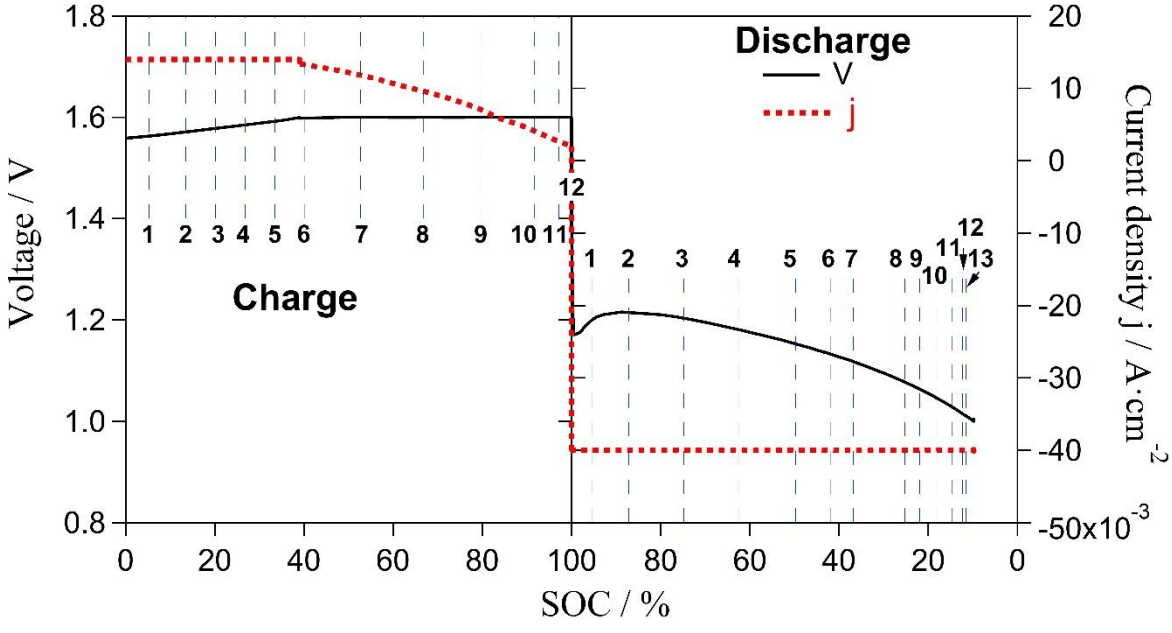

Figure 6.2 The charge-discharge curves during cycling for Raman sampling. The numbers indicate the SOC used to sample the catholyte for Raman measurements.

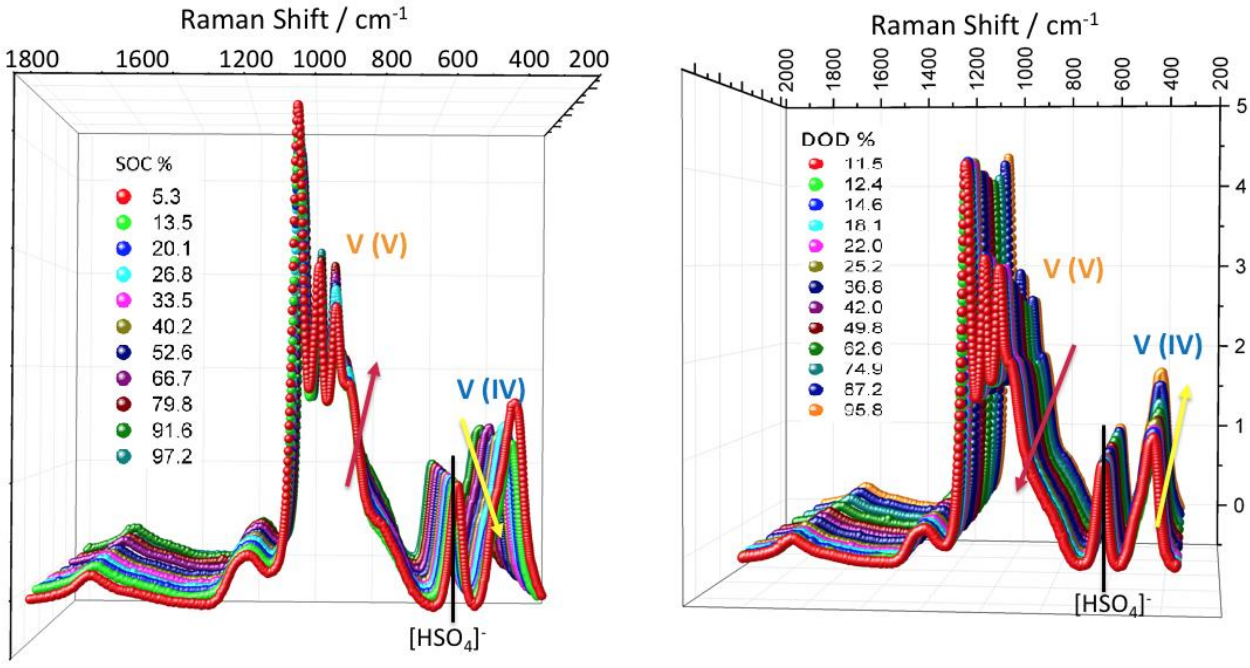

Figure 6.3 Raman spectra of concentrated vanadium solutions include V(IV)/V(V) species solutions in sulfuric acid from 350 to 1800 cm^{-1} at different SOC and DOD. The peaks are normalized to the peak at 594 cm^{-1}.

The Raman spectra of aqueous V(IV)/V(V) solutions contain bands from the HSO_4^- and SO_4^{2-}. We can recognise their coordinated V(V) and V(IV) species like $VO_2SO_4^-$, $VO_2(SO_4)_2^{3-}$ with the oxidation number of +5 or $VO(SO_4)_2^{2-}$, $VOHSO_4^+$ for vanadium +4, which were proposed in the concentrated H_2SO_4 solutions [52, 141] (More details of the species in Table 6.2 and Table 6.3). A cation VO^{2+} is widely accepted as a V(IV) species due to the octahedrally coordinated $VO(H_2O)_5^{2+}$, based on crystallographic data V–O interatomic distance for VO^{2+} plus radius of O^{2-} as reported by Krakowiak and co-authors [3]. According the literature [52], the solubility of $VOSO_4$ decrease with increasing the concentration of H_2SO_4. However, Oriji and co-workers [259] observed that the Stokes radius of V(IV) species increases at the higher concentration of H_2SO_4 (>5M) which can be explained due to the forming a complex formation with SO_4^{2-} and/or HSO_4^-. Although the splitting of V 3d-orbitals in VO^{2+} remains almost unchanged even at the concentration higher than 5 M H_2SO_4, VO^{2+} tends to form ion pair with these anions and becomes less mobile. It is well accepted that the outermost electronic states of V(IV) species are substantially independent of the H_2SO_4 concentration, and the oxidation potential of V(IV)

remains almost constant. However, from the study of Oriji [259], the cyclic voltammograms the oxidation wave of V(IV) is principally quasi-reversible. The CV curves tend to become reversible with increasing H_2SO_4 concentration. In acidic media, a cation of VO_2^+ is accepted as V(IV) species of $VO_2(H_2O)_4^+$. Completely opposite is the situation with V(V) where the d–d transition depends on the concentration of H_2SO_4 [259].

In order to study the evolution of the system and the equilibria established during the charge-discharge process, Figure 6.3 and 6.4 shows the Raman spectra and the difference spectra, respectively. In the spectra, the vanadium (IV) species in the solutions are detected in the range 350-550 cm^{-1} and vanadium (V) species are detected in the range 700-1000 cm^{-1}. A comparison between the spectra of the two systems shows that during the charge of VRFB process the intensity of the vanadium (V) increase whereas vanadium (IV) species decreases. In contrary, during discharge process vanadium (V) decreases while vanadium (IV) species increase. The spectra shows very strong absorption bands at 1040 cm^{-1} (ν_s $(SO_3)[HSO_4]^-$), 986 cm^{-1} (ν_s $[VO_2(OH_2)_4]^+$), 936 cm^{-1} and 986 cm^{-1} (ν_{as} $[VO_2^+]$ and ν_s $[VO_2^+]$), and 427 cm^{-1} correspond to ν_s(V-O-V) [V(IV)].

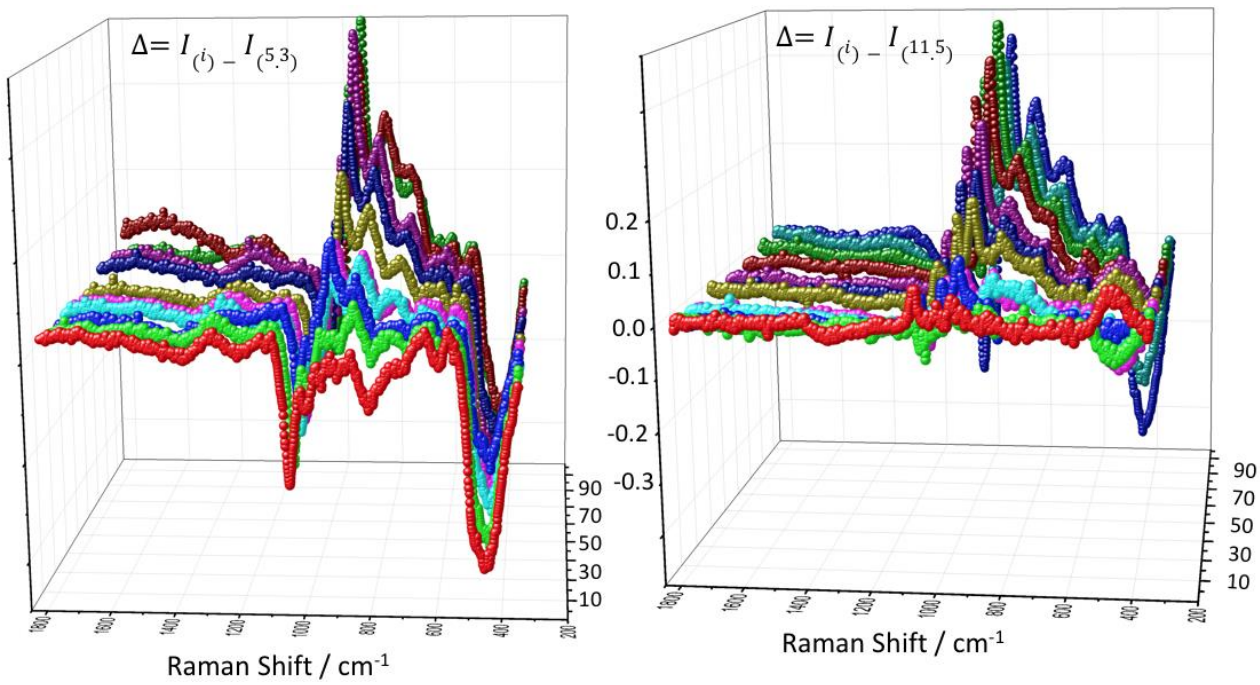

Figure 6.4 Difference Raman spectra of concentrated vanadium solutions include V(IV)/V(V) species solutions in sulfuric acid from 350 to 1800 cm^{-1} at different SOC and DOD. The peaks are normalized to the peak at 594 cm^{-1}. Related difference spectra of Figure 6.3, where for SOC is: 13.5, 20.1, 26.8, 33.5, 40.2, 52.6, 66.7, 79.8, 91.6 and 97.2; for DOD is: 12.4, 14.6, 18.1, 22.0, 25.2, 36.8, 42.0, 49.8, 62.6, 74.9, 87.2 and 95.8.

In order to study the evolution of the system and the equilibria established in the two electrode reservoirs, a correlative assignation of all the vibrations present into the vibrational spectra is done and reported in Figure 6.5, Tables 6.2 and 6.3. The concentration of vanadium is a function of the saturation solubility of the different oxidation states that are formed during charging and discharging in the positive and negative half-cell solutions [260]. Vanadium in its +5 oxidation state exhibits a rich aqueous chemistry; the detected species are strongly dependent upon the pH and vanadium concentration [261]. The real existence form of vanadium ions under the operating medium of VRFB is quite complicated and unclear. The dissolved states of V(IV) and V(V) in concentrated sulfuric acid (H_2SO_4) solutions were investigated via spectroscopic method (Figure 6.5).

Each of the samples with a different SOC or DOD: 12 taken during the charge and 13 taken during the discharge was decomposed for separated peaks and created an assignment (Table 6.2 and 6.3). The Raman spectra of the H-O-H is recorded in the range 1500-1800 cm^{-1}, and the overlapping of different species observed in the range 1300-1100 cm^{-1} which can be a combination of species [H_3O^+], [(S-O) [V^{n+}...SO_4^{2-}] and [HSO_4^-].

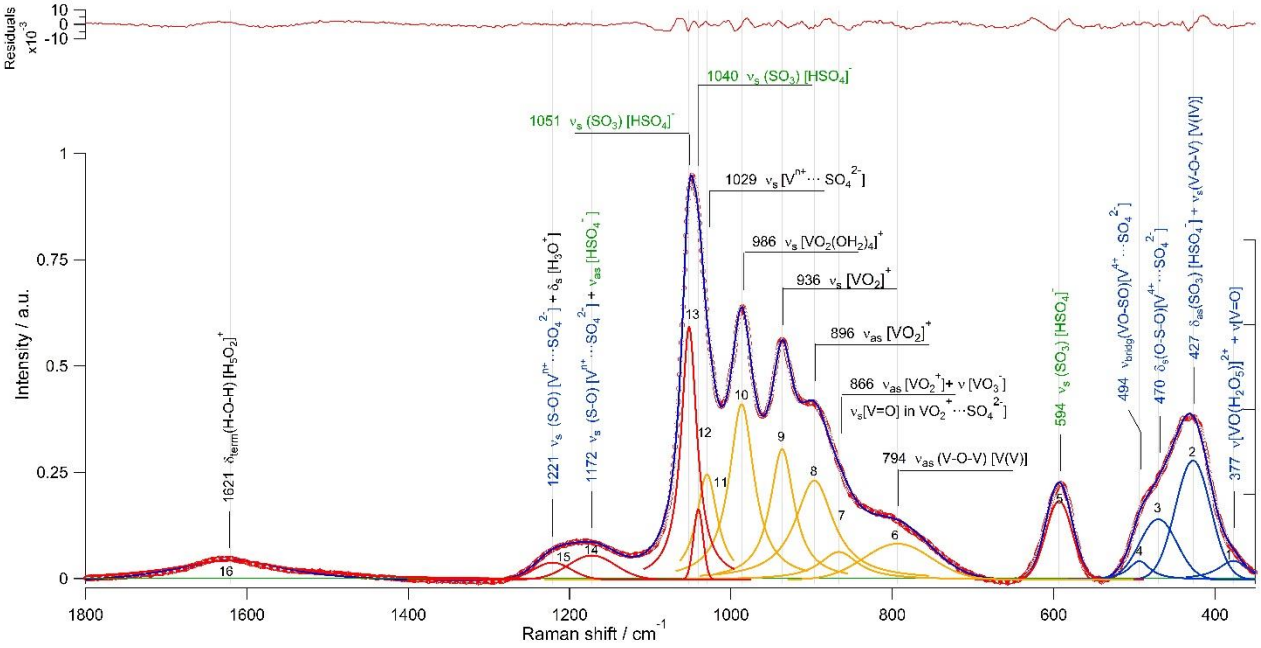

Figure 6.5 The Raman spectra decomposition and its assignment of a positive electrolyte during charge (SOC 13.5 %).

The ratio between intensity of diagnostic peaks and that of reference specie (peak at 594 cm^{-1}, which corresponds to ν_s $[HSO_4]^-$) permit to follow the change in composition of the vanadium and acid species during the charge and discharge cycling in VRFB operation.

Figure 6.6, 6.7 and 6.8 show the trend of the Raman intensity ration for the diagnostic peaks versus the SOC% for the positive electrolyte. In Figure 6.6, Raman intensity ratios for diagnostic peaks (377, 427, 470 and 494 cm^{-1}) in the positive electrode is demonstrated. The intensity ratio decrease as the SOC increases due to their attribution to V(IV) species. In theory, V(IV) decreases and V(V) increases during charging process, and vice versa. Figure 6.7 demonstrates the Raman intensity ratios for diagnostic peaks (794, 866, 896, 936 and 986

cm^{-1}) in the positive electrode. Contrary to the above trend of ratio, the intensity ratios increase with the increasing SOC. They are assigned to V(V) species. As expected, no significant changes of H_2SO_4 species on SOC% is revealed.

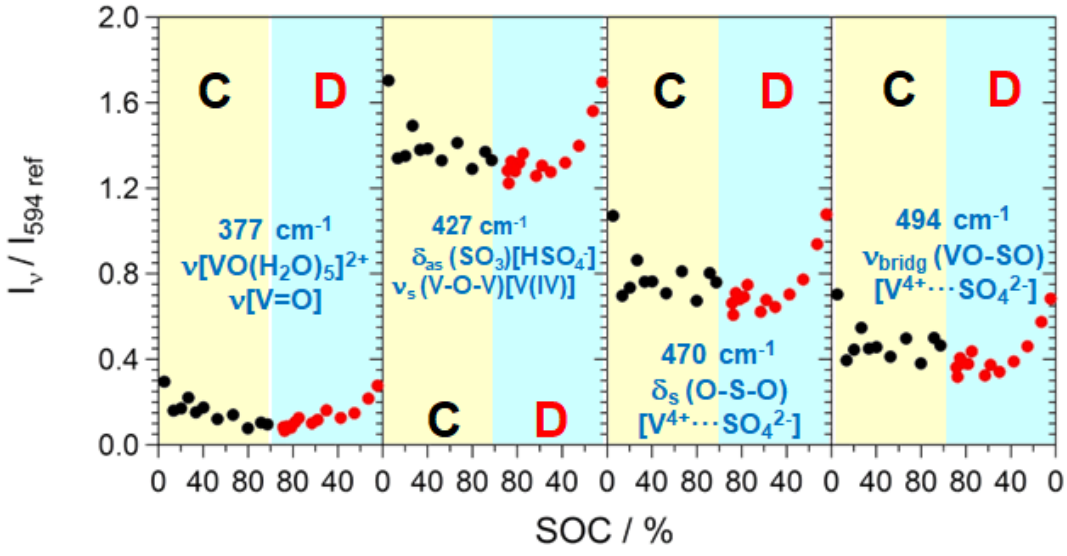

Figure 6.6 Raman Intensity ratio for three diagnostic peaks (377, 427, 470, 494 cm^{-1}) in the positive electrode. C = charge; D = discharge. The intensity ratio decrease as the SOC increases due to their attribution to V(IV) species.

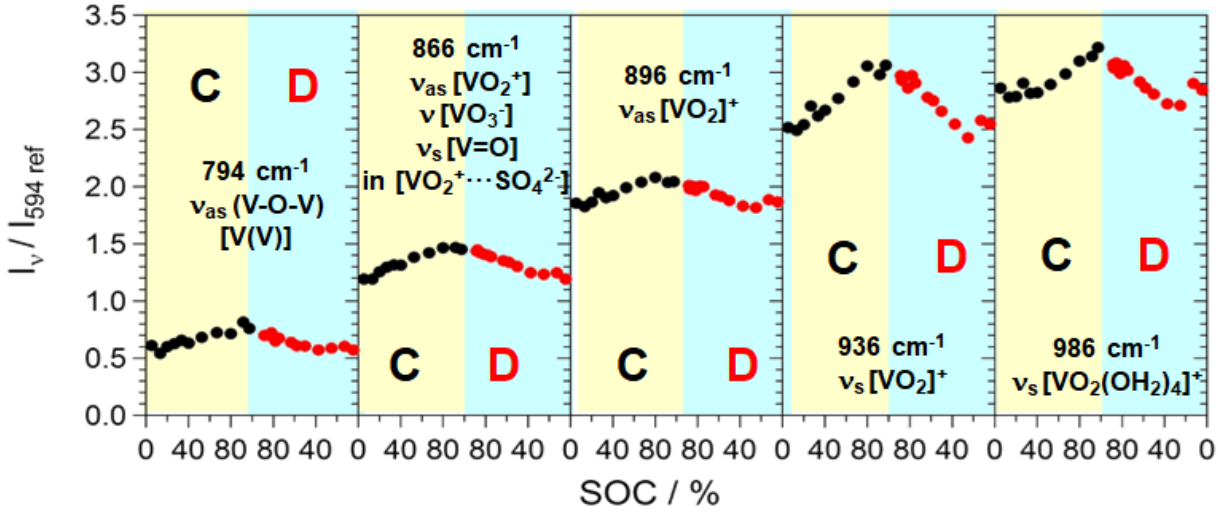

Figure 6.7 Raman Intensity ratio for three diagnostic peaks (794, 866, 896,936,986 cm^{-1}) in the positive electrode. C = charge; D = discharge. The intensity ratio increase as the SOC increases due to their attribution to V(V) species.

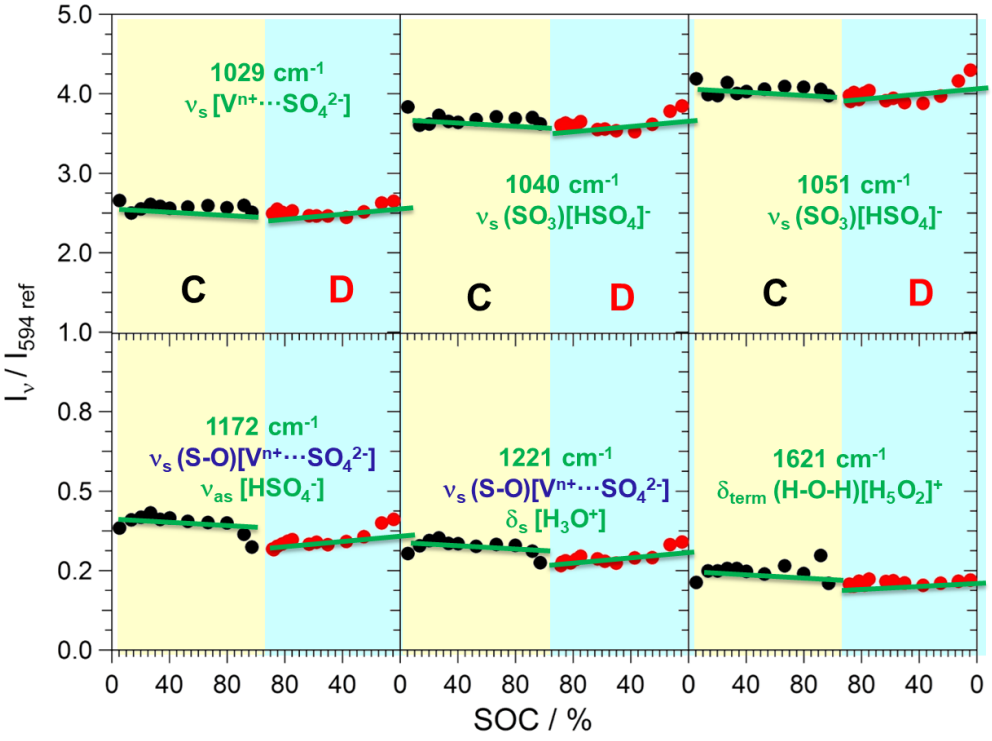

Figure 6.8 Raman Intensity ratio for three diagnostic peaks (1172, 1221 and 1621 cm^{-1}) in the positive electrode. C = charge; D = discharge. No significant changes of H_2SO_4 species on SOC% is revealed.

The ratio of Raman intensities of the V(IV) and V(V) species are significantly diagnostic in the positive electrolyte during charge and discharge process owning the coordination complexes (Figure 6.6, 6.7 and 6.8). This is likely due to presence of stable oxygenated coordination complexes of vanadium and of their strong interactions with HSO_4^- and SO_4^{2-} ligands. Indeed, some significant numbers of the equilibria between V(IV) and V(V) complexes exist in this electrode which play a crucial role in the modulation of the electrochemical performance of the VRFB.

Taken all together, charge and discharge processes are the result of a distribution of vanadium IV and V species which are well described by the Pourbaix equilibria [262] which are shown in the equations 6.4 to 6.6 for vanadium (IV) species and equations 6.7 to 6.10 for vanadium (V) species.

$$VO^{2+} + H_2O \Leftrightarrow HVO_2^{+} + H^{+} \quad (6.4)$$

$$2HVO_2^{+} + H_2O \Leftrightarrow HV_2O_5^{-} + 3H^{+} \quad (6.5)$$

$$2VO^{2+} + 3H_2O \Leftrightarrow HV_2O_5^{-} + 5H^{+} \quad (6.6)$$

$$VO_2^{+} + 2H_2O \Leftrightarrow H_2VO_4^{-} + 2H^{+} \quad (6.7)$$

$$H_3V_2O_7^{-} + H_2O \Leftrightarrow 2H_2VO_4^{-} + H^{+} \quad (6.8)$$

$$H_2VO_4^{-} \Leftrightarrow HVO_4^{2-} + H^{+} \quad (6.9)$$

$$HVO_4^{2-} \Leftrightarrow VO_4^{3-} + H^{+} \quad (6.10)$$

According to the equilibria, vanadium (IV) can create three species VO^{2+}, HVO_2^{+} and $HV_2O_5^{-}$ in the possible reaction and conformation. The equilibrium number 1, the VO^{2+} in the acid media forms a vanadyl(IV) hydroxide ion HVO_2^{+} , which can be the distorted octahedral coordination.

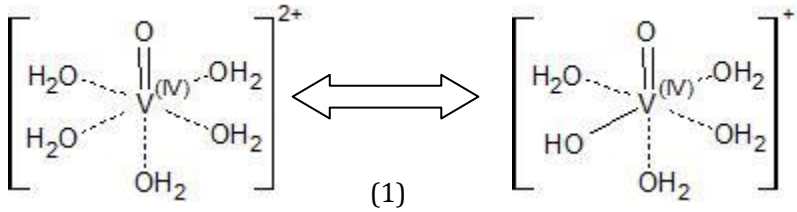

(1)

VO^{2+} - Oxovanadium (IV) HVO_2^{+} -Vanadyl(IV) hydroxide ion

(2)

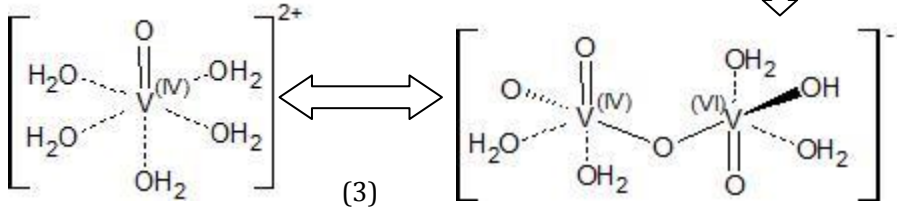

(3)

Oxovanadium (IV) $HV_2O_5^{-}$ - Divanadyl (IV) (oxido) hydroxide ion

Equilibrium number 2 can be proposed as a HVO_2^+ into $H_2VO_5^-$ ion with the coordination of square pyramidal.

Equilibria number 3 can be proposed as a oxovanadium (IV) forms also to divanadyl(IV)(oxido) hydroxide ion.

Whereas for vanadium (V) specises 5 equilibria take places. The results have indicated the existence of different vanadium monomeric as well dimeric species coordinated with sulfate ions in solution. This may explain the phenomenon that higher H_2SO_4 concentration can prevent precipitation of VO_2^+ions [52, 141] to V_2O_5 by forming sulfate complexes with VO_2^+ or the increase in stability could be achieved due todimerizationof VO_2^+ ions to $H_3V_2O_7^-$ specie.

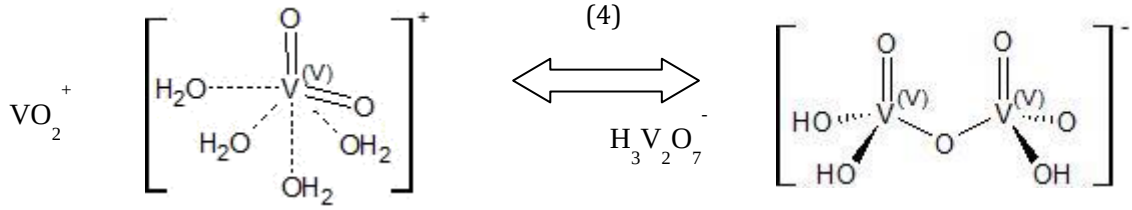

Dioxovanadium (V), vanadyl(V) ion [2, 3]

Trihydrogen «*pyro*»-vanadate ion [1]

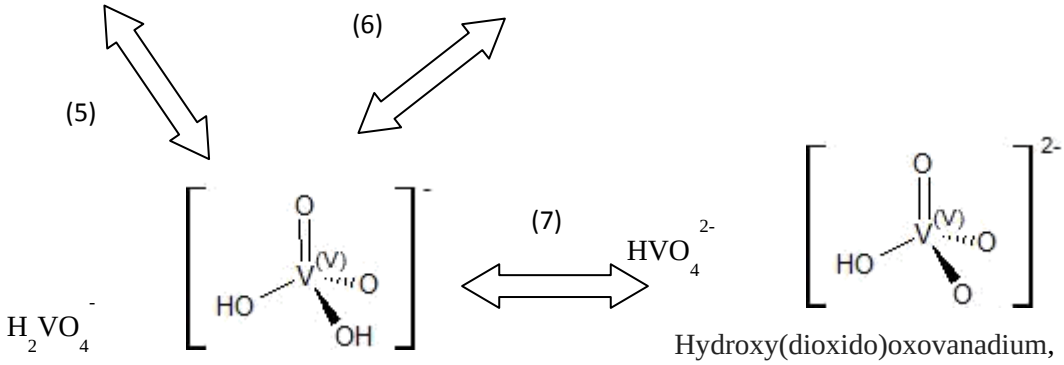

Dihydroxy(oxido)oxovanadium, dihydrogenvanadate ion

Hydroxy(dioxido)oxovanadium, hydrogenvanadate ion[1]

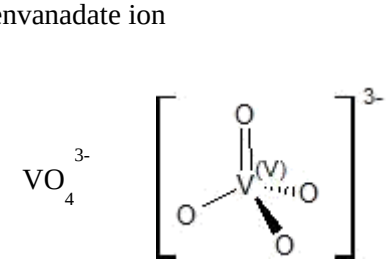

Trioxido(oxo)vanadium, orthovanadate ion[1]

Table 6.2 Raman band assignments of the positive electrolyte solution at different state of charge.

Peak pos.	SOC, %											Band assignments[b]	Ref.
1	377(vw)	377(vw)	377(vw)	377(vw)	377(vw)	377(vw)	377(vw)	377(vw)	377(vw)	377(vw)	377(vw)	ν $[VO(H_2O_5)]^{2+}$ ν [V=O]	[[263]]
2	427(m)	427(m)	427(m)	427(m)	427(m)	427(m)	427(m)	421(m)	421(m)	421(m)	421(m)	δ_{as} (SO_3) $[HSO_4]^-$ ν_s(V-O-V) [V(IV)]	[[141, 264]]
3	470(w)	470(w)	470(w)	470(w)	470(w)	470(w)	470(w)	470(w)	470 (w)	470(w)	470(w)	δ_s (O-S-O) $[V^{4+}\cdots SO_4^{2-}]$	[[264, 265]]
4	49 (vw)	494(vw)	494(vw)	494(vw)	494(vw)	494(vw)	494(vw)	494(vw)	494(vw)	494(vw)	494(vw)	ν_{bring}(VO–SO) $[V^{4+}\cdots SO_4^{2-}]$	[[141]]
5	594(m)	594(m)	594(m)	594(m)	594(m)	594(m)	594(m)	594(m)	594(m)	594(m)	594(m)	ν_s (SO_3) $[HSO_4]^-$	[[141, 266]]
6	794(w)	794(w)	794(w)	794(w)	794(w)	794(w)	794(w)	794(w)	794(w)	794(w)	794(w)	ν_{as} (V-O-V) [V(V)]	[[263, 266, 267]]
7	866(vw)	866(vw)	866(vw)	866(vw)	866(vw)	866(vw)	866(vw)	866(vw)	866(vw)	866(vw)	866(vw)	ν_{as} $[VO_2^+]$ + ν$[VO_3^-]$, ν_s [V=O]in $[V^+\cdots SO_4^{2-}]$	[[141, 264, 268]]
8	896(m)	896(m)	896(m)	896(m)	896(m)	896(m)	896(m)	896(m)	896(m)	896(m)	896(m)	ν_{as} $[VO_2^+]$	[[264, 266]]
9	936(m)	936(m)	936(m)	936(m)	936(m)	936(m)	936(m)	936(m)	936(m)	936(m)	936(m)	ν_s $[VO_2^+]$	[[141, 266, 269]]
10	986(s)	986(s)	986(s)	986(s)	986(s)	986(s)	986(s)	986(s)	986(s)	986(s)	986(s)	ν_s $[VO_2(OH_2)_4]^+$	[[141, 265, 269]]
11	1029(m)	1029(m)	1029(m)	1029(m)	1029(m)	1029(m)	1029(m)	1029(m)	1029(m)	1029(m)	1029(m)	ν_s $[V^{n+}\cdots SO_4^{2-}]$	[[264]]
12	1040(w)	1040(w)	1040(w)	1040(w)	1040(w)	1040(w)	1040(w)	1040(w)	1040(w)	1040(w)	1040(w)	ν_s (SO_3) $[HSO_4]^-$	[[264]]
13	1051(vs)	1051(vs)	1051(vs)	1051(vs)	1051(vs)	1051(vs)	1051(vs)	1051(vs)	1051(vs)	1051(vs)	1051(vs)	ν_s (SO_3) $[HSO_4]^-$	[[265]]
14	1172(vw)	1172(vw)	1172(vw)	1172(vw)	1172(vw)	1172(vw)	1172(vw)	1172(vw)	1172(vw)	1172(vw)	1172(vw)	ν_s (S-O) $[V^{n+}\ldots SO_4^{2-}]$ ν_{as} $[HSO_4]^-$	[[263, 266, 268]]
15	1221(vw)	1221(vw)	1221(vw)	1221(vw)	1221(vw)	1221(vw)	1221(vw)	1221(vw)	1221(vw)	1221(vw)	1221(vw)	ν_s (S-O) $[V^{n+}\ldots SO_4^{2-}]$ δ_s $[H_3O]^+$	[[141, 268]]
16	1621(vw)	1621(vw)	1621(vw)	1621(vw)	1621(vw)	1621(vw)	1621(vw)	1621(vw)	1621(vw)	1621(vw)	1621(vw)	δ_{term} (H-O-H) $[H_5O_2]^+$	[[270]]

[a] vs = very strong, s = strong, m = medium, w = weak, vw = very weak; [b] ν = stretching, δ = bending, as = antisymmetrical, s = symmetrical, n^+ = 4 or 5.

Table 6.3 Raman band assignments of the solution contained into the positive electrolyte at different depth of discharge.

	DOD, %														
Peak pos.														**Band assignments[b]**	Ref.
1	377 (vw)	377 (vw)	377(vw)	377 (vw)	377 (vw)	377 (vw)	377 (vw)	377(vw)	377 (vw)	377 (vw)	377 (vw)	377 (vw)	377(vw)	ν $[VO(H_2O_5)]^{2+}$ ν [V=O]	[[263]]
2	427 (m)	427 (m)	427 (m)	427 (m)	427 (m)	427 (m)	427 (m)	421 (m)	421 (m)	421 (m)	421 (m)	427 (m)	427 (m)	δ_{as} (SO_3) $[HSO_4]^-$ ν_s(V-O-V) [V(IV)]	[[141, 264]]
3	470 (w)	470 (w)	470 (w)	470 (w)	470 (w)	470 (w)	470 (w)	470 (w)	470 (w)	470 (w)	470 (w)	470 (w)	470 (w)	δ_s (O-S-O) $[V^{4+}\cdots SO_4^{2-}]$	[[264, 265]]
4	494 (vw)	494 (vw)	494(vw)	494 (vw)	494 (vw)	494 (vw)	494 (vw)	494 (vw)	494 (vw)	494 (vw)	494 (vw)	494 (vw)	494 (vw)	ν_{bring}(VO–SO) $[V^{4+}\cdots SO_4^{2-}]$	[[141]]
5	594(m)	594(m)	594(m)	594(m)	594(m)	594(m)	594(m)	594(m)	594(m)	594(m)	594(m)	594(m)	594(m)	ν_s (SO_3) $[HSO_4]^-$	[[141, 266]]
6	794(w)	794(w)	794(w)	794(w)	794(w)	794(w)	794(w)	794(w)	794(w)	794(w)	794(w)	794(w)	794(w)	ν_{as} (V-O-V) [V(V)]	[[263, 266, 267]]
7	866(vw)	866(vw)	866(vw)	866(vw)	866(vw)	866(vw)	866(vw)	866(vw)	866(vw)	866(vw)	866(vw)	866(vw)	866(vw)	ν_{as} $[VO_2^+]$ + ν$[VO_3^-]$, ν_s [V=O]in $[V^+\cdots SO_4^{2-}]$	[[141, 264, 268]]
8	896(m)	896(m)	896(m)	896(m)	896(m)	896(m)	896(m)	896(m)	896(m)	896(m)	896(m)	896(m)	896(m)	ν_{as} $[VO_2^+]$	[[264, 266]]
9	936(m)	936(m)	936(m)	936(m)	936(m)	936(m)	936(m)	936(m)	936(m)	936(m)	936(m)	936(m)	936(m)	ν_s $[VO_2^+]$	[[141, 266]]
10	986(s)	986(s)	986(s)	986(s)	986(s)	986(s)	986(s)	986(s)	986(s)	986(s)	986(s)	986(s)	986(s)	ν_s $[VO_2(OH_2)_4]^+$	[[141, 265, 269]]
11	1029(m)	1029(m)	1029(m)	1029(m)	1029(m)	1029(m)	1029(m)	1029(m)	1029(m)	1029(m)	1029(m)	1029(m)	1029(m)	ν_s $[V^{n+}\cdots SO_4^{2-}]$	[[268]]
12	1040(w)	1040(w)	1040(w)	1040(w)	1040(w)	1040(w)	1040(w)	1040(w)	1040(w)	1040(w)	1040(w)	1040(w)	1040(w)	ν_s (SO_3) $[HSO_4]^-$	[[268]]
13	1051(vs)	1051(vs)	1051(vs)	1051(vs)	1051(vs)	1051(vs)	1051(vs)	1051(vs)	1051(vs)	1051(vs)	1051(vs)	1051(vs)	1051(vs)	ν_s (SO_3) $[HSO_4]^-$	[[265]]
14	1172(vw)	1172(vw)	1172(vw)	1172(vw)	1172(vw)	1172(vw)	1172(vw)	1172(vw)	1172(vw)	1172(vw)	1172(vw)	1172(vw)	1172(vw)	ν_s (S-O) $[V^{n+}\ldots SO_4^{2-}]$ ν_{as} $[HSO_4]^-$	[[263, 266, 268]]
15	1221(vw)	1221(vw)	1221(vw)	1221(vw)	1221(vw)	1221(vw)	1221(vw)	1221(vw)	1221(vw)	1221(vw)	1221(vw)	1221(vw)	1221(vw)	ν_s (S-O) $[V^{n+}\ldots SO_4^{2-}]$ δ_s $[H_3O]^+$	[[141]]
16	1621(vw)	1621(vw)	1621(vw)	1621(vw)	1621(vw)	1621(vw)	1621(vw)	1621(vw)	1621(vw)	1621(vw)	1621(vw)	1621(vw)	1621(vw)	δ_{term} (H-O-H) $[H_5O_2]^+$	[[270]]

6.4 Conclusion

Raman spectra were recorded, for V(IV)/V(V) redox couples, as a function of state of charge (SOC) and depth of discharge (DOD). A deep analysis of Raman spectra was shown for positive reactions. Changes in complexation, involving VO^{2+}/VO_2^+ with HSO_4^- and SO_4^{2-} species, are put in evidence. These changes are due to presence of stable oxygenated coordination V-complexes and to their strong interactions with HSO_4^- and SO_4^{2-} ligands. Taken all together, charge and discharge processes are the result of a distribution of vanadium IV and V species which are well described by the Pourbaix equlibria and Red-Ox processes. This study allows to identify unequivocally the presence of dimers in the VRFB feeds. In detail, the main outcome of the spectroscopic experiments is the catholyte includes a variety of vanadium species beyond VO^{2+} and VO_2^+, including dimers such as $HV_2O_5^-$ (V(IV)) and $H_3V_2O_7^-$ (V(V)). The impact of these additional vanadium species may be accounted for to rationalize the charge/discharge behavior of VRFBs.

From the spectra, it is clearly to find that Vanadium (IV) decreases with increasing SOC, and is converted to Vanadium (V). Based on the decomposition of Raman spectra, 16 peaks were fixed correspond to all species in the catholyte during VRFB operation. Among them, 4 peaks are assigned to Vanadium (IV), whereas 5 peaks to Vanadium (V). Other peaks are correlated to sulphuric acid, water species, and possibly vanadium-sulfate complex.

Based on our result, it is evident that the dissolved variety of different ionic species in catholyte establish a complex series of equilibria. The concentrations of these ionic species are changed upon the charge/discharge processes (related to SOC), which may have important effects on the overall performance and durability of the system.

However, to establish the accurate peak position to specific Vanadium(IV) and Vanadium (V) species, other Raman and FTIR measurements may be taken based on varied concentration of sulfuric acid and vanadium. To build the library of the Raman and FTIR spectra may help to

create a model for simulation of the side reaction during the process. For the next step, the interplay between the performance of the VRFB cell, the state of charge (SOC), the concentration of intermediate chemical species may be further elucidated by means of a theoretical model describing the equilibria equations identified by confocal micro-Raman spectroscopy (combining mass balance, charge balance) and current-voltage relationships.

Chapter VII Conclusion

The research activity carried out over the course of the PhD activity focused on the synthesis and characterization of new hybrid inorganic-organic proton-conducting membranes as alternatives to classic perfluorinated polymers, such as Nafion, for application in VRFBs.

Two types of hybrid inorganic-organic proton-conducting membrane materials were synthesized for different applications:

1) Nafion was doped with WO_3nanofiller in order to improve the ion selectivity by reducing vanadium crossover while maintaining at the same time the high proton conductivity. The good proton conductivity of [Nafion/(WO_3)]$_x$ membranes, which is comparable to the Nafion 212 benchmark, can be expected to apply on VRFB at both low and high current density values (*i.e.*, from 20 to 200 mA cm^{-2}).
2) SPEEK membrane with optimized degree of sulfonation (DS) was used as an alternative low-cost membrane to perfluorinated polymers. SPEEK was doped with WO_3 to reduce the vanadium crossover. The obtained [SPEEK/(WO_3)]$_x$ membranes possess slightly lower proton conductivity in comparison with Nafion membranes. However, they demonstrate extremely high ion selectivity due to their low vanadium permeability. This family of membranes may be applied to VRFB systems operating at medium and low current density range (below 100 mA cm^{-2}), due to their medium proton conductivity may not be suitable to achieve electrical balance at extremely high current densities (150-200 mA cm^{-2}).

In Chapter 3, the preparation, physicochemical and the electrochemical characterization of two hybrid membranes consisting of WO_3 nanoparticles dispersed in a Nafion matrix is reported. The hybrid membranes are prepared by a solvent-casting procedure. Based on the results of TGA measurements, the introduction of WO_3 nanoparticles does not alter significantly the thermal degradation events of the Nafion host and the hybrid membranes maintain the same very good thermal stability as pristine Nafion. On the other hand, MDSC

reveals that in [Nafion/$(WO_3)_{0.024}$] the endothermic events associated to the Nafion PTFE domains are shifted to higher temperatures by *ca.* 10-20°C. This evidence is attributed to the formation of *"dynamic crosslinks"* between the WO_3 nanoparticles and the Nafion host, that stabilize the hybrid membrane. The incorporation of nanofiller also affects the conformation of the PTFE backbone chains of the Nafion host, inhibiting the $15_7 \rightarrow 10_3$ conformational transition as revealed by ATR-FTIR spectroscopy, which is influenced by the water plasticization effect.

The hydrophilic domains of the Nafion host are reduced in size as the content of WO_3 is raised. The water uptake of hybrid membranes decreases with the increasing loading of WO_3 nanofillers; as a consequence, the pathways of charge migration become more tortuous, slightly reducing the conductivity at 30°C from $3.64 \cdot 10^{-2}$ S·cm^{-1} for recast Nafion to $2.45 \cdot 10^{-2}$ S·cm^{-1} for [Nafion/$(WO_3)_{0.329}$]. At temperature more than 30°C, the ion conduction is taking place through a mechanism involving "delocalization bodies" (DBs). A DB corresponds to a portion of the material where the protons are able to move so fast as to be considered delocalized; the long-range charge transfer occurs as different DBs come into contact with one another. In fully-hydrated Nafion-based systems the DBs typically correspond to the water-swollen hydrophilic domains. In this interpretation framework, a high conductivity is achieved in the presence of large hydrophilic domains swollen with liquid water that can easily come into contact with one another, such as in the case of recast Nafion.

On the other side, the higher charge migration tortuosity expected for the proposed hybrid membranes would correspond to a dramatically lower permeability to vanadium species. The tortuosity for protons is likely much less than that for vanadium, as the vanadium ions are likely only staying in bulk water, while the protons are also delocalized at the Nafion-nanofiller interfaces in the presence of water (interface water) [215]. The vanadium permeability result of recast Nafion to VO^{2+} is $55.8 \cdot 10^{-7}$cm^2·min^{-1}, more than twice larger than the permeability of [Nafion/$(WO_3)_{0.329}$] (measured at $23.1 \cdot 10^{-7}$ cm^2·min^{-1}). As a result, the ion selectivity of hybrid membranes (up to $10.6 \cdot 10^3$ S·min·cm^{-3} for [Nafion/$(WO_3)_{0.329}$]) is much

improved in comparison with recast Nafion ($6.5 \cdot 10^3$ S·min·cm^{-3}) as benchmark. Finally, the introduction of WO_3 nanofiller into Nafion matrix improves the long-term dimensional stability of the hybrid membranes under conditions mimicking those found in VRFBs during operation as well. High dimensional stability indicates the high chemical stability (membrane is not chemically degraded) or low swelling ratio, which is beneficial to VRFB operation. Therefore, the new family of [Nafion/$(WO_3)_x$] hybrid membranes may be promising candidates for application as IEMs in VRFBs.

In Chapter 4, the [Nafion/$(WO_3)_x$] hybrid inorganic-organic membranes are further characterized by SEM for morphology study. The hybrid membranes reveal a unique morphology, where: (i) most of the membrane consists of a Nafion matrix with homogeneously dispersed WO_3 filler; and (ii) on one side of the membrane a WO_3-rich layer is formed. This morphology may play a crucial role to limit the crossover of vanadium species, that is significantly reduced in comparison with pristine Nafion. The lowest vanadium crossover is detected for the [Nafion/$(WO_3)_{0.587}$] membrane, that comprises 20 wt% of WO_3. As a result, the VRFB mounting the optimized [Nafion/$(WO_3)_{0.587}$] hybrid membrane exhibits a coulombic efficiency of 93%, 5% higher in comparison with the Nafion 212 reference. The reduced permeation of vanadium species is also revealed by the lower discharge capacity decay and longer self-discharge times that, for the optimized [Nafion/$(WO_3)_{0.587}$] hybrid membrane, are respectively 1.5 times lower and 1.5 times longer than those revealed from the pristine Nafion 212 reference. In conclusion, the introduction of WO_3 nanoparticles into a Nafion matrix allows to obtain [Nafion/$(WO_3)_x$] hybrid inorganic-organic membranes that:

(i) are able to address several issues affecting the pristine Nafion IEM, with a particular reference to high vanadium permeability;

(ii) yield improved results in single-cell VRFB tests; and, accordingly;

(iii) are highly promising for practical VRFB applications.

Chapter 5 reports the preparation, the physicochemical properties and the VRFB single cell cycling performance of hybrid membranes consisting of WO_3 nanoparticles dispersed in a cost-effective SPEEK matrix (20 \$/m^2,which is 25 times lower than the cost of Nafion membrane). The hybrid membranes are prepared by solvent-casting method as well. In the hybrid membranes, the introduction of WO_3 nanoparticles does not alter significantly the thermal degradation events of the SPEEK host and the hybrid membranes maintain very good thermal stability. With the increase of WO_3 nanofiller mass ratio, the volumetric density of dynamic crosslinks between WO_3 and SPEEK would be stronger and the hydrophilic domains formed by -SO_3H groups would be smaller, which would further restrain the water absorption of hybrid membrane and makes the membrane more difficult to swell. Such dynamic crosslinks stabilize the system and inhibit the swelling of the hydrophilic domains of the SPEEK hostand reduce WU%. The newly formed bonds between WO_3 and the SPEEK host have a strong impact on the structure of the hybrid membranes at the mesoscale. Accordingly, the higher charge migration tortuosity expected for the proposed hybrid membranes would correspond to a dramatically lower permeability to vanadium species, due to the vanadium ions only transport through the bulk water and protons can also move toward interface water. Indeed, it is shown that the permeability of Nafion 212 to VO^{2+} is $55.8\cdot10^{-7}cm^2\cdot min^{-1}$, more than 20 times larger than the permeability of [SPEEK/$(WO_3)_{0.20}$] (measured at $1.9\cdot10^{-7}$ $cm^2\cdot min^{-1}$). As a result, the ion selectivity of hybrid membranes (up to $2.1\cdot10^4$ $S\cdot min\cdot cm^{-3}$ for [SPEEK/$(WO_3)_{0.20}$]) is much improved in comparison with recast Nafion ($6.5\cdot10^3$ $S\cdot min\cdot cm^{-3}$). The VRFB single cell assembled with the composite membrane of [SPEEK /$(WO_3)_{0.20}$] exhibits higher coulombic efficiency (CE, 98.2%) and energy efficiency (EE, 71.8%) than that assembled with Nafion 212 as reference (CE 96.6% and EE 68.4%) at the current density of 80 mA cm^{-2}. Furthermore, the[SPEEK /$(WO_3)_{0.20}$] membrane maintains a stable performance during 30 cycles at the current density of 50 mA cm^{-2} and Nafion 212 is tested under the same condition as benchmark. [SPEEK/$(WO_3)_x$] hybrid membranes could be used as promising low-cost and high-performance membrane for VRFB application, owing to their good conductivity, remarkable ion selectivity and long-term stability in comparison to Nafion 212 as benchmark.

As it is well-known[125], there are hydrophilic domains (-SO_3H) and hydrophobic domains (backbone) inside Nafion and SPEEK membranes. Inside the membranes, some water typically locates very close to the interfaces between the hydrophilic and the hydrophobic domains. This kind of water is called interface water and can mainly transport protons [198, 245], but not vanadium species. The other type of water locates deeply into the hydrophilic domains and are able to migrate vanadium ions. This kind of water is named bulk water. It is reported that the water confined in SPEEK showed a lower amount of "bulk" water in comparison with Nafion [271]. The backbone of SPEEK was found to be more rigid and more hydrophobic than that of Nafion. These observations suggest that the phase segregation in SPEEK is less pronounced than that in Nafion, which may contribute to the diminished methanol crossover characteristics of SPEEK noted in experiments on direct methanol fuel cells (DMFC). Based on the Nafion and SPEEK based hybrid membranes, it may be concluded that the incorporation of WO_3 nanofillerleads to the formation of hydrogen bonds and dynamic crosslinks, that break the hydrophilic domains and therefore reduce the amount of bulk water which locates inside the hydrophilic domains. The lower amount of bulk water may be the critical issue to reduce the vanadium permeability significantly, while the amount of interface water may further increase. For the future work, we may use FT-IR ATR absorption spectra to focus more on the content change of bulk water [198, 245] and interface water to further explain the related mechanism of vanadium permeability reduction in hybrid membranes.

It is also observed that, in order to reach a higher ion selectivity and lower vanadium permeability based on inorganic-organic hybrid membranes, reducing the water uptake and IEC is a viable approach. This target may be reached through polymer blending method as well [272, 273]. However, compared with polymer blending approach, the proton conductivity of inorganic-organic hybrid membranes is not significantly reduced, thus they show considerable superiority for VRFB application [221, 242]. It is reported that SPEEK/mesoporous silica 10% hybrid membrane possesses proton conductivity 10 mS cm^{-1}, which is comparable to pristine SPEEK (DS=74%) with proton conductivity 11.3 mS cm^{-1}

[221]. While for SPEEK/PVDF 10% blend membranes the proton conductivity drops to 7 mS cm^{-1} by the work from the same group [242].

In summary, the membranes characterization presented in this work follows a general approach which involved the study of the materials' thermal, electrical and structural properties obtained from different measurement techniques (TGA, MDSC, BES, FT-IR, Raman etc.). In detail, the thermal properties of hybrid membranes are probed both by HR-TGA and by MDSC to study the thermal stability and endothermic transitions of the hybrid membranes. Vibrational spectroscopy studies are carried out by ATR-FTIR and Raman spectroscopy, to elucidate the secondary structure of hybrid membranes and study the interactions taking place between the nanofiller and the polymer matrix. The electrical response of hybrid membranes is determined by BES in order to determine the ionic conductivity (in this work mainly proton conductivity) and the permeability towards VO^{2+} is measured by UV-VIS spectrometry. A structural model and the related conductivity mechanism for the hybrid membranes are proposed, in order to rationalize the experimental results and correlate the electrical response with the transport properties. The ion exchange capacity (IEC) and the water uptake (WU) of each hybrid membrane are determined, in order to investigate the influence of nanofiller on hydrophilic domains of the polymer matrix. At the final step, ex-situ chemical stability test is measured for dimensional stability and to evaluate the degradation issue in the simulated operating environment.

By correlating the results of these experiments, it is possible to highlight the interactions between the different components present within the membranes. All the investigated materials consist of a combination of hydrophobic and hydrophilic domains, whose interactions can be modulated with the introduction of inorganic nanofillers. The hydrophobic polymer matrix provides the material high thermal and mechanical stability, while the hydrophilic domains are responsible for the membrane's proton conductivity. It seems the different types of water existed in the membranes plays an important role in reducing the vanadium permeability, namely bulk water and interface water. The vanadium

ions may likely migrate easily only through the 'bulk' water, while protons are able to passing through the 'interface' water as well. The incorporation of WO_3 nanofiller leads to the formation of hydrogen bonds and dynamic crosslinks may break the hydrophilic domains and therefore reduce the amount of bulk water, which is located inside the hydrophilic domains. The lower amount of bulk water may be the critical issue to reduce the vanadium permeability significantly. Therefore, the transport of vanadium ions is more hindered than that of protons. It should be noted that the bulk water inside SPEEK is lower than Nafion, and also the acidity of SPEEK is much lower than Nafion, which makes difference between the two membranes. Although the water content and microstructure of the materials are also important, a major contributor to the higher conductivity of Nafion is due to its greater acidity and its effect on effective ion density. Altogether, the interactions between the different domains govern the membranes' macroscopic properties that need to be improved in order to optimize and predict the behavior of these materials under operating conditions in VRFB system.

The membrane materials prepared and studied in this Ph.D. project are summarized in Table 7.1.

Table 7.1. Summary of the proposed proton exchange membranes for VRFB.

Membrane	Water Uptake / %	Ion Exchange Capacity ^{calculated} / mEq g^{-1}	Conductivity at 30 °C / S cm^{-1}	VO^{2+} Permeability / $cm^2 \cdot min^{-1}$	Selectivity/ $S \cdot min \cdot cm^{-3}$
Recast Nafion	18.0	0.92	$3.6 \cdot 10^{-2}$	$55.8 \cdot 10^{-7}$	$6.5 \cdot 10^{3}$
[Nafion/$(WO_3)_{0.329}$]	12.5	0.81	$2.5 \cdot 10^{-2}$	$23.1 \cdot 10^{-7}$	$1.1 \cdot 10^{4}$
[Nafion/$(WO_3)_{0.587}$]	9.3	0.74	$2.9 \cdot 10^{-2}$	$13.2 \cdot 10^{-7}$	$2.2 \cdot 10^{4}$
Recast SPEEK	35.1	1.73	$3.6 \cdot 10^{-3}$	$25.5 \cdot 10^{-7}$	$1.4 \cdot 10^{3}$
[SPEEK/$(WO_3)_{0.09}$]	32.6	1.63	$4.4 \cdot 10^{-3}$	$4.9 \cdot 10^{-7}$	$9.0 \cdot 10^{3}$
[SPEEK/$(WO_3)_{0.20}$]	30.2	1.52	$4.0 \cdot 10^{-3}$	$1.9 \cdot 10^{-7}$	$2.1 \cdot 10^{4}$

All the listed materials show good proton conductivity (>$3.6 \cdot 10^{-3}$ S/cm), which is sufficient for their use as IEM in VRFB system. In particular, the proton conductivity at VRFB increases in the order:

Recast SPEEK < [SPEEK/$(WO_3)_{0.20}$]<[SPEEK/$(WO_3)_{0.09}$] < [Nafion/$(WO_3)_{0.329}$] < [Nafion/$(WO_3)_{0.587}$] < Recast Nafion

The highest conductivity was obtained for the Recast Nafion membrane. However, [SPEEK/$(WO_3)_x$] membranes demonstrate slightly increasing proton conductivity compared to Recast SPEEK. The highest ion selectivity is observed from [Nafion/$(WO_3)_{0.587}$] and [SPEEK/$(WO_3)_{0.20}$]. The above mentioned 'ex-situ' features are coherent with the results obtained from single VRFB cell test, as shown in Figure 7.1.

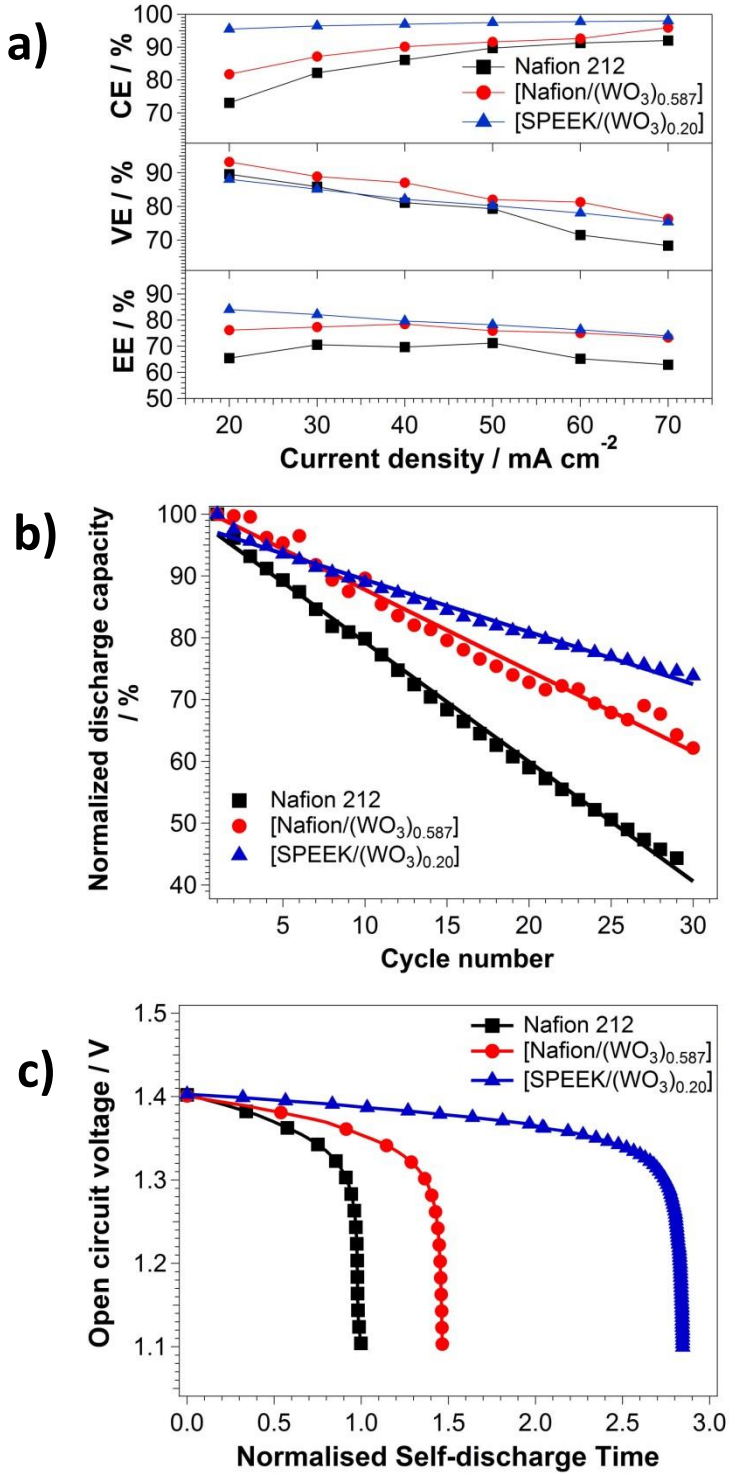

Figure 7.1 (a) Efficiencies VRFBs assembled with different membranes at a current density ranging from 20 to 70 mA cm^{-2}; (b) Normalized discharge capacity decay of single VRFB tested at 50 mA·cm^{-2}; (c) OCV curve of the VRFB, while the self-discharge time of Nafion 212 to reach 1.1 V is normalized to be 1.0.

The higher coulombic efficiencies, longer OCV self-discharge time and lower discharge capacity decay of hybrid membranes compared to Nafion 212 as benchmark are in accord with the lower vanadium permeability as measured by UV-vis spectra. While the very stable efficiencies and performance of VRFB with hybrid membranes operated at fixed current density, it is consistent with the relatively good chemical stability. If the degradation of the hybrid membrane occurs, the permeability of vanadium ions will gradually increase, which will lead to decreasing efficiencies and unstable performance during VRFB operation. Among them, [SPEEK/$(WO_3)_{0.20}$] demonstrates the highest CE and EE, thus indicating the best overall performance during the VRFB single cell test.

In conclusion, this work demonstrated that doping different IEMs with WO_3 nanofillers that can interact with the different components present within the composite material is an ideal solution to improve the ion selectivity of polymeric membranes, while maintaining good proton conductivity. With respect to the literature, the high ion selectivity (over $2.0 \cdot 10^4 S \cdot min \cdot cm^{-3}$) obtained from the [Nafion/$(WO_3)_{0.587}$] and [SPEEK/$(WO_3)_{0.20}$] is even higher as reported SPEEK/Graphene ($1.62 \cdot 10^4$ S·min·cm^{-3})[274] and Nafion/PTFE membrane ($1.3 \cdot 10^4$ S·min·cm^{-3}) [275].

To further improve the membranes, it may be an effective approach to combine the inorganic-organic hybrid membrane and polymer blending membranes preparation method together in order to obtain three-phase membrane (Polymer A/inorganic nanofiller/Polymer B). The inorganic nanofiller may contribute to maintain the good proton conductivity of composite membranes, which will be better than traditional polymer blending method. And since the sulfonated hydrocarbon polymer is still an interesting direction, to develop a easily sulfonated hydrocarbon membrane with more rigid and stable backbone will be vital to further substitute SPEEK based membranes, such as sulfonated poly(ether sulfone).

Finally, Raman spectra were recorded, for V(IV)/V(V) redox couples, as a function of state of charge (SOC) and depth of discharge (DOD). A deep analysis of Raman spectra was shown for positive reactions. Changes in complexation, involving VO^{2+}/VO_2^+ with HSO_4^- and SO_4^{2-} species, are put in evidence. These changes are due to presence of stable oxygenated coordination V-complexes and to their strong interactions with HSO_4^- and SO_4^{2-} ligands. Taken all together, charge and discharge processes are the result of a distribution of vanadium IV and V species which are well described by the Pourbaix equlibria and Red-Ox processes. This study allows to identify unequivocally the presence of dimers in the VRFB feeds. In detail, the main outcome of the spectroscopic experiments is the catholyte includes a variety of vanadium species beyond VO^{2+} and VO_2^+, including dimers such as $HV_2O_5^-$ (V(IV)) and $H_3V_2O_7^-$ (V(V)). The impact of these additional vanadium species may be accounted for to rationalize the charge/discharge behavior of VRFBs. Based on our result, it is evident that the dissolved variety of different ionic species in catholyte establish a complex series of equilibria. The concentrations of these ionic species are changed upon the charge/discharge processes (related to SOC), which may have important effects on the overall performance and durability of the system.

References

1. Greenwood, N.N. and A. Earnshaw, *Chemistry of the Elements, Butterworth-Heinemann, Oxford.* 1984: p. 1148.
2. Greenwood, N.N. and A. Earnshaw, *Chemistry of the Elements, Butterworth-Heinemann, Oxford.* 1984: p. 1144.
3. Krakowiak, J., D. Lundberg, and I. Persson, *A coordination chemistry study of hydrated and solvated cationic vanadium ions in oxidation states +III, +IV, and +V in solution and solid state.* Inorganic Chemistry, 2012. **51**(18): p. 9598-9609.
4. Dunn, B., H. Kamath, and J.M. Tarascon, *Electrical energy storage for the grid: A battery of choices.* Science, 2011. **334**(6058): p. 928-935.
5. Yang, Z., et al., *Electrochemical energy storage for green grid.* Chemical Reviews, 2011. **111**(5): p. 3577-3613.
6. Wang, W., et al., *Recent progress in redox flow battery research and development.* Advanced Functional Materials, 2013. **23**(8): p. 970-986.
7. Weber, A.Z., et al., *Redox flow batteries: A review.* Journal of Applied Electrochemistry, 2011. **41**(10): p. 1137-1164.
8. Skyllas-Kazacos, M., et al., *Progress in flow battery research and development.* Journal of the Electrochemical Society, 2011. **158**(8): p. R55-R79.
9. Lin, K., et al., *Alkaline quinone flow battery.* Science, 2015. **349**(6255): p. 1529-1532.
10. Winter, M. and R.J. Brodd, *What are batteries, fuel cells, and supercapacitors?* Chemical Reviews, 2004. **104**(10): p. 4245-4269.
11. Perry, M.L. and A.Z. Weber, *Advanced redox-flow batteries: A perspective.* Journal of the Electrochemical Society, 2016. **163**(1): p. A5064-A5067.
12. Zhang, H., et al., *Advanced charged membranes with highly symmetric spongy structures for vanadium flow battery application.* Energy and Environmental Science, 2013. **6**(3): p. 776-781.
13. Xu, Q. and T.S. Zhao, *Fundamental models for flow batteries.* Progress in Energy and Combustion Science, 2015. **49**: p. 40-58.
14. Soloveichik, G.L., *Battery technologies for large-scale stationary energy storage.* Annual Review of Chemical and Biomolecular Engineering, 2011. **2**: p. 503-527.
15. Zhou, X.L., et al., *Critical transport issues for improving the performance of aqueous redox flow batteries.* Journal of Power Sources, 2017. **339**: p. 1-12.
16. Wang, W.H. and X.D. Wang, *Investigation of Ir-modified carbon felt as the positive electrode of an all-vanadium redox flow battery.* Electrochimica Acta, 2007. **52**(24): p. 6755-6762.
17. Zeng, Y.K., et al., *A comparative study of all-vanadium and iron-chromium redox flow batteries for large-scale energy storage.* Journal of Power Sources, 2015. **300**: p. 438-443.

18. Mohammadi, T., S.C. Chieng, and M. Skyllas Kazacos, *Water transport study across commercial ion exchange membranes in the vanadium redox flow battery.* Journal of Membrane Science, 1997. **133**(2): p. 151-159.
19. Sun, C., et al., *Investigations on transfer of water and vanadium ions across Nafion membrane in an operating vanadium redox flow battery.* Journal of Power Sources, 2010. **195**(3): p. 890-897.
20. Teng, X., et al., *Nafion/organic silica modified TiO_2 composite membrane for vanadium redox flow battery via in situ sol–gel reactions.* Journal of Membrane Science, 2009. **341**(1): p. 149-154.
21. Zlotorowicz, A., et al., *The permselectivity and water transference number of ion exchange membranes in reverse electrodialysis.* Journal of Membrane Science, 2017. **523**: p. 402-408.
22. Sukkar, T. and M. Skyllas-Kazacos, *Modification of membranes using polyelectrolytes to improve water transfer properties in the vanadium redox battery.* Journal of Membrane Science, 2003. **222**(1): p. 249-264.
23. Thaller, L.H., *Electrically rechargeable redox flow cell*. 1976, Google Patents.
24. Skyllas-Kazacos, M., M. Kazacos, and R. McDermott, *Vanadium charging cell and vanadium dual battery system. Patent Appl. No*. 1988, PCT/AU88/00473, Dec.
25. Hodes, G., J. Manassen, and D. Cahen, *Electrocatalytic Electrodes for the Polysulfide Redox System.* Journal of the Electrochemical Society, 1980. **127**(3): p. 544-549.
26. Skyllas-Kazacos, M., *Novel vanadium chloride/polyhalide redox flow battery.* Journal of Power Sources, 2003. **124**(1): p. 299-302.
27. Zhang, L., et al., *Development of carbon coated membrane for zinc/bromine flow battery with high power density.* Journal of Power Sources, 2013. **227**: p. 41-47.
28. Brushett, F.R., J.T. Vaughey, and A.N. Jansen, *An all-organic non-aqueous lithium-ion redox flow battery.* Advanced Energy Materials, 2012. **2**(11): p. 1390-1396.
29. Leung, P., et al., *Progress in redox flow batteries, remaining challenges and their applications in energy storage.* RSC Advances, 2012. **2**(27): p. 10125-10156.
30. Larcher, D. and J.M. Tarascon, *Towards greener and more sustainable batteries for electrical energy storage.* Nature Chemistry, 2015. **7**(1): p. 19-29.
31. Chakrabarti, M.H., R.A.W. Dryfe, and E.P.L. Roberts, *Evaluation of electrolytes for redox flow battery applications.* Electrochimica Acta, 2007. **52**(5): p. 2189-2195.
32. Ponce de León, C., et al., *Redox flow cells for energy conversion.* Journal of Power Sources, 2006. **160**(1): p. 716-732.
33. Wang, W., et al., *A new redox flow battery using Fe/V redox couples in chloride supporting electrolyte.* Energy and Environmental Science, 2011. **4**(10): p. 4068-4073.
34. Green, M.A., et al., *New All-Vanadium Redox Flow Cell.* Journal of the Electrochemical Society, 1986. **133**(5): p. 1057-1058.
35. Sum, E., M. Rychcik, and M. Skyllas-kazacos, *Investigation of the V(V)/V(IV) system for use in the positive half-cell of a redox battery.* Journal of Power Sources, 1985. **16**(2): p. 85-95.
36. Skyllas-Kazacos, M., et al., *Characteristics and performance of 1 kW UNSW vanadium redox battery.* Journal of Power Sources, 1991. **35**(4): p. 399-404.
37. Zhao, P., et al., *Characteristics and performance of 10kW class all-vanadium redox-flow battery stack.* Journal of Power Sources, 2006. **162**(2): p. 1416-1420.

38. Kim, S., et al., *1 kW/1 kWh advanced vanadium redox flow battery utilizing mixed acid electrolytes.* Journal of Power Sources, 2013. **237**: p. 300-309.
39. Tokuda, N., et al., *Development of a redox flow battery system.* SEI Technical Review, 2000(50): p. 88-94.
40. Skyllas-Kazacos, M., et al., *Recent advances with UNSW vanadium-based redox flow batteries.* International Journal of Energy Research, 2010. **34**(2): p. 182-189.
41. Kear, G., A.A. Shah, and F.C. Walsh, *Development of the all-vanadium redox flow battery for energy storage: A review of technological, Financial and policy aspects.* International Journal of Energy Research, 2012. **36**(11): p. 1105-1120.
42. Huang, K.-L., et al., *Research progress of vanadium redox flow battery for energy storage in China.* Renewable Energy, 2008. **33**(2): p. 186-192.
43. Wilson, E.J. and C.J. Geankoplis, *Liquid mass transfer at very low reynolds numbers in packed beds.* Industrial and Engineering Chemistry Fundamentals, 1966. **5**(1): p. 9-14.
44. Skyllas-Kozocos, M. and F. Grossmith, *Efficient Vanadium Redox Flow Cell.* Journal of the Electrochemical Society, 1987. **134**(12): p. 2950-2953.
45. Rychcik, M. and M. Skyllas-Kazacos, *Characteristics of a new all-vanadium redox flow battery.* Journal of Power Sources, 1988. **22**(1): p. 59-67.
46. Tang, Z., et al., *Composition and conductivity of membranes equilibrated with solutions of sulfuric acid and vanadyl sulfate.* Journal of the Electrochemical Society, 2013. **160**(9): p. F1040-F1047.
47. Lawton, J.S., A. Jones, and T. Zawodzinski, *Concentration dependence of VO2+ crossover of nafion for vanadium redox flow batteries.* Journal of the Electrochemical Society, 2013. **160**(4): p. A697-A702.
48. Aaron, D., et al., *Polarization curve analysis of all-vanadium redox flow batteries.* Journal of Applied Electrochemistry, 2011. **41**(10): p. 1175-1182.
49. Aaron, D.S., et al., *Dramatic performance gains in vanadium redox flow batteries through modified cell architecture.* Journal of Power Sources, 2012. **206**: p. 450-453.
50. Zhu, S.Q., et al., *Influence of flow channel structure and electrolyte flow state on the performance of VRB.* Battery, 2008. **38**: p. 285-287.
51. Liu, Q.H., et al., *High Performance Vanadium Redox Flow Batteries with Optimized Electrode Configuration and Membrane Selection.* Journal of the Electrochemical Society, 2012. **159**(8): p. A1246-A1252.
52. Rahman, F. and M. Skyllas-Kazacos, *Vanadium redox battery: Positive half-cell electrolyte studies.* Journal of Power Sources, 2009. **189**(2): p. 1212-1219.
53. Rahman, F. and M. Skyllas-Kazacos, *Solubility of vanadyl sulfate in concentrated sulfuric acid solutions.* Journal of Power Sources, 1998. **72**(2): p. 105-110.
54. Zhang, J., et al., *Effects of additives on the stability of electrolytes for all-vanadium redox flow batteries.* Journal of Applied Electrochemistry, 2011. **41**(10): p. 1215-1221.
55. Liang, X., et al., *Effect of l-glutamic acid on the positive electrolyte for all-vanadium redox flow battery.* Electrochimica Acta, 2013. **95**: p. 80-86.
56. Pezeshki, A.M., et al., *High performance electrodes in vanadium redox flow batteries through oxygen-enriched thermal activation.* Journal of Power Sources, 2015. **294**: p. 333-338.

57. Xi, J., et al., *Nafion/SiO<inf>2</inf>hybrid membrane for vanadium redox flow battery.* Journal of Power Sources, 2007. **166**(2): p. 531-536.
58. Li, X., et al., *Ion exchange membranes for vanadium redox flow battery (VRB) applications.* Energy and Environmental Science, 2011. **4**(4): p. 1147-1160.
59. Schwenzer, B., et al., *Membrane development for vanadium redox flow batteries.* ChemSusChem, 2011. **4**(10): p. 1388-1406.
60. Eckroad, S., *Vanadium redox flow batteries: an in-depth analysis.* Electric Power Research Institute, Palo Alto, CA, 2007. **1014836**.
61. Zhang, D., et al., *An integrally thin skinned asymmetric architecture design for advanced anion exchange membranes for vanadium flow batteries.* Journal of Materials Chemistry A, 2015. **3**(33): p. 16948-16952.
62. Jang, J.K., et al., *Highly proton conductive, dense polybenzimidazole membranes with low permeability to vanadium and enhanced H<inf>2</inf>SO<inf>4</inf>absorption capability for use in vanadium redox flow batteries.* Journal of Materials Chemistry A, 2016. **4**(37): p. 14342-14355.
63. Zhang, H., et al., *Silica modified nanofiltration membranes with improved selectivity for redox flow battery application.* Energy and Environmental Science, 2012. **5**(4): p. 6299-6303.
64. Lu, W., et al., *High-performance porous uncharged membranes for vanadium flow battery applications created by tuning cohesive and swelling forces.* Energy and Environmental Science, 2016. **9**(7): p. 2319-2325.
65. Parasuraman, A., et al., *Review of material research and development for vanadium redox flow battery applications.* Electrochimica Acta, 2013. **101**: p. 27-40.
66. Manahan, M.P., et al., *Carbon nanoporous layer for reaction location management and performance enhancement in all-vanadium redox flow batteries.* Journal of Power Sources, 2013. **222**: p. 498-502.
67. Rychcik, M. and M. Skyllas-Kazacos, *Evaluation of electrode materials for vanadium redox cell.* Journal of Power Sources, 1987. **19**(1): p. 45-54.
68. Qiu, G., et al., *Pore-scale analysis of effects of electrode morphology and electrolyte flow conditions on performance of vanadium redox flow batteries.* Journal of Power Sources, 2012. **219**: p. 223-234.
69. Chen, D., et al., *Optimized anion exchange membranes for vanadium redox flow batteries.* ACS Applied Materials and Interfaces, 2013. **5**(15): p. 7559-7566.
70. Kaneko, H., et al., *Vanadium redox reactions and carbon electrodes for vanadium redox flow battery.* Electrochimica Acta, 1991. **36**(7): p. 1191-1196.
71. Inoue, M., et al., *Carbon Fiber Electrode for Redox Flow Battery.* Journal of the Electrochemical Society, 1987. **134**(3): p. 756-757.
72. Sun, B. and M. Skyllas-Kazacos, *Chemical modification of graphite electrode materials for vanadium redox flow battery application-part II. Acid treatments.* Electrochimica Acta, 1992. **37**(13): p. 2459-2465.
73. Sun, B. and M. Skyllas-Kazacos, *Modification of graphite electrode materials for vanadium redox flow battery application-I. Thermal treatment.* Electrochimica Acta, 1992. **37**(7): p. 1253-1260.

74. Flox, C., et al., *Strategies for enhancing electrochemical activity of carbon-based electrodes for all-vanadium redox flow batteries.* Applied Energy, 2013. **109**: p. 344-351.
75. Zhang, W., et al., *Electrochemical activation of graphite felt electrode for VO 2+/VO2 + redox couple application.* Electrochimica Acta, 2013. **89**: p. 429-435.
76. Di Blasi, A., et al., *Investigation of several graphite-based electrodes for vanadium redox flow cell.* Journal of Power Sources, 2013. **227**: p. 15-23.
77. Flox, C., et al., *Thermo-chemical treatments based on NH3/O2 for improved graphite-based fiber electrodes in vanadium redox flow batteries.* Carbon, 2013. **60**: p. 280-288.
78. Jin, J., et al., *Identifying the active site in nitrogen-doped graphene for the VO2+/VO<inf>2</inf>+redox reaction.* ACS Nano, 2013. **7**(6): p. 4764-4773.
79. Kim, K.J., et al., *The effects of surface modification on carbon felt electrodes for use in vanadium redox flow batteries.* Materials Chemistry and Physics, 2011. **131**(1-2): p. 547-553.
80. Gao, C., et al., *Influence of Fenton's reagent treatment on electrochemical properties of graphite felt for all vanadium redox flow battery.* Electrochimica Acta, 2013. **88**: p. 193-202.
81. Li, W., J. Liu, and C. Yan, *Reduced graphene oxide with tunable C/O ratio and its activity towards vanadium redox pairs for an all vanadium redox flow battery.* Carbon, 2013. **55**: p. 313-320.
82. Sun, B. and M. Skyllas-Kazakos, *Chemical modification and electrochemical behaviour of graphite fibre in acidic vanadium solution.* Electrochimica Acta, 1991. **36**(3-4): p. 513-517.
83. Tsai, H.M., et al., *Preparation and electrochemical activities of iridium-decorated graphene as the electrode for all-vanadium redox flow batteries.* Electrochimica Acta, 2012. **77**: p. 232-236.
84. Chandrabose Raghu, S., et al., *Electrochemical behaviour of titanium/iridium(IV) oxide: Tantalum pentoxide and graphite for application in vanadium redox flow battery.* Journal of Power Sources, 2013. **238**: p. 103-108.
85. Yao, C., et al., *Carbon paper coated with supported tungsten trioxide as novel electrode for all-vanadium flow battery.* Journal of Power Sources, 2012. **218**: p. 455-461.
86. Yao, C., et al., *Cell architecture upswing based on catalyst coated membrane (CCM) for vanadium flow battery.* Journal of Power Sources, 2013. **237**: p. 19-25.
87. González, Z., et al., *Enhanced performance of a Bi-modified graphite felt as the positive electrode of a vanadium redox flow battery.* Electrochemistry Communications, 2011. **13**(12): p. 1379-1382.
88. Li, B., et al., *Bismuth nanoparticle decorating graphite felt as a high-performance electrode for an all-vanadium redox flow battery.* Nano Letters, 2013. **13**(3): p. 1330-1335.
89. Kim, K.J., et al., *Novel catalytic effects of Mn<inf>3</inf>O<inf>4</inf>for all vanadium redox flow batteries.* Chemical Communications, 2012. **48**(44): p. 5455-5457.
90. Flox, C., et al., *Active nano-CuPt3 electrocatalyst supported on graphene for enhancing reactions at the cathode in all-vanadium redox flow batteries.* Carbon, 2012. **50**(6): p. 2372-2374.
91. Prifti, H., et al., *Membranes for redox flow battery applications.* Membranes, 2012. **2**(2): p. 275-306.

92. Zawodzinski Jr, T.A., et al., *Water uptake by and transport through Nafion(R)117 membranes.* Journal of the Electrochemical Society, 1993. **140**(4): p. 1041-1047.
93. Hickner, M.A., *Water-mediated transport in ion-containing polymers.* Journal of Polymer Science, Part B: Polymer Physics, 2012. **50**(1): p. 9-20.
94. Du, H.Y., et al., *High performance of catalysts supported by directly grown PTFE-free micro-porous CNT layer in a proton exchange membrane fuel cell.* Journal of Materials Chemistry, 2011. **21**(8): p. 2512-2516.
95. Chaparro, A.M., et al., *Catalyst layers for proton exchange membrane fuel cells prepared by electrospray deposition on Nafion membrane.* Journal of Power Sources, 2011. **196**(9): p. 4200-4208.
96. Pei, P., et al., *Analysis on the PEM fuel cells after accelerated life experiment.* International Journal of Hydrogen Energy, 2010. **35**(7): p. 3147-3151.
97. Tang, A., J. Bao, and M. Skyllas-Kazacos, *Dynamic modelling of the effects of ion diffusion and side reactions on the capacity loss for vanadium redox flow battery.* Journal of Power Sources, 2011. **196**(24): p. 10737-10747.
98. Luo, Q., et al., *Capacity decay and remediation of nafion-based all-vanadium redox flow batteries.* ChemSusChem, 2013. **6**(2): p. 268-274.
99. Xie, G. and T. Okada, *Water Transport Behavior in Nafion 117 Membranes.* Journal of the Electrochemical Society, 1995. **142**(9): p. 3057-3062.
100. Chen, D., et al., *Composite blend polymer membranes with increased proton selectivity and lifetime for vanadium redox flow batteries.* Journal of Power Sources, 2013. **231**: p. 301-306.
101. Chen, D. and M.A. Hickner, *V5+degradation of sulfonated Radel membranes for vanadium redox flow batteries.* Physical Chemistry Chemical Physics, 2013. **15**(27): p. 11299-11305.
102. Kim, S., et al., *Chemical and mechanical degradation of sulfonated poly(sulfone) membranes in vanadium redox flow batteries.* Journal of Applied Electrochemistry, 2011. **41**(10): p. 1201-1213.
103. Kim, S., et al., *Cycling performance and efficiency of sulfonated poly(sulfone) membranes in vanadium redox flow batteries.* Electrochemistry Communications, 2010. **12**(11): p. 1650-1653.
104. Sukkar, T. and M. Skyllas-Kazacos, *Membrane stability studies for vanadium redox cell applications.* Journal of Applied Electrochemistry, 2004. **34**(2): p. 137-145.
105. Fujimoto, C., et al., *Vanadium redox flow battery efficiency and durability studies of sulfonated Diels Alder poly(phenylene)s.* Electrochemistry Communications, 2012. **20**: p. 48-51.
106. Chen, D., et al., *Directly fluorinated polyaromatic composite membranes for vanadium redox flow batteries.* Journal of Membrane Science, 2012. **415-416**: p. 139-144.
107. Teng, X., et al., *Nafion/organic silica modified TiO<inf>2</inf>composite membrane for vanadium redox flow battery via in situ sol-gel reactions.* Journal of Membrane Science, 2009. **341**(1-2): p. 149-154.
108. Luo, Q., et al., *Modification of Nafion membrane using interfacial polymerization for vanadium redox flow battery applications.* Journal of Membrane Science, 2008. **311**(1-2): p. 98-103.

109. Xing, D., et al., *Effect of amination agent on the properties of quaternized poly(phthalazinone ether sulfone) anion exchange membrane for vanadium redox flow battery application.* Journal of Membrane Science, 2010. **354**(1-2): p. 68-73.
110. Mauritz, K.A. and R.M. Warren, *Microstructural evolution of a silicon oxide phase in a perfluorosulfonic acid ionomer by an in situ sol-gel reaction. 1. Infrared spectroscopic studies.* Macromolecules, 1989. **22**(5): p. 1730-1734.
111. Xi, J., et al., *Nafion/SiO2 hybrid membrane for vanadium redox flow battery.* Journal of Power Sources, 2007. **166**(2): p. 531-536.
112. Wang, N., et al., *Nafion/TiO_2 hybrid membrane fabricated via hydrothermal method for vanadium redox battery.* Journal of Solid State Electrochemistry, 2012. **16**(4): p. 1577-1584.
113. Aziz, M.A. and S. Shanmugam, *Zirconium oxide nanotube–Nafion composite as high performance membrane for all vanadium redox flow battery.* Journal of Power Sources, 2017. **337**: p. 36-44.
114. Zlotorowicz, A., S. Sunde, and F. Seland, *Zirconium hydrogen phosphate as an additive in electrocatalytic layers for the oxygen evolution reaction in PEM water electrolysis.* International Journal of Hydrogen Energy, 2015. **40**(32): p. 9982-9988.
115. Teng, X., et al., *Nafion/organically modified silicate hybrids membrane for vanadium redox flow battery.* Journal of Power Sources, 2009. **189**(2): p. 1240-1246.
116. Xi, J., et al., *Self-assembled polyelectrolyte multilayer modified Nafion membrane with suppressed vanadium ion crossover for vanadium redox flow batteries.* Journal of Materials Chemistry, 2008. **18**(11): p. 1232-1238.
117. Zeng, J., et al., *Studies on polypyrrole modified nafion membrane for vanadium redox flow battery.* Electrochemistry Communications, 2008. **10**(3): p. 372-375.
118. Luo, Q., et al., *Preparation and characterization of Nafion/SPEEK layered composite membrane and its application in vanadium redox flow battery.* Journal of Membrane Science, 2008. **325**(2): p. 553-558.
119. Luo, X., et al., *Influences of Permeation of Vanadium Ions through PVDF-g-PSSA Membranes on Performances of Vanadium Redox Flow Batteries.* The Journal of Physical Chemistry B, 2005. **109**(43): p. 20310-20314.
120. Ma, J., et al., *Designing a new process to prepare amphoteric ion exchange membrane with well-distributed grafted chains for vanadium redox flow battery.* Journal of Membrane Science, 2012. **419-420**: p. 1-8.
121. Qiu, J., et al., *Preparation of ETFE-based anion exchange membrane to reduce permeability of vanadium ions in vanadium redox battery.* Journal of Membrane Science, 2007. **297**(1-2): p. 174-180.
122. Tian, B., C.W. Yan, and F.H. Wang, *Proton conducting composite membrane from Daramic/Nafion for vanadium redox flow battery.* Journal of Membrane Science, 2004. **234**(1-2): p. 51-54.
123. Ding, C., et al., *Vanadium flow battery for energy storage: Prospects and challenges.* Journal of Physical Chemistry Letters, 2013. **4**(8): p. 1281-1294.
124. Rikukawa, M. and K. Sanui, *Proton-conducting polymer electrolyte membranes based on hydrocarbon polymers.* Progress in Polymer Science (Oxford), 2000. **25**(10): p. 1463-1502.
125. Kreuer, K.D., *On the development of proton conducting polymer membranes for hydrogen and methanol fuel cells.* Journal of Membrane Science, 2001. **185**(1): p. 29-39.

126. Xing, P., et al., *Synthesis and characterization of sulfonated poly(ether ether ketone) for proton exchange membranes.* Journal of Membrane Science, 2004. **229**(1-2): p. 95-106.
127. Mai, Z., et al., *Sulfonated poly(tetramethydiphenyl ether ether ketone) membranes for vanadium redox flow battery application.* Journal of Power Sources, 2011. **196**(1): p. 482-487.
128. Wei, W., et al., *Poly(tetrafluoroethylene) reinforced sulfonated poly(ether ether ketone) membranes for vanadium redox flow battery application.* Journal of Power Sources, 2012. **208**: p. 421-425.
129. Jia, C., J. Liu, and C. Yan, *A multilayered membrane for vanadium redox flow battery.* Journal of Power Sources, 2012. **203**: p. 190-194.
130. Chen, D., et al., *Preparation and properties of sulfonated poly(fluorenyl ether ketone) membrane for vanadium redox flow battery application.* Journal of Power Sources, 2010. **195**(7): p. 2089-2095.
131. Chen, D., et al., *Sulfonated poly (fluorenyl ether ketone) membrane with embedded silica rich layer and enhanced proton selectivity for vanadium redox flow battery.* Journal of Power Sources, 2010. **195**(22): p. 7701-7708.
132. Chen, D., et al., *Synthesis and characterization of novel sulfonated poly(arylene thioether) ionomers for vanadium redox flow battery applications.* Energy and Environmental Science, 2010. **3**(5): p. 622-628.
133. Chen, D., et al., *Selective anion exchange membranes for high coulombic efficiency vanadium redox flow batteries.* Electrochemistry Communications, 2013. **26**(1): p. 37-40.
134. Hwang, G.J. and H. Ohya, *Crosslinking of anion exchange membrane by accelerated electron radiation as a separator for the all-vanadium redox flow battery.* Journal of Membrane Science, 1997. **132**(1): p. 55-61.
135. Jung, M.S.J., et al., *Polysulfone-based anion exchange membranes demonstrate excellent chemical stability and performance for the all-vanadium redox flow battery.* Journal of Materials Chemistry A, 2013. **1**(35): p. 10458-10464.
136. Zhang, S., et al., *Preparation of chloromethylated/quaternized poly(phthalazinone ether ketone) anion exchange membrane materials for vanadium redox flow battery applications.* Journal of Membrane Science, 2010. **363**(1-2): p. 243-249.
137. Zhang, B., et al., *Quaternized poly(phthalazinone ether ketone ketone) anion exchange membrane with low permeability of vanadium ions for vanadium redox flow battery application.* Journal of Power Sources, 2012. **217**: p. 296-302.
138. Wang, Y., et al., *Study on the chemical stability of the anion exchange membrane of grafting dimethylaminoethyl methacrylate.* Journal of Membrane Science, 2011. **376**(1-2): p. 70-77.
139. Qiu, J., et al., *Performance of vanadium redox flow battery with a novel amphoteric ion exchange membrane synthesized by two-step grafting method.* Journal of Membrane Science, 2009. **342**(1-2): p. 215-220.
140. Wen, Y., et al., *Investigation on the stability of electrolyte in vanadium flow batteries.* Electrochimica Acta, 2013. **96**: p. 268-273.
141. Kausar, N., R. Howe, and M. Skyllas-Kazacos, *Raman spectroscopy studies of concentrated vanadium redox battery positive electrolytes.* Journal of Applied Electrochemistry, 2001. **31**(12): p. 1327-1332.

142. Vijayakumar, M., et al., *Structure and stability of hexa-aqua V(III) cations in vanadium redox flow battery electrolytes.* Physical Chemistry Chemical Physics, 2012. **14**(29): p. 10233-10242.
143. Vijayakumar, M., et al., *Elucidating the higher stability of vanadium(V) cations in mixed acid based redox flow battery electrolytes.* Journal of Power Sources, 2013. **241**: p. 173-177.
144. Vijayakumar, M., et al., *Towards understanding the poor thermal stability of V5+electrolyte solution in Vanadium Redox Flow Batteries.* Journal of Power Sources, 2011. **196**(7): p. 3669-3672.
145. Vijayakumar, M., et al., *Nuclear magnetic resonance studies on vanadium(IV) electrolyte solutions for vanadium redox flow battery.* Journal of Power Sources, 2010. **195**(22): p. 7709-7717.
146. Wu, X., et al., *Influence of organic additives on electrochemical properties of the positive electrolyte for all-vanadium redox flow battery.* Electrochimica Acta, 2012. **78**: p. 475-482.
147. He, Z., et al., *Effects of organic additives containing-NH<inf>2</inf>and-SO<inf>3</inf>H on electrochemical properties of vanadium redox flow battery.* Electrochimica Acta, 2013. **106**: p. 556-562.
148. Chang, F., et al., *Coulter dispersant as positive electrolyte additive for the vanadium redox flow battery.* Electrochimica Acta, 2012. **60**: p. 334-338.
149. Jia, Z., et al., *Effect of polyhydroxy-alcohol on the electrochemical behavior of the positive electrolyte for vanadium redox flow batteries.* Journal of the Electrochemical Society, 2012. **159**(6): p. A843-A847.
150. Liyu Li, et al., *A Stable Vanadium Redox‐Flow Battery with High Energy Density for Large‐Scale Energy Storage.* Adv. Energy Mater., 2001. **1**: p. 394-400.
151. Jia, C., J. Liu, and C. Yan, *A significantly improved membrane for vanadium redox flow battery.* Journal of Power Sources, 2010. **195**(13): p. 4380-4383.
152. Sun, C.-N., et al., *Evaluation of Diels–Alder poly(phenylene) anion exchange membranes in all-vanadium redox flow batteries.* Electrochemistry Communications, 2014. **43**: p. 63-66.
153. Thayumanasundaram, S., et al., *Hybrid inorganic–organic proton conducting membranes based on Nafion, SiO_2 and triethylammonium trifluoromethanesulfonate ionic liquid.* Electrochimica Acta, 2010. **55**(4): p. 1355-1365.
154. Di Noto, V., et al., *Hybrid inorganic–organic proton conducting membranes based on Nafion and 5 wt% of M_xO_y (M= Ti, Zr, Hf, Ta and W). Part II: Relaxation phenomena and conductivity mechanism.* Journal of Power Sources, 2009. **187**(1): p. 57-66.
155. Di Noto, V., et al., *Hybrid inorganic–organic proton conducting membranes based on Nafion and 5 wt.% of M_xO_y (M= Ti, Zr, Hf, Ta and W): Part I. Synthesis, properties and vibrational studies.* Electrochimica Acta, 2007. **53**(4): p. 1618-1627.
156. Mu, D., et al., *Rice Paper Reinforced Sulfonated Poly(ether ether ketone) as Low-Cost Membrane for Vanadium Flow Batteries.* ACS Sustainable Chemistry and Engineering, 2017. **5**(3): p. 2437-2444.
157. Bower, N.W., *Principles of Instrumental Analysis. 4th edition (Skoog, D. A.; Leary, J. J.).* Journal of Chemical Education, 1992. **69**(8): p. A224.
158. manual, D.d.s.c.o.s., *© 1997, 1998 by TA Instruments, 109 Lukens Drive, New Castle, DE 19720.*
159. Schonhals, A. and F. Kremer, Broadband Dielectric Spectroscopy, Springer, Berlin, 2003.

160. Knauth, P. and M.L. Di Vona, *Solid State Proton Conductors: Properties and Applications in Fuel Cells, Chapter 5.* 2012 John WILEY & Sons Ltd., 2012. **A Powerful Tool for the Determination of Charge Transfer Mechanisms in Ion Conductors**.
161. Alpha-A impedance analyzer Instrument Manual, N.
162. Zeng, Y.K., et al., *A high-performance flow-field structured iron-chromium redox flow battery.* Journal of Power Sources, 2016. **324**: p. 738-744.
163. Joseph, J., C.-Y. Tseng, and B.-J. Hwang, *Phosphonic acid-grafted mesostructured silica/Nafion hybrid membranes for fuel cell applications.* Journal of Power Sources, 2011. **196**(18): p. 7363-7371.
164. Maneeratana, V., et al., *Fractal inorganic-organic interfaces in hybrid membranes for efficient proton transport.* Advanced Functional Materials, 2013. **23**(22): p. 2872-2880.
165. Giffin, G.A., et al., *Characterization of sulfated-zirconia/Nafion® composite membranes for proton exchange membrane fuel cells.* Journal of Power Sources, 2012. **198**: p. 66-75.
166. Di Noto, V., et al., *New inorganic–organic proton conducting membranes based on Nafion and hydrophobic fluoroalkylated silica nanoparticles.* Journal of Power Sources, 2010. **195**(23): p. 7734-7742.
167. Granqvist, C.G., E. Avendaño, and A. Azens, *Electrochromic coatings and devices: survey of some recent advances.* Thin Solid Films, 2003. **442**(1): p. 201-211.
168. Shinde, P.A., et al., *Single-step hydrothermal synthesis of WO3-MnO2 composite as an active material for all-solid-state flexible asymmetric supercapacitor.* International Journal of Hydrogen Energy, 2018. **43**(5): p. 2869-2880.
169. Qadri, M.U., et al., *WO3 thin films for optical gas sensing.* Procedia Engineering, 2011. **25**: p. 260-263.
170. Lee, W., et al., *Mesoporous tungsten oxynitride as electrocatalyst for promoting redox reactions of vanadium redox couple and performance of vanadium redox flow battery.* Applied Surface Science, 2018. **429**: p. 187-195.
171. Jingkun, X., et al., *Synthesis, Characterization, and Gas Sensing Properties of WO3 Nanoplates.* Rare Metal Materials and Engineering, 2017. **46**(5): p. 1241-1244.
172. Chandrabose Raghu, S., et al., *Electrochemical behaviour of titanium/iridium(IV) oxide: Tantalum pentoxide and graphite for application in vanadium redox flow battery.* Journal of Power Sources, 2013. **238**: p. 103-108.
173. Wei, X. and P.K. Shen, *Electrochromics of single crystalline WO3·H2O nanorods.* Electrochemistry Communications, 2006. **8**(2): p. 293-298.
174. Negro, E., et al., *The influence of the cationic form and degree of hydration on the structure of Nafion™.* Solid State Ionics, 2013. **252**: p. 84-92.
175. Di Noto, V., et al., *Structure, properties and proton conductivity of Nafion/[(TiO_2)·(WO_3)$_{0.148}$]YTiO_2 nanocomposite membranes.* Electrochimica Acta, 2010. **55**(4): p. 1431-1444.
176. Page, K.A., K.M. Cable, and R.B. Moore, *Molecular origins of the thermal transitions and dynamic mechanical relaxations in perfluorosulfonate ionomers.* Macromolecules, 2005. **38**(15): p. 6472-6484.
177. De Almeida, S. and Y. Kawano, *Thermal behavior of Nafion membranes.* Journal of Thermal Analysis and Calorimetry, 1999. **58**(3): p. 569-577.

178. Di Noto, V., et al., *Interplay between Mechanical, Electrical, and Thermal Relaxations in Nanocomposite Proton Conducting Membranes Based on Nafion and a [$(ZrO_2)\cdot(Ta_2O_5)_{0.119}$] Core–Shell Nanofiller.* Journal of the American Chemical Society, 2012. **134**(46): p. 19099-19107.
179. Di Noto, V., et al., *Structure, properties and proton conductivity of Nafion/[$(TiO_2)(WO_3)_{0.148}$] ψTiO_2 nanocomposite membranes.* Electrochimica Acta, 2010. **55**(4): p. 1431-1444.
180. Buzzoni, R., et al., *Interaction of H_2O, CH_3OH,$(CH_3)_2O$, CH_3CN, and pyridine with the superacid perfluorosulfonic membrane Nafion: an IR and Raman study.* The Journal of Physical Chemistry, 1995. **99**(31): p. 11937-11951.
181. Grosmaire, L., et al., *Probing proton dissociation in ionic polymers by means of in situ ATR-FTIR spectroscopy.* Physical Chemistry Chemical Physics, 2008. **10**(11): p. 1577-1583.
182. Gruger, A., et al., *Nanostructure of Nafion® membranes at different states of hydration: An IR and Raman study.* Vibrational Spectroscopy, 2001. **26**(2): p. 215-225.
183. Kustova, G.N., et al., *Vibrational spectra of $WO_3\cdot nH_2O$ and WO_3 polymorphs.* Vibrational Spectroscopy, 2011. **55**(2): p. 235-240.
184. Barraclough, C. and J. Stals, *Spectral and structural studies of some Group VIA dioxydihalides.* Australian Journal of Chemistry, 1966. **19**(5): p. 741-750.
185. Di Noto, V., et al., *New inorganic–organic proton conducting membranes based on Nafion® and [(ZrO2)·(SiO2)0.67] nanoparticles: Synthesis vibrational studies and conductivity.* Journal of Power Sources, 2008. **178**(2): p. 561-574.
186. Daniel, M., et al., *Infrared and Raman study of WO_3 tungsten trioxides and WO_3, xH_2O tungsten trioxide tydrates.* Journal of solid state chemistry, 1987. **67**(2): p. 235-247.
187. Garcia-Sanchez, R.F., et al., *Thermal effects associated with the Raman spectroscopy of WO_3 gas-sensor materials.* The Journal of Physical Chemistry A, 2013. **117**(50): p. 13825-13831.
188. Rougier, A., et al., *Characterization of pulsed laser deposited WO_3 thin films for electrochromic devices.* Applied Surface Science, 1999. **153**(1): p. 1-9.
189. Di Noto, V., et al., *Inorganic-organic membranes based on Nafion, [$(ZrO_2)\cdot(HfO_2)_{0.25}$] and [$(SiO_2)\cdot(HfO_2)_{0.28}$] nanoparticles. Part II: Relaxations and conductivity mechanism.* International Journal of Hydrogen Energy, 2012. **37**(7): p. 6215-6227.
190. Di Noto, V., et al., *Structure-relaxation interplay of a new nanostructured membrane based on tetraethylammonium trifluoromethanesulfonate ionic liquid and neutralized Nafion 117 for high-temperature fuel cells.* Journal of the American Chemical Society, 2010. **132**(7): p. 2183-2195.
191. Skyllas-Kazacos, M., et al., *Progress in flow battery research and development.* Journal of The Electrochemical Society, 2011. **158**(8): p. R55-R79.
192. Kim, J., J.-D. Jeon, and S.-Y. Kwak, *Nafion-based composite membrane with a permselective layered silicate layer for vanadium redox flow battery.* Electrochemistry Communications, 2014. **38**: p. 68-70.
193. Weber, A.Z., et al., *Redox flow batteries: a review.* Journal of Applied Electrochemistry, 2011. **41**(10): p. 1137.
194. Mohammadi, T. and M. Skyllas Kazacos, *Evaluation of the chemical stability of some membranes in vanadium solution.* Journal of Applied Electrochemistry, 1997. **27**(2): p. 153-160.

195. Ashraf Gandomi, Y., D.S. Aaron, and M.M. Mench, *Influence of membrane equivalentweight and reinforcement on ionic species crossover in all-vanadium redox flow batteries.* Membranes, 2017. **7**(2): p. Article #29.
196. Sun, C., et al., *[Nafion/(WO3)x] hybrid membranes for vanadium redox flow batteries.* Solid State Ionics, 2018. **319**: p. 110-116.
197. Di Noto, V., et al., *Hybrid inorganic–organic proton conducting membranes based on Nafion and 5wt.% of MxOy (M=Ti, Zr, Hf, Ta and W): Part I. Synthesis, properties and vibrational studies.* Electrochimica Acta, 2007. **53**(4): p. 1618-1627.
198. Di Noto, V., et al., *Structure, properties and proton conductivity of Nafion / [(Ti O2) ś (W O3)0.148]ψ Ti O2 nanocomposite membranes.* Electrochimica Acta, 2010. **55**(4): p. 1431-1444.
199. Gubler, L. and G.G. Scherer, *A proton-conducting polymer membrane as solid electrolyte - Function and required properties*, in *Advances in Polymer Science*. 2008. p. 1-14.
200. Tang, Z., et al. *Proton exchange membrane performance characterization in VRFB*. in *ECS Transactions*. 2012.
201. Li, L., et al., *Effect of sulfonated poly(ether ether ketone) membranes with different sulfonation degrees on the performance of vanadium redox flow battery.* Acta Chimica Sinica, 2009. **67**(24): p. 2785-2790.
202. Lei, L., et al., *Highly stable ionic-covalent cross-linked sulfonated poly(ether ether ketone) for direct methanol fuel cells.* Journal of Power Sources, 2017. **350**: p. 41-48.
203. Seetharaman, S., et al., *Sulfonated poly (ether ether)-based composite proton-exchange membrane for energy production.* International Journal of Polymeric Materials and Polymeric Biomaterials, 2011. **60**(10): p. 742-753.
204. Arthanareeswaran, G., D. Mohan, and M. Raajenthiren, *Preparation and performance of polysulfone-sulfonated poly(ether ether ketone) blend ultrafiltration membranes. Part I.* Applied Surface Science, 2007. **253**(21): p. 8705-8712.
205. Xi, J., et al., *Effect of degree of sulfonation and casting solvent on sulfonated poly(ether ether ketone) membrane for vanadium redox flow battery.* Journal of Power Sources, 2015. **285**: p. 195-204.
206. Zaidi, S.M.J., et al., *Proton conducting composite membranes from polyether ether ketone and heteropolyacids for fuel cell applications.* Journal of Membrane Science, 2000. **173**(1): p. 17-34.
207. Tripathi, B.P. and V.K. Shahi, *Surface redox polymerized SPEEK-MO2-PANI (M = Si, Zr and Ti) composite polyelectrolyte membranes impervious to methanol.* Colloids and Surfaces A: Physicochemical and Engineering Aspects, 2009. **340**(1-3): p. 10-19.
208. Elakkiya, S., et al., *Enhancement of fuel cell properties in polyethersulfone and sulfonated poly (ether ether ketone) membranes using metal oxide nanoparticles for proton exchange membrane fuel cell.* International Journal of Hydrogen Energy, 2018.
209. Kulesza, P.J., et al. *Enhancement of the eleetrocatalytic reduction of oxygen at tungsten oxide modified carbon-supported RuSex nanoparticles and Co-porphyrin centers*. in *ECS Transactions*. 2007.
210. Jalani, N.H., K. Dunn, and R. Datta, *Synthesis and characterization of Nafion®-MO2 (M = Zr, Si, Ti) nanocomposite membranes for higher temperature PEM fuel cells.* Electrochimica Acta, 2005. **51**(3): p. 553-560.

211. Di Noto, V., et al., *Hybrid inorganic-organic nanocomposite polymer electrolytes based on Nafion and fluorinated TiO<inf>2</inf>for PEMFCs.* International Journal of Hydrogen Energy, 2012. **37**(7): p. 6169-6181.
212. Di Noto, V., et al., *Inorganic-organic membranes based on Nafion, [(ZrO<inf>2</inf>) ·(HfO<inf>2</inf>)<inf>0.25</inf>] and [(SiO<inf>2</inf>) ·(HfO<inf>2</inf>)<inf>0.28</inf>]. Part I: Synthesis, thermal stability and performance in a single PEMFC.* International Journal of Hydrogen Energy, 2012. **37**(7): p. 6199-6214.
213. Di Noto, V., et al., *Inorganic-organic membranes based on Nafion, [(ZrO<inf>2</inf>) ·(HfO<inf>2</inf>)<inf>0.25</inf>] and [(SiO<inf>2</inf>) ·(HfO<inf>2</inf>)<inf>0.28</inf>] nanoparticles. Part II: Relaxations and conductivity mechanism.* International Journal of Hydrogen Energy, 2012. **37**(7): p. 6215-6227.
214. Di Noto, V., et al., *New nanocomposite hybrid inorganic-organic proton-conducting membranes based on functionalized silica and PTFE.* ChemSusChem, 2012. **5**(9): p. 1758-1766.
215. Di Noto, V., et al., *Interplay between mechanical, electrical, and thermal relaxations in nanocomposite proton conducting membranes based on nafion and a [(ZrO <inf>2</inf>)(Ta<inf>2</inf>O<inf>5</inf>)<inf>0.119</inf>] core-shell nanofiller.* Journal of the American Chemical Society, 2012. **134**(46): p. 19099-19107.
216. Di Noto, V., et al. *New hybrid inorganic-organic proton conducting membranes based on Nation and a [(ZrO<inf>2</inf>)·(Ta<inf>2</inf>O<inf>5</inf>)<inf>0.119</inf>] oxide core-shell nanofiller*. in *Materials Research Society Symposium Proceedings*. 2012.
217. Lin, C.H., M.C. Yang, and H.J. Wei, *Amino-silica modified Nafion membrane for vanadium redox flow battery.* Journal of Power Sources, 2015. **282**: p. 562-571.
218. Nawn, G., et al., *Electric response and conductivity mechanism reciprocity in H3PO4-doped Polybenzimidazole-4N-ZrO2 nanocomposite membranes.* Solid State Ionics, 2018. **320**: p. 172-176.
219. Nawn, G., et al., *Nanocomposite Membranes based on Polybenzimidazole and ZrO2 for High-Temperature Proton Exchange Membrane Fuel Cells.* ChemSusChem, 2015. **8**(8): p. 1381-1393.
220. Di Noto, V., et al., *Broadband electric spectroscopy of proton conducting SPEEK membranes.* Journal of Membrane Science, 2012. **390-391**: p. 58-67.
221. Li, Z., et al., *Sulfonated poly(ether ether ketone)/mesoporous silica hybrid membrane for high performance vanadium redox flow battery.* Journal of Power Sources, 2014. **257**: p. 221-229.
222. Liu, Y., et al., *Interface engineering and its effect on WO3 -based photoanode and tandem cell.* ACS Applied Materials and Interfaces, 2018. **10**(15): p. 12639-12650.
223. Miecznikowski, K., P.J. Kulesza, and S. Fiechter, *Application of Black Pearl carbon-supported WO3 nanostructures as hybrid carriers for electrocatalytic RuSex nanoparticles.* Applied Surface Science, 2011. **257**(19): p. 8215-8222.
224. Shinde, P.A., et al., *Single-step hydrothermal synthesis of WO<inf>3</inf>-MnO<inf>2</inf>composite as an active material for all-solid-state flexible*

asymmetric supercapacitor. International Journal of Hydrogen Energy, 2018. **43**(5): p. 2869-2880.

225. Faraji, M., A. Hassanzadeh, and M. Mohseni, *Interlaced WO<inf>3</inf>-carbon nanotube nanocomposite electrodeposited on graphite as a positive electrode in vanadium redox flow battery.* Thin Solid Films, 2017. **642**: p. 188-194.
226. Hosseini, M.G., et al., *High-power positive electrode based on synergistic effect of N- and WO<inf>3</inf>-decorated carbon felt for vanadium redox flow batteries.* Carbon, 2018. **136**: p. 444-453.
227. Lufrano, F., et al., *Sulfonated polysulfone as promising membranes for polymer electrolyte fuel cells.* Journal of Applied Polymer Science, 2000. **77**(6): p. 1250-1256.
228. Silva, V.S., et al., *Proton electrolyte membrane properties and direct methanol fuel cell performance - I. Characterization of hybrid sulfonated poly(ether ether ketone)/zirconium oxide membranes.* Journal of Power Sources, 2005. **140**(1): p. 34-40.
229. Di Noto, V., et al., *Hybrid inorganic-organic proton conducting membranes based on Nafion and 5 wt.% of M<inf>x</inf>O<inf>y</inf>(M = Ti, Zr, Hf, Ta and W). Part I. Synthesis, properties and vibrational studies.* Electrochimica Acta, 2007. **53**(4): p. 1618-1627.
230. Gil, M., et al., *Direct synthesis of sulfonated aromatic poly(ether ether ketone) proton exchange membranes for fuel cell applications.* Journal of Membrane Science, 2004. **234**(1-2): p. 75-81.
231. Shi, Y. and R.A. Weiss, *Sulfonated poly(ether ether ketone) ionomers and their high temperature shape memory behavior.* Macromolecules, 2014. **47**(5): p. 1732-1740.
232. Wilhelm, F.G., et al., *Cation permeable membranes from blends of sulfonated poly(ether ether ketone) and poly(ether sulfone).* Journal of Membrane Science, 2002. **199**(1): p. 167-176.
233. Yin, B., et al., *Nano oxides incorporated sulfonated poly(ether ether ketone) membranes with improved selectivity and stability for vanadium redox flow battery.* Journal of Solid State Electrochemistry, 2016. **20**(5): p. 1271-1283.
234. Wootthikanokkhan, J. and N. Seeponkai, *Methanol permeability and properties of DMFC membranes based on sulfonated PEEK/PVDF blends.* Journal of Applied Polymer Science, 2006. **102**(6): p. 5941-5947.
235. Pan, J., et al., *Layered zirconium phosphate sulfophenylphosphonates reinforced sulfonated poly (fluorenyl ether ketone) hybrid membranes with high proton conductivity and low vanadium ion permeability.* Journal of Membrane Science, 2013. **443**: p. 19-27.
236. Chang, J.H., et al., *Proton-conducting composite membranes derived from sulfonated hydrocarbon and inorganic materials.* Journal of Power Sources, 2003. **124**(1): p. 18-25.
237. Kopitzke, R.W., et al., *Conductivity and water uptake of aromatic-based proton exchange membrane electrolytes.* Journal of the Electrochemical Society, 2000. **147**(5): p. 1677-1681.
238. Tseng, C.Y., et al., *Sulfonated polyimide proton exchange membranes with graphene oxide show improved proton conductivity, methanol crossover impedance, and mechanical properties.* Advanced Energy Materials, 2011. **1**(6): p. 1220-1224.
239. Kim, J., J.D. Jeon, and S.Y. Kwak, *Nafion-based composite membrane with a permselective layered silicate layer for vanadium redox flow battery.* Electrochemistry Communications, 2014. **38**: p. 68-70.

240. Ashraf Gandomi, Y., D.S. Aaron, and M.M. Mench, *Influence of membrane equivalentweight and reinforcement on ionic species crossover in all-vanadium redox flow batteries.* Membranes, 2017. **7**(2).
241. Chen, D., et al., *Advanced acid-base blend ion exchange membranes with high performance for vanadium flow battery application.* Journal of Membrane Science, 2018. **553**: p. 25-31.
242. Li, Z., et al., *Preparation and characterization of sulfonated poly(ether ether ketone)/poly(vinylidene fluoride) blend membrane for vanadium redox flow battery application.* Journal of Power Sources, 2013. **237**: p. 132-140.
243. Nagarale, R.K., G.S. Gohil, and V.K. Shahi, *Sulfonated poly(ether ether ketone)/polyaniline composite proton-exchange membrane.* Journal of Membrane Science, 2006. **280**(1-2): p. 389-396.
244. Naffakh, M., et al., *Thermal decomposition of technological polymer blends 1. Poly (aryl ether ether ketone) with a thermotropic liquid crystalline polymer.* Polymer degradation and stability, 1999. **66**(3): p. 405-413.
245. Di Noto, V., et al., *New inorganic-organic proton conducting membranes based on Nafion®and [(ZrO<inf>2</inf>)·(SiO<inf>2</inf>)<inf>0.67</inf>] nanoparticles: Synthesis vibrational studies and conductivity.* Journal of Power Sources, 2008. **178**(2): p. 561-574.
246. Viswanathan, V., et al., *Cost and performance model for redox flow batteries.* Journal of Power Sources, 2014. **247**: p. 1040-1051.
247. Cuce, E., et al., *Toward aerogel based thermal superinsulation in buildings: A comprehensive review.* Renewable and Sustainable Energy Reviews, 2014. **34**: p. 273-299.
248. Eckroad, S., *Vanadium Redox Flow Batteries, An In-Depth Analysis*

EPRI Project Manager 2007. **1014836**
249. Skyllas-Kazacos, M. and M. Kazacos, *State of charge monitoring methods for vanadium redox flow battery control.* Journal of Power Sources, 2011. **196**(20): p. 8822-8827.
250. Tang, Z., et al. *Monitoring the state of charge of operating vanadium redox flow batteries*. in *ECS Transactions*. 2012.
251. Lawton, J.S., et al., *Ion effects on vanadium transport in Nafion membranes for vanadium redox flow batteries.* Journal of the Electrochemical Society, 2017. **164**(13): p. A2987-A2991.
252. Xiong, B., et al., *Extended Kalman filter method for state of charge estimation of vanadium redox flow battery using thermal-dependent electrical model.* Journal of Power Sources, 2014. **262**: p. 50-61.
253. Binyu, X., et al. *State of charge estimation of an all-vanadium redox flow battery based on a thermal-dependent model*. in *Asia-Pacific Power and Energy Engineering Conference, APPEEC*. 2013.
254. Holland-Cunz, M.V., J. Friedl, and U. Stimming, *Anion effects on the redox kinetics of positive electrolyte of the all-vanadium redox flow battery.* Journal of Electroanalytical Chemistry, 2018. **819**: p. 306-311.
255. Post, K. and R.G. Robins, *Thermodynamic diagrams for the vanadium-water system at 298·15K.* Electrochimica Acta, 1976. **21**(6): p. 401-405.
256. Zhu, H.Q., et al., *Graphite-carbon nanotube composite electrodes for all vanadium redox flow battery.* Journal of Power Sources, 2008. **184**(2): p. 637-640.

257. Jiang, B., et al., *A comparative study of Nafion series membranes for vanadium redox flow batteries.* Journal of Membrane Science, 2016. **510**: p. 18-26.
258. Kazacos, M., M. Cheng, and M. Skyllas-Kazacos, *Vanadium redox cell electrolyte optimization studies.* Journal of Applied Electrochemistry, 1990. **20**(3): p. 463-467.
259. Oriji, G., Y. Katayama, and T. Miura, *Investigation on V(IV)/V(V) species in a vanadium redox flow battery.* Electrochimica Acta, 2004. **49**(19): p. 3091-3095.
260. Skyllas-Kazacos, M., C. Peng, and M. Cheng, *Evaluation of Precipitation Inhibitors for Supersaturated Vanadyl Electrolytes for the Vanadium Redox Battery.* Electrochemical and Solid-State Letters, 1999. **2**(3): p. 121-122.
261. Sadoc, A., et al., *Structure and stability of VO2+ in aqueous solution: A car-parrinello and static ab initio study.* Inorganic Chemistry, 2007. **46**(12): p. 4835-4843.
262. Cotton, F.A., et al., *Advanced Inorganic Chemistry, 6th Ed., John Wiley & Sons, New York* 1999: p. 723.
263. Griffith, W.P. and P.J.B. Lesniak, *Raman studies on species in aqueous solutions. Part III. Vanadates, molybdates, and tungstates.* Journal of the Chemical Society A: Inorganic, Physical, and Theoretical Chemistry, 1969: p. 1066-1071.
264. Nakamoto, K., *Infrared and Raman Spectra of Inorganic and Coordination Compound Part B.* **2nd Edition**: p. 436.
265. Kanamori, K., et al., *Raman Spectral Study on the Structure of a Hydrolytic Dimer of the Aquavanadium(III) Ion.* Inorganic Chemistry, 1991. **30**(20): p. 3832-3836.
266. Madic, C., et al., *Dimerization of Aquadioxovanadium(V) Ion in Concentrated Perchloric and Sulfuric Acid Media1a.* Inorganic Chemistry, 1984. **23**(4): p. 469-476.
267. Twu, J., et al., *Raman spectroscopic studies of the thermal decomposition mechanism of ammonium metavanadate.* Journal of Materials Chemistry, 1997. **7**(11): p. 2273-2277.
268. Colthup, D.N., *Introduction to Infrared and Raman Spectroscopy.* **2nd Edition**: p. 376.
269. Irish, D.E. and H. Chen, *Equilibria and proton transfer in the bisulfate-sulfate system.* Journal of Physical Chemistry, 1970. **74**(21): p. 3796-3801.
270. Tomikawa, K. and H. Kanno, *Raman study of sulfuric acid at low temperatures.* Journal of Physical Chemistry A, 1998. **102**(30): p. 6082-6088.
271. Mahajan, C.V. and V. Ganesan, *Atomistic simulations of structure of solvated sulfonated poly(ether ether ketone) Membranes and their comparisons to nafion: I. Nanophase segregation and hydrophilic domains.* Journal of Physical Chemistry B, 2010. **114**(25): p. 8357-8366.
272. Liu, S., et al., *Novel sulfonated poly (ether ether keton)/polyetherimide acid-base blend membranes for vanadium redox flow battery applications.* Electrochimica Acta, 2014. **130**: p. 90-96.
273. Ling, X., et al., *Preparation and characterization of sulfonated poly(ether sulfone)/sulfonated poly(ether ether ketone) blend membrane for vanadium redox flow battery.* Journal of Membrane Science, 2012. **415-416**: p. 306-312.
274. Dai, W., et al., *Sulfonated Poly(Ether Ether Ketone)/Graphene composite membrane for vanadium redox flow battery.* Electrochimica Acta, 2014. **132**: p. 200-207.
275. Teng, X., et al., *A high performance polytetrafluoroethene/Nafion composite membrane for vanadium redox flow battery application.* Journal of Power Sources, 2013. **240**: p. 131-139.